# MODIFICATION OF FUNGAL BIOMASS BY IMMOBILIZATION AND HYDROTHEMRAL CARBONIZATION FOR THE REMOVAL OF CR(VI)

HO KWOK PAN

PhD

The Hong Kong Polytechnic University

2020

The Hong Kong Polytechnic University

Department of Applied Biology and Chemical Technology

# Modification of Fungal Biomass by Immobilization and Hydrothermal Carbonization for the Removal of Cr(VI)

Ho Kwok Pan

A thesis submitted in partial fulfillment of the requirements for the degree of

**DOCTOR OF PHILOSOPHY**

Jun 2019

# Certification of Originality

I hereby declare that this thesis is my own work and that, to the best of my knowledge and belief, it reproduces no material previously published or written, nor material that has been accepted for the award of any other degree or diploma, except where due acknowledge has been made in the text.

Ho Kwok Pan

# Abstract

Fungal biomass, *Mucor rouxii* (MR), was immobilized by a novel silica-doped calcium alginate method and the immobilized MR was applied as an adsorbent for the removal of Cr(VI) from aqueous solution. The Cr(VI) removal ability of the silica-doped calcium-alginate-immobilized *Mucor rouxii* (SCAIM) was examined in batch and continuous modes. The batch Cr(VI) removal studies were investigated as a function of contact time, solution pH, initial Cr(VI) concentration, adsorbent dosage, temperature and agitation speed. The experimental results demonstrated that the obtained SCAIM displayed higher experimental maximum Cr(VI) removal capacities ($Q_{Cr(VI)}$ = 131.8 ±1.4 mg/g) than MR (79.54 ± 1.19 mg/g). The maximum Cr(VI) removal capacity of MR was greatly enhanced after immobilization. Continuous removal of Cr(VI) was studied in a fixed-bed column by varying the flow rate and the initial concentration of Cr(VI) influent. Moreover, the surface morphology and elemental composition of pristine and Cr-loaded adsorbents were characterized by scanning electron microscopy (SEM), Fourier-transform infrared spectroscopy (FTIR), energy-dispersive X-ray spectroscopy (EDX) and X-ray photoelectron spectroscopy (XPS). Based on the results of adsorption studies and characterizations, a four-step Cr(VI) adsorption-reduction mechanism was proposed: (1) adsorption of the anionic Cr(VI) on the positively-charged adsorption sites (e.g., amine groups) through the electrostatic interaction; (2) reduction of the adsorbed Cr(VI) to Cr(III) by the adjacent reductive surface groups (e.g., hydroxyl groups); (3) adsorption of

the Cr(III) by the carboxylic acid groups; and (4) desorption of the Cr(III) due to the electrostatic repulsion. The obtained results suggest that the SCAIM is a promising adsorbent for the removal and detoxification of Cr(VI) from aqueous solutions.

Silica-doped zirconium-alginate-immobilized *M. rouxii* (SZAIM) beads were successfully prepared by the subsequent soaking of the SCAIM beads in the 4% zirconyl chloride solution. The XPS results demonstrated the complete replacement of the Ca(II) ions in calcium alginate by the Zr(IV) ions through the ion-exchange mechanism. The obtained SZAIM beads exhibited improved experimental maximum Cr(VI) removal capacity ($Q_{Cr(VI)}$ = 169.6 ± 2.6 mg/g) than that of the SCAIM beads since the Zr(IV) ions in SZAIM beads served as extra adsorption sites for Cr(VI).

Further, *Mucor rouxii* was transformed to hydrochars by a one-pot hydrothermal carbonization process, and the hydrothermal carbonized MR (HTC-MR) was applied as an adsorbent for the removal of Cr(VI) from aqueous solutions. Moreover, the doping of nitrogen groups onto HTC-MR was done by the co-carbonization of MR with the amine-containing modifying agents, such as ammonium hydroxide, acrylamide (AA), diethanolamine (DEA), polyethyleneimine (PEI), triethylenetetramine (TETA) and urea. The Cr(VI) removal capacity ($Q_{Cr(VI)}$) of HTC-MR was significantly enhanced by the functionalization of nitrogen groups. The hydrothermal carbonization process was then optimized by varying different reaction parameters, including reaction temperature, reaction time and modifying agent dosage. Besides,

the HTC-MR was synthesized in the presence of eutectic salt ($CaCl_2$-$FeCl_3$) in order to improve the surface area and porosity of HTC-MR.

Batch adsorption experiments were conducted to evaluate the Cr(VI) removal capacities ($Q_{Cr(VI)}$) of HTC-MR, 0.5DEA-HTC-MR and 0.5PEI-HTC-MR. It was clearly observed that the three HTC materials showed excellent removal capacity to Cr(VI). The Cr(VI) removal capacities of HTC-MR, 0.5DEA-HTC-MR and 0.5PEI-HTC-MR were optimized with several factors, including contact time, solution pH, initial Cr(VI) concentration, adsorbent dosage and temperature. The kinetic profile of $Q_{Cr(VI)}$ demonstrated that the Cr(VI) was rapidly removed by HTC-MR, 0.5DEA-HTC-MR and 0.5PEI-HTC-MR from the solution phase in the first one hour, and the Cr(VI) removal rate slowed down afterward. The HTC-MR showed faster Cr(VI) removal rate and higher equilibrium Cr(VI) removal capacity than the raw MR. Moreover, the Cr(VI) removal capacities of HTC-MR, 0.5DEA-HTC-MR and 0.5PEI-HTC-MR at 3-day contact time were 158.4 ± 0.7, 209.5 ± 2.5 and 239.3 ± 2.7, respectively. The adsorption results indicated that DEA and PEI were effective for further increasing the Cr(VI) removal capacity of HTC-MR.

The optimum pH for Cr(VI) removal by HTC-MR was pH 2.0, while a high Cr(VI) removal capacity by 0.5DEA-HTC-MR and 0.5PEI-HTC-MR was obtained at pH 2.0 to 4.0. The anionic Cr(VI) ions were adsorbed onto the positively-charged adsorbent surface through the electrostatic interaction. The fractional power model was the best-fit model to simulate the

Cr(VI) removal kinetics of HTC-MR and 0.5PEI-HTC-MR with the lowest RMSE value and the highest correlation coefficient. Meanwhile, the Cr(VI) removal kinetics of 0.5DEA-HTC-MR was better described by the Elovich kinetic model. The Langmuir isotherm was the best-fit model to fit the experimental isotherm data of HTC-MR, 0.5DEA-HTC-MR and 0.5PEI-HTC-MR, and the simulated maximum total Cr adsorption capacity was 115.7 ± 10.8, 269.8 ± 5.9 and 414.6 ± 11.5 mg/g, respectively. Four different desorption agents (e.g., 0.5 M $HNO_3$, 2.0 M $HNO_3$, 0.5 M NaOH and 2.0 M NaOH) were tested for their Cr(VI) desorption performance on the Cr-laden HTC materials. Desorption results showed that both $HNO_3$ and NaOH solutions were effective desorption agents but with different Cr desorption mechanisms. Physical and chemical characteristics of HTC materials were examined by elemental analysis (EA), $N_2$ adsorption/desorption isotherm, Fourier-transformed Infrared spectroscopy (FTIR), 13C nuclear magnetic resonance spectroscopy (13C NMR), X-ray photoelectron spectroscopy (XPS) and isothermal titration calorimetry (ITC). In summary, the hydrothermal carbonized *M. rouxii* (HTC-MR) was a promising adsorbent for the removal of Cr(VI) in the aqueous phase. Diethanolamine (DEA) and polyethyleneimine (PEI) effectively improved the Cr(VI) removal capacity of HTC-MR by surface functionalization. The Cr(VI) was removed from the aqueous solution by HTC materials through (1) direct adsorption mechanism and (2) adsorption-coupled reduction mechanism. Finally, the magnetic $Fe_3O_4$-0.5PEI-HTC-MR was fabricated by incorporating $Fe_3O_4$ nanoparticles into 0.5PEI-HTC-MR, so the $Fe_3O_4$-0.5PEI-HTC-MR

could be recovered by external magnetic field after Cr(VI) adsorption process.

# Acknowledgements

I wish to express my sincere gratitude to my supervisor Dr. Lo Wai-hung, Thomas, for his kind guidance, constant supervision and constructive suggestions throughout the entire period of this study.

I am also grateful to Dr. Lo Lai-shan, Dr. Lam Yan-yan, Ms. Wang Qian, Mr. Chan Kwan-shing, Mr. Kim Chi-fai and my research colleagues for their valuable supports and helps. I am particularly grateful for the assistance given by the technicians of the ABCT department.

I wish to thank my family and friends for their continuous support and encouragement. My special thanks are extended to all members of the hiking groups “Hikingwindfire” for providing me with an opportunity to enjoy the breathtaking scenery of Hong Kong’s countryside.

Finally, I would like to thank the Research Committee of the Hong Kong Polytechnic University and the Research Grants Council (RGC) of Hong Kong SAR for funding this project.

# Tables of Contents

**Certification of Originality** ..... **i**

**Abstract** ..... **ii**

**Acknowledgements** ..... **vii**

**Tables of Contents** ..... **viii**

**List of Abbreviations** ..... **xv**

**List of Figures** ..... **xix**

**List of Tables** ..... **xxvi**

**1. Introduction** ..... **2**

1.1 Motivation ..... 3

1.2 Objectives ..... 8

1.3 Organization of thesis ..... 10

**2. Literature Review** ..... **12**

2.1 Immobilization of biomaterials ..... 13

2.2 Hydrothermal carbonization of biomaterials ..... 19

2.3 Biosorption modelling ..... 27

2.3.1 Adsorption kinetic models ..... 27

2.3.2 Adsorption isotherm models ..... 31

2.4 Cr(VI) removal mechanism .....36

**3. Materials and Methods.....45**

3.1 Instrumentations.....46

3.2 Chemicals.....47

3.3 Cultivation of *M. rouxii* .....48

3.4 Immobilization of *M. rouxii*.....49

3.4.1 Silica-doped calcium alginate.....49

3.4.2 Silica-doped zirconium alginate .....50

3.5 Preparation of hydrothermal carbonized *M. rouxii*.....51

3.5.1 Preparation of hydrothermal carbonized *M. rouxii* (HTC-MR).....51

3.5.2 Incorporation of zirconium oxide in hydrothermal carbonized *M. rouxii* ($ZrO_2$-$NH_4$-HTC-MR).....52

3.5.3 Hydrothermal carbonized *M. rouxii* in the eutectic salt template (HTC-MR-CaFe) .....52

3.5.4 Preparation of magnetic hydrothermal carbonized *M. rouxii* ($Fe_3O_4$-0.5PEI-HTC-MR) .....53

3.6 Cr(VI) removal studies .....54

3.6.1 Basic procedures for Cr(VI) removal studies .....54

3.6.2 Screening of cationic and anionic pollutants .....56

3.6.3 Effect of contact time ..... 57

3.6.4 Effect of pH ..... 57

3.6.5 Effect of initial Cr(VI) concentration ..... 57

3.6.6 Effect of adsorbent dosage ..... 58

3.6.7 Effect of temperature and thermodynamic study ..... 58

3.6.8 Cr desorption study ..... 59

3.6.9 Continuous Cr(VI) removal study ..... 60

3.7 Characterization of adsorbents ..... 61

**4. Removal of Cr(VI) by Immobilized *M. rouxii* ..... 63**

4.1 Physical and basic chemical properties of silica-doped calcium-alginate-immobilized *M. rouxii* ..... 64

4.1.1 $N_2$ adsorption/desorption isotherm ..... 64

4.1.2 Physical properties ..... 67

4.1.3 Chemical stability ..... 70

4.1.4 Mechanical strength ..... 75

4.2 Screening of cationic and anionic pollutants ..... 77

4.3 Removal of Cr(VI) by silica-doped calcium-alginate-immobilized *M. rouxii* 79

4.3.1 Effect of contact time ..... 79

4.3.2 Effect of pH ..... 84

4.3.3 Kinetic modelling....91

4.3.4 Cr(VI) reduction kinetic model....96

4.3.5 Intra-particle diffusion analysis....103

4.3.6 Effect of initial Cr(VI) concentration....108

4.3.7 Isotherm modelling....111

4.3.8 Effect of adsorbent dosage....117

4.3.9 Effect of temperature....122

4.3.10 Effect of agitation speed....127

4.3.11 Cr desorption studies....130

4.4 Continuous Cr(VI) removal by silica-doped calcium-alginate-immobilized *M. rouxii*....132

4.4.1 Column adsorption....132

4.4.2 Column desorption....135

4.5 Removal of Cr(VI) by silica-doped zirconium-alginate-immobilized *M. rouxii*....137

4.5.1 Screening of anionic pollutants....137

4.5.2 Effect of pH....139

4.5.3 Effect of contact time and kinetic modelling....141

4.5.4 Effect of initial concentration and isotherm modelling....147

4.6 Characterizations of immobilized *M. rouxii* ..... 150

4.6.1 Fourier-transform Infrared spectroscopy (FTIR) ..... 150

4.6.2 Scanning electron microscopy (SEM) ..... 157

4.6.3 X-ray photoelectron spectroscopy (XPS) ..... 163

4.7 Cr(VI) removal mechanisms ..... 195

**5. Removal of Cr(VI) by Hydrothermal Carbonized *M. rouxii* ..... 202**

5.1 Physical and basic chemical properties of hydrothermal carbonized *M. rouxii* ..... 203

5.1.1 $N_2$ adsorption/desorption isotherm ..... 203

5.1.2 Dynamic light scattering ..... 207

5.1.3 Elemental analysis (EA) ..... 208

5.2 Preparation of hydrothermal carbonized *M. rouxii* ..... 216

5.2.1 Effect of the modifying agent ..... 216

5.2.2 Effect of temperature ..... 219

5.2.3 Effect of time ..... 222

5.2.4 Effect of modifying agent dosage ..... 224

5.2.5 Incorporation of zirconium oxide in HTC-MR ..... 229

5.2.6 Preparation of HTC-MR in the eutectic salt template ..... 231

5.3 Removal of Cr(VI) by hydrothermal carbonized *M. rouxii* ..... 234

5.3.1 Screening of cationic and anionic pollutants ..... 234

5.3.2 Effect of contact time ..... 237

5.3.3 Kinetic modelling ..... 241

5.3.4 Effect of pH ..... 245

5.3.5 Effect of initial Cr(VI) concentration ..... 250

5.3.6 Isotherm modelling ..... 252

5.3.7 Effect of adsorbent dosage ..... 256

5.3.8 Effect of temperature ..... 258

5.3.9 Cr desorption study ..... 261

5.4 Removal of Cr(VI) by magnetic hydrothermal carbonized *M. rouxii* ($Fe_3O_4$-0.5PEI-HTC-MR) ..... 266

5.4.1 Effect of contact time and kinetic modelling ..... 266

5.4.2 Effect of pH ..... 269

5.4.3 Effect of initial Cr(VI) concentration and isotherm modelling ..... 271

5.5 Characterization of hydrothermal carbonized *M. rouxii* ..... 274

5.5.1 Fourier-transform Infrared spectroscopy (FTIR) ..... 274

5.5.2 Nuclear magnetic resonance spectroscopy (NMR) ..... 279

5.5.3 X-ray photoelectron spectroscopy (XPS) ..... 282

5.5.4 Isothermal titration calorimetry (ITC) ..... 300

5.6 Cr(VI) removal mechanisms.....307

**6. Conclusions.....311**

**7. Further Studies.....315**

**References.....317**

# List of Abbreviations

| | |
|---|---|
| $a$ | Initial adsorption rate at zero-coverage (mg/g-min) from Elovich model |
| AA | Acrylamide |
| $b$ | Elovich constant (g/mg) |
| $b_L$ | Langmuir constant (L/mg) |
| $b_T$ | Tempkin constant (J/mol), which is related to the heat of adsorption |
| $B_D$ | Dubinin-Radushkevich isotherm constant ($mol^2/kJ^2$) |
| $B_t$ | Boyd number |
| BV | Bed volume |
| $C_0$ | Initial concentration of Cr(VI) without adding adsorbent (mg/L) |
| CA | Calcium alginate |
| CAIM | Calcium-alginate-immobilized *M. rouxii* |
| $C_e$ | Equilibrium concentration of Cr(VI) with adding adsorbent (mg/L) |
| $C_{OC}^*$ | Content of equivalent organic compound per unit of biomass (mg/g) |
| $Cr(III)_{rel}$ | Cr(III) released per gram adsorbent (mg/g) |
| $D_{app}$ | Apparent intra-particle diffusion coefficient ($cm^2$/min) |
| DDI | Distilled-deionized water |
| DEA | Diethanolamine |
| $\varepsilon_D$ | Polanyi potential |
| E | Mean free energy of sorption (kJ/mol) |
| EDX | Energy dispersive X-ray spectroscopy |
| FTIR | Fourier-transformed Infrared spectroscopy |

| | |
|---|---|
| h | Half-length of diffusion path (cm) |
| HTC-MR | Hydrothermal carbonized *M. rouxii* |
| ICP-OES | Inductive coupled plasma optical emission spectrometry |
| K | Equilibrium constant |
| $k_1$ | Pseudo-first-order kinetic constant (1/min) |
| $k_2$ | Pseudo-second-order kinetic constant (g/mg-min) |
| $k_f$ | Fractional power kinetic constant (mg/g-min$^{v}$) |
| $K_F$ | Freundlich constant (mg/g) |
| $k_h$ | Han kinetic constant (min$^{-1}$) |
| $k_{id}$ | Intra-particle diffusion kinetic constant (mg/g-min$^{0.5}$) |
| $k_P$ | Park kinetic constant (min$^{-1}$) |
| $K_s$ | Sips isotherm constant (L/g) |
| $K_T$ | Tempkin isotherm constant (L/g) |
| M | Mass of adsorbent used (g/L) |
| MAS | Magic angle spinning |
| MR | *Mucor rouxii* |
| $m_s$ | Sips exponent |
| Mw | Molecular weight (g/mol) |
| n | Freundlich exponent |
| $NH_4OH$ | Ammonium hydroxide |
| $n_m$ | Sips isotherm constant (L/mg) |
| NMR | Nuclear magnetic resonance spectroscopy |
| PEI | Polyethyleneimine |
| q | Adsorption capacity (mg/g) |
| Q | Dubinin-Radushkevich isotherm constant (mg/g) |

| | |
|---|---|
| $Q_{Cr(VI)}$ | Cr(VI) removal capacity (mg/g) |
| $q_e$ | Equilibrium adsorption capacity (mg/g) |
| $q_e$ | Equilibrium adsorption capacity (mg/g) |
| $q_{max}$ | Maximum adsorption capacity (mg/g) |
| $q_t$ | Sorption capacity at time t (mg/g) |
| $q_{tot}$ | Total Cr adsorption capacity (mg/g) |
| R | Gas constant, 8.314 J/mol-K |
| $R_E$ | Approaching equilibrium parameter |
| RMSE | Root-mean-square error |
| $S_{BET}$ | Surface area calculated from Brunauer–Emmett–Teller method |
| SCA | Silica-doped calcium alginate |
| SCAIM | Silica-doped calcium-alginate-immobilized *M. rouxii* |
| SEM | Scanning electron microscopy |
| SZA | Silica-doped zirconium alginate |
| SZAIM | Silica-doped zirconium-alginate-immobilized *M. rouxii* |
| T | Temperature (K) |
| $t_0$ | Elovich time constant (min) |
| $t_b$ | Breakthrough time (min) |
| $t_{eqm}$ | Equilibrium time |
| TETA | Triethylenetetramine |
| UV-vis | Ultraviolet-visible spectroscopy |
| V | Volume of adsorption volume (L) |
| $V_b$ | Breakthrough volume (BV) |
| v | Fractional power model exponent |
| XPS | X-ray photoelectron spectroscopy |

| | |
|---|---|
| ZA | Zirconium alginate |
| ZAIM | Zirconium-alginate-immobilized *M. rouxii* |
| $\Delta G$ | Gibb's free energy change (J/mol) |
| $\Delta H$ | Enthalpy change (J/mol) |
| $\Delta S$ | Entropy change (J/mol-K) |
| $\%Cr(VI)_{re}$ | Percentage Cr(VI) removal (%) |
| $\%Cr_{ads}$ | Percentage total Cr adsorption (%) |
| $\%D_{Cr}$ | Percentage Cr desorption (%) |
| $\%D_{Cr(VI)}$ | Percentage Cr(VI) desorption (%) |
| [B] | Biomass concentration (g/L) |
| $[Cr(VI)]_0$ | Initial Cr(VI) concentration (mg/L) |
| $[Cr(VI)]_t$ | Cr(VI) concentration at time t (mg/L) |

# List of Figures

Figure 2-1 Possible reaction pathway and contribution of the Cr(VI) removal by the magnetic corncob biochar/polypyrrole composite (Yang et al., 2018).....40
Figure 2-2 Mechanism of the Cr(VI) adsorption by the biochars (An et al., 2018). .....41
Figure 3-1 Batch and continuous fixed-bed column adsorption studies on the removal of Cr(VI).....60
Figure 4-1 Micrographs of (a) CA, (b) SCA, (c) CAIM and (d) SCAIM after 7 days immersion in pH 2 solution. .....72
Figure 4-2 Micrographs of dried CA, SCA, CAIM and SCAIM immersed in 25 mM EDTA solution.....73
Figure 4-3 Silica shell remained after immersing a SCA bead in 25 mM EDTA solution for 24 h. .....74
Figure 4-4 Compression load at 5% strain of different rehydrated bead adsorbents. .....76
Figure 4-5 Screening results of six cationic and five anionic pollutants by SCAIM. (Experimental conditions: Initial concentration of pollutants = 500 ppm, adsorbent dosage = 1 g/L, t = 3 d, temperature = 25ºC and agitation = 250 rpm) .....78
Figure 4-6 Cr(VI) removal kinetics and total Cr adsorption kinetics of (a) CA and (b) SCA. (Experimental conditions: $[Cr(VI)]_0$ = 100 ppm, adsorbent dosage = 10 g/L, t = 3 d, pH 2.0, temperature = 25ºC and agitation = 250 rpm) .....82
Figure 4-7 Cr(VI) removal kinetics and total Cr adsorption kinetics of (a) CAIM and (b) SCAIM. (Experimental conditions: $[Cr(VI)]_0$ = 100 ppm, adsorbent dosage = 10 g/L, t = 3 d, pH 2.0, temperature = 25ºC and agitation = 250 rpm) .....83
Figure 4-8 Effect of pH on the $\%Cr(VI)_{re}$ and $\%Cr_{ads}$ on (a) CA and (b) SCA. (Experimental conditions: $[Cr(VI)]_0$ = 100 ppm, adsorbent dosage = 10 g/L, t = 3 d, pH 1.0 - 7.0, temperature = 25ºC and agitation = 250 rpm) .....88
Figure 4-9 Effect of pH on the $\%Cr(VI)_{re}$ and $\%Cr_{ads}$ on (a) CAIM and (b) SCAIM. (Experimental conditions: $[Cr(VI)]_0$ = 100 ppm, adsorbent dosage = 10 g/L, t = 3 d, pH 1.0 - 7.0, temperature = 25ºC and agitation = 250 rpm).....89
Figure 4-10 (a) Speciation diagram of 100 ppm Cr(VI) in solution simulated by Visual MINTEQ; and (b) effect of pH on zeta-potential of MR.....90
Figure 4-11 Cr(VI) removal kinetic modelling curves of (a) MR and (b) SCA. (Experimental conditions: $[Cr(VI)]_0$ = 50 ppm, adsorbent dosage = 1 g/L, t = 3 d, pH 2.0, temperature = 25ºC and agitation = 250 rpm).....93
Figure 4-12 Cr(VI) removal kinetic modelling curves of (a) CAIM and (b) SCAIM. (Experimental conditions: $[Cr(VI)]_0$ = 50 ppm, adsorbent dosage = 1 g/L, t = 3 d, pH

2.0, temperature = 25°C and agitation = 250 rpm) ..... 94
Figure 4-13 Modelling curves of Cr(VI) reduction kinetic models for MR. ..... 99
Figure 4-14 Modelling curves of Cr(VI) reduction kinetic models for (a) CA and (b) SCA. 100
Figure 4-15 Modelling curves of Cr(VI) reduction kinetic models for (a) CAIM and (b) SCAIM. ..... 101
Figure 4-16 Intra-particle diffusion plot of the Cr(VI) removal and total Cr adsorption on MR and SCAIM. ..... 107
Figure 4-17 Intra-particle diffusion plots of the Cr(VI) removal and total Cr adsorption on (a) CA, (b) SCA and (c) CAIM. ..... 108
Figure 4-18 Effect of initial Cr(VI) concentration on $\%Cr(VI)_{re}$ of different immobilized adsorbents. (Experimental conditions: $[Cr(VI)]_0$ = 10 - 2000 ppm, adsorbent dosage = 10 g/L, t = 3 d, pH 2, temperature = 25°C and agitation = 250 rpm) ..... 110
Figure 4-19 Total Cr adsorption isotherm modelling curves of MR. (Experimental conditions: $[Cr(VI)]_0$ = 20 - 300 ppm, adsorbent dosage = 1 g/L, t = 24 h, pH 2, temperature = 25°C and agitation = 250 rpm) ..... 113
Figure 4-20 Total Cr adsorption isotherm modelling curves of (a) CA and (b) SCA. (Experimental conditions: $[Cr(VI)]_0$ = 10 - 2000 ppm, adsorbent dosage = 10 g/L, t = 3 d, pH 2, temperature = 25°C and agitation = 250 rpm) ..... 114
Figure 4-21 Total Cr adsorption isotherm modelling curves of (a) CAIM and (b) SCAIM. (Experimental conditions: $[Cr(VI)]_0$ = 10 - 2000 ppm, adsorbent dosage = 10 g/L, t = 3 d, pH 2, temperature = 25°C and agitation = 250 rpm) ..... 115
Figure 4-22 Effect of adsorbent dosage on the $Q_{Cr(VI)}$ and $\%Cr(VI)_{re}$ by MR. (Experimental conditions: $[Cr(VI)]_0$ = 100 ppm, adsorbent dosage = 0.2 - 10 g/L, t = 24 h, pH 2, temperature = 25°C and agitation = 250 rpm) ..... 119
Figure 4-23 Effect of adsorbent dosage on the $Q_{Cr(VI)}$ and $\%Cr(VI)_{re}$ by (a) CA and (b) SCA. (Experimental conditions: $[Cr(VI)]_0$ = 100 ppm, adsorbent dosage = 1 - 50 g/L, t = 3 d, pH 2, temperature = 25°C and agitation = 250 rpm) ..... 120
Figure 4-24 Effect of adsorbent dosage on the $Q_{Cr(VI)}$ and $\%Cr(VI)_{re}$ by (a) CAIM and (b) SCAIM. (Experimental conditions: $[Cr(VI)]_0$ = 100 ppm, adsorbent dosage = 1 - 50 g/L, t = 3 d, pH 2, temperature = 25°C and agitation = 250 rpm) ..... 121
Figure 4-25 Effect of temperature on the Cr(VI) removal kinetics. (a) MR and (b) SCAIM. (Experimental conditions: **MR**, $[Cr(VI)]_0$ = 100 ppm, adsorbent dosage = 1 g/L, t = 24 h, pH 2, temperature = 20, 25 and 40°C and agitation = 250 rpm; **SCAIM**, $[Cr(VI)]_0$ = 50 ppm, adsorbent dosage = 1 g/L, t = 3 d, pH 2, temperature = 4, 25 and 40°C and agitation = 250 rpm) ..... 125
Figure 4-26 Effect of agitation speed on the Cr(VI) removal kinetics. (a) MR and (b) SCAIM. (Experimental conditions: **MR**, $[Cr(VI)]_0$ = 100 ppm, adsorbent dosage = 1 g/L, t = 3 d, pH 2, temperature = 25°C, agitation = 50, 250 and 500 rpm; **SCAIM**, $[Cr(VI)]_0$ = 50

ppm, adsorbent dosage = 1 g/L, t = 3 d, pH 2, temperature = 25°C, agitation = 100, 250 and 400 rpm) ..... 128
Figure 4-27 Intra-particle diffusion plot of Cr(VI) removal by SCAIM at different agitation speeds. ..... 129
Figure 4-28 Percentage Cr desorption from Cr-laden SCAIM by different desorption agents. (Experimental conditions: **adsorption**, $[Cr(VI)]_0$ = 50 ppm, adsorbent dosage = 10 g/L, t = 3 d, pH 2, temperature = 25°C and agitation = 250 rpm; **desorption**, adsorbent dosage = 20 g/L, t = 1 d, temperature = 25°C and agitation = 250 rpm) ..... 131
Figure 4-29 Breakthrough curves for different inlet Cr(VI) concentrations and flow rates. (Experimental conditions: $[Cr(VI)]_0$ = 10 - 50 ppm, bed height = 50 cm, pH 2.0, flow rate = 0.5 - 1.0 ml/min, temperature = 22.5°C) ..... 134
Figure 4-30 Cr desorption profile of Cr-laden SCAIM column using 2M $HNO_3$ solution. (Experimental conditions: **adsorption**, $[Cr(VI)]_0$ = 50 ppm, flow rate = 1.0 ml/min, pH 2, temperature = 22.5°C; **desorption**, desorption agent = 2 M $HNO_3$ solution, flow rate = 0.25 ml/min, temperature = 22.5°C) ..... 136
Figure 4-31 Screening results of five anionic pollutants by SZAIM. (Experimental conditions: $[Cr(VI)]_0$ = 500 ppm, adsorbent dosage = 1 g/L, t = 3 d, temperature = 25°C and agitation = 250 rpm) ..... 138
Figure 4-32 Effect of pH on the $\%Cr(VI)_{re}$ and $\%Cr_{ads}$ on SZAIM. (Experimental conditions: $[Cr(VI)]_0$ = 100 ppm, adsorbent dosage = 10 g/L, t = 3 d, pH 1 - 7, temperature = 25°C and agitation = 250 rpm) ..... 140
Figure 4-33 Cr(VI) removal kinetics and total Cr adsorption kinetics of SZAIM. (Experimental conditions: $[Cr(VI)]_0$ = 100 ppm, adsorbent dosage = 10 g/L, t = 3 d, pH 2, temperature = 25°C and agitation = 250 rpm) ..... 144
Figure 4-34 (a) Cr(VI) removal kinetics and total Cr adsorption kinetics of SZAIM; and (b) Cr(VI) removal kinetic modelling curves of SZAIM. (Experimental conditions: $[Cr(VI)]_0$ = 50 ppm, adsorbent dosage = 1 g/L, t = 3 d, pH 2, temperature = 25°C and agitation = 250 rpm) ..... 145
Figure 4-35 (a) Effect of initial Cr(VI) concentration on $\%Cr(VI)_{re}$ and $\%Cr_{ads}$ of SZAIM; and (b) total Cr adsorption isotherm modelling curves of SZAIM. (Experimental conditions: $[Cr(VI)]_0$ = 10 - 2000 ppm, adsorbent dosage = 10 g/L, t = 3 d, pH 2, temperature = 25°C and agitation = 250 rpm) ..... 148
Figure 4-36 FTIR spectra of the freely suspended and immobilized *M. rouxii*. ..... 155
Figure 4-37 Possible binding structures of the metal-carboxylate complex. ..... 155
Figure 4-38 SEM images of (a) CA (x 90), (b) SCA (x 70), (c) CAIM (x 50), (d) SCAIM (x 50) and (b) the silica particles doped on SCA surface (x 1000). ..... 159
Figure 4-39 EDX spectra of pristine CA (Top) and SCA (Bottom). ..... 160
Figure 4-40 EDX spectra of pristine CAIM (Top) and SCAIM (Bottom). ..... 161

Figure 4-41 EDX spectra of pristine Cr-loaded CAIM (Top) and Cr-loaded SCAIM (Bottom). .....162
Figure 4-42 Wide scan XPS spectra of (a) pristine and (b) Cr-laden *M. rouxii* (pH 2, 1 day). .....167
Figure 4-43 High-resolution XPS spectra of pristine and Cr-laden *M. rouxii*: (a) C1s and (b) N1s. .....168
Figure 4-44 High-resolution XPS spectra of pristine and Cr-laden *M. rouxii*: (a) O1s and (b) P2p. .....169
Figure 4-45 Cr2p spectra of Cr-laden *M. rouxii* at different (a) contact time and (b) solution pH. .....170
Figure 4-46 Wide scan XPS spectra of (a) CA and (b) SCA. .....178
Figure 4-47 Wide scan XPS spectra of (a) SCAIM and (b) Cr-laden SCAIM. .....179
Figure 4-48 High-resolution XPS spectra of the pristine and Cr-laden SCAIM: (a) C1s and (b) N1s. .....180
Figure 4-49 High-resolution XPS spectra of the pristine and Cr-laden SCAIM: (a) O1s (b) P2p and (c) Si2p. .....181
Figure 4-50 Cr2p spectra of (a) the different Cr-loaded bead adsorbents and (b) the Cr-loaded SCAIM with different contact times. .....182
Figure 4-51 Ca2p spectra of pristine and Cr-loaded SCAIM with different contact times. ..183
Figure 4-52 Wide scan XPS spectra of (a) SZAIM and (b) Cr-laden SZAIM. .....190
Figure 4-53 High-resolution XPS spectra of the pristine and Cr-laden SZAIM: (a) C1s, (b) N1s and (c) O1s. .....191
Figure 4-54 High-resolution XPS spectra of the Cr-laden SZAIM with 3-day contact with Cr(VI) solution: (a) Zr3d and (b) Cr2p. .....192
Figure 4-55 The Cr(VI) adsorption-coupled reduction mechanism .....201
Figure 5-1 $Q_{Cr(VI)}$, $q_{tot}$ and $Cr(III)_{rel}$ of raw MR and HTC materials. (Experimental conditions: [Cr(VI)] = 500 ppm, adsorbent dosage = 1 g/L, t = 1 d, pH 2, temperature = 25°C and agitation = 250 rpm) .....218
Figure 5-2 $Q_{Cr(VI)}$, $q_{tot}$ and $Cr(III)_{rel}$ of (a) HTC-MR, (b) 0.5DEA-HTC-MR and (c) 0.5PEI-HTC-MR prepared in different reaction temperature. (Experimental conditions: [Cr(VI)] = 500 ppm, adsorbent dosage = 1 g/L, t = 1 d, pH 2, temperature = 25°C and agitation = 250 rpm) .....221
Figure 5-3 $Q_{Cr(VI)}$, $q_{tot}$ and $Cr(III)_{rel}$ of (a) HTC-MR, (b) 0.5DEA-HTC-MR and (c) 0.5PEI-HTC-MR prepared in different reaction time. (Experimental conditions: [Cr(VI)] = 500 ppm, adsorbent dosage = 1 g/L, t = 1 d, pH 2, temperature = 25°C and agitation = 250 rpm) .....223
Figure 5-4 $Q_{Cr(VI)}$, $q_{tot}$ and $Cr(III)_{rel}$ of (a) 0.5DEA-HTC-MR and (b) 0.5PEI-HTC-MR prepared in different dosages of modifying agent. (Experimental conditions: [Cr(VI)] =

500 ppm, adsorbent dosage = 1 g/L, t = 1 d, pH 2, temp = 25°C) ..... 226
Figure 5-5 Cr(VI) removal kinetics of 0.5PEI-HTC-MR with different molecular weights of PEI. (Experimental conditions: [Cr(VI)] = 500 ppm, adsorbent dosage = 1 g/L, t = 1 d, pH 2, temperature = 25°C and agitation = 250 rpm) ..... 228
Figure 5-6 The $Q_{Cr(VI)}$, $q_{tot}$ and $Cr(III)_{rel}$ values of $NH_4$-HTC-MR, $ZrO_2$ and $ZrO_2$-$NH_4$-HTC-MR. (Experimental conditions: [Cr(VI)] = 500 ppm, adsorbent dosage = 1 g/L, t = 1 d, pH 2, temperature = 25°C and agitation = 250 rpm) ..... 230
Figure 5-7 Temperature-composition phase diagram of $CaCl_2$ and $FeCl_3$ binary system (CRCT, 2015). ..... 233
Figure 5-8 $Q_{Cr(VI)}$ values of HTC-MR and HTC-MR-CaFe. (Experimental conditions: [Cr(VI)] = 500 ppm, adsorbent dosage = 1 g/L, t = 1 d, pH 2, temperature = 25°C and agitation = 250 rpm) ..... 233
Figure 5-9 Screening results of six cationic and five anionic pollutants by HTC-MR, 0.5DEA-HTC-MR and 0.5PEI-HTC-MR. (Experimental conditions: [Cr(VI)] = 500 ppm, adsorbent dosage = 1 g/L, t = 1 d, temperature = 25°C and agitation = 250 rpm) 236
Figure 5-10 Effect of contact time on the $Q_{Cr(VI)}$, $q_{tot}$ and $Cr(III)_{rel}$ by (a) MR, (b) HTC-MR and (c) 0.5AA-HTC-MR. (Experimental conditions: [Cr(VI)] = 500 ppm, adsorbent dosage = 1 g/L, t = 1 d, pH 2, temperature = 25°C and agitation = 250 rpm) ..... 239
Figure 5-11 Effect of contact time on the $Q_{Cr(VI)}$, $q_{tot}$ and $Cr(III)_{rel}$ by (a) 0.5DEA-HTC-MR, (b) 0.5PEI-HTC-MR and (c) 0.5Urea-HTC-MR. (Experimental conditions: [Cr(VI)] = 500 ppm, adsorbent dosage = 1 g/L, t = 1 d, pH 2, temperature = 25°C and agitation = 250 rpm) ..... 240
Figure 5-12 Cr(VI) removal kinetic modelling curves of (a) HTC-MR, (b) 0.5DEA-HTC-MR and (c) 0.5PEI-HTC-MR. ..... 243
Figure 5-13 Effect of pH on $Q_{Cr(VI)}$, $q_{tot}$ and $Cr(III)_{rel}$ of (a) HTC-MR, (b) 0.5DEA-HTC-MR and (c) 0.5PEI-HTC-MR. (Experimental conditions: [Cr(VI)] = 500 ppm, adsorbent dosage = 1 g/L, t = 1 d, pH 1- 7, temperature = 25°C and agitation = 250 rpm) ..... 248
Figure 5-14 Effect of pH on zeta-potential of HTC-MR, 0.5DEA-HTC-MR and 0.5PEI-HTC-MR. ..... 249
Figure 5-15 Speciation diagram of 500 ppm Cr(VI) solution simulated by Visual MINTEQ. ..... 249
Figure 5-16 Effect of initial Cr(VI) concentration on $Q_{Cr(VI)}$, $q_{tot}$ and $Cr(III)_{rel}$ of (a) HTC-MR, (b) 0.5DEA-HTC-MR and (c) 0.5PEI-HTC-MR. (Experimental conditions: [Cr(VI)] = 10 - 500 ppm, adsorbent dosage = 1 g/L, t = 1 d, pH 2, temperature = 25°C and agitation = 250 rpm) ..... 251
Figure 5-17 Total Cr adsorption isotherm of (a) HTC-MR, (b) 0.5DEA-HTC-MR and (c) 0.5PEI-HTC-MR. ..... 254
Figure 5-18 Effect of adsorbent dose on the Cr(VI) removal capacity and the percentage

Cr(VI) removal. (Experimental conditions: [Cr(VI)] = 100 - 500 ppm, adsorbent dosage = 0.1 - 2.0 g/L, t = 1 d, pH 2, temperature = 25ºC and agitation = 250 rpm).....257
Figure 5-19 Cr(VI) removal kinetics at different temperature. (a) HTC-MR, (b) 0.5DEA-HTC-MR and (c) 0.5PEI-HTC-MR. (Experimental conditions: [Cr(VI)] = 500 ppm, adsorbent dosage = 1 g/L, t = 1 d, pH 2, temperature = 4, 25, 40ºC and agitation = 250 rpm).....259
Figure 5-20 Percentage Cr(VI) desorption and percentage Cr desorption from Cr-laden HTC materials by different desorption agents: A = 0.5 M $HNO_3$, B = 2.0 M $HNO_3$, C = 0.5 M NaOH and D = 2.0 M NaOH. (Experimental conditions: **adsorption**, [Cr(VI)] = 500 ppm, adsorbent dosage = 1 g/L, t = 1 d, pH 2, temperature = 25ºC and agitation = 250 rpm; **desorption**, adsorbent dosage = 2 g/L, t = 1 d, temperature = 25ºC and agitation = 250 rpm).....264
Figure 5-21 Adsorption-desorption cycle (A: 0.5 M $HNO_3$, B: 2.0 M $HNO_3$, C: 0.5 M NaOH and D: 2.0 M NaOH). .....265
Figure 5-22 Cr(VI) removal kinetics of $Fe_3O_4$, $Fe_3O_4$-0.5PEI-HTC-MR and 0.5PEI-HTC-MR. (Experimental conditions: [Cr(VI)] = 500 ppm, adsorbent dosage = 1 g/L, t = 1 d, pH 2, temperature = 25ºC and agitation = 250 rpm) .....267
Figure 5-23 Modelling curves and experimental data of Cr(VI) removal kinetics of $Fe_3O_4$-0.5PEI-HTC-MR.....267
Figure 5-24 Effect of pH on Cr(VI) removal capacity, total Cr adsorption capacity and Cr(III) release by $Fe_3O_4$-0.5PEI-HTC-MR. (Experimental conditions: [Cr(VI)] = 500 ppm, adsorbent dosage = 1 g/L, t = 1 d, pH 1 - 7, temperature = 25ºC and agitation = 250 rpm) .....270
Figure 5-25 Effect of initial Cr(VI) concentration on Cr(VI) removal capacity ($Q_{Cr(VI)}$), total Cr adsorption capacity ($q_{tot}$) and Cr(III) release ($Cr(III)_{rel}$) by $Fe_3O_4$-0.5PEI-HTC-MR. (Experimental conditions: [Cr(VI)] = 10 - 500 ppm, adsorbent dosage = 1 g/L, t = 1 d, pH 2, temperature = 25ºC and agitation = 250 rpm) .....272
Figure 5-26 Total Cr adsorption isotherm of $Fe_3O_4$-0.5PEI-HTC-MR.....272
Figure 5-27 FTIR spectra of MR and HTC materials.....277
Figure 5-28 NMR spectra of the adsorbents. .....281
Figure 5-29 Formation mechanism of 5-hydroxylmethylfurfural from N-acetyl-glucosamine (Shu, 1998).....281
Figure 5-30 C1s spectra of (a) HTC-MR, (b) 0.5DEA-HTC-MR and (c) 0.5PEI-HTC-MR. .....289
Figure 5-31 C1s spectra of (a) Cr-HTC-MR, (b) Cr-0.5DEA-HTC-MR and (c) Cr-0.5PEI-HTC-MR.....290
Figure 5-32 N1s spectra of (a) HTC-MR, (b) 0.5DEA-HTC-MR and (c) 0.5PEI-HTC-MR. .....291

Figure 5-33 N1s spectra of (a) Cr-HTC-MR, (b) Cr-0.5DEA-HTC-MR and (c) Cr-0.5PEI-HTC-MR. ..... 292
Figure 5-34 O1s spectra of (a) HTC-MR, (b) 0.5DEA-HTC-MR and (c) 0.5PEI-HTC-MR. ..... 293
Figure 5-35 O1s spectra of (a) Cr-HTC-MR, (b) Cr-0.5DEA-HTC-MR and (c) Cr-0.5PEI-HTC-MR. ..... 294
Figure 5-36 Cr2p spectra of (a) Cr-HTC-MR, (b) Cr-0.5DEA-HTC-MR and (c) Cr-0.5PEI-HTC-MR. ..... 295
Figure 5-37 Fe2p spectra of (a) pristine and (b) Cr-laden $Fe_3O_4$-0.5PEI-HTC-MR. ..... 296
Figure 5-38 (a) Titration thermogram and (b) plot of heat released versus molar ratio for Cr(VI) adsorption on MR. ..... 302
Figure 5-39 (a) Titration thermogram and (b) plot of heat released versus molar ratio for Cr(VI) adsorption on HTC-MR. ..... 303
Figure 5-40 (a) Titration thermogram and (b) plot of heat released versus molar ratio for Cr(VI) adsorption on 0.5DEA-HTC-MR. ..... 304
Figure 5-41 (a) Titration thermogram and (b) plot of heat released versus molar ratio for Cr(VI) adsorption on 0.5PEI-HTC-MR. ..... 305
Figure 5-42 The Cr(VI) removal mechanism by the HTC materials. ..... 310

# List of Tables

Table 2-1 Cr(VI) adsorption capacity of calcium alginate-based materials.....16
Table 2-2 Adsorption of anionic contaminants by metal-alginate materials.....17
Table 2-3 Application of hydrothermal carbons. .....23
Table 2-4 Adsorption of water contaminants by hydrothermal carbonized materials. .....25
Table 2-5 Removal of Cr(VI) by hydrothermal carbonized materials. .....26
Table 2-6 Classification of the kinetic curve based on the $R_E$ value. .....31
Table 2-7 Removal of Cr(VI) through the adsorption-coupled reduction mechanism by different types of adsorbents. .....43
Table 3-1 Solution pH for adsorption of various cationic and anionic pollutants. .....56
Table 4-1 Textural properties of MR and SCAIM beads. .....66
Table 4-2 Physical properties of CA, SCA, CAIM and SCAIM. .....69
Table 4-3 Kinetic modelling parameters for Cr(VI) removal by MR, SCA, CAIM and SCAIM. .....95
Table 4-4 Modelling parameters of the reduction kinetic models. .....102
Table 4-5 Isotherm modelling parameters for total Cr adsorption on different adsorbents. .....116
Table 4-6 Modelling parameters of the fractional power model for the Cr(VI) removal by SCAIM at different temperatures. .....126
Table 4-7 Thermodynamic parameters of Cr(VI) removal on MR and SCAIM. .....126
Table 4-8 Modelling parameters of the fractional power model for the Cr(VI) removal by SCAIM at different agitation speeds. .....129
Table 4-9 Cr(VI) removal by SCAIM in a fixed-bed column at different process conditions. .....134
Table 4-10 Kinetic modelling parameters for Cr(VI) removal by MR, SCAIM and SZAIM. .....146
Table 4-11 Isotherm modelling parameters for total Cr adsorption on MR, SCAIM and SZAIM. .....149
Table 4-12 Assignment table of the FTIR signals of different adsorbents. .....156
Table 4-13 Surface compositions of pristine and Cr-laden *M. rouxii*. .....166
Table 4-14 Binding energies, atomic concentrations and chemical shifts of pristine and Cr(VI)-laden *M. rouxii* and the standard compounds. .....171
Table 4-15 Surface compositions of pristine and Cr-laden CA, SCA and SCAIM beads. .....177
Table 4-16 Binding energies, atomic concentrations and chemical shifts of pristine and Cr(VI)-laden calcium-alginate-based adsorbents and the standard compounds. .....184
Table 4-17 Surface compositions of pristine and Cr-laden ZA and SZAIM beads. .....189

Table 4-18 Binding energies, atomic concentrations and chemical shifts of Cr(VI)-laden SZAIM. ..... 193
Table 5-1 BET surface area and BJH pore volume of MR, HTC-MR, HTC-MR-CaFe, 0.5DEA-HTC-MR and 0.5PEI-HTC-MR. ..... 206
Table 5-2 Elemental composition of HTC materials. ..... 215
Table 5-3 Cr(VI) removal kinetic modelling parameters of HTC-MR, 0.5DEA-HTC-MR and 0.5PEI-HTC-MR. ..... 244
Table 5-4 Isotherm modelling parameter of HTC-MR, 0.5DEA-HTC-MR and 0.5PEI-HTC-MR. ..... 255
Table 5-5 Modelling parameters from fractional power model for the Cr(VI) removal by HTC-MR, 0.5DEA-HTC-MR and 0.5PEI-HTC-MR at different temperatures. ..... 260
Table 5-6 Cr(VI) removal kinetic modelling parameters of $Fe_3O_4$-0.5PEI-HTC-MR and 0.5PEI-HTC-MR. ..... 268
Table 5-7 Isotherm modelling parameters of $Fe_3O_4$-0.5PEI-HTC-MR and 0.5PEI-HTC-MR. ..... 273
Table 5-8 Assignment table of the FTIR signals of MR and HTC materials. ..... 278
Table 5-9 Surface composition of pristine and Cr-laden adsorbents. ..... 283
Table 5-10 Binding energies, atomic concentration and chemical shift of pristine and Cr-loaded MR, HTC-MR, 0.5DEA-HTC-MR, 0.5PEI-HTC-MR and Fe3O4-0.5PEI-HTC-MR. ..... 297
Table 5-11 Thermodynamic parameters of Cr(VI) adsorption on MR, HTC-MR, 0.5DEA-HTC-MR and 0.5PEI-HTC-MR. ..... 306

# 1. Introduction

## 1.1 Motivation

Chromium is a transition metal, found naturally in chromite ore. Chromium has been used in many industries, such as electroplating, leather tanning, metal finishing and dyeing. The discharge of chromium-bearing wastewaters from these industries poses a serious threat to the environment and public health. Chromium exists in both trivalent chromium Cr(III) and hexavalent chromium Cr(VI) forms in aqueous solutions. Chromium(VI) is more toxic than chromium(III). Cr(VI) is mutagenic, teratogenic, carcinogenic and genotoxic to living organisms, while Cr(III) is an essential nutrient. The International Agency for Research on Cancer (IARC) has classified Cr(VI) as Group 1 (human carcinogen) and Cr(III) as Group 3 (not classifiable due to its carcinogenicity to humans). Excessive intake of Cr(VI) leads to cancers of the lung, nose and nasal sinuses (IARC, 2012). The limit of total chromium in drinking water set by the World Health Organization is 50 μg/L (WHO, 2011).

Some conventional methods such as chemical precipitation, chemical reduction, ion exchange, membrane filtration and electrochemical treatment have been developed for removing Cr(VI) in the aqueous phase (Owlad et al., 2009; Fu and Wang, 2011; Barrera Diaz et al., 2012). However, the production of toxic sludge is the main drawback of chemical precipitation and chemical reduction methods, while ion exchange, membrane filtration and electrochemical methods consume large amounts of energy and hence require expensive equipment and monitoring systems. Therefore, it is crucial to develop an alternative low-cost

technology for the removal of Cr(VI) from industrial effluents. Adsorption using low-cost materials is an efficient, environmental-friendly, cost-effective and innovative technique that converts waste materials into high added value adsorbents, and replaces the conventional Cr(VI) removal methods. Several types of adsorbents have been identified to effectively remove Cr(VI) from aqueous solutions, including industrial solid wastes and biomaterials (Selvi et al., 2001; Owlad et al., 2009; Setshedi et al., 2013; Lv et al., 2014). Previous results (Lo, 2013) in our laboratory demonstrated that a freely suspended filamentous fungal biomass, *Mucor rouxii*, could effectively remove Cr(VI) by adsorption coupled-reduction mechanism. However, the separation of metal-laden powdered adsorbents is a remarkable technical challenge after the completion of the Cr(VI) adsorption process. The immobilization of adsorbents in a support material has advantages, such as high adsorbent loading, minimal clogging under continuous Cr(VI) removal process and efficient adsorbent regeneration. Calcium alginate has been widely applied as an immobilization agent for various kinds of adsorbents to remove heavy metals and dyes from aqueous solutions owing to its nontoxic, inexpensive and biodegradable nature (Hassan et al., 2014; Jung et al., 2016; Garlaschelli et al., 2017). However, poor physical and chemical stability of calcium alginate is an obstacle to its application in wastewater treatment. To improve the mechanical strength and chemical stability of calcium alginate, silica particles can be doped on the surface of calcium alginate. In this study, the doped silica was prepared from two silicon alkoxide precursors, tetraethylorthosilicate (TEOS) and N-[3-

(trimethoxysilyl)propyl]ethylenediamine (ENTMOS), so the doped silica was functionalized with ethylenediamine groups that would also participate in the Cr(VI) adsorption. Doping of silica particles was a promising method to reinforce the mechanical strength, chemical stability and porosity of calcium alginate. Research studies demonstrated that the silica-coated calcium alginate showed excellent permeability to low molecular weight substances, so it was utilized as bio-artificial organs (Sakai et al., 2002b; c). To the best of my knowledge, there was no report focusing on the immobilization of microbial biomass using silicate-coated calcium alginate and its application in Cr(VI) removal. Hence, this research aims to develop a novel silica-doped calcium alginate material to immobilize the *M. rouxii* fungal biomass and investigate its Cr(VI) removal performance in batch and continuous modes.

Alginate gels, on the other hand, which had crosslinked with multivalent cations (e.g., $Fe^{3+}$, $Al^{3+}$, $La^{3+}$, $Zr^{4+}$, $Ce^{4+}$) attracted much attention because of their high adsorption capacities and reusability compared with calcium alginate. The $Ca^{2+}$ of calcium alginate could be replaced by multivalent cations through the ion-exchange mechanism. The multivalent ions have a strong affinity towards anionic pollutants (e.g., fluoride, phosphate, As(V), Cr(VI)). Zirconium and its salts generally have a low order of toxicity. There is no report on the carcinogenic effect of zirconium in human, rat and mice. In this study, the *M. rouxii* was immobilized with the silica-doped zirconium(IV) alginate material. It is expected that the silica-doped zirconium(IV) alginate immobilized *M. rouxii* (SZAIM) beads should have higher Cr(VI) adsorption capacity,

superior mechanical strength and chemical properties compared with *M. rouxii* immobilized with calcium alginate. However, there are no reports that look at the immobilization of microbial materials by silica-doped zirconium(IV) alginate and its application in Cr(VI) removal. This research thus also aims to prepare the novel SZAIM using $Zr^{4+}$ as the crosslinking ions and evaluate its Cr(VI) removal performance.

Other than the immobilization of *M. rouxii*, a thermochemical modification technique has also been established to enhance the Cr(VI) removal performance of *M. rouxii*. Hydrothermal carbonization is a thermochemical process converting biomass to carbonaceous products under subcritical water. Carbohydrates (e.g., glucose and sucrose) were commonly used as the carbon sources for the preparation of hydrothermal carbons (or hydrochars) (Titirici et al., 2008; Sevilla and Fuertes, 2009; Harmas et al., 2016; Poerschmann et al., 2017; Zhao et al., 2017a). Hydrothermal carbons have been widely investigated as electrodes materials, electrocatalysts, photocatalysts, heterogeneous catalysts, biofuels, gas storage materials and soil additives (Reza et al., 2014; Tekin et al., 2014; Titirici et al., 2015; Wei et al., 2016). Hydrochars usually exhibit superior heavy metals adsorption performance compared with activated carbon due to the higher concentration of oxygenated functional groups (OFGs) and a lower degree of condensation (Tekin et al., 2014; Lei et al., 2016). Recently, the utilization of waste biomass as a sustainable raw material for the production of valuable hydrochars have attracted significant attention because it reduces the cost of hydrothermal carbonization process and provides a

solution of solid waste problem (Xiao et al., 2012; Parshetti et al., 2014; Lei et al., 2016; Rohrdanz et al., 2016). Nitrogen-doped hydrochars can be simply synthesized by the one-pot hydrothermal process with the nitrogen-containing carbon sources (Kumar et al., 2014; Lin et al., 2016). The fungal biomass is primarily composed of carbohydrate, chitin, protein, fat and nucleic acid. The nitrogen-rich fungal biomass was a promising carbon and nitrogen source for preparing the nitrogen-doped hydrochars. Nitrogen groups such as amine functional groups can be protonated in acidic conditions and have been known to offer sites for binding with Cr(VI) due to the electrostatic attraction between the protonated nitrogen groups and the anionic Cr(VI). Nevertheless, little research on the hydrothermal carbonization of fungal biomass has been carried out (Gao et al., 2014; Xu et al., 2017). This motivates to probe the application of one-step hydrothermal carbonization of a nitrogen-rich filamentous fungus (*M. rouxii*) coupled with different amine-containing modifying agents (e.g., diethanolamine and polyethyleneimine) for synthesizing different types of novel amino-functionalized hydrochars with enhanced Cr(VI) removal performance. The Cr(VI) removal ability of the amino-functionalized hydrothermal carbonized *M. rouxii* (HTC-MR) has been evaluated with synthetic Cr(VI) wastewater in batch adsorption mode under different operating conditions. Magnetic properties have also been introduced to the hydrochars with the use of iron oxide particles so that the magnetic hydrochars can be separated by an external magnetic field after the Cr(VI) adsorption process.

## 1.2 Objectives

The objectives of this research are listed as follows:

1. To immobilize the processed fungal biomass of *Mucor rouxii* in silica-doped calcium-alginate and silica-doped zirconium-alginate by the entrapment method for the removal of Cr(VI) in polluted water.
2. To synthesize amino-functionalized hydrochars by the hydrothermal carbonization of *M. rouxii* coupled with different amine-containing modifying agents for the removal of Cr(VI) in polluted water.
3. To evaluate the effects of operating parameters, such as pH, contact time and initial Cr(VI) concentration on the Cr(VI) removal performance of silica-doped calcium-alginate-immobilized *Mucor rouxii*, silica-doped zirconium-alginate-immobilized *Mucor rouxii* and hydrothermal carbonized *Mucor rouxii*.
4. To simulate the Cr adsorption kinetics and isotherms on silica-doped calcium-alginate-immobilized *Mucor rouxii*, silica-doped zirconium-alginate-immobilized *Mucor rouxii* and hydrothermal carbonized *Mucor rouxii* using different kinetic and isotherm models.
5. To evaluate the Cr(VI) removal performance of a continuous column reactor packed with silica-doped calcium-alginate-immobilized *Mucor rouxii*.

6. To investigate the porosity characteristics, chemical stability and mechanical strength of silica-doped calcium-alginate-immobilized *Mucor rouxii* by $N_2$ adsorption/ desorption isotherm, chemical stability test and mechanical strength test.
7. To characterize the surface properties and chemical characteristics of silica-doped calcium-alginate-immobilized *Mucor rouxii*, silica-doped zirconium-alginate-immobilized *Mucor rouxii* and hydrothermal carbonized *Mucor rouxii* by Fourier-transform Infrared spectroscopy (FTIR), nuclear magnetic resonance spectroscopy (NMR) and X-ray photoelectron spectroscopy (XPS)
8. To investigate the physical and basic chemical properties of hydrothermal carbonized *Mucor rouxii* by $N_2$ adsorption/ desorption isotherm, dynamic light scattering (DLS) and elemental analysis (EA).
9. To elucidate the Cr(VI) removal mechanisms of silica-doped calcium-alginate-immobilized *Mucor rouxii*, silica-doped zirconium-alginate-immobilized *Mucor rouxii* and hydrothermal carbonized *Mucor rouxii*.

## 1.3 Organization of thesis

There are seven chapters in this dissertation. The chapters are organized as follows:

**Chapter 1 Introduction**

The current chapter.

**Chapter 2 Literature Review**

This reviews the literature related to immobilization of biomaterials, hydrothermal carbonization of biomaterials, applications for Cr(VI) removal and Cr(VI) removal mechanisms.

**Chapter 3 Materials and Methods**

This describes the chemicals and instruments used in the experiments and states the experimental procedures used for data collection.

**Chapter 4 Removal of Cr(VI) by Immobilized *M. rouxii***

This presents, discusses and interprets the surface characteristics, Cr(VI) removal performances and Cr(VI) removal mechanisms of silica-doped calcium-alginate-immobilized *M. rouxii*.

**Chapter 5 Removal of Cr(VI) by Hydrothermal Carbonized *M. rouxii***

This presents, discusses and interprets the surface characteristics, Cr(VI) removal performances and Cr(VI) removal mechanisms of hydrothermal carbonized *M. rouxii*.

**Chapter 6 Conclusions**

This summarizes the major findings of this research.

**Chapter 7 Further Studies**

This provides some recommendations for further studies.

# 2. Literature Review

## 2.1 Immobilization of biomaterials

Biomass has emerged as an economic and ecofriendly adsorbent for the removal of heavy metals from the aqueous phase. Various kinds of biomass, such as bacteria, algae and fungi (Lesmana et al., 2009; Abbas et al., 2014; He and Chen, 2014), have been proven to be effective in heavy metal adsorption. The biomass surface carries various types of functional groups, such as amino, amide and carboxyl groups, which offer sites for effective binding with heavy metals. Microbial biomasses are usually in the form of small particles with low density and mechanical strength. The biosorbents commonly exhibit high adsorption capacity, rapid adsorption and a fast mass transfer rate. However, biosorbents often suffer from swelling, encounter problems in separating biosorbents, have difficulties in adsorbent regeneration and reuse, and in the development of high pressure drop when used in column adsorption. The literature has confirmed that immobilization is the most plausible solution for these problems.

Different synthetic (such as polyvinyl alcohol, polysulfone, polyacrylamide, polyurethane and silica gel) and natural materials (including alginate, chitosan, gelatin, and carboxymethylcellulose) have been used as immobilization materials for biomass due to their good chemical stability, thermos-stability, mechanical strength and porosity to the diffusion of adsorbate (Sag, 2001; de-Bashan and Bashan, 2010; Bouabidi et al., 2018; Velkova et al., 2018). After immobilization, biomass is entrapped in the interior of the immobilization material, so the mass transfer resistance of the immobilization material can limit the adsorption rate.

Calcium alginate is a biodegradable and nontoxic supporting material. Alginate chains contain D-mannuronic and L-guluronic acid, which can be cross-linked with calcium ions and form a rigid hydrogel structure. Therefore, calcium alginate was used as a material for the immobilization of biomass for Cr(VI) adsorption (Table 2-1). Ramteke and Gogate (2016) immobilized the modified sludge biomass (MSB) using calcium alginate (CA) and polyvinylalcohol (PVA). However, the MSB-CA and MSB-PVA showed poor Cr(VI) biosorption capacity of 13.62 and 28.87 mg/g, respectively. The coating of the aminopropyl-silicate membrane on calcium alginate was first fabricated through a sol-gel synthesis by Sakai et al. (2002a). The aminopropyl-silicate/Ca-alginate gel beads exhibited high biocompatibility and permeability to small molecules (such as glucose, insulin), so it was used as a microcapsule-shaped bioartificial pancreas. However, no literature reported the use of silicate-coated calcium alginate to immobilize biosorbent and remove Cr(VI) from the aqueous solution. The amino groups on the aminopropyl-silicate should be capable of interacting with Cr(VI) ions. Silica-coated calcium alginate was a potential immobilization material because it not only acted as supporting material but also provided extra adsorption sites for Cr(VI) ions.

Alginate, on the other hand, is a biopolymer that can undergo cross-linking with different multivalent metal ions (e.g., Mg(II), Ba(II), Al(III), Fe(III), La(III), Ce(III) and Zr(IV)) instantly instead of the divalent Ca(II) ions. Recently, alginate gels were successfully prepared with various cross-linking agents (Table 2-2), and the metal-ion-anchored alginate materials

were used for the removal of anionic water pollutants (e.g., phosphate, fluoride, As(V), As(III) and Cr(VI)). The adsorption results demonstrated that the anionic pollutants possessed stronger attraction force to the tetravalent Zr(IV) ions than the divalent Ca(II) ions (Gopalakannan and Viswanathan, 2016; Kumar and Viswanathan, 2017). However, only a handful of articles have reported the use of the metal-ion-anchored alginate material as an immobilization material. Cui et al. (2016) immobilized biochar using magnesium-alginate/chitosan, which exhibited a Langmuir maximum adsorption capacity of 46.56 mg/g. Commercial clay (bentonite) and synthetic clay (hydrotalcite) were encapsulated by alginate gel that cross-linked with Mg(II), Ca(II), La(III), Ce(III) and Zr(IV) (Gopalakannan and Viswanathan, 2016). The prepared biocomposite beads showed fair adsorption capacity to phosphate.

Table 2-1 Cr(VI) adsorption capacity of calcium alginate-based materials.

| **Biomass** | **Immobilization material** | **q (mg/g)** | **Reference** |
|---|---|---|---|
| *Auricularia auricula* | Calcium alginate | 27.25 | (Zang et al., 2017) |
| Modified sludge biomass | Calcium alginate | 13.62 | (Ramteke and Gogate, 2016) |
| | Polyvinylalcohol | 28.87 | |
| | Polyvinylalcohol-carboxymethylcellulose | 52.21 | |
| | Polyvinylalcohol-carboxymethylcellulose-activated carbon | 57.11 | |
| *Trichoderma viride* | Calcium alginate | 16.08* | (Bishnoi et al., 2007) |
| *Pediastrum boryanum* | Calcium alginate | 23.8* | (Ozer et al., 2012) |
| | Calcium gelatin | 29.6* | |
| *Spirulina platensis* | Spirulina platensis extract | 41.12* | (Kwak et al., 2015) |
| *Lentinus sajor-caju* | Carboxymethylcellulose | 32.2* | (Arica and Bayramoğlu, 2005) |
| *Spirulina platensis* | Calcium alginate | 33.1 | (Gokhale et al., 2009) |
| *Nostoc calcicola* | Calcium alginate | 12.23 | (Anjana et al., 2007) |
| *Chroococcus sp.* | | 21.36 | |
| *Lyngbya putealis* | Calcium alginate | 7.72* | (Kiran and Kaushik, 2008) |
| *Paenibacillus xylanilyticus* | PVA-Alginate | 20.83* | (Rawat et al., 2013) |
| Yeast | Pozzolana | 47.61* | (Djafer et al., 2013) |
| *Murcor rouxii* | Silica-doped calcium alginate | 131.8 | **Present study** |
| | Silica-doped zirconium alginate | 169.6 | **Present study** |

*$q_{max}$ estimated from Langmuir isotherm

Table 2-2 Adsorption of anionic contaminants by metal-alginate materials.

| Adsorbate | Immobilized adsorbent | q (mg/g) | Reference |
|---|---|---|---|
| Phosphate | Zr@AlgBent biocomposite beads | 30.25 | (Gopalakannan and Viswanathan, 2016) |
| | Ce@AlgBent biocomposite beads | 26.13 | |
| | La@AlgBent biocomposite beads | 20.68 | |
| | Ca@AlgBent biocomposite beads | 11.68 | |
| | Mg@AlgBent biocomposite beads | 10.55 | |
| | Zr@AlgHT biocomposite beads | 19.00 | |
| | Ce@AlgHT biocomposite beads | 16.55 | |
| | La@AlgHT biocomposite beads | 13.04 | |
| | Ca@AlgHT biocomposite beads | 11.04 | |
| | Mg@AlgHT biocomposite beads | 9.22 | |
| | Magnesium-alginate/chitosan modified biochar microspheres | 46.56* | (Cui et al., 2016) |
| | N-isopropylacrylamide/aluminum alginate | 17.47 | (Wan et al., 2016) |
| | Alginate/Fe(III) hydrogel capsules | 9.70 | (Siwek et al., 2016) |
| Fluoride | Aluminum alginate | 79.30 | (Zhou et al., 2014) |
| | Porous zirconium alginate beads | 32.80* | (Zhou et al., 2015) |
| | La(III)-cross-linked seaweed | 11.02 | (Paudyal et al., 2013) |
| | Zr(IV)-cross-linked seaweed | 18.05 | |

*$q_{max}$ estimated from Langmuir isotherm

Table 2-2 (con't) Adsorption of anionic contaminants by metal-alginate materials.

| **Adsorbate** | **Immobilized adsorbent** | **q (mg/g)** | **Reference** |
|---|---|---|---|
| As(V) | Fe(III)-doped alginate gel | 0.38 | (Min and Hering, 1998) |
| | Fe-doped calcium alginate beads | 19.32 | (Banerjee et al., 2007) |
| As(III) | Fe-doped calcium alginate beads | 8.00 | (Banerjee et al., 2007) |
| Cr(VI) | Ca@AlgGel composites | 19.40 | (Kumar and Viswanathan, 2017) |
| | Ce@AlgGel composites | 24.50 | |
| | Zr@AlgGel composites | 25.40 | |
| | Barium alginate | 36.50* | (Uzaşçı et al., 2014) |
| | Silica-doped calcium alginate immobilized *M. rouxii* | 131.8 | **Present study** |
| | Silica-doped zirconium alginate immobilized *M. rouxii* | 169.6 | **Present study** |

*$q_{max}$ estimated from Langmuir isotherm

## 2.2 Hydrothermal carbonization of biomaterials

Hydrothermal carbonization is a thermo-chemical process converting waste biomass materials to carbonaceous products under subcritical water. The carbonization temperature depended on the type of biomass and its decomposition temperature. Normally, the hydrothermal temperature ranged from 150 - 250°C. In recent years, hydrochars has attracted increasing attention due to its low carbonization temperature, non-chemical consumption, as well as high thermal and oxidation stability.

Hydrothermal carbons have been synthesized using different kinds of carbon sources, such as saccharides (Titirici et al., 2008; Sevilla and Fuertes, 2009), chitosan (Yang et al., 2012; Shen et al., 2016), synthetic polymers (Gu et al., 2013; Wang et al., 2015a; Wu et al., 2015) and other organic compounds (Tan et al., 2015; Wang et al., 2015b; Lin et al., 2016). Organic waste materials have been demonstrated to be sustainable alternative carbon sources for hydrothermal carbonization. A wide range of waste organic materials was reported as a carbon source for the hydrothermal carbonization, such as food waste (Parshetti et al., 2014), rice straw (Liu et al., 2015), rice husk (Ding et al., 2016), corn stalk (Lei et al., 2016), forest waste (Xiao et al., 2012), biomass from landscape management areas (Rohrdanz et al., 2016), recycled paper mill sludge (Makela et al., 2015), human biowaste (Afolabi et al., 2015) and beetroot chips (Rillig et al., 2010). Hydrothermal carbonization of the nitrogen-

rich biomass is a good precursor for preparing nitrogen-doped hydrochars. The amino-functionalized hydrothermal carbon was successfully synthesized from chitosan (Yang et al., 2012; Xiao et al., 2013; Laginhas et al., 2016), eggshell membranes (Xiao et al., 2013) and bamboo fungi (Gao et al., 2014; Xu et al., 2017). Besides, Baccile et al. (2011) reported that the amine groups could be doped onto hydrochars by adding glycine as a nitrogen source in the hydrothermal carbonization of glucose.

Hydrochars is a useful material in different application areas (Table 2-3), such as fluorescence imaging (Mehta et al., 2015; Wang et al., 2015a), supercapacitor (Zhu et al., 2011; Tan et al., 2015; Jayaraman et al., 2017), fuel cell electrode (Paraknowitsch et al., 2009; Gu et al., 2017), gas storage (Falco et al., 2013), catalysts (Wen et al., 2017), soil additives (Rillig et al., 2010; Rohrdanz et al., 2016) and water pollutant sensors (Liu et al., 2015). Hydrochars was prepared in a relatively lower temperature than activated carbon, so it was usually rich in oxygen functional groups (e.g., hydroxyl, carboxyl) and nitrogen functional groups (e.g., amine, amide). Hence, hydrothermal carbon materials were an effective adsorbent for the removal of water contaminants (

Table 2-4), such as heavy metals (Demir-Cakan et al., 2009; Chen et al., 2011; Zhang et al., 2011; Jian et al., 2018), synthetic dyes (Parshetti et al., 2014; Alatalo et al., 2016; Chen et al., 2016), ammonia (Ibrahim et al., 2018) and herbicide (Zhao et al., 2017b).

Fungal biomass is primarily composed of carbohydrate, chitin, protein, fat and nucleic acid. The nitrogen-rich fungi was a promising carbon and nitrogen source for preparing the nitrogen-doped hydrochars. Nitrogen groups such as amines can be protonated in acidic conditions, and are responsible for Cr(VI) adsorption due to electrostatic attraction. Previous results (Lo, 2013) showed that the *M. rouxii* was capable of removing Cr(VI) in the aqueous solutions through the adsorption-coupled reduction mechanism, but the removal rate was slow and the equilibrium was not reached within three days. Hydrothermal carbonization was a green treatment process that converted waste biomass material to hydrochars. The obtained hydrochars had higher Cr(VI) removal capacity and a faster removal rate. Moreover, the co-carbonization of *M. rouxii* with amine-containing modifying agents would further functionalize the hydrochars with amine groups. Porous hydrochars could be synthesized by hydrothermal carbonization in the presence of eutectic salt, which would act as a soft template for the synthesis of functional carbon with a very high surface area (Fechler et al., 2013). Magnetic properties could be introduced to hydrochars by the incorporation of $Fe_3O_4$ particles so that the hydrochars could be recovered by external magnetic field after the adsorption process (Chen

et al., 2014; Wu et al., 2014).

Table 2-3 Application of hydrothermal carbons.

| **Hydrochars** | **Carbon source** | **Application** | **Reference** |
|---|---|---|---|
| HTC-material | Beetroot chips | Effects on plant and fungi growth | (Rillig et al., 2010) |
| Amino-functionalized fluorescent carbon nanoparticles | Chitosan | Bio-imaging | (Yang et al., 2012) |
| Fluorescent carbon nanoparticles | Polyacrylamide | Fluorescent | (Gu et al., 2013) |
| Carbon dots | Ginger juice | HepG2 cell imaging | (Li et al., 2014a) |
| Carbon dots | Sugar cane juice | Cellular imaging | (Mehta et al., 2014) |
| Functionalized carbon nanospheres | Glucose, polyethyleneimine | Extraction of nanoparticles and catalytic reduction of p-nitrophenol | (Kumar et al., 2014) |
| Copper-containing carbon dots | $Cu(NO_3)_2$, PMAA | Fluorescence | (Ren et al., 2015) |
| Polyethyleneimine-functionalized fluorescent carbon dots | Citric acid, polyethyleneimine | Fluorescence | (Wang et al., 2015a) |
| Carbon dots | Pulp-free apple juice | cell imaging | (Mehta et al., 2015) |
| Photoluminescent carbon dots | Rice straw | Fluorescent sensor for Fe(III) | (Liu et al., 2015) |
| Hydrochars | Landscape waste | Improving soil properties | (Rohrdanz et al., 2016) |
| Fluorescent carbon dots | S. aureus, E. coli | Live/dead detection of microorganisms | (Hua et al., 2017) |

Table 2-3 (con't) Application of hydrothermal carbons.

| **Hydrochars** | **Carbon source** | **Application** | **Reference** |
|---|---|---|---|
| Mesoporous carbons | Pine needles, pine cones, oak leaves | Not being tested | (Titirici et al., 2007) |
| Nitrogen-doped carbons | Chitosan, D(+)-glucosamine hydrochloride | Not being tested | (Zhao et al., 2010) |
| Hydrochars | Glucose, sucrose, potato starch | Not being tested | (Sevilla and Fuertes, 2009) |
| Nitrogen-containing hydrothermal carbon | D-glucose, glycine | Not being tested | (Baccile et al., 2011) |
| Functionalized carbon materials | Glucose, cellulose powder | Not being tested | (Falco et al., 2011) |
| Nitrogen-doped hydrothermal carbons | Spirulina platensis, glucose | Not being tested | (Falco et al., 2012) |
| Carbonaceous hydrogels | Chitin nanofibers, glucose | Not being tested | (Nata et al., 2012) |
| Hydrochars | Coconut fiber, eucalyptus leaves | Not being tested | (Liu and Balasubramanian, 2012) |
| Hydrochars | Corn stalk, forest waste | Not being tested | (Xiao et al., 2012) |
| Hydrochars | Cellulose, lignin, D-xylose, wood meal | Not being tested | (Kang et al., 2012) |
| Hydrothermal carbonization of glucose | Glucose | Not being tested | (Fechler et al., 2013) |
| Carbon nanoparticles | α-cellulose | Not being tested | (Abd Hamid et al., 2015) |
| Diamond-like carbon nanofoam | Sucrose, naphthalene | Not being tested | (Frese et al., 2017) |
| Hydrochars | Paper mill sludge residue | Not being tested | (Makela et al., 2015) |
| Hydrochars | Glucose | Not being tested | (Poerschmann et al., 2017) |
| Hydrochars | Cactus cladodes | Not being tested | (Volpe et al., 2018) |

Table 2-4 Adsorption of water contaminants by hydrothermal carbonized materials.

| **Adsorbent** | **Adsorbate** | **q (mg/g)** | **$t_{eqm}$** (h) | **pH** | **Reference** |
|---|---|---|---|---|---|
| Fungus/attapulgite (F/ATP) composites | U(VI) | 152 | 24 | 4.5 | (Cheng et al., 2015) |
| Dual-Core Fe2O3@Carbon Structure | Cu(II) | 97.79 | 12 | 5.0 | (Wang et al., 2017) |
| Carboxylate-Rich Carbonaceous Materials | Pb(II)<br>Cd(II) | 351.4<br>88.8 | 72 | 6.0 | (Demir-Cakan et al., 2009) |
| Meso- and microporous soft templated hydrothermal carbons | Methylene blue | 112.17 | 24 | 6.0 | (Alatalo et al., 2016) |
| Hydrophilic $Fe_3O_4$/carbon composites | Rhodamine B | 43.86 | 2.5 | raw | (Chen et al., 2016) |
| Amino-rich hydrothermal carbon-coated electrospun polyacrylonitrile fiber | 2,4-dichloro-phenoxyacetic acid | 164.47 | 48 | 3.0 | (Zhao et al., 2017b) |
| Attapulgite clay@carbon (ATP@C) nanocomposite | Pb(II) | 263.83 | 30 | 6.0 | (Chen et al., 2011) |
| Hydrothermally produced hydrochars | Cu(II) | 0.1693 | 1 | 4.8 | (Jian et al., 2018) |
| Hydrothermal carbonization of urban food waste | Acridine orange<br>Rhodamine 6G | 79.365<br>71.428 | 2 | 8.0 | (Parshetti et al., 2014) |
| Hydrothermal carbonization of coffee husk | Methylene blue | 34.85 | 2 | 5.5 | (Ronix et al., 2017) |
| Hydrothermal Carbonization of Wetland Biomass | Ammonia | 45.04 | 2 | 9.35 | (Ibrahim et al., 2018) |

Table 2-5 Removal of Cr(VI) by hydrothermal carbonized materials.

| **Adsorbents** | **$Q_{Cr(VI)}$ (mg/g)** | **$q_{tot}$ (mg/g)** | **$t_{eqm}$** | **pH** | **Reference** |
|---|---|---|---|---|---|
| Amino-functionalized carbon spheres | / | 243.6 | 24 h | 2.0 | (Wang et al., 2012b) |
| Novel montmorillonite supported carbon nanosphere adsorbent | 156.25 | / | 180 min | 2.0 | (Li et al., 2014b) |
| Magnetic carbon nanoadsorbents (calcination) | 275.6 | / | 30 min | 2.0 | (Qiu et al., 2015) |
| Hydrophilic $Fe_3O_4$/carbon composites | 61.69 | / | 2.5 h | 4.0 | (Chen et al., 2016) |
| Amino-rich hydrothermal carbon-coated electrospun polyacrylonitrile fiber | 290.70 | / | 48 h | 2.0 | (Zhao et al., 2017b) |
| Activated carbon coated silica sand | 1.538 | / | 2 h | 2.0 | (Huang et al., 2017b) |
| Hydrothermal carbonization of chitosan | 388.60 | / | 12 h | 2.0 | (Shen et al., 2016) |
| Hydrothermal carbonization of corn stalk | 80 | / | 60 min | 1.0 | (Lei et al., 2016) |
| Hydrothermal carbonization of rice husk | 31.1 | / | 48 h | 6.0 | (Ding et al., 2016) |
| Attapulgite clay@carbon (ATP@C) nanocomposite | / | 177.7 | 30 h | 2.0 | (Chen et al., 2011) |
| Dual-Core Fe2O3@Carbon Structure | 104 | / | 12 h | 2.0 | (Wang et al., 2017) |
| Nitrogen-enriched carbon spheres | 285 | / | 2 h | 2.0 | (Lin et al., 2016) |
| Hydrothermal carbonized *M. rouxii* | 162.0 | 116.8 | 24 h | 2.0 | **Presented study** |
| Polyethyleneimine-modified hydrothermal carbonized *M. rouxii* | 239.3 | 202.7 | 24 h | 2.0 | **Presented study** |

## 2.3 Biosorption modelling

### 2.3.1 Adsorption kinetic models

The kinetic study is essential to express the adsorption process ~~to~~ as a function of time. The kinetic results were simulated with five different kinetic models, namely the pseudo-first-order kinetic model, the pseudo-second-order, the intra-particle diffusion, the fractional power and the Elovich kinetic models.

#### 2.3.1.1 Pseudo-first-order model

The Lagergren's pseudo-first-order kinetic model is expressed as follows:

$$\frac{dq_t}{dt} = k_1(q_e - q_t)$$

The model can be transformed into linear form as follows:

$$\ln(q_e - q_t) = -k_1 t + lnq_e$$

where $q_e$ is the equilibrium sorption capacity (mg/g); $q_t$ is the adsorption capacity at time t (mg/g); and, $k_1$ is the pseudo-first-order kinetic rate constant (1/min).

For the linear regression, the $k_1$ and $q_e$ can be determined from the plot of $\ln(q_e-q_t)$ against t.

### 2.3.1.2 Pseudo-second-order model

The Lagergren's pseudo-second-order kinetic model is given as follows:

$$\frac{dq_t}{dt} = k_2(q_e - q_t)^2$$

The model can be transformed into the following linearized equation.

$$\frac{t}{q_t} = \frac{1}{k_2 q_e^2} + \frac{1}{q_e} t$$

where $q_e$ is the equilibrium sorption capacity (mg/g); $q_t$ is the adsorption capacity at time t (mg/g); and, $k_2$ is the pseudo-second-order kinetic rate constant (g/mg-min).

For the linear regression, the $k_2$ and $q_e$ can be determined from the plot of $t/q_t$ against t.

### 2.3.1.3 Fractional power model

The fractional power model was modified from the Freundlich equation and was firstly developed to simulate the desorption of phosphate from the soil using the anion-exchange resin (Dalal, 1974).

$$q_t = \mathrm{k}_f t^v$$

The model can be transformed into linear equation as follows.

$$\ln q_t = \ln k_f + v \ln t$$

where $k_f$ is the fractional power kinetic constant (mg/g-min$^v$), while v is the fractional power exponent.

The constants v and $k_f$ can be determined from the plot of $\ln q_t$ against ln *t*. The value of $k_f v$ represents the adsorption rate at t = 1 min.

### 2.3.1.4 Intra-particle diffusion model

The intra-particle diffusion model is useful in identifying and distinguishing the diffusion processes involved in the adsorption (Choy et al., 2004). If the intra-particle diffusion plot is linear and passes through origin, the adsorption process is only controlled by the intra-particle diffusion. However, if the plot exhibits multi-linear characteristic, the overall adsorption process may be controlled by one or more steps, such as external film diffusion. (Bilgili, 2006). The intra-particle diffusion model is expressed in the following equation:

$$q_t = k_{id} t^{0.5}$$

where $k_{id}$ is the intra-particle diffusion kinetic constant ($mg/g \cdot min^{0.5}$).

The intra-particle diffusion kinetic constant ($k_{id}$) can be determined from the plot of $q_t$ against $t^{0.5}$.

The Boyd plot is the plot of $B_t$ against $q_t/q_e$, which is utilized to determine the actual rate-controlling step that is involved in the adsorption process (Viegas et al., 2014).

$$\frac{q_t}{q_e} = 1 - \frac{6}{\pi^2} e^{-B_t}$$

$$B_t = -0.4977 - \ln\left(1 - \frac{q_t}{q_e}\right)$$

If the Boyd plot is nonlinear and did not pass through the origin, the film diffusion would be the rate-determining step. If the plot is linear and passes through the origin, the adsorption rate would be controlled by the intra-particle diffusion.

### 2.3.1.5 Elovich model

The Elovich kinetic model is useful in simulating the chemisorption of adsorbate on a solid surface without desorption, so the adsorption rate decreases with increasing surface coverage (or time). The Elovich model is expressed as follows:

$$\frac{dq_t}{dt} = ae^{-bq_t}$$

The model can be transformed into linear equation.

$$q_t = \frac{1}{b} ln(t + t_0) - \frac{1}{b} lnt_0$$

where $q_t$ is the adsorption capacity at time t (mg/g); *a* is the initial adsorption rate (mg/g-min) at zero-coverage; *b* is the Elovich constant (g/mg) which is related to the equilibrium adsorption capacity g; and, $t_0$ is the Elovich time constant (min).

When $t >> t_0$, $t + t_0 \approx t$ and $t_0 = 1 / ab$, the above equation is transform into the following,

$$q_t = \frac{1}{b} lnt + \frac{1}{b} ln(ab)$$

The constants *a* and *b* can be determined from the plot of $q_t$ against ln *t*, and the approaching equilibrium parameter ($R_E$) can be calculated from the following equation.

$$R_E = \frac{1}{q_e b}$$

Wu et al. (2009) employed the $R_E$ constant to classify the kinetics of the adsorption. Table 2-6 lists the classification. The smaller $R_E$ value represents the faster adsorption. Therefore, the adsorption kinetics are classified into the four zones based on the curvature of curve. Table 2-6 lists the classification of the kinetic curve and the corresponding $R_E$ value.

Table 2-6 Classification of the kinetic curve based on the $R_E$ value.

| Zone | Curve | $R_E$ |
|---|---|---|
| I | Slow rising | > 0.3 |
| II | Mild rising | 0.3 – 0.1 |
| III | Rapid rising | 0.1 – 0.02 |
| IV | Instant approaching equilibrium | < 0.02 |

### 2.3.2 Adsorption isotherm models

The isotherm study aims to investigate the relationship between the uptakes of adsorbate and the equilibrium adsorbate concentration. The adsorption capacity (qe) was calculated by the following equation.

$$q_e = (C_0 - C_e) \times \frac{V}{M}$$

where $C_0$ is the initial concentration of Cr(VI) (mg/L); $C_e$ is the equilibrium concentration of Cr(VI) (mg/L); V is the adsorption volume (L) and M is the mass of adsorbent used (g/L).

Several isotherm models, namely Langmuir, Freundlich, Tempkin, Dubinin-Radushkevich and Sips isotherm model, were commonly employed to simulate the adsorption equilibrium.

### 2.3.2.1 Freundlich model

The Freundlich isotherm model was first applied by Freundlich (1906). It was the first empirical isotherm which was developed based on the multilayer adsorption on the adsorption with different adsorption energies. The stronger adsorption sites are occupied first. The binding energy (or heat of adsorption) decreases with the increasing degree of site occupation. Compared with the Langmuir isotherm, the Freundlich isotherm was more suitable for describing the adsorption behavior on the heterogeneous surface. The nonlinear and linearized equations of Freundlich isotherm are expressed as follows:

$$\text{Nonlinear:} \qquad q_e = K_F C_e^{1/n}$$

$$\text{Linearized:} \quad \ln q_e = ln K_F + \frac{1}{n} ln C_e$$

where $K_F$ is the Freundlich constant (mg/g) and n is the Freundlich exponent.

#### 2.3.2.2 Langmuir model

The Langmuir isotherm is the first and most commonly used isotherm model to describe the adsorption (Langmuir, 1916). Langmuir model assumes: (1) the homogenous adsorption that all the adsorption sites on the adsorbent surface have the same adsorption energy; (2) the monolayer adsorption that each adsorption site can only bind with one adsorbate molecule; and (3) the localized adsorption that the adsorbates were-fixed on a definite site. The nonlinear and linearized equations of the Langmuir isotherm are expressed as follows:

$$\text{Nonlinear:} \quad q_e = \frac{q_{max} b_L C_e}{1 + b_L C_e}$$

$$\text{Linearized:} \quad \frac{C_e}{q_e} = \frac{1}{q_{max} b_L} = \frac{b_L C_e}{q_{max}}$$

where $q_{max}$ is the maximum adsorption capacity (mg/g) and $b_L$ is the Langmuir constant.

### 2.3.2.3 Tempkin model

The theory of the Tempkin isotherm model is similar to the Freundlich isotherm model, The Tempkin isotherm assumes the heat of adsorption decreased with increasing surface coverage (Tempkin and Pyzhev, 1940). However, the Tempkin model assumes that the heat of adsorption decreases linearly, instead of logarithmically as in the Freundlich model. The nonlinear and linearized equations of the Tempkin isotherm are expressed as follows:

$$\text{Nonlinear:} \quad q_e = \frac{RT}{b_T} ln(K_T C_e)$$

$$\text{Linearized:} \quad q_e = \frac{RT}{b_T} lnK_T + \frac{RT}{b_T} lnC_e$$

where $K_T$ is the Tempkin isotherm constant (L/g); $b_T$ is the Tempkin constant (J/mol), which is related to the heat of adsorption; R is the gas constant (8.314 J/mol-K) and T is the temperature (K).

### 2.3.2.4 Dubinin-Radushkevich model

The Dubinin-Radushkevich isotherm model is the first model developed for describing the adsorption characteristics by the porous adsorbent (Dubinin and Radushkevich, 1947).

$$q_e = \mathrm{Q}\exp(-B_D \varepsilon_D^2)$$

$$\varepsilon_D = RT ln(1 + \frac{1}{C_e})$$

$$\ln q_e = \ln \mathrm{Q} - B_D R^2 T^2 ln(1 + \frac{1}{C_e})^2$$

where Q is the Dubinin-Radushkevich isotherm constant (mg/g); $B_D$ is the Dubinin-Radushkevich isotherm constant ($mol^2/kJ^2$) and $\varepsilon_D$ is the Polanyi potential.

The mean free energy of sorption (E) is correlated with the $B_D$ by the following equation. The value E is employed to estimate the type of adsorption reaction. If E < 8 kJ/mol, the adsorption is classified as physisorption. If the E value is between 8-16 kJ/mol, the adsorption reaction is classified as ion-exchange. If E > 16 kJ/mol, the adsorption reaction is classified as chemisorption.

$$\mathrm{E} = \frac{1}{\sqrt{2B_D}}$$

### 2.3.2.5 Sips model

The Sips isotherm model is a combination of the Langmuir isotherm and Freundlich isotherm (Sips, 1948). The Sips model is simply reduced to the Freundlich model at a lower adsorbate concentration, but it is reduced to the Langmuir isotherm at a higher adsorbate concentration.

$$q_e = \frac{K_s C_e^{m_s}}{1 + n_m C_e^{m_s}}$$

where $K_s$ is the Sips isotherm constant (L/g); $n_m$ is the Sips isotherm constant (L/mg) and $m_s$ is the Sips exponent.

## 2.4 Cr(VI) removal mechanism

The Cr(VI) ions could be removed from aqueous solutions by different kinds of adsorbents (Table 2-7), such as fungi (Ramrakhiani et al., 2011; Garza-González et al., 2017), fruit peel (Saranya et al., 2018), coffee waste (Prabhakaran et al., 2009), food waste (Daneshvar et al., 2002), agricultural waste (Escudero et al., 2009), plant material (Elangovan et al., 2008; Surendran and Baral, 2018), bracken fern (Lopez-Garcia et al., 2010), biochar (An et al., 2018; Yang et al., 2018; Zhang et al., 2018) and activated carbon (Gong et al., 2013). As literature reported that generally there are four Cr(VI) removal mechanisms by adsorbents: (1) adsorption, (2) direct reduction, (3) indirect reduction and (4) simultaneous adsorption and reduction by the extracellular polymeric substances.

*(1) Adsorption*

Under the acidic conditions, the oxygen functional groups (e.g., hydroxyl, carboxyl and carboxylic acid) and nitrogen functional groups (e.g., amine) on the surface of adsorbent were protonated and positively charged to form $-OH_2^+$, $>C=OH^+$, $-COOH_2^+$ and $-NH_3^+$ (Zhou et al., 2016; Luo et al., 2017). The protonated surface had a strong electrostatic attraction to the anionic Cr(VI) ($HCrO_4^-$ or $CrO_4^{2-}$). The Cr(VI) adsorption due to electrostatic attraction usually declined with increasing solution pH (Gong et al., 2013). The electrostatic interaction between the anionic Cr(VI) and the $NH_3^+$ groups was found to be a possible mechanism for Cr(VI) adsorption by the amino-functionalized mesoporous silica (Lee et al., 2018).

$$-\mathrm{OH} + \mathrm{HCrO_4^-} \rightarrow -\mathrm{OH_2^+} \cdots \mathrm{HCrO_4^-}$$

$$> \mathrm{C=O} + \mathrm{HCrO_4^-} \rightarrow > \mathrm{C=OH^+} \cdots \mathrm{HCrO_4^-}$$

$$-\mathrm{COOH} + \mathrm{HCrO_4^-} \rightarrow -\mathrm{COOH_2^+} \cdots \mathrm{HCrO_4^-}$$

$$-\mathrm{NH_2} + \mathrm{HCrO_4^-} \rightarrow -\mathrm{NH_3^+} \cdots \mathrm{HCrO_4^-}$$

*(2) Direct reduction*

Cr(VI) was directly reduced to Cr(III) in the aqueous phase by the electron-donor groups (e.g., amine and hydroxyl groups) on the surface of adsorbent, i.e. the groups having lower reduction potential values than that of Cr(VI) (+1.3 V) (Park et al., 2005). Shen et al. (2013) reported the detoxification mechanisms of Cr(VI) by the tetraethylenepentamine-functionalized nanosized magnetic polymer adsorbents (TEPA-NMPs). They found that the ether, hydroxyl groups and $Fe_3O_4$ magnetic core in the adsorbents would participate in the redox process.

$$-\mathrm{NH_3^+}\cdots\mathrm{HCrO_4^-} + 6\mathrm{H^+} + 3\mathrm{Fe^{2+}} \rightarrow -\mathrm{NH_2}\cdots\mathrm{Cr^{3+}} + 3\mathrm{Fe^{3+}} + 4\mathrm{H_2O}$$

$$3-\mathrm{C}-\mathrm{OH} + 2-\mathrm{NH_3^+}\cdots\mathrm{HCrO_4^-} + 8\mathrm{H^+} \rightarrow 2-\mathrm{NH_2}\cdots\mathrm{Cr^{3+}} + 3>\mathrm{C}=\mathrm{O} + 8\mathrm{H_2O}$$

*(3) Indirect reduction*

The indirect Cr(VI) reduction was also named as the adsorption-coupled reduction. Adsorption-coupled reduction mechanism was the typical mechanism generally accepted by a pool of researcher (Shen et al., 2013; Sun et al., 2016; Zhou et al., 2016; Luo et al., 2017). The adsorption-coupled reduction mechanism comprised of four steps: (i) the adsorption of anionic Cr(VI) to the positively-charged surface groups due to electrostatic attraction; (ii) the reduction of Cr(VI) to Cr(III) by adjacent electron-donor groups; (iii) the release of the Cr(III) to the aqueous phase due to electronic repulsion between the positively-charged groups and Cr(III) ions; and (iv) the chelation of the cationic Cr(III) by the carboxylic acid groups (-COOH).

The reduction of Cr(VI) to Cr(III) are commonly involved in the Cr(VI) removal mechanism rather than the pure Cr(VI) adsorption (Figure 2-1 and 2-2). The Cr(VI) adsorption and reduction were strongly influenced by solution pH (Shen et al., 2013). The Cr(VI) reduction was catalyzed in the acidic environment, while the Cr(III) adsorption increased for pH > 4 (Gong et al., 2013). Tian et al. (2016) proposed that the adsorbed Cr(VI) on the magnetic $Fe_3O_4$/Halloysite nanohybrid was partly reduced to the Cr(III) using XPS analysis. Part of the reduced Cr(III) was adsorbed on the adsorbent surface through the precipitation and chelation, while another part of Cr(III) was released back to solution phase due to the electrostatic repulsion (Fellenz et al., 2017; Yang et al., 2018). In addition, the humic acid was coated on the surface of $Fe_3O_4$ by Jiang et al. (2014). The humic acid was found to be responsible for the

reduction of Cr(VI) to Cr(III). The humic acid could also act as a ligand and form complex with Cr(III) via a coupled reduction-complexation mechanism. The Cr K-edge EXAFS demonstrated that the six neighboring oxygen atoms likely in an octahedral geometry was found in the Cr-loaded humic acid coated $Fe_3O_4$ materials.

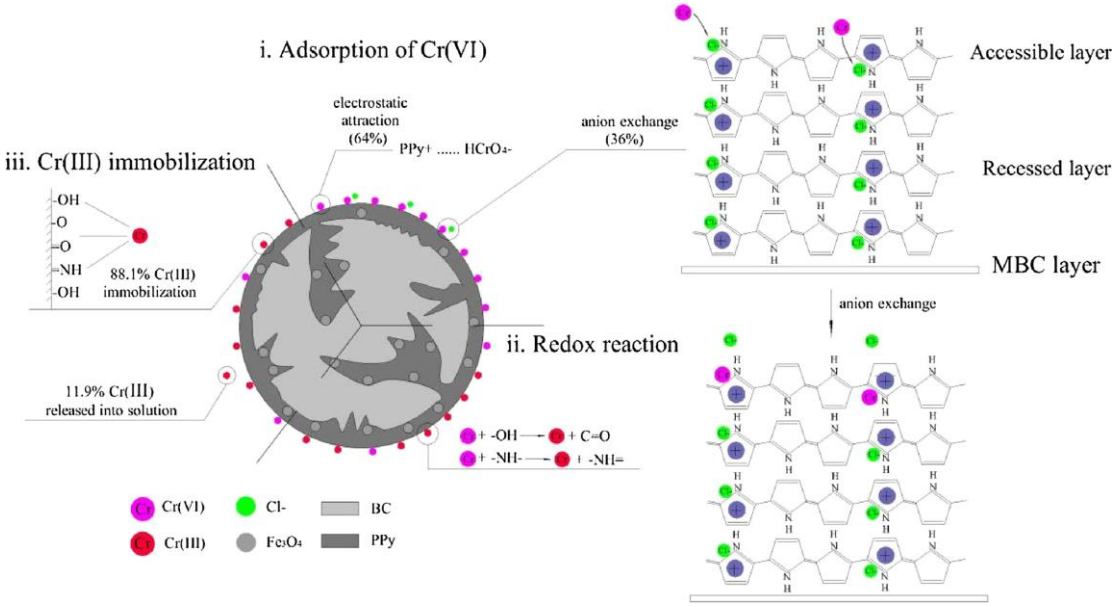


Figure 2-1 Possible reaction pathway and contribution of the Cr(VI) removal by the magnetic corncob biochar/polypyrrole composite (Yang et al., 2018).

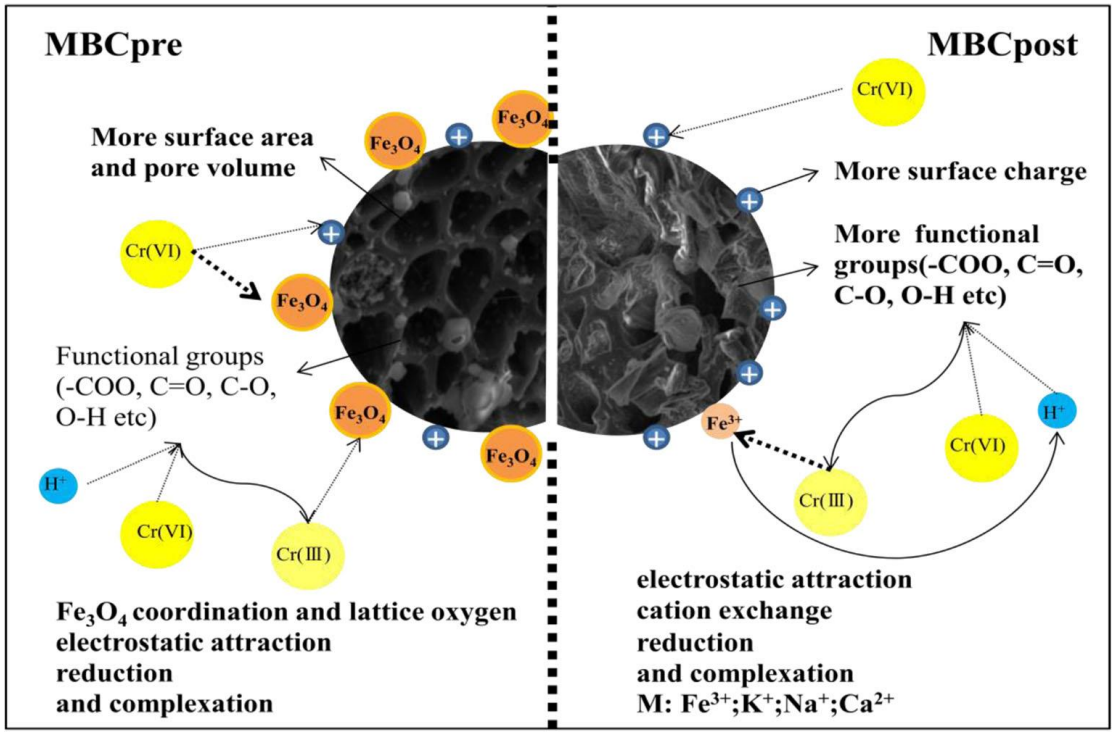


Figure 2-2 Mechanism of the Cr(VI) adsorption by the biochars (An et al., 2018).

*(4) Simultaneous adsorption and reduction by extracellular polymeric substances*

Wei et al. (2018) reported the simultaneous Cr(VI) adsorption and reduction by the extracellular polymeric substances (EPS) from bacteria. Four types of interactions, namely ion-exchange, chelation, reduction and surface physical sorption, occurred in the Cr(VI) removal process. In the initial stage of Cr(VI) removal, the Cr(VI) was adsorbed on EPS through the ion-exchange and chelation. With the sorption proceeding, most of the adsorbed Cr(VI) ions are reduced to Cr(III) by the benzenoid amine (–NH–) groups on EPS. The hydrogen ions in the solution phase are consumed due to protonation of surface groups and the Cr(VI) reduction. Finally, the generated Cr(III) bind onto the EPS surface via the chelation and surface physical sorption.

Table 2-7 Removal of Cr(VI) through the adsorption-coupled reduction mechanism by different types of adsorbents.

| **Adsorbent** | **$Q_{Cr(VI)}$ (mg/g)** | **$q_{max}$ (mg/g)** | **$t_{eqm}$** | **pH** | **Reference** |
|---|---|---|---|---|---|
| Bracken fern | / | 83 | 24 h | 2.0 | (Lopez-Garcia et al., 2010) |
| *Artocarpus heterophyllus* peel | 64.47 | / | 2 h | 2.0 | (Saranya et al., 2018) |
| Spent Tea | / | 44.9 | / | 4.0 | (Prabhakaran et al., 2009) |
| Coffee dust | / | 39.0 | / | 4.0 | |
| Soya cake | / | 0.28 | 15 h | 8.0 | (Daneshvar et al., 2002) |
| Grape stalk waste | / | / | / | 3.0 | (Escudero et al., 2009) |
| Mangrove leaves | 8.87 | / | 6 h | 5.0 | (Elangovan et al., 2008) |
| Water lily | 8.44 | / | / | 5.0 | |
| *Sorghastrum Nutans L. Nash* | 15 | / | 10 h | 1.5 | (Surendran and Baral, 2018) |
| *Cladosporium cladosporioides* | 491.85 | / | 288 h | 1.0 | (Garza-González et al., 2017) |
| Polyethyleneimine-Functionalized Corn Bract | 438 | / | 24 h | 2.0 | (Luo et al., 2017) |
| m-phenylenediamine-modified magnetic chitosan | 227.27 | / | 24 h | <4.0 | (Wan et al., 2018) |
| Wheat-residue derived black carbon | / | 21.34 | 4 h | 1.0 | (Wang et al., 2010) |
| Corn stalk biochar | 25.683 | / | 24 h | 2.0 | (An et al., 2018) |
| Tobacco petiole biochar | 195.2 | / | 9 h | 1.0 | (Zhang et al., 2018) |
| Ramie biochars | / | 82.2 | 24 h | 2.0 | (Zhou et al., 2016) |
| Tannic acid immobilized powdered activated carbon | 5.639 | / | 24 h | 7.0 | (Gong et al., 2013) |
| Magnetic corncob biochar/polypyrrole composite | / | 19.23 | / | / | (Yang et al., 2018) |

Table 2-7 (con't) Removal of Cr(VI) through the adsorption-coupled reduction mechanism by different types of adsorbents.

| **Adsorbent** | **$Q_{Cr(VI)}$ (mg/g)** | **$q_{max}$ (mg/g)** | **$t_{eqm}$** | **pH** | **Reference** |
|---|---|---|---|---|---|
| Vivianite | 3.15 | / | 24 h | 7.0 | (Bae et al., 2018) |
| Humic-acid-coated magnetite | / | 3.37 | 2 h | / | (Jiang et al., 2014) |
| Synthesized multilayer material coated nanoscale zerovalent iron | 84.4 | / | / | 3.0 | (Wu et al., 2018) |
| (3-aminopropyl)trimethoxysilane functionalized mesoporous silica | / | 84.90 | / | 2.9 | (Lee et al., 2018) |
| Amino-functionalized MCM-41 | 86.4 | 50.8 | 24 h | 2.0 | (Fellenz et al., 2017) |
| Magnetized natural zeolite-polypyrrole composite | 53.2 | / | / | / | (Mthombeni et al., 2018) |
| Magnetic $Fe_3O_4$/Halloysite nanohybrid | 132.86 | / | 36 h | 2.0 | (Tian et al., 2016) |
| Magnetic triethylene tetramine-graphene oxide ternary nanocomposite | 180.12 | / | 2 h | 2.0 | (Sun et al., 2016) |
| Tetraethylenepentamine functionalized nanosized magnetic polymer | 303.0 | / | 3 h | 2.0 | (Shen et al., 2013) |
| Extracellular polymeric substances from *Klebsiella sp. J1* (bacteria) | 53.3 | / | 12 h | 4.0 | (Wei et al., 2018) |

# 3. Materials and Methods

## 3.1 Instrumentations

For the cultivation of fungal materials, the PDA plates were incubated in a Shel Lab 2020 low-temperature incubator at 25ºC, and the cultivations of fungal biomass in liquid YPG medium were agitated in an Innova 2300 platform shaker at 250 rpm. The fungal biomass was dried in a Memmert universal oven at 60ºC and was ground into powder form by a laboratory blender.

The Batch Cr(VI) removal experiments were conducted in a Uniwist 400 orbital shaker at 250 rpm shaking. The solution pH of samples was measured by an Orion Star A211 pH benchtop meter. The suspended adsorbents in the metal solution were separated by the Hettich Mikro 120 centrifuge at 14000 rpm for 1 minute. The total Cr concentration of the supernatant was determined by the Agilent 710 inductive coupled plasma optical emission spectrometer (ICP-OES, Agilent, USA), while Cr(VI) concentration was monitored by the GENESYS 20 visible spectrophotometer (Thermo Fisher Scientific, USA) at 540 nm after the formation of color complex with the 1,5-diphenylcarbazide.

## 3.2 Chemicals

All chemicals were obtained from commercial suppliers and used without further purification. Potato Dextrose Agar, yeast extract, mycological peptone and D-glucose were purchased from Oxoid Microbiology Product. Sodium alginate, ammonium persulfate (≥98%), Tetraethylorthosilicate (TEOS, ≥99%), N-[3-(Trimethoxysilyl) propyl]ethylenediamine (ENTMOS, 97%), diethanolamine (DEA, 98.5%), polyethyleneimine (PEI, MW = 800 and 25000) and iron(II) chloride tetrahydrate (≥99%) was purchased from Sigma-Aldrich. Calcium chloride dihydrate (≥99%) and sodium hydroxide (98%), acrylamide (AA, 98.5%), triethylenetetramine (TETA, 95%), zirconyl chloride octahydrate (>98%) and iron(III) chloride hexahydrate (≥99%) were obtained from Acros Organics. Sodium chromate anhydrous (>99.5%) was purchased from Merck. Nitric acid (69%) and n-hexane (95%) were obtained from ANAQUA (HONG KONG) CO. LTD. Urea was purchased from Fisher Scientific, while ammonium hydroxide ($NH_4OH$, 25%) was obtained from BDH.

## 3.3 Cultivation of *M. rouxii*

*M. rouxii* was maintained on a PDA (Oxoid CM 139) slant at 4ºC. The seed culture was prepared by the loop-inoculation method and was cultivated in 20 ml liquid YPG medium (1% yeast extract, 0.3% mycological peptone and 0.4% D-glucose) at pH 4.5 and 25ºC under 250 rpm shaking. After the incubation for 1 day, the seed culture was transferred to 400 ml YPG medium and then cultivated for 3 days at the same condition. The fungal biomass was harvested by the filtration and washed with DDI water. The biomass was dried in an oven at 60ºC, then pulverized and sieved by a 180 μm sieve.

## 3.4 Immobilization of *M. rouxii*

### 3.4.1 Silica-doped calcium alginate

*M. rouxii* was immobilized using the calcium alginate (CA) and silica-doped calcium alginate (SCA) methods. The obtained bead adsorbents were named as calcium-alginate-immobilized *M. rouxii* (CAIM) and silica-doped calcium-alginate-immobilized *M. rouxii* (SCAIM), respectively. The immobilized *M. rouxii* (IM) beads were prepared as follows: A biomass suspension of *M. rouxii* at 40 g/L was mixed with the 4% sodium alginate solution at the fungal biomass to sodium alginate mass ratio of 1:1. After thorough mixing, the resulting mixture was dropped into a gelation solution containing 4% calcium chloride and 0.1% ammonium persulfate using a peristaltic pump. The drops gelled and formed spherical beads upon the contact with gelation solution. The CAIM beads were then re-suspended in the fresh gelation solution with a constant and gentle agitation overnight to complete the gelation.

For the doping of silica particles, the CAIM beads were then transferred in an ice-cold n-hexane, and N-[3-(Trimethoxysilyl)propyl]-ethylenediamine (ENTMOS) was added to the solution mixture followed by stirring for 1 minute. Tetraethylorthosilicate (TEOS) was subsequently added to the mixture which followed by another 1-minute stirring. The volume ratio of alginate : n-hexane : ENTMOS : TEOS was 10 : 14 : 0.9 : 0.9 (Sakai et al., 2002a; Lim et al., 2009). The obtained SCAIM beads were finally re-suspended in the fresh gelation solution with constant and gentle agitation for overnight. Meanwhile, the calcium alginate (CA)

and silica-coated calcium alginate (SCA) beads were prepared by the same experimental procedures but without the addition of *M. rouxii*.

### 3.4.2 Silica-doped zirconium alginate

Zirconium alginate (ZA), silica-doped zirconium alginate (SZA), zirconium-alginate-immobilized *M. rouxii* (ZAIM) and silica-doped zirconium-alginate-immobilized *M. rouxii* (SZAIM) beads were prepared from immersing the corresponding calcium-alginate-based adsorbents in the 4% zirconyl chloride solution for 24 h.

## 3.5 Preparation of hydrothermal carbonized *M. rouxii*

### 3.5.1 Preparation of hydrothermal carbonized *M. rouxii* (HTC-MR)

In a typical synthesis, the hydrothermal carbonized *M. rouxii* (HTC-MR) was prepared via a one-pot hydrothermal process. First, 1.0 g of *M. rouxii* (MR) powder was suspended in 20 ml DDI water. After vigorous stirring for 5 minutes, the homogeneous biomass suspension was transferred to a Teflon lined stainless steel autoclave (50 ml volume) and heated at 200°C for 12 h. The as-synthesized HTC-MR was recovered by the centrifugation at 8000 rpm for 10 minutes, washed with DDI water for 3 times, and dried in the LABCONCO FreeZone 2.5 Liter -50°C Benchtop Freeze Dryer.

For the preparation of amino-functionalized HTC-MR, 0.5 g of the amine-containing modifying was co-carbonized with MR under hydrothermal condition. The hydrochars prepared by the addition of acrylamide (AA), diethanolamine (DEA), polyethyleneimine (PEI), Urea, ammonium hydroxide ($NH_4OH$) and triethylenetetramine (TETA) was named AA-HTC-MR, DEA-HTC-MR, PEI-HTC-MR, Urea-HTC-MR, $NH_4OH$-HTC-MR and TETA-HTC-MR, respectively. The hydrothermal process was optimized by varying the reaction temperature and time from 160 – 240°C and 6 – 18 h, respectively. Moreover, the modifying agent dosage was optimized within the range of 0.1 – 1.0 g/g MR.

### 3.5.2 Incorporation of zirconium oxide in hydrothermal carbonized *M. rouxii* ($ZrO_2$-$NH_4$-HTC-MR)

The zirconium oxide (or zirconia) was incorporated into the HTC-MR by the following one-pot hydrothermal process: First, 0.11 g (0.035 mol) of $ZrOCl_2 \cdot 8H_2O$ and 1 g of *M. rouxii* were dissolved in 20 ml DDI water. Next, the ammonium hydroxide solution (approximately 30%) was slowly added into the solution mixture under the magnetic stirring followed by the sonication for 30 min to obtain a homogeneous solution. After that, the solution mixture was transferred to a Teflon-lined stainless steel autoclave (50 ml volume) and heated at 200°C for 12 h. Finally, the product was recovered by the centrifugation at 8000 rpm for 10 minutes, washed with DDI water 3 times, and dried in the LABCONCO FreeZone 2.5 Liter -50°C Benchtop Freeze Dryer.

### 3.5.3 Hydrothermal carbonized *M. rouxii* in the eutectic salt template (HTC-MR-CaFe)

Nine grams of $CaCl_2$-$FeCl_3$ eutectic salt mixture (Eutectic salt ratio: 36 mol% of $CaCl_2$ and 64 mol% of $FeCl_3$) was dissolved in 5 ml of DDI water. Then, 1 g of *M. rouxii* was suspended in the salt solution mixture. After that, the solution mixture was transferred to a Teflon lined stainless steel autoclave (50 ml volume) and heated at 200°C for 12 h. Finally, the product was recovered by the centrifugation at 8000 rpm for 10 minutes, washed with DDI water for 3 times, and dried in the LABCONCO FreeZone 2.5 Liter -50°C Benchtop Freeze Dryer.

### 3.5.4 Preparation of magnetic hydrothermal carbonized *M. rouxii* ($Fe_3O_4$-0.5PEI-HTC-MR)

The magnetic hydrothermal carbonized *M. rouxii* was fabricated by a simple one-step hydrothermal reaction. In a typical synthesis, 0.1305 g of $FeCl_2 \cdot 4H_2O$ and 0.2690 g of $FeCl_3 \cdot 6H_2O$ were dissolved in 10 ml of DDI water. The concentrated NaOH solution was then slowly added to the above solution under sonication until the solution pH reached 12.0. Black $Fe_3O_4$ would form immediately and could be easily separated by an external magnetic field. It was washed with DDI water 3 times and re-suspended in 20 ml DDI water. After that, 1 g of *M. rouxii* and 0.5 ml of polyethyleneimine (PEI, Mw = 800) were added into the $Fe_3O_4$ suspension. Subsequently, the solution mixture was transferred to a Teflon-lined stainless steel autoclave (50 ml volume) and heated at 200°C for 12 h. Finally, the product was recovered by the centrifugation at 8000 rpm for 10 minutes, washed with DDI water 3 times, and dried in the LABCONCO FreeZone 2.5 Liter -50°C Benchtop Freeze Dryer.

## 3.6 Cr(VI) removal studies

### 3.6.1 Basic procedures for Cr(VI) removal studies

The Cr(VI) removal study was carried out in batch adsorption mode. In a typical experimental setup, 1 g/L of adsorbent was added into 10 ml of 500 ppm Cr(VI) solution in a 30 ml Nalgene polypropylene tube. The pH of the solution was adjusted by adding a negligible volume of 0.1 - 2 M $HNO_3$ and NaOH solutions. The tubes without the adsorbent were used as the control tubes. The solution mixture was shaken for 24 h at 25ºC to achieve the adsorption equilibrium by an orbital shaker operated at 250 rpm. At a certain time of shaking, the suspended adsorbent was separated by the centrifugation at 14000 rpm for 1 min. Meanwhile, the supernatant of immobilized beads was directly obtained without the centrifugation step.

The total Cr concentration of the supernatant was determined by the Agilent 710 inductive coupled plasma optical emission spectrometer (ICP-OES, Agilent, USA), while Cr(VI) concentration was monitored by the GENESYS 20 visible spectrophotometer (Thermo Fisher Scientific, USA) at 540 nm after the formation of color complex with the 1,5-diphenylcarbazide. The Cr(III) concentration in the supernatant was then calculated from the difference between the total Cr and Cr(VI) concentrations. The Cr(VI) removal capacity ($Q_{Cr(VI)}$), total Cr adsorption capacity ($q_{tot}$), percentage Cr(VI) removal ($\%Cr(VI)_{re}$) and percentage total Cr adsorption ($\%Cr_{ads}$) were then calculated by the following equations:

$$Q_{Cr(VI)} = \frac{[Cr(VI)]_{initial} - [Cr(VI)]_{final}}{\text{the weight of adsorbent added}} \times \text{volume}$$

$$q_{tot} = \frac{[Cr_{tot}]_{initial} - [Cr_{tot}]_{final}}{\text{the weight of adsorbent added}} \times \text{volume}$$

$$\%Cr(VI)_{re} = \frac{[Cr(VI)]_{initial} - [Cr(VI)]_{final}}{[Cr(VI)]_{initial}} \times 100\%$$

$$\%Cr_{ads} = \frac{[Cr_{tot}]_{initial} - [Cr_{tot}]_{final}}{[Cr_{tot}]_{initial}} \times 100\%$$

### 3.6.2 Screening of cationic and anionic pollutants

The procedure adsorption experiment was conducted in a similar way as mentioned in the previous section with a single metal system. Various cationic and anionic pollutants, including Cd(II), Cr(III), Cu(II), Ni(II), Pb(II), Zn(II), As(V), As(III), Cr(VI), fluoride and phosphate, were tested. The concentration of cationic pollutants and As (III) was measured by ICP-OES analysis, while the concentration of As(V) and phosphate was analyzed by UV-vis method. The concertation of fluoride was detected using Mettler Toledo Fluoride ion selective electrode. The solution pH for the adsorption study was listed in Table 3-1.

Table 3-1 Solution pH for adsorption of various cationic and anionic pollutants.

| Adsorbate | pH |
|---|---|
| As(V) | 2.0 |
| As(III) | 7.0 |
| Cr(VI) | 2.0 |
| Fluoride | 4.0 |
| Phosphate | 4.0 |
| Cd(II) | 7.0 |
| Cr(III) | 5.5 |
| Cu(II) | 5.0 |
| Ni(II) | 7.5 |
| Pb(II) | 5.0 |
| Zn(II) | 7.0 |

### 3.6.3 Effect of contact time

The kinetic experiments were conducted in a 100 ml Nalgene polypropylene bottle with 50 ml $Na_2CrO_4$ solution under similar experimental conditions as stated in Section 3.6.1. The concentrations of Cr(VI) and total Cr in the solutions were analyzed by the UV-vis spectrometry and ICP-OES analysis at the designated time interval.

### 3.6.4 Effect of pH

The effects of pH on the $Q_{Cr(VI)}$ and $q_{tot}$ values were investigated with the typical adsorption experimental setup as mentioned in Section 3.6.1, with solution pH varied from 1.0 - 7.0 for 1-day contact time, and at 25ºC and 250 rpm agitation speed. The solution pH was adjusted by adding diluted $HNO_3$ and NaOH solution. The concentrations of Cr(VI) and total Cr in the solution mixture were measured by the UV-vis method and ICP-OES analysis with specific dilution.

### 3.6.5 Effect of initial Cr(VI) concentration

The effects of initial Cr(VI) concentration on the $Q_{Cr(VI)}$ and $q_{tot}$ values were studied by the typical adsorption experimental setup as mentioned in Section 3.6.1 with varying of the Cr(VI) concentration from 10 - 1000 ppm.

### 3.6.6 Effect of adsorbent dosage

The effects of adsorbent dosage on the $Q_{Cr(VI)}$ and $q_{tot}$ values were studied by using the typical adsorption experimental setup as described in Section 3.6.1 with varying of the adsorbent dosage from 0.1 to 2.0 g/L.

### 3.6.7 Effect of temperature and thermodynamic study

The effects of temperature on the Cr(VI) removal kinetics and total Cr adsorption kinetics were studied with the same experimental procedure as mentioned in Section 3.6.3. Three temperatures, 4, 25 and 40°C, were studied. The thermodynamic parameters, including Gibb's free energy change (ΔG), enthalpy change (ΔH), and entropy change (ΔS), were estimated by the plot of lnK versus 1/T (Van't Hoff plot). The ΔH and ΔS values could be estimated from the slope and intercept of the Van't Hoff plot, respectively. The Gibbs free energy (ΔG) was calculated by the Van't Hoff equation.

$$\ln\left(\frac{K_1}{K_2}\right) = \frac{-\Delta H}{R}\left(\frac{1}{T_1} - \frac{1}{T_2}\right)$$

$$\Delta G = \Delta H - T\Delta S$$

where $K_1$ is the equilibrium constant at $T_1$, $K_2$ is the equilibrium constant at $T_2$, and R is the gas constant 8.314 J/mol-K.

### 3.6.8 Cr desorption study

The desorption studies utilized the Cr-laden SCAIM collected after the Cr(VI) adsorption at 25°C, pH 2.0, adsorbent dosage of 10 g/L, initial Cr(VI) concentration of 50 ppm and agitation speed of 250 rpm for 72 h. The desorption studies were carried out by suspending the Cr-laden SCAIM in different desorption agents, namely 0.5 M $HNO_3$, 0.25 M $H_2SO_4$, 0.5 M HCl, 0.5 M citric acid, $H_2O$, 2 M $HNO_3$, 1 M $H_2SO_4$, 2 M HCl, 2 M citric acid, 2 M $CaCl_2$. The Cr desorption performances of the Cr-laden HTC-MR, 0.5DEA-HTC-MR and 0.5PEI-HTC-MR were investigated with four different desorption agents, namely 0.5 M $HNO_3$, 2.0 M $HNO_3$, 0.5 M NaOH and 2.0 M NaOH. The desorbed solutions were examined with the UV-vis method and ICP-OES analysis to determine the concentration of Cr(VI) and total Cr, respectively. The percentage Cr(VI) desorption ($\%D_{Cr(VI)}$) and percentage Cr desorption ($\%D_{Cr}$) were calculated by the following equations.

$$\%D_{Cr(VI)} = \frac{Amount\ of\ Cr(VI)\ desorbed}{Amount\ of\ Cr\ adsorbed} \times 100\%$$

$$\%D_{Cr} = \frac{Amount\ of\ Cr\ desorbed}{Amount\ of\ Cr\ adsorbed} \times 100\%$$

### 3.6.9 Continuous Cr(VI) removal study

A schematic diagram of the fixed-bed column is shown in Figure 3-1. The length of the acrylic column was 60 cm with a 1 cm internal diameter. The top and bottom ends of the column were packed with glass wool and then packed with SCAIM beads to obtain the desired column height. The pH 2.0 Cr(VI) solution was fed into the column in an up-flow direction at the desired flow rate using a peristaltic pump. Based on the result of the batch study, the pH of the influent Cr(VI) solution was adjusted to 2.0 using 0.1 M $HNO_3$ or 0.1 M NaOH. Samples were collected from the outlet of the column using a fraction collector at specific time intervals.

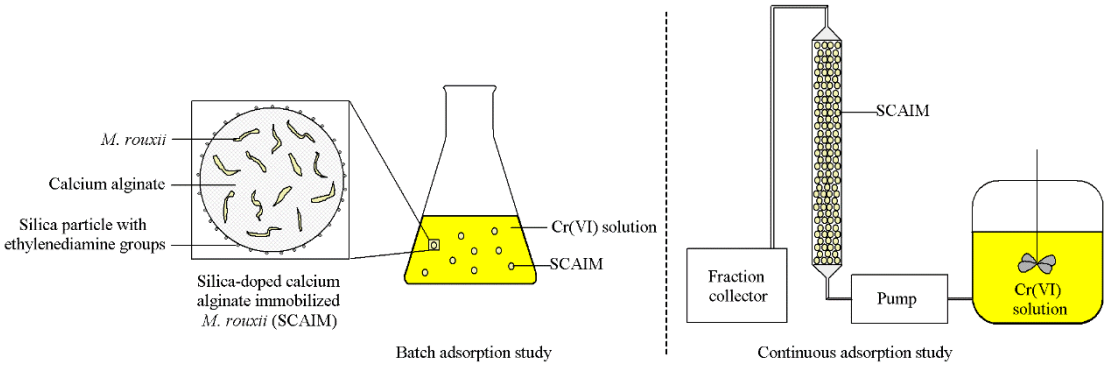


Figure 3-1 Batch and continuous fixed-bed column adsorption studies on the removal of Cr(VI).

## 3.7 Characterization of adsorbents

The Fourier-transform Infrared (FTIR) spectra of adsorbents were recorded on a Nicolet 380 FTIR spectrometer (Thermo Fisher Scientific, USA) in a wavenumber range of 400 - 4000 $cm^{-1}$. The surface morphologies of the *M. rouxii* biomass and immobilized biomass beads were examined using a JSM-6490 scanning electron microscopy (SEM) (JEOL, Japan). The $^{13}C$ solid-state magic angle spinning (MAS) nuclear magnetic resonance (NMR) spectrum of HTC materials was acquired on a JEOL ECZ500R 500 MHz solid-state NMR spectrometer using 8 mm zirconia rotors sipping at a MAS frequency of $\nu_{MAS}$ = 7.5 kHz. The chemical shifts were referenced relative to the tetramethylsilane (TMS; $\delta$ = 0 ppm). The $^{13}C$ spectra were externally referenced to the adamantane CH signal at 29.46 ppm with respect to the TMS scale. The X-ray photoelectron spectroscopy (XPS) experiments were conducted using an Axis Ultra DLD X-ray photoelectron spectrometer (Kratos Analytical, UK) with Al Kα X-ray as the excitation source. The deconvolution of the XPS peaks was processed using the Kratos Vision Processing software. The nitrogen adsorption/ desorption isotherm was recorded at 77K using an ASAP 2020 physisorption analyzer (Micromeritics, USA). Prior to the measurements, the samples were evacuated and degassed for 6 h at 110ºC. The specific surface area and pore size distribution of adsorbents were calculated by employing the Brunauer–Emmett–Teller (BET) (Brunauer et al., 1938) and Barrett-Joyner-Halenda (BJH) methods (Barrett et al., 1951), respectively. The surface charges and the isoelectric points of the *M. rouxii* and HTC materials

were determined by a 3000HSA zetasizer (Malvern, UK). The thermodynamic characteristics of the Cr(VI) adsorption on the *M. rouxii* and HTC materials were investigated a MicroCal PEAQ-ITC automated ultrasensitive isothermal titration calorimeter (Malvern, UK).

# 4. Removal of Cr(VI) by Immobilized *M. rouxii*

# 4.1 Physical and basic chemical properties of silica-doped calcium-alginate-immobilized *M. rouxii*

## 4.1.1 $N_2$ adsorption/desorption isotherm

The surface area and porosity of the *M. rouxii* (MR) and silica-doped calcium-alginate-immobilized *M. rouxii* (SCAIM) beads were characterized by $N_2$ adsorption/ desorption isotherm with the Brunauer-Emmett-Teller (BET) analysis, Barrett-Joyner-Halenda (BJH) analysis and Horvath-Kawazoe (Original HK) method. Table 4-1 summarizes the textural properties of dried *M. rouxii* (MR) and silica-doped calcium-alginate-immobilized *M. rouxii* (SCAIM) beads. The MR exhibited a low BET surface area of 10.11 $m^2/g$, while the SCAIM beads had a BET surface area of 111.2 $m^2/g$. The BET surface area of MR increased by approximately 100 $m^2/g$ after immobilization using silica-doped calcium alginate. The single point adsorption total pore volumes of MR and SCAIM were 2.43E-2 ± 6.17E-4 and 2.47E-2 $cm^3/g$, respectively.

The pore size distribution was also obtained from the Barrett-Joyner-Halenda (BJH) analysis. The results showed that most of the pores in MR and SCAIM were mesopores ranging from 2 to 50 nm in size. The mean pore radius was 2.965 ± 0.007 and 3.060 nm in MR and SCAIM, respectively. Therefore, the total pore volume and mean pore radius did not change after immobilization using silica-doped calcium alginate. It should be noted that the SCAIM beads did not at all contain macropores. The absence of macropores in SCAIM can be explained

by the fact that the calcium alginate hydrogel structure shrank during the drying process of SCAIM beads.

The external surface area was, furthermore, estimated based on the particle size, and the external surface areas of MR and SCAIM were 1.201 ± 0.012 and 0.298 $m^2/g$, respectively. The size of SCAIM beads (2.740 ± 0.092 mm) was much larger than the MR powder (4995 ± 511 nm), so the SCAIM should have smaller external surface area than MR. The BET surface area of SCAIM was comparable to that of calcium alginate reported by other literature (Hassan et al., 2014).

The pore volume and surface area of the MR were in fact underestimated since the MR swelled after being suspended in aqueous solutions, and thus introducing some porosity to the biomass. Moreover, in a typical Cr(VI) removal experiment, SCAIM was re-conditioned in DDI water at pH 2.0 before the batch of Cr(VI) removal studies. Thus, SCAIM should have a larger surface area and pore volume for Cr(VI) adsorption due to the swelling of the calcium alginate structure. In addition, the results of intra-particle diffusion analysis (Section 4.3.5) indicated that the intra-particle diffusion was one of the rate-determining steps of the Cr(VI) removal reaction by MR and SCAIM. The MR and SCAIM should be porous enough that allowed the intra-particle diffusion of Cr(VI).

Table 4-1 Textural properties of MR and SCAIM beads.

| Adsorbent | | MR | SCAIM |
|---|---|---|---|
| Particle Size | | 4995 ± 511 nm | 2.740 ± 0.092 mm |
| Total BET surface area[a] ($m^2$/g) | | 10.11 ± 0.33 | 111.2 ± 5.4 |
| External surface area[b] ($m^2$/g) | | 1.201 ± 0.012 | 0.298 ± 0.083 |
| Total pore volume[c] ($cm^3$/g) | | 2.43E-2 ± 6.17E-4 | 2.47E-2 ± 8.35E-4 |
| Pore Volume[d] ($cm^3$/g) | Micropore (< 2 nm) | 1.20E-3 ± 9.55E-5 | 1.05E-3 ± 1.29E-4 |
| | Mesopore (2 - 50 nm) | **1.68E-2 ± 5.98E-4** | **2.24E-2 ± 3.94E-4** |
| | Macropore[c] (> 50 nm) | 6.73E-3 ± 4.31E-5 | ND[f] |
| Pore Area[d] ($m^2$/g) | Micropore (< 2 nm) | 0.995 ± 0.039 | 0.752 ± 0.021 |
| | Mesopore (2 - 50 nm) | **10.85 ± 0.35** | **16.06 ± 0.74** |
| | Macropore (> 50 nm) | 0.438 ± 0 | ND[f] |
| Mean pore radius (nm) | | 2.965 ± 0.007 | 3.060 ± 0.094 |

[a]Specific surface area was calculated with the Brunauer-Emmett-Teller (BET) analysis; [b]The external surface area was calculated based on the particle size; [c]Total pore volume was calculated from single point adsorption at $P/P_0$ =0.99; [d]The pore volumes of mesopore and macropore, and pore surface areas in each pore size range were obtained from Barrett-Joyner-Halenda (BJH) analysis; [e]The micropore volume was obtained from the Horvath-Kawazoe (Original HK) method; and [f]Not detected.

### 4.1.2 Physical properties

Table 4-2 lists the particle size and density of calcium-alginate (CA), silica-doped calcium alginate (SCA), calcium-alginate-immobilized *M. rouxii* (CAIM) and silica-doped calcium-alginate-immobilized *M. rouxii* (SCAIM). The diameters of the dried CA, SCA, CAIM and SCAIM beads were 0.715 ± 0.058, 0.814 ± 0.173, 1.182 ± 0.084 and 1.432 ± 0.125 mm, respectively. In a typical Cr(VI) removal experiment, the bead adsorbents were first rehydrated in DDI water for 24 h before the Cr(VI) removal studies. The diameters of the rehydrated CA, SCA, CAIM and SCAIM beads were 2.752 ± 0.198, 2.415 ± 0.086, 3.380 ± 0.176 and 2.740 ± 0.092 mm, respectively. The rehydration of bead adsorbents led to an increase in particle size and porosity. The diameters of the dried SCA and SCAIM beads were slightly larger than those of CA and CAIM beads. The increase in the diameter of the dried SCA and SCAIM beads was contributed by the doping of silica particles on the CA and CAIM beads. However, the diameters of the rehydrated SCA and SCAIM beads were slightly smaller than those of CA and CAIM beads. It was because the doped silica hindered the swelling of alginate beads.

The water content in the bead adsorbents was also measured by the following procedure. The weight of the dried bead adsorbents was first recorded using a Mettler Toledo MS204S analytical balance. The same samples were then rehydrated at 25°C for 24 h and were weighed again to determine the amount of water absorbed in the samples. The water content of the rehydrated adsorbents was calculated using the following equation:

$$\text{Water content} = \frac{m_{rehydrated} - m_{dried}}{m_{rehydrated}} \times 100\%$$

where $m_{dried}$ is the weight (g) of the dried sample, and $m_{rehydrated}$ is the weight (g) of the same sample after the rehydration process at 25°C for 24 h.

As shown in Table 4-2, the water contents of CA, SCA, CAIM and SCAIM were 95.15, 91.01, 92.13 and 80.80%, respectively. Highly cross-linked hydrogel structure of calcium alginate was able to entrap a large fraction of water. Thus, the calcium-alginate-based adsorbents were highly porous and permeable to Cr(VI). As a result, the density of the rehydrated adsorbents was similar to the density of water (1 g/cm$^3$). The solid contents of CA, SCA, CAIM and SCAIM were 4.85, 8.99, 7.87 and 19.20%, respectively. The SCAIM beads contained the highest solid content among the four tested adsorbents due to the immobilized biomass and doped silica.

The composition of the solid content in the immobilized *M. rouxii* (CAIM and SCAIM) was furthermore determined by the EDTA dissolution test. In that, the calcium alginate structure of CAIM and SCAIM beads was dissolved by suspending the beads in 0.5 M EDTA solution for 24 h. The remaining solid portion (MR and silica) was recovered by centrifugation at 14000 rpm for 5 min and was dried at 60°C for over 24 h. The results of the EDTA dissolution test indicated that the CAIM beads contained 82.51% of MR and 17.49% of calcium alginate, while the SCAIM was composed of 59.90% MR, 26.40% calcium alginate and 13.70% silica. Additionally, the Ca(II) content of the calcium-alginate-based adsorbents was analyzed by

using microwave digestion followed by the ICP-OES analysis. The Ca(II) contents of CA, SCA, CAIM and SCAIM were 7.753 ± 0.051, 7.923 ± 0.738, 4.755 ± 0.260 and 4.399 ± 0.019%, respectively. The Ca(II) content seemed to be closely related to the weight percentage of calcium alginate.

Table 4-2 Physical properties of CA, SCA, CAIM and SCAIM.

| Dried beads | CA | SCA | CAIM | SCAIM |
|---|---|---|---|---|
| Particle size (mm) | 0.715 ± 0.058 | 0.814 ± 0.173 | 1.182 ± 0.084 | 1.432 ± 0.125 |
| Density (g/cm$^3$) | 3.035 ± 0.641 | 2.384 ± 0.639 | 2.072 ± 0.511 | 1.408 ± 0.535 |
| %MR[1] | | | 82.51 | 59.90 |
| %Ca-Alg[1] | | | 17.49 | 26.40 |
| %Silica[1] | | | / | 13.70 |
| %Ca(II)[2] | 7.753 ± 0.051 | 7.923 ± 0.738 | 4.755 ± 0.260 | 4.399 ± 0.019 |
| | | | | |
| Rehydrated beads | CA | SCA | CAIM | SCAIM |
| Particle size (mm) | 2.752 ± 0.198 | 2.415 ± 0.086 | 3.380 ± 0.176 | 2.740 ± 0.092 |
| Density (g/cm$^3$) | 1.097 ± 0.340 | 1.015 ± 0.155 | 1.125 ± 0.251 | 1.046 ± 0.150 |
| Water content (%) | 95.15 | 91.01 | 92.13 | 80.80 |
| Solid content (%) | 4.85 | 8.99 | 7.87 | 19.20 |

[1]Obtained by the EDTA dissolution test; [2]Obtained by using microwave digestion followed by the ICP-OES analysis.

### 4.1.3 Chemical stability

In the Cr(VI) removal study, an acidic adsorption environment was used to enhance the electrostatic interaction between the protonated *M. rouxii* and anionic Cr(VI) ions. However, the calcium ions in the alginate beads might be replaced by the high concentration of proton, and as a result the gel structure might collapse. Therefore, the stability of the four types of bead adsorbents (CA, SCA, CAIM and SCAIM) in an acidic environment was investigated. This was done by immersing the samples in an acidic condition (pH 2.0) for 7 days. The morphology of the gel beads after immersion for a 7-day period was observed using a CKX53 Inverted Microscope (Olympus, USA). The micrographs in Figure 4-1 show that the four tested adsorbents could well tolerate the acidic environment, and no biomass leaching was observed from the immobilized *M. rouxii* (CAIM and SCAIM) beads. The calcium-alginate-based adsorbents exhibited excellent acid stability, so they can be used to remove Cr(VI) in an acidic environment.

Calcium-alginate-based adsorbents, on the other hand, was unstable in the presence of chelating agents (e.g., EDTA), because the chelating agent would extract the calcium ions from the calcium alginate beads. The calcium ion is a crucial component for maintaining the structure of the alginate gel, which can collapse after losing the calcium ions. Therefore, the stability of gel beads in the EDTA solution was investigated. In this study, the four types of bead adsorbents were immersed in 25 mM EDTA solutions, and the micrographs (Figure 4-2)

were taken after 15 min immersion and 1 h immersion to investigate the EDTA resisting ability of the bead adsorbents. As expected, the CA and CAIM beads could not tolerate the 25 mM EDTA solutions and dissociated in one hour. However, the stability of CA and CAIM beads in the EDTA solutions was improved after the doping of silica. The micrograph clearly shows that the bead structure of SCA and SCAIM remained intact with a transparent silica shell after a one-hour immersion in the 25 mM EDTA solutions. After the one-day immersion in the EDTA solution, the silica remained stable in the solution (Figure 4-3). The micrograph demonstrated that the silica shell was successfully coated on the alginate gel beads. The silica shell was stable in chelating environments, and it was capable of protecting the alginate gel beads from the attack of the chelating agents.

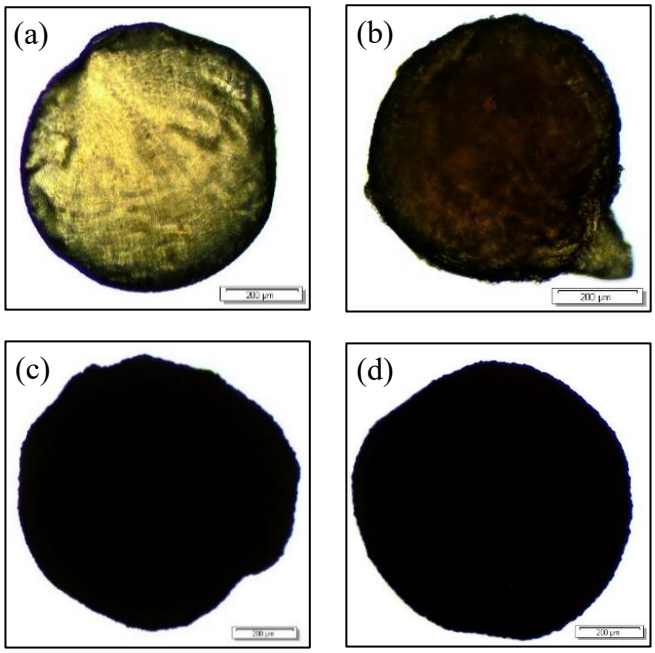


Figure 4-1 Micrographs of (a) CA, (b) SCA, (c) CAIM and (d) SCAIM after 7 days immersion in pH 2 solution.

| | Contact time | |
|---|---|---|
| | 15 min | 1 h |
| CA | 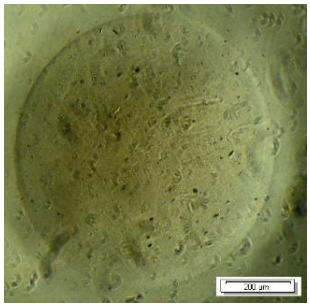 | Dissociated |
| SCA | 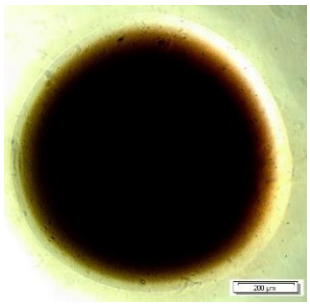 | 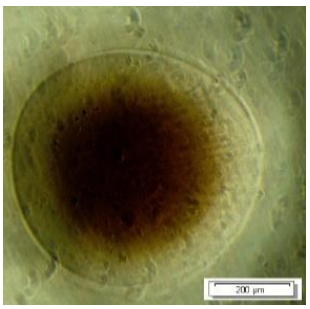 |
| CAIM | 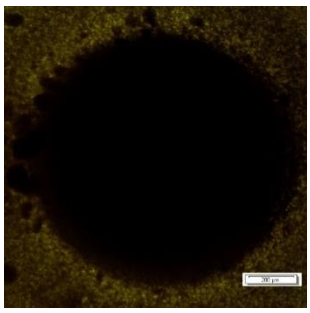 | Dissociated |
| SCAIM | 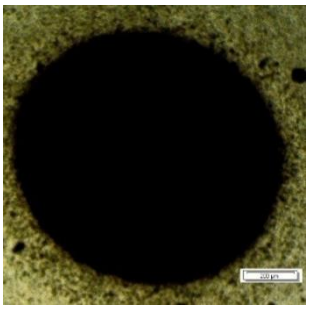 | 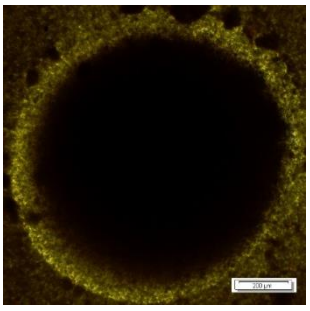 |

Figure 4-2 Micrographs of dried CA, SCA, CAIM and SCAIM immersed in 25 mM EDTA solution.

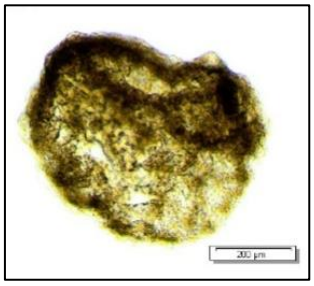

Figure 4-3 Silica shell remained after immersing a SCA bead in 25 mM EDTA solution for 24 h.

### 4.1.4 Mechanical strength

The mechanical strength test was performed to analyze the effect of silica coating on the mechanical strength of the rehydrated calcium-alginate-based beads. The compression load at 5% strain of the rehydrated beads (CA, SCA, CAIM and SCAIM) was measured by using a TA1 texture analyzer (Lloyd, USA) with a 10 mm diameter ebonite piston. Figure 4-4 shows the compression load at 5% strain of the four types of bead adsorbents. The CA beads without silica coating had a significantly lower mechanical strength (3.970 N) compared with the SCA beads (6.357 N). A similar observation was also obtained in the case of CAIM and SCAIM beads, and so it can be concluded that the doping of silica improved the mechanical strength of calcium-alginate-based beads.

The CAIM and SCAIM beads showed higher compression loads of 7.349 and 9.888 N as compared with the CA and SCA beads. The mechanical strength of CA beads was increased after the immobilization of biomass owing to the increase in the solid content of the beads. Previous result (Lo, 2013) showed that the MR biomass was effective for the removal of Cr(VI). Higher biomass content could enhance both the rigidity and the Cr(VI) removal capacity of the SCAIM beads. However, the network structure of calcium alginate would be damaged if the biomass contents in the calcium-alginate-based beads were too high. Therefore, for further investigation, it was important to optimize the biomass content in the SCAIM beads while considering both the mechanical strength and the Cr(VI) removal capacity.

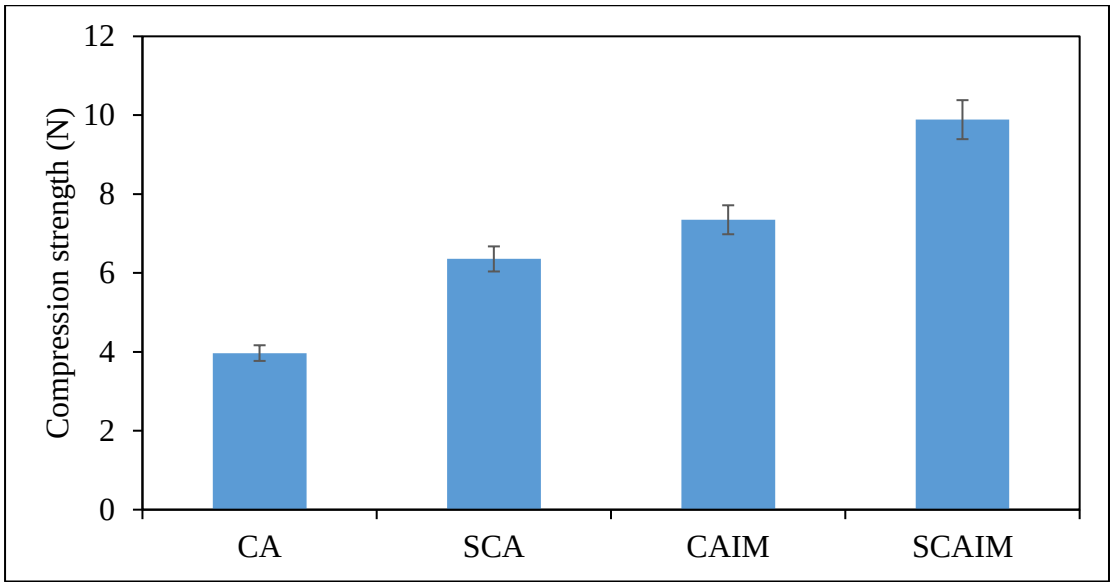


Figure 4-4 Compression load at 5% strain of different rehydrated bead adsorbents.

## 4.2 Screening of cationic and anionic pollutants

The adsorption ability of silica-doped calcium-alginate-immobilized *M. rouxii* (SCAIM) beads to the six cationic and five anionic pollutants were investigated in batch adsorption mode. The screening results are illustrated in Figure 4-5. In the solution containing initial concentration of 500 ppm divalent metal ions, the adsorption capacities (q) of SCAIM beads for removing Cd(II), Cu(II), Ni(II), Pb(II) and Zn(II) were 150.3 ± 0.9, 78.11 ± 0.5, 64.21 ± 2.2, 260.1 ± 3.4 and 85.40 ± 1.2 mg/g, respectively (equivalent to 1.337 ± 0.008, 1.230 ± 0.008, 1.094 ± 0.037, 1.255 ± 0.015, 1.306 ± 0.018 mmol/g, respectively). The SCAIM beads exhibited remarkable adsorption of the cationic divalent heavy metals (Demirbaş, 2005; Zhang et al., 2017). However, the SCAIM was less efficient in adsorbing Cr(III) (q = 26.25 ± 0.7 mg/g or 0.505 ± 0.013 mmol/g). The adsorption studies on cationic pollutants were carried out at pH 5.0 to 7.5 (Table 3-1) in order to prevent the alkaline precipitation. At these pH conditions, the amine groups (pKa ~ 10) on the surface of SCAIM should be protonated, so the cationic heavy metal ions would be adsorbed by the protonated amine groups through the ion-exchange mechanism. The adsorption capacity to trivalent Cr(III) was less than those of divalent cations due to the charge balance. In addition, the SCAIM performed was able to best remove Cr(VI) ($Q_{Cr(VI)}$ = 131.8 ±1.4 mg/g) upon the tested anionic pollutants at pH 2.0. The fluoride adsorption capacity of SCAIM was 84.25 ± 1.6 mg/g. Besides, the SCAIM beads were less effective in removing As(V), As(III) and phosphate from the aqueous solutions.

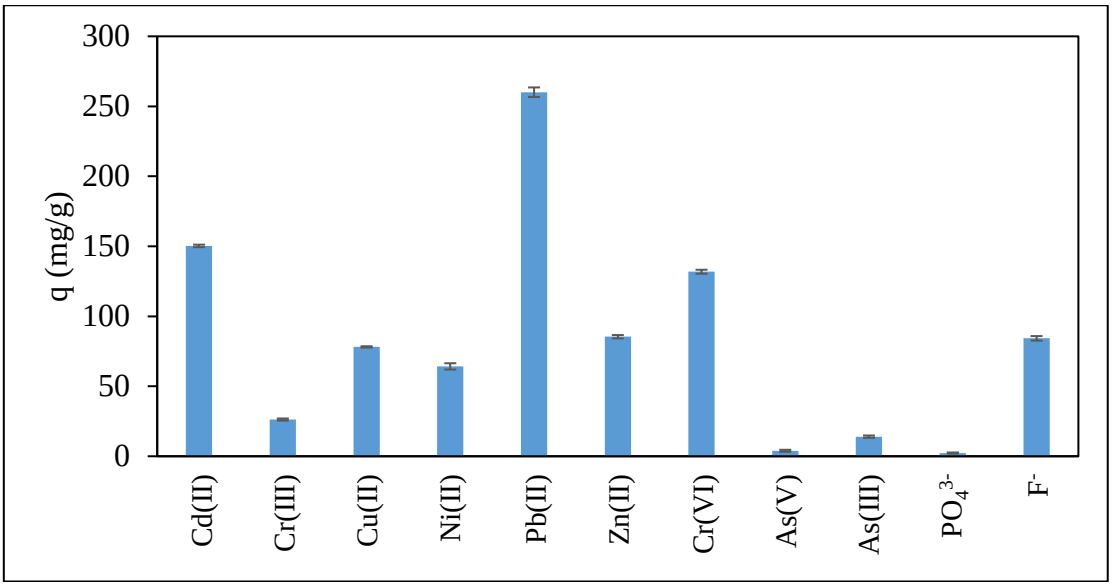


Figure 4-5 Screening results of six cationic and five anionic pollutants by SCAIM. (Experimental conditions: Initial concentration of pollutants = 500 ppm, adsorbent dosage = 1 g/L, t = 3 d, temperature = 25°C and agitation = 250 rpm)

## 4.3 Removal of Cr(VI) by silica-doped calcium-alginate-immobilized *M. rouxii*

### 4.3.1 Effect of contact time

Kinetic studies were carried out with two types of Ca-alginate materials without biomass (CA and SCA) and two types of Ca-alginate immobilized with 60% (w/v) of *M. rouxii* (CAIM and SCAIM) at 25ºC, pH 2.0 and initial Cr(VI) concentration of 100 ppm for 3 d with an adsorbent dosage of 10 g/L. The Cr(VI) concentration in the aqueous phase ([Cr(VI)]) was directly determined by UV-vis analysis, while the Cr(III) concentrations in the aqueous phase ([Cr(III)]) were calculated by the difference between the total Cr concentration measured by ICP-OES analysis and the Cr(VI) concentration determined by UV-vis analysis.

Figure 4-6 andFigure 4-7 plot the kinetic profiles of percentage Cr(VI) removal ($\%Cr(VI)_{re}$), percentage total Cr adsorption ($\%Cr_{ads}$), [Cr(VI)] and [Cr(III)] during Cr(VI) adsorption by the four tested adsorbents at pH 2.0. The $\%Cr(VI)_{re}$ value represents the percentage of Cr(VI) removed by the adsorbent, whereas the $\%Cr_{ads}$ value represents the percentage of total Cr adsorbed onto the surface of the adsorbent.

Figure 4-6a illustrates that the $\%Cr(VI)_{re}$ and $\%Cr_{ads}$ increased slowly with time during Cr(VI) adsorption by the CA. The Cr(VI) concentration was found to slowly decrease to 54.4 ppm after 3 days, while the Cr(III), which was not present initially, appeared in the solution phase after approximately 1.5 day, and thereafter its concentration slowly increased. These

results demonstrated that the Cr(VI) was reduced to Cr(III) when came into the contact with CA at pH 2.0. The polysaccharide-based alginate matrix contained a large amount of reductive hydroxyl groups that were protonated under acidic conditions. These positively charged protonated reductive hydroxyl groups could bind to Cr(VI) anions via electrostatic interactions and then reduced them to Cr(III). The reduced Cr(III) was partly coordinated by the carboxylate groups of the alginate chains and partly released into the aqueous phase. This result indicated that the calcium alginate beads alone was able to remove Cr(VI) via an adsorption-coupled reduction mechanism.

As shown in Figure 4-7b, the SCAIM showed the fastest Cr(VI) removal rate among the four tested adsorbents. The rapid Cr(VI) removal by the SCAIM was especially observed in the first 2 h due to the strong electrostatic attraction between the anionic Cr(VI) and the positively-charged surface groups on the SCAIM. As the degree of surface coverage increased, the Cr(VI) removal rate decreased after 2 h. It is worthy to note that the $\%Cr(VI)_{re}$ continued to increase with a slower rate after 4 h of Cr(VI) adsorption by SCAIM and could not reach the equilibrium even after 3 days due to the continual reduction of Cr(VI) by the electron-donor groups present in the biomass-filled alginate matrix. Besides, the solution pH kept on increasing with the contact time, indicating the consumption of protons during the reduction of Cr(VI) to Cr(III).

The $\%Cr_{ads}$ by the SCAIM also rose sharply in the first two hours and reached equilibrium

after 3 days (Figure 4-7b). The total Cr adsorption equilibrium should be a dynamic equilibrium that the Cr(III) releasing rate was equal to the Cr(VI) adsorption rate. The Cr(III) appeared in the solution phase after 2 h and gradually increased afterward. The amount of Cr(III) in the aqueous phase after 3 days was significantly larger than those found in the cases of CA, SCA and CAIM, demonstrating that the SCAIM had the highest reduction rate of Cr(VI) to Cr(III). Ten g/L of SCAIM required about 3 days of contact time to completely remove 100 mg/L of Cr(VI) in the aqueous phase at pH 2.0. Same amounts of other tested alginate-based adsorbents, i.e., CA, SCA and CAIM, took longer time to do so.

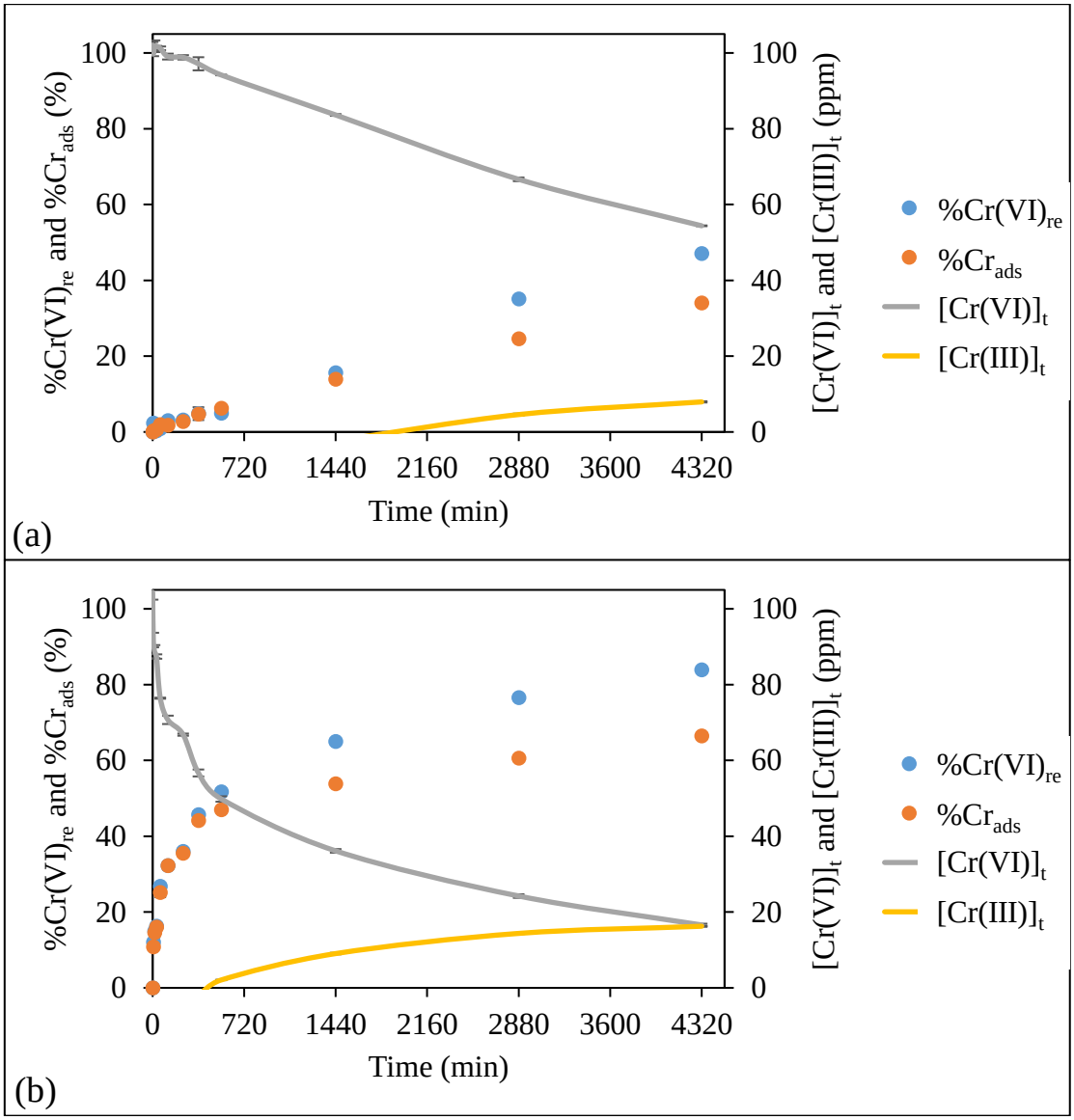


Figure 4-6 Cr(VI) removal kinetics and total Cr adsorption kinetics of (a) CA and (b) SCA. (Experimental conditions: $[Cr(VI)]_0$ = 100 ppm, adsorbent dosage = 10 g/L, t = 3 d, pH 2.0, temperature = 25°C and agitation = 250 rpm)

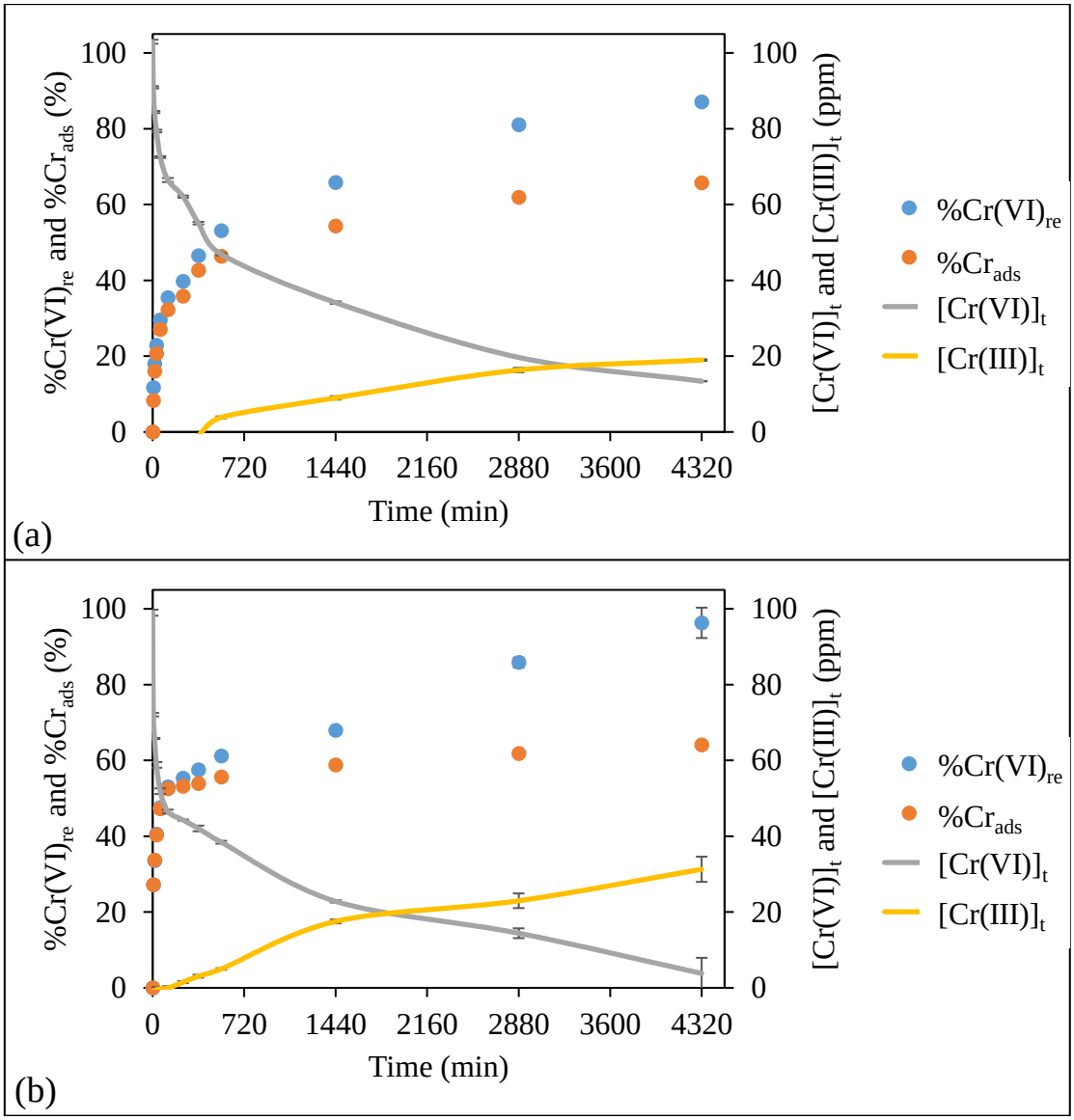


Figure 4-7 Cr(VI) removal kinetics and total Cr adsorption kinetics of (a) CAIM and (b) SCAIM. (Experimental conditions: $[Cr(VI)]_0$ = 100 ppm, adsorbent dosage = 10 g/L, t = 3 d, pH 2.0, temperature = 25°C and agitation = 250 rpm)

### 4.3.2 Effect of pH

Solution pH governs the speciation of Cr(VI) and also the dissociation or protonation of the active functional groups on the adsorbent surface. To examine the influence of pH on Cr(VI) removal characteristics of the four types of calcium-alginate-based adsorbents (CA, SCA, CAIM and SCAIM), the equilibrium Cr(VI) and Cr(III) concentration profiles ($[Cr(VI)]_{eq}$ and $[Cr(III)]_{eq}$,) were investigated at various pH values ranging from 1.0 to 7.0. Figure 4-8 and Figure 4-9 report the effect of solution pH on $[Cr(VI)]_{eq}$, $[Cr(III)]_{eq}$, percentage Cr(VI) removal ($\%Cr(VI)_{re}$) and percentage total Cr adsorption ($\%Cr_{ads}$) by the two immobilization materials (CA and SCA) and the two immobilized *M. rouxii* beads (CAIM and SCAIM).

Figure 4-9b displays the equilibrium Cr(VI) and Cr(III) concentrations after 3 days of adsorption by the CA versus pH. The equilibrium Cr(VI) concentration was found to decrease gradually from 100.5 ppm to 0.199 ppm as the solution pH decreased from 5.0 to 1.0. It was because the electrostatic adsorption of Cr(VI) was more favorable in a more acidic environment. The highest Cr(VI) removal and thus the lowest equilibrium Cr(VI) concentration were observed at solution pH 1.0. Figure 4-10b illustrates the speciation of Cr(VI) as a function of pH in the aqueous solution. At pH less than 5.0, the Cr(VI) mainly exists in the forms of $HCrO_4^-$ and $Cr_2O_7^{2-}$ with $HCrO_4^-$ as the predominant species. Furthermore, the polysaccharide-based alginate matrix contained a large amount of reductive protonated hydroxyl groups under acidic conditions. These protonated hydroxyl groups could bind to $HCrO_4^-$ and $Cr_2O_7^{2-}$ through

electrostatic interactions. The more acidic the conditions, the larger the amount of protonated hydroxyl groups in the CA beads, the more positive the surface charge of the CA beads, the faster is the removal rate of Cr(VI) in the solution phase. Besides, the largest amount of Cr(III) was released from the CA at pH 1.0. As shown in Figure 4-8 and Figure 4-9, the trends of [Cr(VI)]eq and [Cr(III)]eq exhibited by the SCA, CAIM and SCAIM were similar to that by CA. At pH 1.0, the largest amounts of Cr(III) were released from the CA, SCA, CAIM and SCAIM, and the equilibrium Cr(III) concentrations were 79.11 ± 1.08, 77.06 ± 0.96, 50.92 ± 1.48 and 66.45 ± 2.62 ppm, respectively. The presence of Cr(III) in the solution phase indicated that the reduction of Cr(VI) should be involved in the Cr(VI) removal mechanism. The adsorbed Cr(VI) ions were reduced by the electron-donor groups in the calcium-alginate-based adsorbents, and then the reduced Cr(III) ions were desorbed by the high concentration of proton through the ion-exchange mechanism.

Figure 4-9b shows that the $\%Cr(VI)_{re}$ exhibited by the SCAIM increased from 47.39 ± 1.08% to 99.29 ± 0.09% when the solution pH decreased from 7.0 to 1.0. The influence of solution pH on the $\%Cr(VI)_{re}$ value exhibited by CAIM was similar to that by SCAIM (Figure 4-9a). Moreover, Figure 4-8a and Figure 4-8b depict that the CA and SCA showed high $\%Cr(VI)_{re}$ values at pH ≤ 2.0. At pH 2.0, the $\%Cr(VI)_{re}$ values of CA, SCA, CAIM and SCAIM were 56.55 ± 0.95, 87.42 ± 0.05, 87.57 ± 0.55 and 97.42 ± 0.05%, respectively. These results revealed that the SCAIM demonstrated the best Cr(VI) removal performance with the highest

%Cr(VI)re among the four tested adsorbents, and Cr(VI) was removed not only by the immobilized *M. rouxii* (CAIM and SCAIM) but also by the immobilization alginate materials (CA and SCA).

Moreover, the surface charges of the freely-suspended *M. rouxii* (MR) at different solution pH were investigated (Figure 4-10b). The zeta-potential of the freely-suspended *M. rouxii* (MR) increased from -31.03 ± 1.03 to +28.77 ± 0.15 mV when the solution pH decreased from 8.0 to 1.0. The point of zero charge was found at pH 4.0. The increase in zeta-potential of MR was contributed by the protonation of functional groups (e.g., amine groups) on the MR surface in the acidic conditions. In addition, the surface groups of the immobilization materials should also be protonated in the same way as explained above, although the overall surface charge of immobilized adsorbents could not be determined. The anionic $HCrO_4^-$ and $Cr_2O_7^{2-}$ bound onto the positively-charged functional groups which were present not only on the biomass surface but also in the alginate matrix through the electrostatic interactions at acidic pH. The employment of alginate hydrogel for immobilizing the biomass can enhance the Cr(VI) removal performance of the biomass and reduce the problem of organic leaching from the biomass.

The $\%Cr_{ads}$ values of the four tested adsorbents increased with decreasing solution pH from 7.0 to 2.0 since the adsorption of Cr(VI) onto the adsorbents through electrostatic interactions was more favorable in a more acidic environment, as explained above. The $\%Cr_{ads}$

values of CA, SCA, CAIM and SCAIM at pH 2.0 were 36.79 ± 0.52, 69.00 ± 0.34, 64.54 ± 0.66 and 82.60 ± 0.45%, respectively. However, when the solution pH further decreased to 1.0, the $\%Cr_{ads}$ values of the adsorbents decreased with the largest $[Cr(III)]_{eq}$ in the aqueous phase. The results indicated that a large portion of the reduced Cr(III) were desorbed from the adsorbent surface due to the strong electrostatic repulsion between Cr(III) and the positively charged groups. The high concentration of protons at pH 1.0 could also facilitate the ion-exchange reaction between Cr(III) and proton ions. Thus, a maximum Cr adsorption was obtained at solution pH 2.0 rather than 1.0 in the Cr(VI) solution.

To summarize, the $\%Cr(VI)_{re}$ and $\%Cr_{ads}$ values of the four tested adsorbents were found to be in the descending order of SCAIM > CAIM ~ SCA > CA. The release of Cr(III) could be observed in all the four cases of the immobilization materials without biomass (CA and SCA) and the immobilized *M. rouxii* (CAIM and SCAIM), indicating that the Cr(VI) could be reduced to Cr(III) by the electron-donor groups present on calcium alginate and biomass surface.

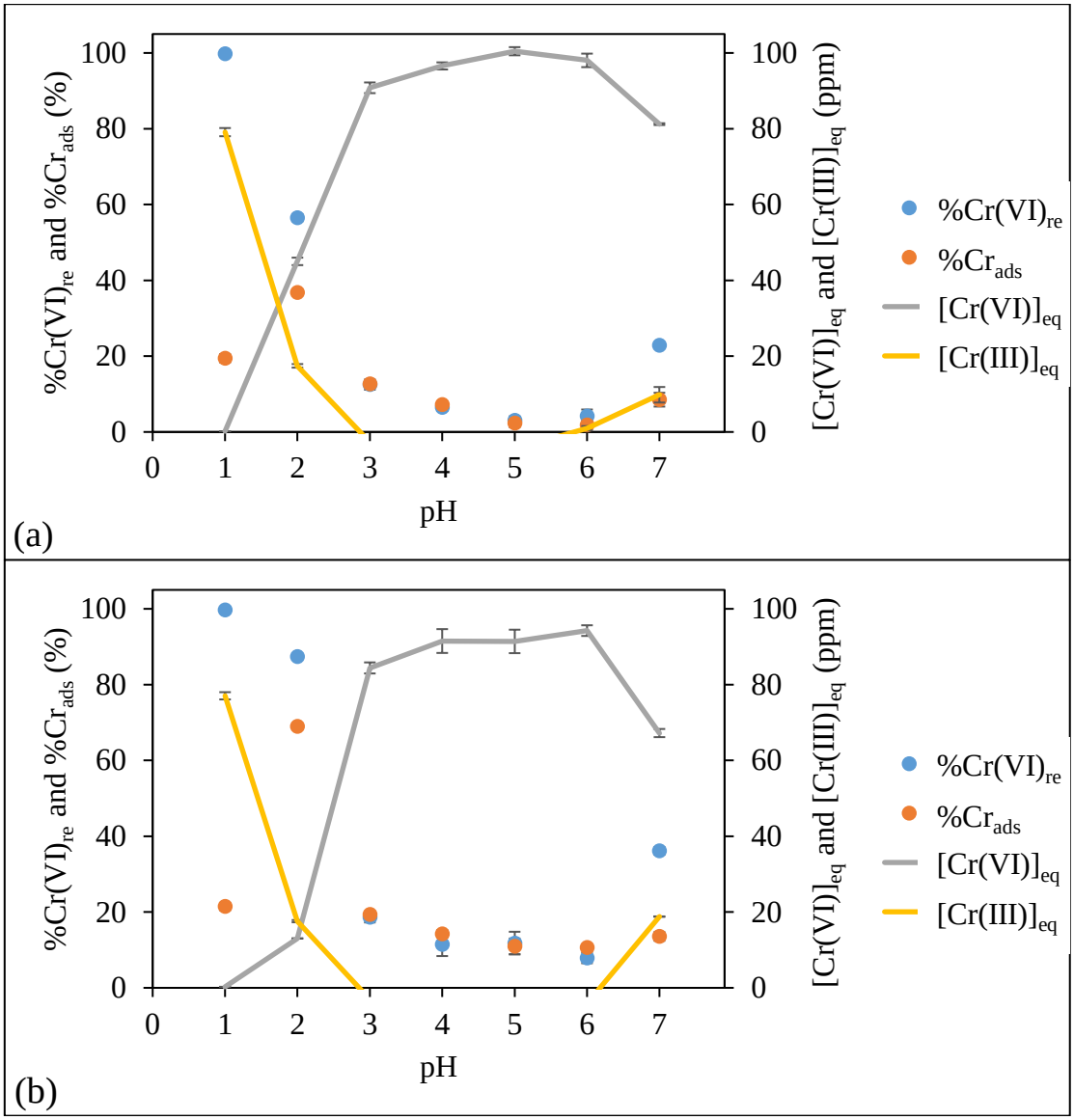


Figure 4-8 Effect of pH on the $\%Cr(VI)_{re}$ and $\%Cr_{ads}$ on (a) CA and (b) SCA. (Experimental conditions: $[Cr(VI)]_0$ = 100 ppm, adsorbent dosage = 10 g/L, t = 3 d, pH 1.0 - 7.0, temperature = 25°C and agitation = 250 rpm)

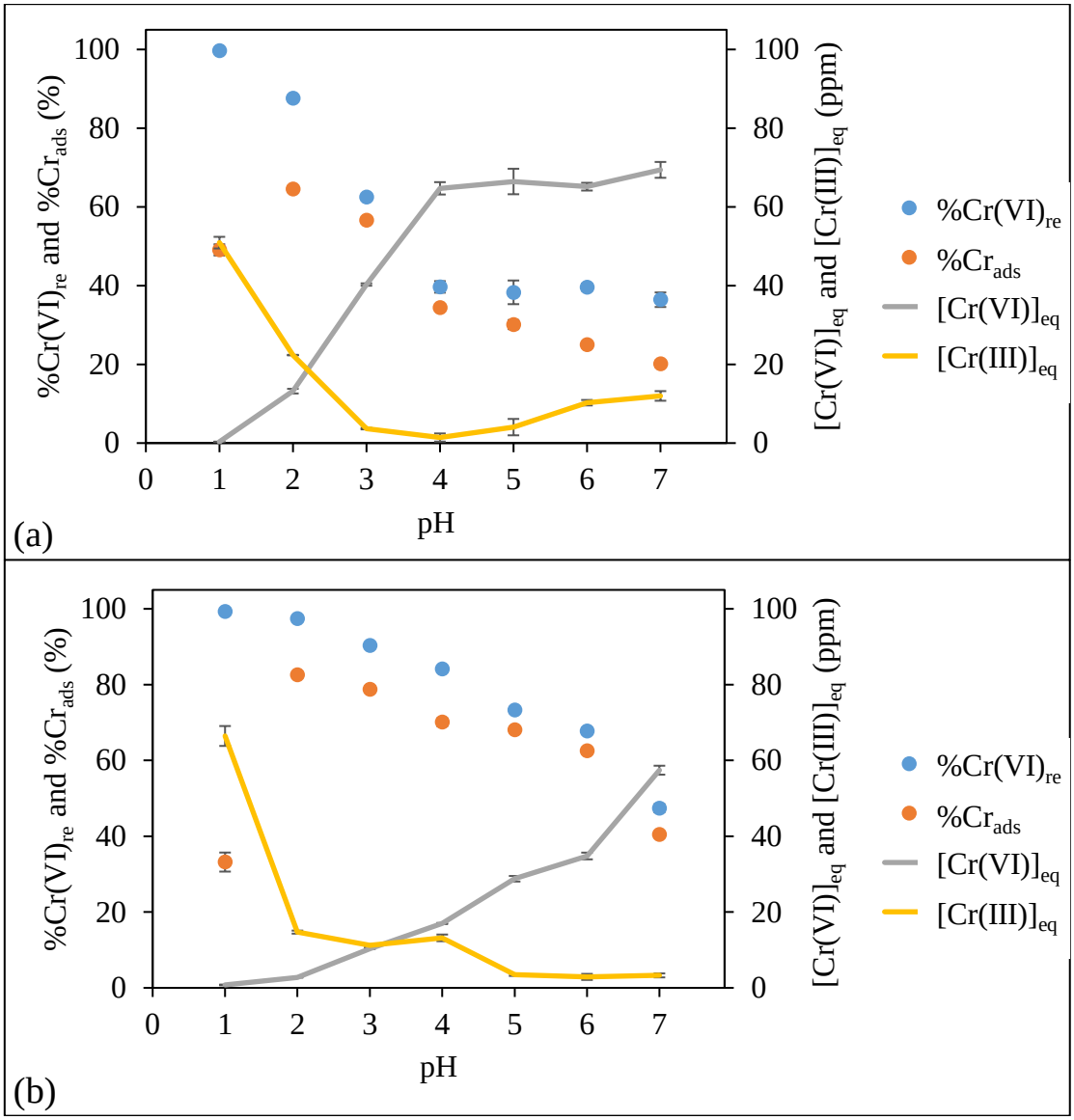


Figure 4-9 Effect of pH on the $\%Cr(VI)_{re}$ and $\%Cr_{ads}$ on (a) CAIM and (b) SCAIM. (Experimental conditions: $[Cr(VI)]_0$ = 100 ppm, adsorbent dosage = 10 g/L, t = 3 d, pH 1.0 - 7.0, temperature = 25ºC and agitation = 250 rpm)

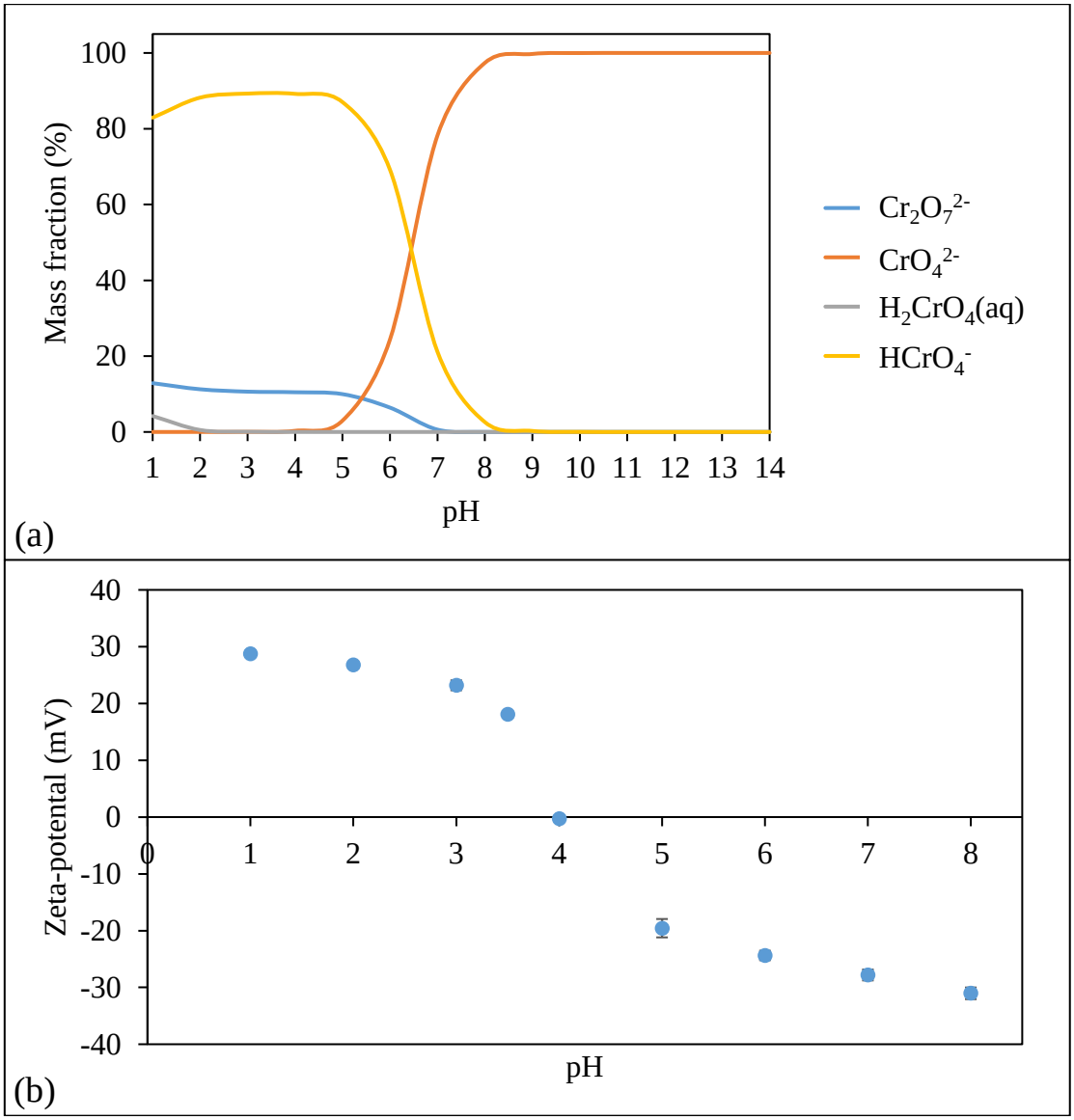


Figure 4-10 (a) Speciation diagram of 100 ppm Cr(VI) in solution simulated by Visual MINTEQ; and (b) effect of pH on zeta-potential of MR.

### 4.3.3 Kinetic modelling

The Cr(VI) removal kinetics on the MR, SCA, CAIM and SCAIM was analyzed using five different adsorption kinetic models, namely pseudo-first-order, pseudo-second-order, Elovich, fractional power and intra-particle diffusion models. The kinetic modelling curves are illustrated in Figure 4-11 and Figure 4-12, while the modelling parameters are listed in Table 4-3. The modelling results of MR were adopted from previous research (Lo, 2013). The root-mean-square error (RMSE) value of each model acted as an indicator for evaluating the goodness of fit.

According to the modelling results (Table 4-3), the fractional power model provided an excellent correlation with the Cr(VI) removal kinetics of MR, SCA, CAIM and SCAIM with the lowest RMSE values and highest correlation coefficients. This is because the fractional power model could well describe the gradual rise of $Q_{Cr(VI)}$ at the later stage of the kinetic curves. Moreover, the fractional power model could calculate the Cr(VI) removal rate at a specific time of 1 min by multiplying the fractional power rate constant ($k_f$) by the fractional power exponent (v). The specific Cr(VI) removal rate ($k_f v$) estimated the rate of Cr(VI) removal by the external surface of the adsorbent. The $k_f v$ values of Cr(VI) removal by MR, SCA, CAIM and SCAIM were 1.835, 0.224 ± 0.009, 0.194 ± 0.002 and 0.630 ± 0.004 mg/g-min, respectively. The freely suspended MR showed the highest specific Cr(VI) removal rate since its surface adsorption sites were highly exposed to the Cr(VI) solution. The immobilized

bead adsorbents gave lower specific Cr(VI) removal rate due to their low external surface areas per unit mass of the adsorbent.

The Cr(VI) removal kinetics of MR and SCAIM was poorly fitted by the intra-particle diffusion model, so the Cr(VI) removal rate of MR was not only controlled by the intra-particle diffusion. However, the intra-particle diffusion model exhibited good simulation to the Cr(VI) removal kinetics of the SCA and CAIM. The intra-particle diffusion would play an important role in the Cr(VI) removal process in SCA and CAIM. The intra-particle diffusion analysis will be further investigated in Section 4.3.5.

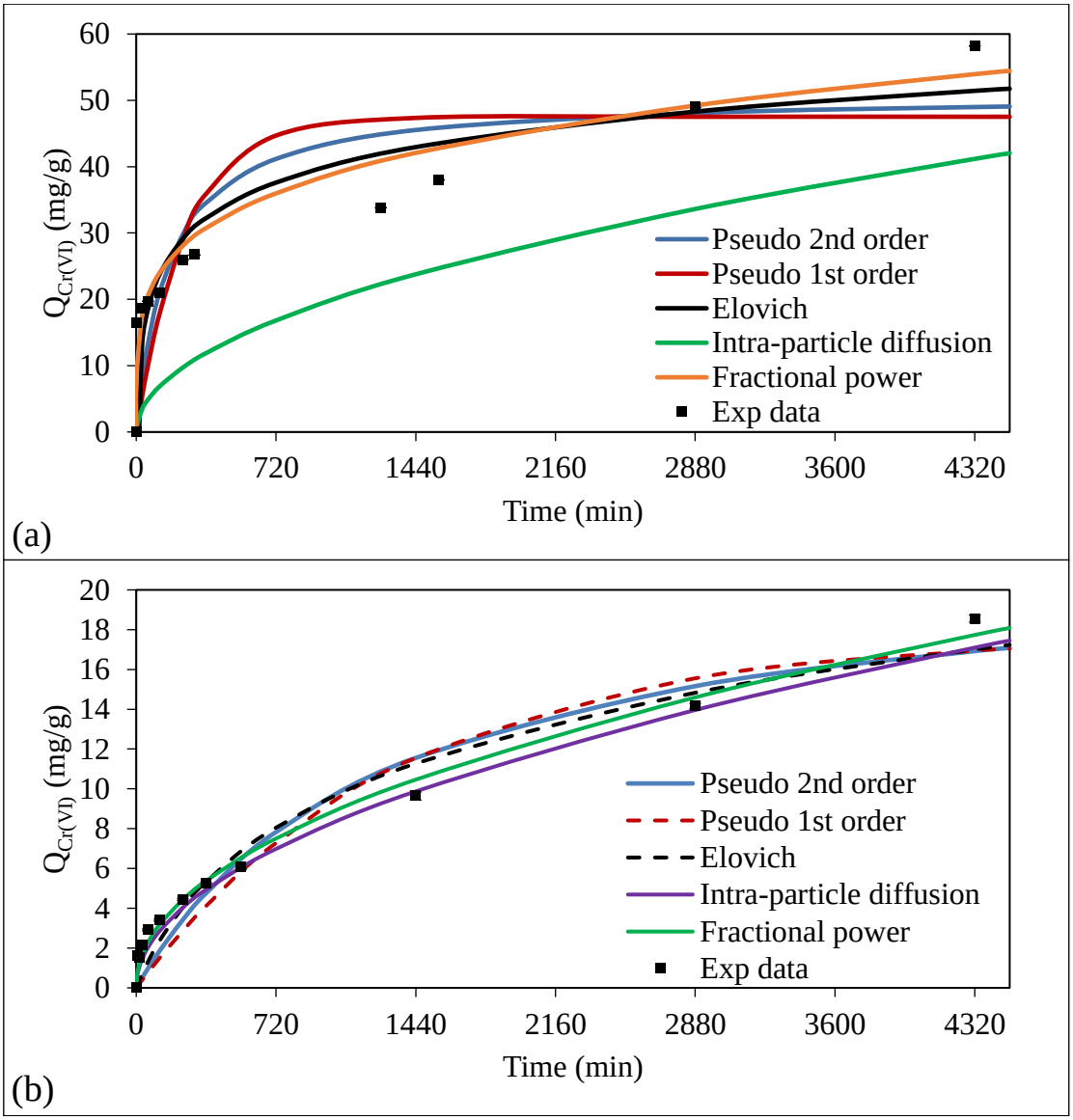


Figure 4-11 Cr(VI) removal kinetic modelling curves of (a) MR and (b) SCA. (Experimental conditions: $[Cr(VI)]_0$ = 50 ppm, adsorbent dosage = 1 g/L, t = 3 d, pH 2.0, temperature = 25°C and agitation = 250 rpm)

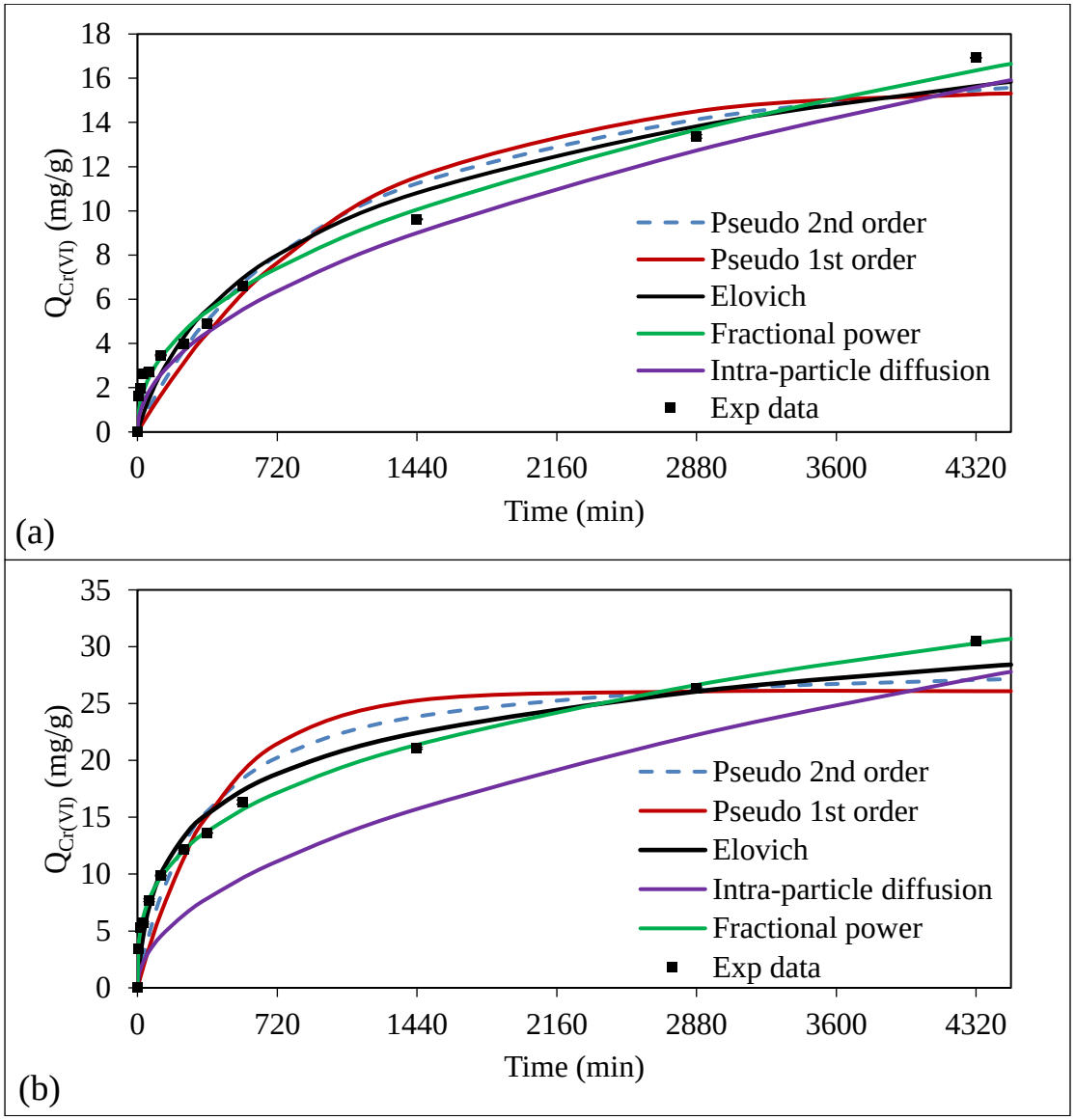


Figure 4-12 Cr(VI) removal kinetic modelling curves of (a) CAIM and (b) SCAIM. (Experimental conditions: $[Cr(VI)]_0$ = 50 ppm, adsorbent dosage = 1 g/L, t = 3 d, pH 2.0, temperature = 25ºC and agitation = 250 rpm)

Table 4-3 Kinetic modelling parameters for Cr(VI) removal by MR, SCA, CAIM and SCAIM.

| Pseudo 1st order | $k_1$ (1/min) | $q_e$ (mg/g) | $R^2$ | RMSE |
|---|---|---|---|---|
| MR | 3.91E-3 | 47.52 | 0.691 | 10.45 |
| SCA | 7.36E-4 ± 1.91E-6 | 17.68 ± 0.17 | 0.920 ± 0.004 | 1.664 ± 0.018 |
| CAIM | 9.41E-4 ± 3.04E-6 | 15.54 ± 0.05 | 0.912 ± 0.005 | 1.599 ± 0.039 |
| SCAIM | 2.40E-3 ± 1.41E-6 | 26.09 ± 0.11 | 0.877 ± 0.004 | 3.453 ± 0.039 |
| Pseudo 2nd order | $k_2$ (g/mg-min) | $q_e$ (mg/g) | $R^2$ | RMSE |
| MR | 1.15E-4 | 50.92 | 0.763 | 9.101 |
| SCA | 3.47E-5 ± 7.57E-7 | 22.05 ± 0.30 | 0.937 ± 0.003 | 1.474 ± 0.018 |
| CAIM | 5.28E-5 ± 7.07E-9 | 19.02 ± 0.03 | 0.933 ± 0.004 | 1.395 ± 0.044 |
| SCAIM | 1.10E-4 ± 1.27E-6 | 29.04 ± 0.16 | 0.923 ± 0.003 | 2.728 ± 0.041 |

| Elovich | b (g/mg) | a (mg/g-min) | $t_0$ (min) | $R^2$ | RMSE |
|---|---|---|---|---|---|
| MR | 0.130 | 1.396 | 5.532 | 0.861 | 6.943 |
| SCA | 0.174 ± 0.004 | 0.024 ± 0.002 | 234.7 ± 6.9 | 0.955 ± 0.002 | 1.255 ± 0.013 |
| CAIM | 0.213 ± 0.001 | 0.029 ± 0.005 | 160.4 ± 3.8 | 0.953 ± 0.004 | 1.175 ± 0.043 |
| SCAIM | 0.188 ± 0.002 | 0.248 ± 0.005 | 21.43 ± 0.64 | 0.974 ± 0.001 | 1.583 ± 0.027 |

| Fractional Power | $k_f$ (mg/g-min$^v$) | v | $k_f v$ (mg/g-min) | $R^2$ | RMSE |
|---|---|---|---|---|---|
| MR | 8.121 | 0.226 | 1.835 | **0.974** | **4.298** |
| SCA | 0.318 ± 0.002 | 0.480 ± 0.002 | 0.224 ± 0.009 | **0.990 ± 0.001** | **0.596 ± 0.013** |
| CAIM | 0.404 ± 0.013 | 0.442 ± 0.004 | 0.194 ± 0.002 | **0.990 ± 0.001** | **0.545 ± 0.016** |
| SCAIM | 2.123 ± 0.008 | 0.318 ± 0.001 | 0.630 ± 0.004 | **0.999 ± 0.003** | **0.340 ± 0.034** |

| Intra-particle diffusion | $k_{diff}$ (mg/g-min$^{0.5}$) | $R^2$ | RMSE |
|---|---|---|---|
| MR | 0.626 | 0.922 | 15.84 |
| SCA | 0.260 ± 0.003 | 0.992 ± 0.005 | 0.774 ± 0.020 |
| CAIM | 0.237 ± 0.008 | 0.995 ± 0.003 | 0.975 ± 0.055 |
| SCAIM | 0.527 ± 0.002 | 0.875 ± 0.002 | 3.483 ± 0.002 |

### 4.3.4 Cr(VI) reduction kinetic model

Two reduction kinetic models, namely the Han model and the Park model, were applied to simulate the Cr(VI) removal kinetics of adsorbents. The Han model (Han et al., 2007) assumes that the Cr(VI) adsorption onto biosorbent is much faster than the following Cr(VI) reduction step. The Cr(VI) reduction on the adsorbent surface follows the pseudo-first-order kinetics, while the Cr adsorption isotherm can be expressed by the Langmuir isotherm. The Han model is shown below,

$$k_h t = ln\frac{[Cr(VI)]_0}{b[Cr(VI)]_0 + 1} - ln\frac{[Cr(VI)]_t}{b[Cr(VI)]_t + 1}$$

where $[Cr(VI)]_0$ is the initial Cr(VI) concentration (mg/L), $[Cr(VI)]_t$ is the Cr(VI) concentration at time t (mg/L), b is the Langmuir constant (L/mg), and $k_h$ is the Han kinetic constant ($min^{-1}$).

The Park model (Park et al., 2007) assumes that the Cr(VI) removal rate follows the pseudo-first-order kinetics with respect to the Cr(VI) concentration and the organic content in the biosorbent that is responsible for the Cr(VI) reduction. The Park model considers the oxidation of organic compounds by Cr(VI), so the Cr(VI) reduction rate is predicted to decrease with time due to the depletion of Cr(VI) and the reduced reactivity of the organic compounds.

The Park model is shown below,

$$k_p(C_{OC}^*[B] - [Cr(VI)]_0)t = \ln\left(\frac{[Cr(VI)]_0(C_{OC}^*[B] - [Cr(VI)]_0 + [Cr(VI)]_t)}{[Cr(VI)]_t C_{OC}^*[B]}\right)$$

where $[Cr(VI)]_0$ is the initial Cr(VI) concentration (mg/L), $[Cr(VI)]_t$ is the Cr(VI) concentration at time t (mg/L), [B] is the biomass concentration (g/L), $C_{OC}^*$ is the content of equivalent organic compound per unit mass of biomass (mg/g), and $k_P$ is the Park kinetic constant ($min^{-1}$).

Figures Figure 4-13 to Figure 4-15 present the modelling curves of the two reduction kinetic models, and Table 4-4 summarizes the modelling parameters. Comparing the RMSE values, the Han model was better fitted to simulate the Cr(VI) removal kinetics on freely suspended MR biomass, while the Park model was better for simulating the immobilized *M. rouxii* (CAIM and SCAIM) and the immobilization materials (CA, SCA). In the freely suspended MR biomass, the adsorption sites were entirely exposed to the Cr(VI) solution, and the Cr(VI) adsorption rate was very fast. The following Cr(VI) reduction step was the rate-determining step for the overall Cr(VI) adsorption-reduction mechanism. In contrast, the Cr(VI) adsorption rate on the immobilized materials was usually limited by the intra-particle diffusion of Cr(VI). The Cr(VI) removal rate was therefore dependent on the availability of adsorption sites and the concentration of Cr(VI). Nevertheless, both Han and Park models overpredicted the Cr(VI) removal kinetics by MR, SCA, CAIM and SCAIM at the initial stage (t < 9 h). Those reduction models have been developed based on the assumption that the removal rate of

Cr(VI) follows the pseudo-first-order kinetics. Although the pseudo-first-order kinetics could not simulate very well the Cr(VI) removal kinetics on the freely suspended and immobilized *M. rouxii* (Table 4-3), the Park's model could still simulate reasonably well the Cr(VI) reduction kinetics on CA, SCA, CAIM and SCAIM with reasonable RMSE values and correlation coefficients ranging from 0.967 to 0.975.

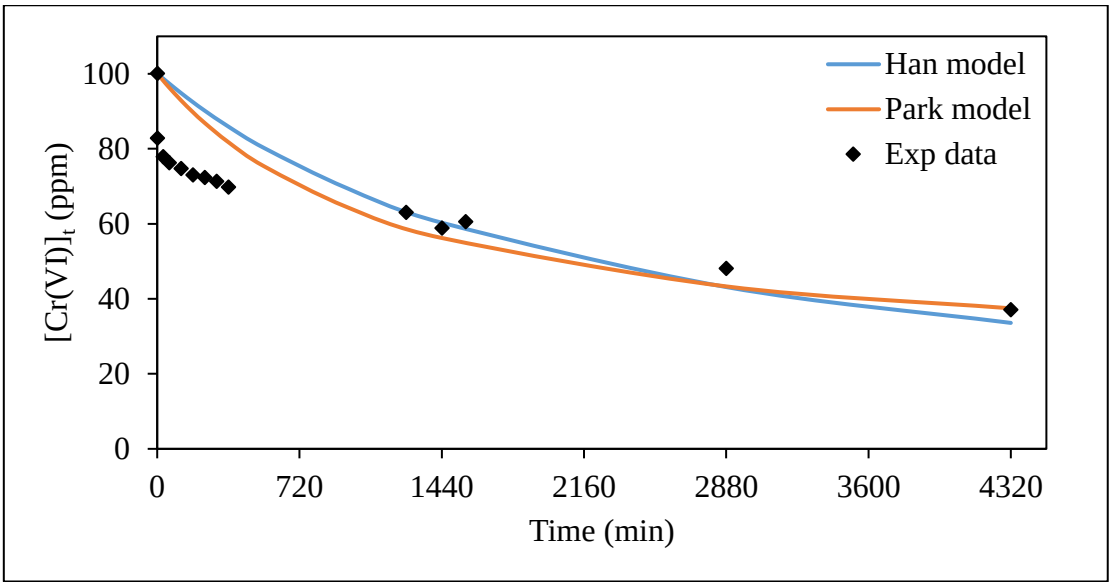


Figure 4-13 Modelling curves of Cr(VI) reduction kinetic models for MR.

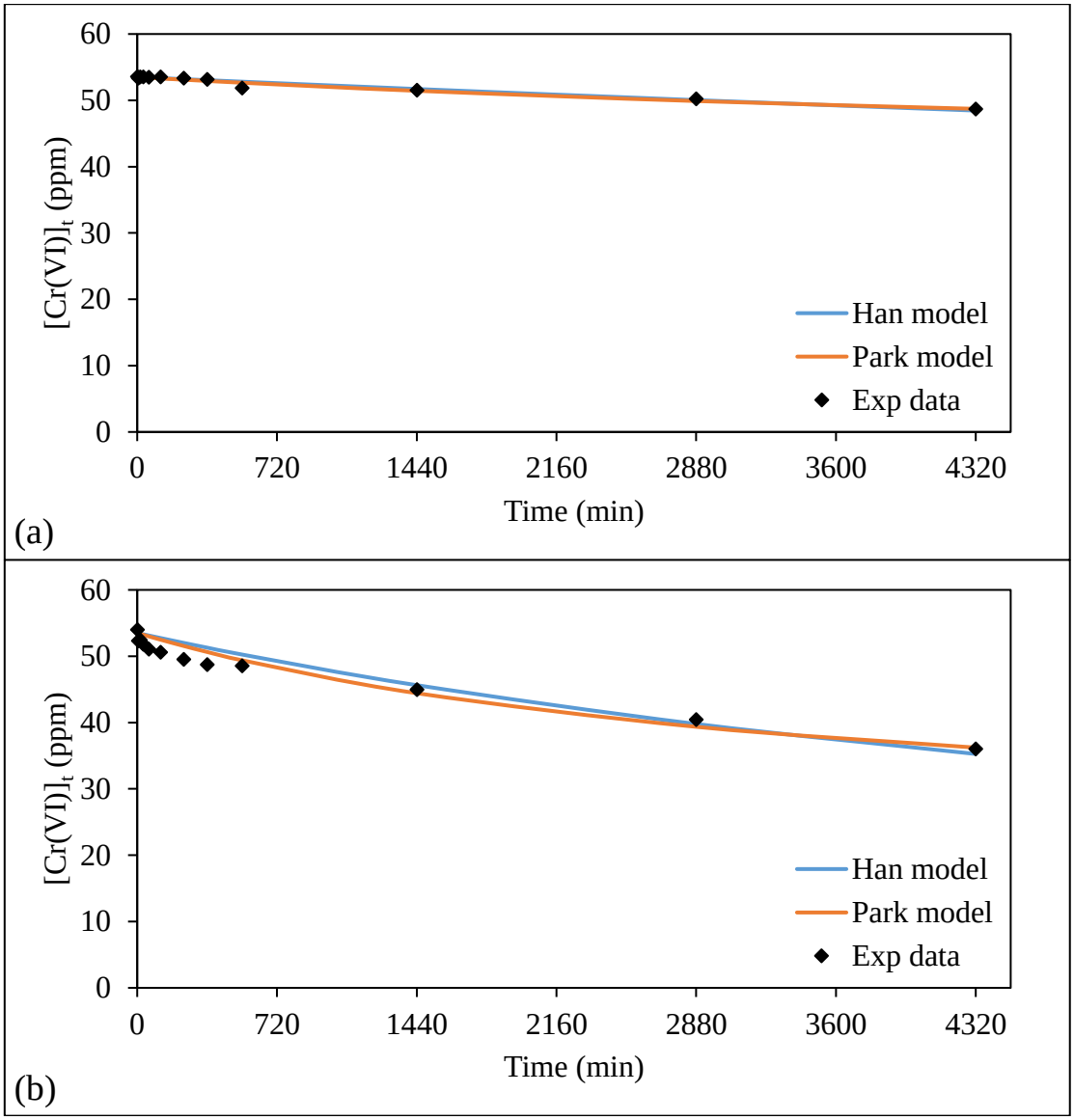


Figure 4-14 Modelling curves of Cr(VI) reduction kinetic models for (a) CA and (b) SCA.

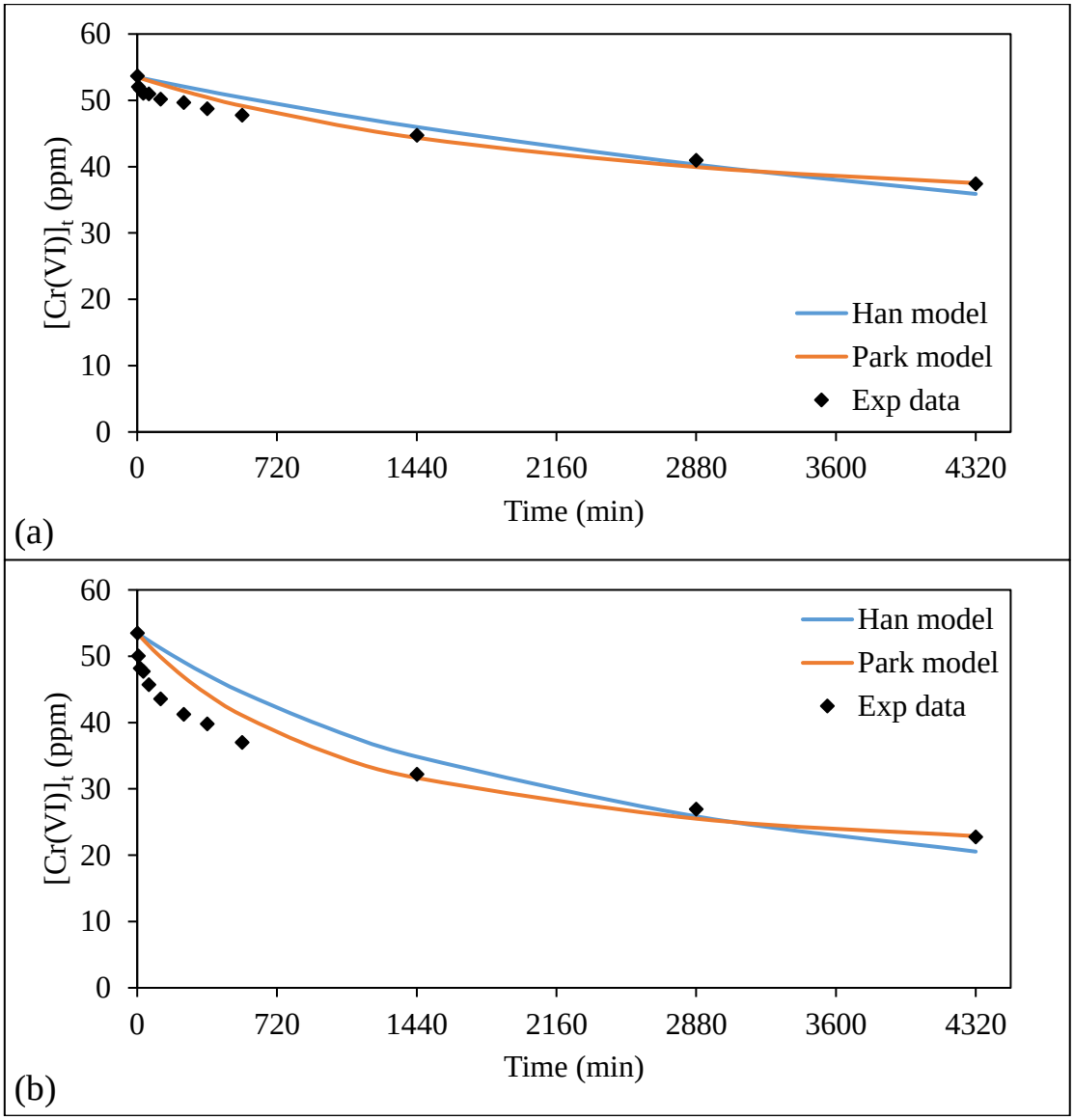


Figure 4-15 Modelling curves of Cr(VI) reduction kinetic models for (a) CAIM and (b) SCAIM.

Table 4-4 Modelling parameters of the reduction kinetic models.

| Han model | b (L/mg) | $k_h$ (1/min) | $R^2$ | RMSE |
|---|---|---|---|---|
| MR | 63.00 | 7.27E-8 | 0.8419 | 12.28 |
| CA | 4.349 ± 0.169 | 1.03E-7 ± 7.33E-9 | 0.964 ± 0.002 | 0.321 ± 0.017 |
| SCA | 30.81 ± 0.38 | 7.26E-8 ± 3.11E-10 | 0.954 ± 0.001 | 1.664 ± 0.014 |
| CAIM | 32.53 ± 0.25 | 6.52E-8 ± 1.06E-10 | 0.916 ± 0.001 | 2.045 ± 0.032 |
| SCAIM | 104.9 ± 0.2 | 6.62E-8 ± 1.34E-10 | 0.891 ± 0.001 | 5.668 ± 0.008 |
| Park model | $C_{OC}$ (mg/g) | $k_p$ (1/min) | $R^2$ | RMSE |
| MR | 71.02 | 9.20E-6 | 0.905 | 13.39 |
| CA | 9.036 ± 0.707 | 3.43E-6 ± 2.25E-7 | 0.975 ± 0.003 | 0.293 ± 0.018 |
| SCA | 24.57 ± 0.16 | 6.61E-6 ± 0 | 0.976 ± 0.001 | 1.396 ± 0.022 |
| CAIM | 19.70 ± 0.08 | 8.98E-6 ± 1.53E-7 | 0.971 ± 0.003 | 1.586 ± 0.032 |
| SCAIM | 33.60 ± 0.02 | 1.83E-5 ± 1.77E-7 | 0.967 ± 0.001 | 4.300 ± 0.036 |

### 4.3.5 Intra-particle diffusion analysis

The adsorption of adsorbate on an adsorbent generally consists of three consecutive steps: (i) the film diffusion of adsorbate to the external surface; (ii) the intra-particle diffusion of adsorbate in the pores of the adsorbent; and (iii) the adsorption of adsorbate on the adsorption site. The step (iii) is normally faster than steps (i) and (ii), so the adsorption is not the rate-determining step for the overall adsorption process. In our case, the Cr(VI) adsorption-coupled reduction was relatively fast, the Cr(VI) removal kinetics by the adsorbents were tend to be controlled by the diffusion processes. The film diffusion is not the limiting factor in a well-agitated system or in high adsorbate concentration.

The intra-particle diffusion plot is useful in identifying and distinguishing the diffusion processes involved in the Cr(VI) removal process of the adsorbents. If the intra-particle diffusion plot is linear and passes through the origin, the adsorption process is only controlled by the intra-particle diffusion. However, if the plot exhibits multi-linear characteristic, the overall adsorption process may be controlled by more than one step, such as external film diffusion and pore diffusion (Bilgili, 2006). Figure 4-16 and Figure 4-17 display the intra-particle diffusion plots of the MR, CA, SCA, CAIM and SCAIM visualizing the relationship between Cr(VI) removal capacity ($Q_{Cr(VI)}$) and the total Cr adsorption capacity ($q_{tot}$) to $t^{0.5}$. The Cr(VI) removal and total Cr adsorption on MR, SCA, CAIM and SCAIM were multi-step processes due to the multilinear characteristic of the intra-particle diffusion plots.

In the case of MR, there was a sharp increase in the $Q_{Cr(VI)}$ and $q_{tot}$ values within 1 min. It represented the instantaneous Cr(VI) adsorption due to the high availability of active adsorption sites located on the external surface of MR. The Cr(VI) adsorption was followed by a rapid reduction as proposed in the Cr(VI) adsorption-coupled reduction mechanism. Once the external adsorption sites were fully occupied (after 1 min), the Cr(VI) ions were required to diffuse inside the pores in the adsorbent to seek for the internal adsorption sites. The Cr(VI) removal rate would be limited by the pore diffusion of Cr(VI) in the MR after 1 min. At 60 min, the $q_{tot}$ attained equilibrium but the $Q_{Cr(VI)}$ still kept on increasing. It was suggested that some of the reduced Cr(III) was removed from the surface MR, while the Cr(VI) adsorption sites became available to adsorb new Cr(VI) ions. The total Cr adsorption equilibrium was, therefore, a dynamic equilibrium, where the Cr(III) releasing rate was equal to the Cr(VI) adsorption rate.

Figure 4-17a shows the lag phase for the $Q_{Cr(VI)}$ and $q_{tot}$ of CA in the first 120 min. The $Q_{Cr(VI)}$ and $q_{tot}$ gradually increased afterward and could not attain the equilibrium at 3 d. This indicated that calcium alginate would also play a significant role in the Cr(VI) removal and total Cr adsorption. Moreover, the intra-particle diffusion plots of Cr(VI) removal on SCA and CAIM (Figure 4-17b and c) were linear but it did not pass through the origin, so the Cr(VI) removal rates by SCA and CAIM were not only controlled by the intra-particle diffusion. After the instantaneous Cr(VI) adsorption on the external surface of SCA and CAIM in the first 5 min, the pore diffusion of Cr(VI) in the immobilized MR and silica particles became the rate-

determining step for the Cr(VI) removal by SCA and CAIM, respectively, from 5 min to 3 d. On the other hand, the total Cr adsorption rate of SCA decreased after 2 h, because the Cr(III) was desorbed from the adsorbent and appeared in the solution phase. A significant amount of Cr(III) was detected in the solution phase after 30-min contact with the CAIM, so the third stage represented the net Cr adsorption on CAIM.

The rate of Cr(VI) removal by the SCAIM was also controlled by different diffusion processes at different time ranges. The first linear region at 0 - 120 min corresponded to the pore diffusion of Cr(VI) in the immobilized MR and the silica particles doped on the SCAIM. As the Cr(VI) removal process, the adsorbate concentration continued to decrease, so the film diffusion become an important rate-controlling step for the Cr(VI) removal by SCAIM. The second linear region at 120 - 360 min indicated that the Cr(VI) removal rate was controlled by the film diffusion of Cr(VI) on the SCAIM. A significant amount of Cr(III) was detected in the solution phase after 360 min. The third region (after 360 min) represented the net Cr uptake in SCAIM as a combined effect of Cr(VI) adsorption and Cr(III) desorption.

The intra-particle diffusion coefficient ($D_{app}$) in the early stage of the adsorption process could be calculated from the slope of intra-particle diffusion plot if the curve were linear and passed through the origin.

$$q_t = q_e \frac{6}{\pi^{1/2}} \frac{{D_{app}}^{1/2}}{h} t^{1/2}$$

where $D_{app}$ is the apparent intra-particle diffusion coefficient ($cm^2$/min); h is the half-length of

diffusion path (= radius of the adsorbent, cm); $q_e$ is the equilibrium sorption capacity (mg/g) and $q_t$ is the adsorption capacity at time t (mg/g)

The intra-particle diffusion plot of Cr(VI) removal kinetics by the SCAIM was a straight line from 0 to 60 min, so the $D_{app}$ value of Cr(VI) ions in the SCAIM beads was estimated to be 5.94E-05 $cm^2$/min.

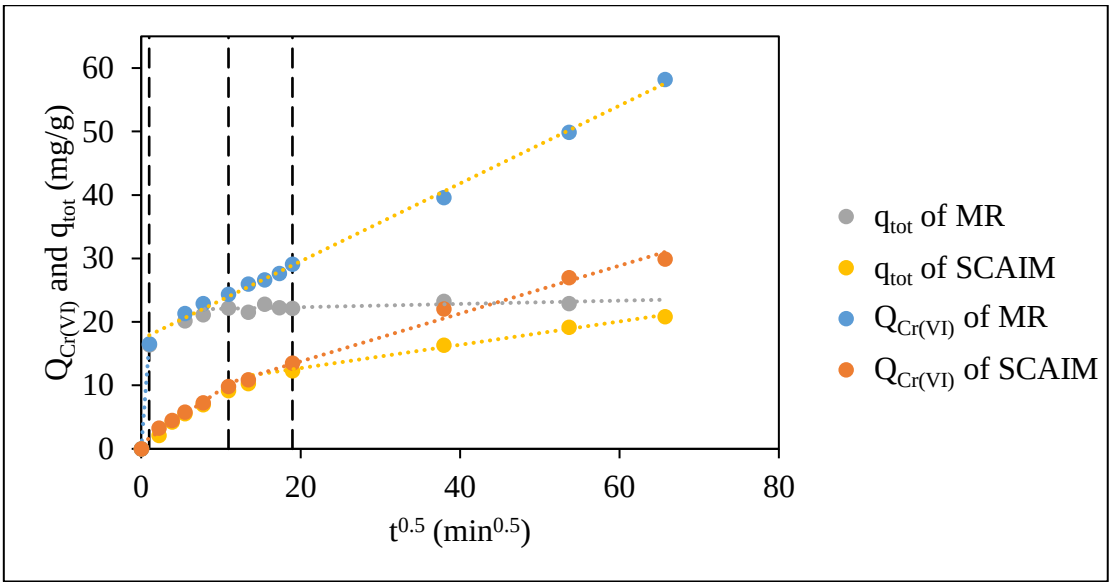


Figure 4-16 Intra-particle diffusion plot of the Cr(VI) removal and total Cr adsorption on MR and SCAIM.

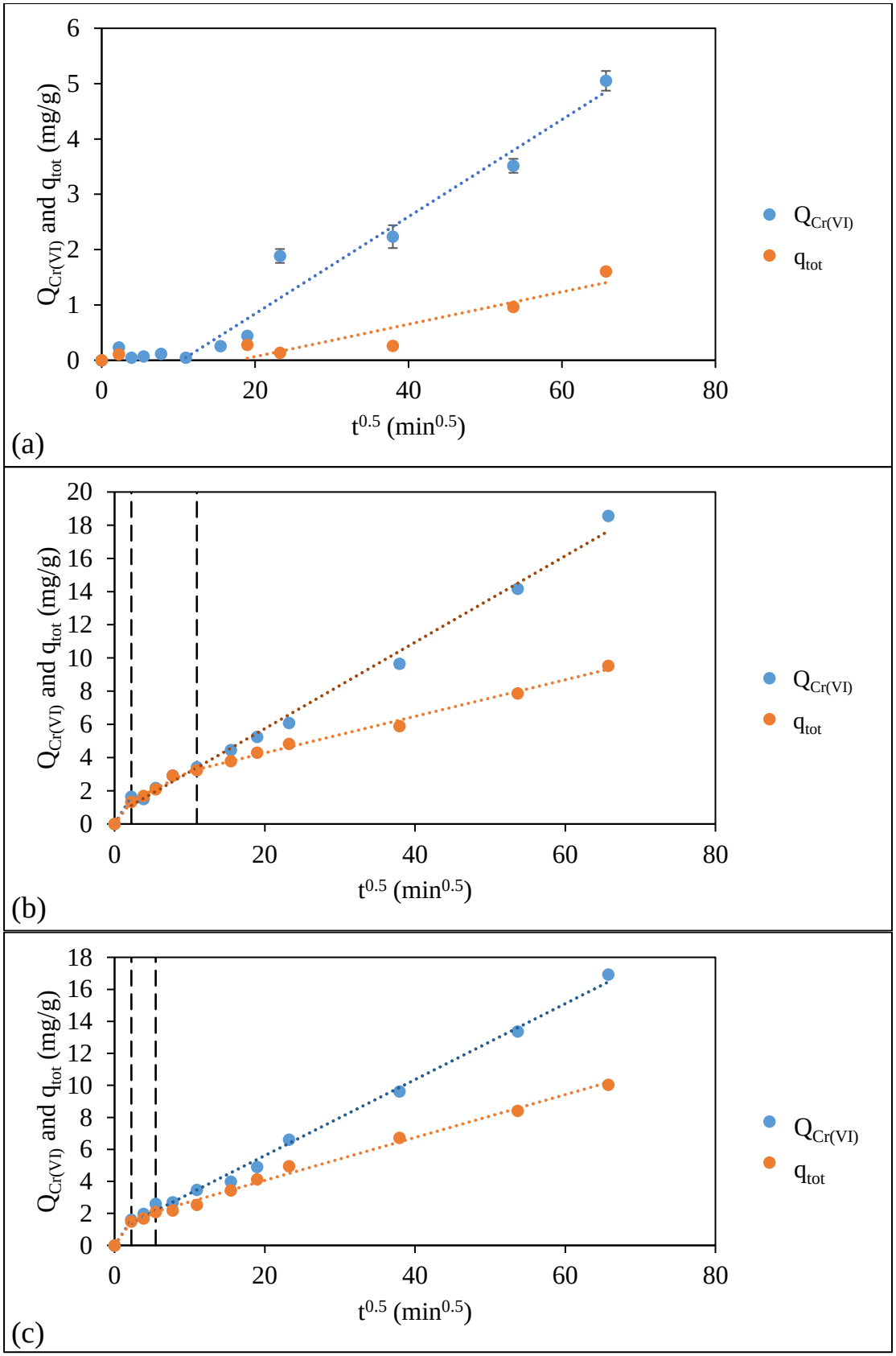


Figure 4-17 Intra-particle diffusion plots of the Cr(VI) removal and total Cr adsorption on (a) CA, (b) SCA and (c) CAIM.Effect of initial Cr(VI) concentration

The effect of initial Cr(VI) concentration on the percentage Cr(VI) removal (%$Cr(VI)_{re}$) of CA, SCA, CAIM and SCAIM is illustrated in Figure 4-18. The %$Cr(VI)_{re}$ of the four tested adsorbents was found to be in the descending order of SCAIM > CAIM ~ SCA > CA at different initial Cr(VI) concentrations. In general, the %$Cr(VI)_{re}$ of the four tested adsorbents decreased with an increase in the initial Cr(VI) concentration. For example, an increase in the initial concentration from 10 to 2000 ppm, the %$Cr(VI)_{re}$ of SCAIM decreased from 99.41 ± 0.30% to 40.09 ± 0.84%. Moreover, it should be noted that the SCAIM exhibited the highest %$Cr(VI)_{re}$ among the four tested adsorbents, while the SCA and CAIM showed significantly higher %$Cr(VI)_{re}$ than CA. These results demonstrated that the immobilized *M. rouxii*, the doped silica and the calcium alginate were the effective components for the Cr(VI) removal in SCAIM. The highest %$Cr(VI)_{re}$ (99.41 ± 0.30%) was achieved with low initial Cr(VI) concentration (10 ppm), suggesting that the SCAIM showed high affinity to Cr(VI).

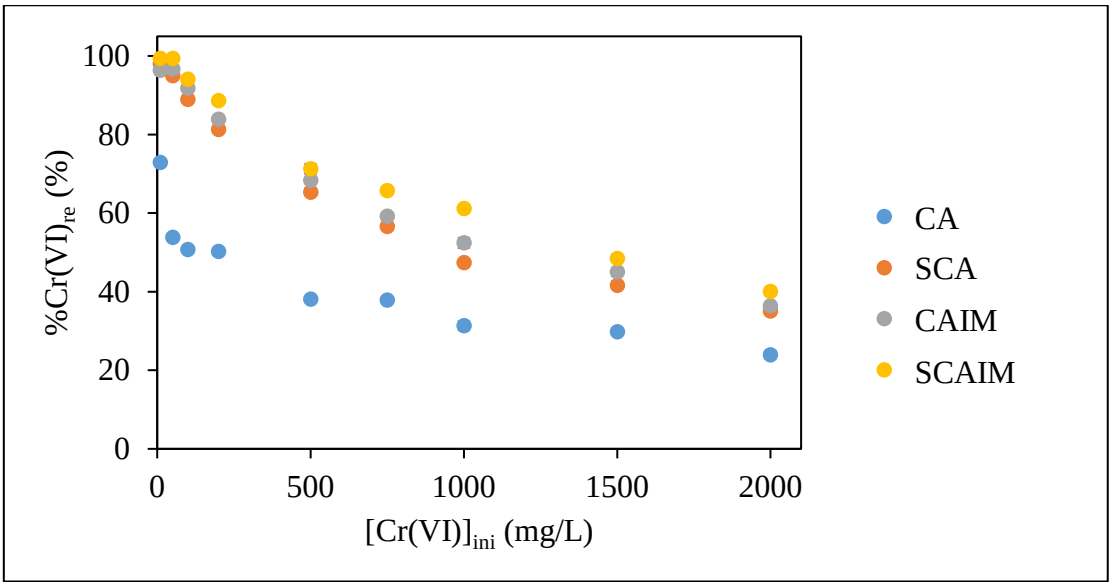


Figure 4-18 Effect of initial Cr(VI) concentration on $\%Cr(VI)_{re}$ of different immobilized adsorbents. (Experimental conditions: $[Cr(VI)]_0$ = 10 - 2000 ppm, adsorbent dosage = 10 g/L, t = 3 d, pH 2, temperature = 25°C and agitation = 250 rpm)

### 4.3.6 Isotherm modelling

Adsorption isotherm study is important for understanding the total Cr adsorption equilibrium and the maximum total Cr adsorption capacity of adsorbents. The effect of initial Cr(VI) concentration on the total Cr adsorption capacities of MR, CA, SCA, CAIM and SCAIM was investigated. The equilibrium adsorption data were then fitted with five different isotherm models, namely Langmuir, Freundlich, Tempkin, Dubinin-Radushkevich and Sips models. Figures Figure 4-19 to Figure 4-21 show the isotherm modelling curves of the five adsorbents, and Table 4-5 lists the modelling parameters. The adsorption data of MR were adopted from previous research (Lo, 2013).

Of the five adsorption isotherm models, the RMSE value of the Sips model was the lowest, indicating that this particular model was the best-fit isotherm model for the five tested adsorbents. The Sips model is a three-parameter isotherm model that can better describe the equilibrium data than those two-parameter models (e.g., Langmuir, Freundlich, Tempkin and Dubinin-Radushkevich models). Moreover, the Sips model is a combination of the Langmuir and Freundlich model, thus making it more suitable for predicting adsorption on heterogeneous surfaces without the limitation of increased adsorbate concentration associated with the Freundlich model. The Sips model is simply reduced to the Freundlich model at a lower adsorbate concentration, but it is reduced to the Langmuir isotherm at a higher adsorbate concentration. The Sips exponents ($m_s$) of MR, CA, SCA, CAIM and SCAIM were 0.903 ±

0.003, 1.042 ± 0.028, 0.675 ± 0.016, 0.770 ± 0.038 and 0.838 ± 0.017, respectively, which were quite close to 1. Therefore, the Sips model was approximately equal to the Langmuir model. With this reason, the total Cr adsorption isotherms were also well simulated by the Langmuir model, which assumes the monolayer coverage of adsorbate on a homogeneous surface with identical adsorption sites.

The Langmuir maximum total Cr adsorption capacities ($q_{max}$) of MR, CA, SCA, CAIM and SCAIM were 80.21 ± 6.05, 45.96 ± 4.09, 61.60 ± 3.22, 69.46 ± 2.90 and 78.15 ± 4.79 mg/g, respectively. It is worthy to note that the $q_{max}$ of SCAIM was comparable to that of MR. The silica-doped calcium alginate was an effective immobilization material which did not reduce the $q_{max}$ of MR. The ethylenediamine groups on the silica and the hydroxyl groups on the calcium alginate could also participate in Cr(VI) adsorption, so the high Cr adsorption capacity of MR was retained. The Cr adsorption ability of the silica was further confirmed by the $q_{max}$ value of SCA (61.60 ± 3.22 mg/g), which was much higher than that of CA (45.96 ± 4.09 mg/g). In addition, the high $q_{max}$ value of CAIM (69.46 ± 2.90 mg/g) demonstrated the contribution of the immobilized cells to the total Cr adsorption capacity of SCAIM. Thus, the silica-doped calcium-alginate-immobilized *M. rouxii* (SCAIM) has a great adsorption potential for the Cr(VI) removal with regard to Cr adsorption capacity.

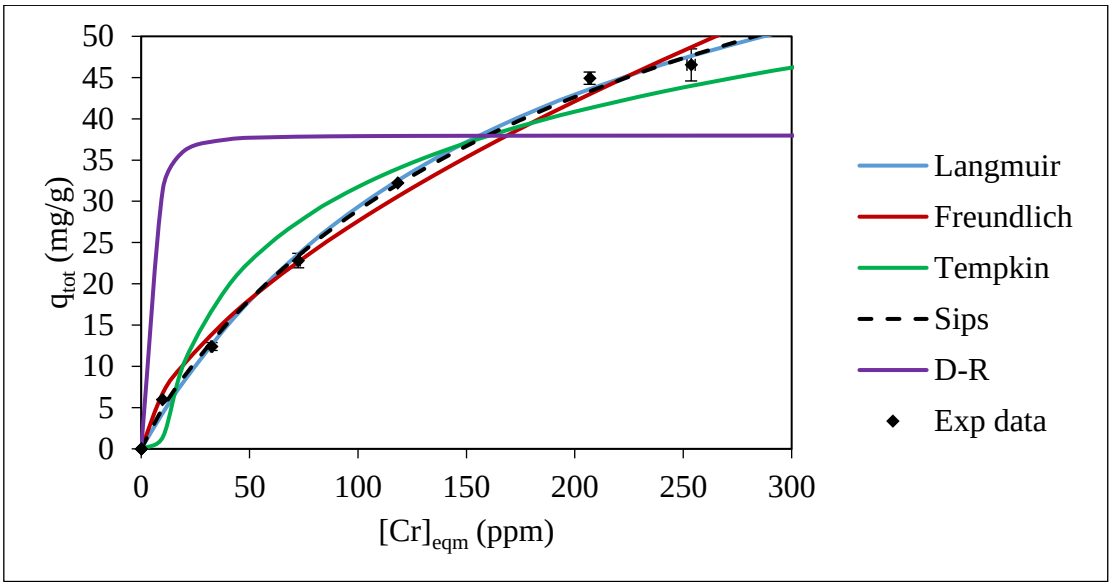


Figure 4-19 Total Cr adsorption isotherm modelling curves of MR. (Experimental conditions: $[Cr(VI)]_0$ = 20 - 300 ppm, adsorbent dosage = 1 g/L, t = 24 h, pH 2, temperature = 25°C and agitation = 250 rpm)

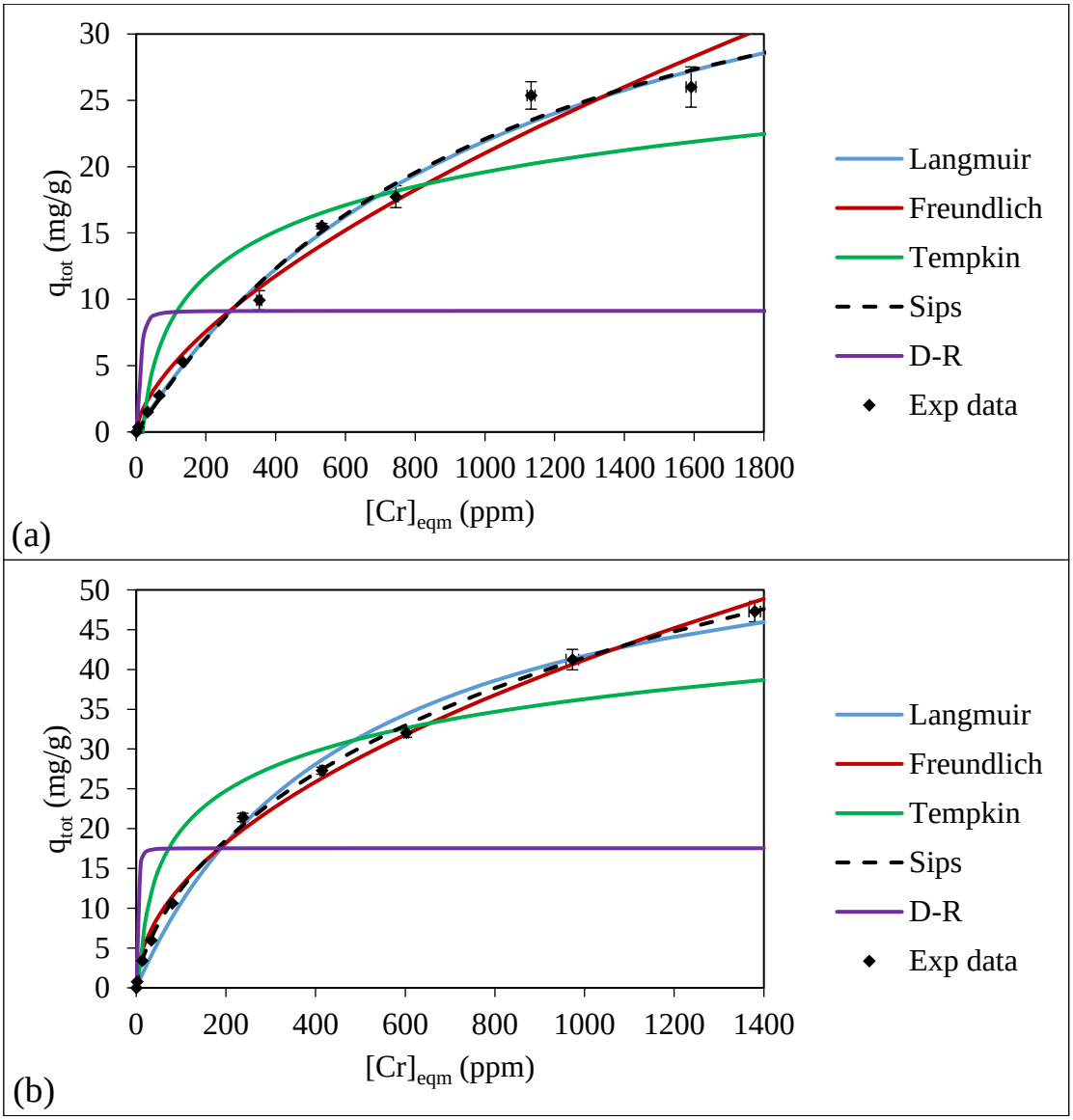


Figure 4-20 Total Cr adsorption isotherm modelling curves of (a) CA and (b) SCA. (Experimental conditions: $[Cr(VI)]_0$ = 10 - 2000 ppm, adsorbent dosage = 10 g/L, t = 3 d, pH 2, temperature = 25°C and agitation = 250 rpm)

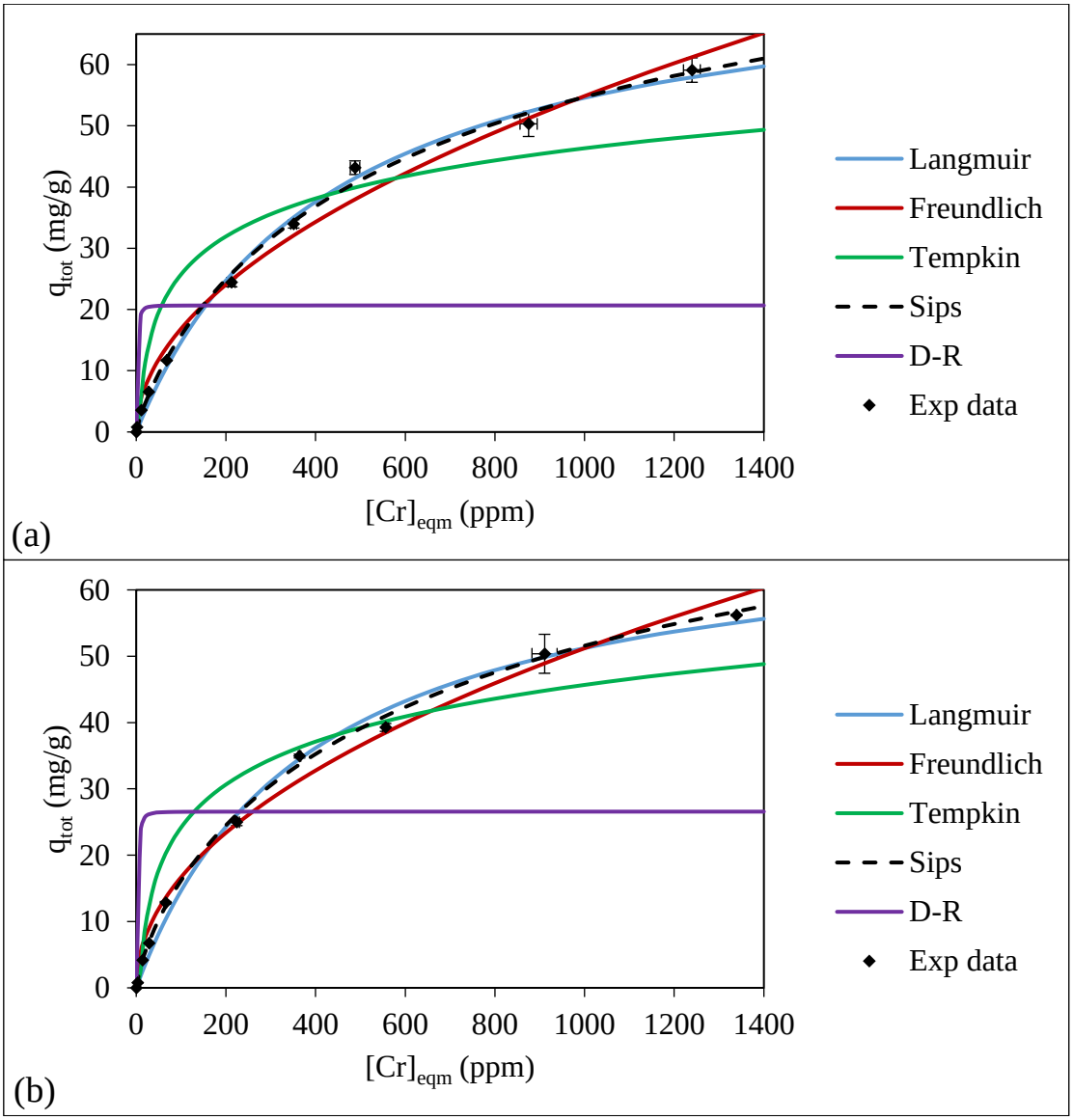


Figure 4-21 Total Cr adsorption isotherm modelling curves of (a) CAIM and (b) SCAIM. (Experimental conditions: $[Cr(VI)]_0$ = 10 - 2000 ppm, adsorbent dosage = 10 g/L, t = 3 d, pH 2, temperature = 25°C and agitation = 250 rpm)

Table 4-5 Isotherm modelling parameters for total Cr adsorption on different adsorbents.

| Langmuir | $q_{max}$ (mg/g) | $b_L$ | $R^2$ | RMSE |
|---|---|---|---|---|
| MR | 80.21 ± 6.05 | 5.76E-3 ± 5.72E-4 | 0.996 ± 0.002 | 1.207 ± 0.251 |
| CA | 45.96 ± 4.09 | 9.12E-4 ± 7.23E-5 | 0.990 ± 0.004 | 1.042 ± 0.161 |
| SCA | 61.60 ± 3.22 | 2.10E-3 ± 1.57E-4 | 0.992 ± 0.001 | 1.633 ± 0.173 |
| CAIM | 69.46 ± 2.90 | 2.77E-3 ± 1.51E-4 | 0.993 ± 0.002 | 1.748 ± 0.187 |
| SCAIM | 78.15 ± 4.79 | 2.32E-3 ± 1.71E-4 | 0.995 ± 0.001 | 1.610 ± 0.029 |
| Freundlich | $K_F$ (mg/g) | n | $R^2$ | RMSE |
| MR | 1.665 ± 0.136 | 1.640 ± 0.057 | 0.993 ± 0.002 | 1.709 ± 0.238 |
| CA | 0.264 ± 0.014 | 1.579 ± 0.036 | 0.981 ± 0.006 | 1.474 ± 0.151 |
| SCA | 1.235 ± 0.062 | 1.970 ± 0.045 | 0.994 ± 0.002 | 1.156 ± 0.031 |
| CAIM | 1.544 ± 0.031 | 1.972 ± 0.025 | 0.988 ± 0.002 | 2.273 ± 0.223 |
| SCAIM | 1.594 ± 0.078 | 1.952 ± 0.049 | 0.988 ± 0.002 | 2.563 ± 0.136 |
| Tempkin | $b_T$ (J/mol) | $K_T$ (L/g) | $R^2$ | RMSE |
| MR | 188.3 ± 7.6 | 0.112 ± 0.005 | 0.936 ± 0.004 | 4.230 ± 0.281 |
| CA | 507.4 ± 23.9 | 0.055 ± 0.001 | 0.829 ± 0.002 | 4.134 ± 0.220 |
| SCA | 346.3 ± 9.60 | 0.159 ± 0.004 | 0.863 ± 0.005 | 6.302 ± 0.286 |
| CAIM | 269.6 ± 3.60 | 0.130 ± 0.001 | 0.900 ± 0.012 | 6.305 ± 0.541 |
| SCAIM | 276.8 ± 9.86 | 0.177 ± 0.005 | 0.850 ± 0.004 | 8.424 ± 0.408 |
| D-R | Q (mg/g) | $B_D$ ($mol^2/kJ^2$) | $R^2$ | RMSE |
| MR | 37.98 ± 0.66 | 3.36E-6 ± 5.69E-8 | 0.854 ± 0.012 | 18.09 ± 0.57 |
| CA | 9.126 ± 0.275 | 1.74E-5 ± 1.37E-7 | 0.558 ± 0.004 | 9.764 ± 0.499 |
| SCA | 17.54 ± 0.19 | 2.04E-6 ± 8.27E-8 | 0.593 ± 0.002 | 16.25 ± 0.49 |
| CAIM | 15.93 ± 0.092 | 4.60E-6 ± 1.58E-6 | 0.540 ± 0.078 | 19.36 ± 1.08 |
| SCAIM | 20.66 ± 0.36 | 1.48E-6 ± 7.30E-8 | 0.578 ± 0.001 | 21.15 ± 0.76 |
| Sips | $n_m$ (L/mg) | $K_s$ (L/g) | $m_s$ | $R^2$ | RMSE |
| MR | 6.94E-3 ± 8.4E-4 | 0.652 ± 0.023 | 0.903 ± 0.003 | **0.997 ± 0.002** | **1.147 ± 0.259** |
| CA | 7.62E-4 ± 3.4E-5 | 0.033 ± 0.005 | 1.042 ± 0.028 | **0.990 ± 0.004** | **1.037 ± 0.157** |
| SCA | 5.54E-3 ± 5.6E-4 | 0.621 ± 0.036 | 0.675 ± 0.016 | **0.999 ± 0.001** | **0.582 ± 0.162** |
| CAIM | 5.96E-3 ± 8.4E-4 | 0.559 ± 0.095 | 0.770 ± 0.038 | **0.994 ± 0.001** | **1.045 ± 0.014** |
| SCAIM | 4.24E-3 ± 1.2E-4 | 0.400 ± 0.029 | 0.838 ± 0.017 | **0.997 ± 0.001** | **1.361 ± 0.043** |

### 4.3.7 Effect of adsorbent dosage

The Cr(VI) removal experiments were conducted by varying the dosage of MR, CA, SCA, CAIM and SCAIM at a constant pH of 2.0 and Cr(VI) initial concentration of 100 ppm. The maximum dosage of freely-suspended MR was limited to 10 g/L due to the high viscosity of the biomass suspension. It formed a highly viscous gel if 50 g/L of MR was applied. However, a superior adsorbent dosage (e.g., 50 g/L) of the immobilized adsorbent can be used without increasing the viscosity of the solution. In this study, the maximum dosage for the immobilized bead adsorbents was 50 g/L. The adsorption time for the freely-suspended MR and the immobilized adsorbent was set as 1 day and 3 days, respectively, as determined in Section 4.3.1.

As shown in Figure 4-22, when the MR dosage increased from 0.2 to 10 g/L, the $\%Cr(VI)_{re}$ increased from 9.66 ± 0.42% to 90.63 ± 0.35%, while the $Q_{Cr(VI)}$ decreased from 36.44 ± 1.17% to 5.14 ± 0.17%. Higher $\%Cr(VI)_{re}$ was achieved with a higher adsorbent dosage because of the larger surface area and more adsorption sites for the Cr(VI) removal. The decrease in Cr(VI) removal capacity was attributed to the unsaturated Cr(VI) adsorption by the excess amount of adsorbent available. Similarly, when the dosage of SCAIM increased from 1 to 15 g/L, the value of $\%Cr(VI)_{re}$ increased from 57.39 ± 0.06% to 98.62 ± 0.23% (Figure 4-24b). The percentage Cr(VI) removal reached a plateau when the SCAIM dosage was higher than 15 g/L. More than 90% of $Q_{Cr(VI)}$ was achieved with SCAIM at the dosage of 10 g/L, so the optimum SCAIM dosage for Cr(VI) removal was set to 10 g/L. It is worthy to note that both the freely-

suspended biomass (MR) and immobilized biomass (SCAIM) showed similar Cr(VI) removal percentages which were approximately 90% at the same dosage of 10 g/L. This means that the Cr(VI) removal ability of biomass did not reduce after the immobilization.

The effect of adsorbent dosage was also investigated using CA, SCA and CAIM (Figures Figure 4-23 and Figure 4-24a). The CA beads showed a low affinity to Cr(VI), so a high $\%Cr(VI)_{re}$ (94.88%) was only achieved at an extremely high dosage (50 g/L) of CA. The SCA and CAIM beads were prepared by doping the Ca-alginate beads with ethylenediamine functionalized silica and the immobilization of biomass in Ca-alginate beads, respectively. Both of them showed similar $\%Cr(VI)_{re}$ of ~95% at the adsorbent dosage of 15 g/L.

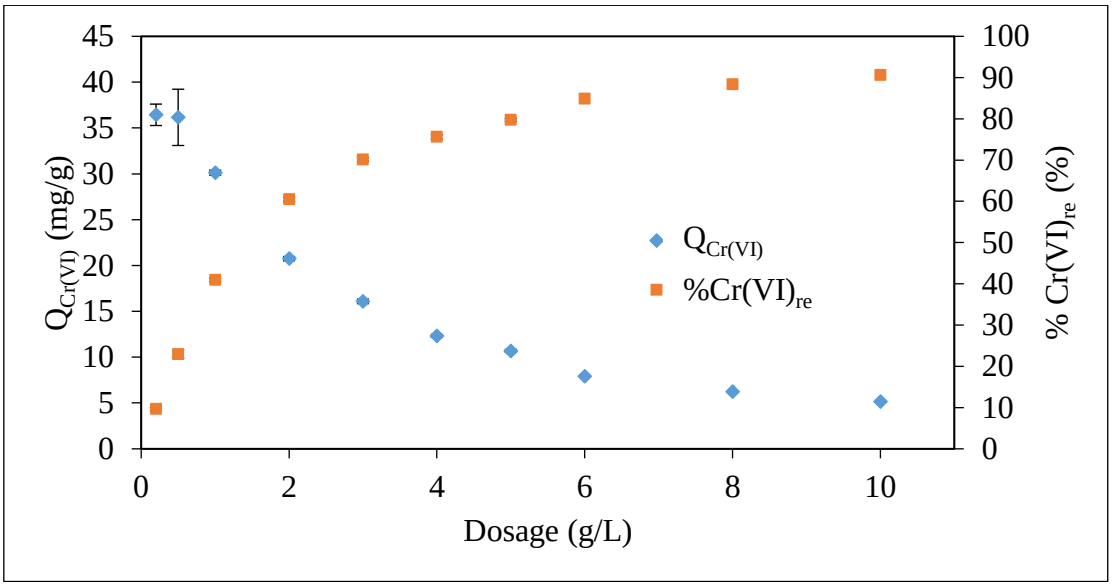


Figure 4-22 Effect of adsorbent dosage on the $Q_{Cr(VI)}$ and $\%Cr(VI)_{re}$ by MR. (Experimental conditions: $[Cr(VI)]_0$ = 100 ppm, adsorbent dosage = 0.2 - 10 g/L, t = 24 h, pH 2, temperature = 25ºC and agitation = 250 rpm)

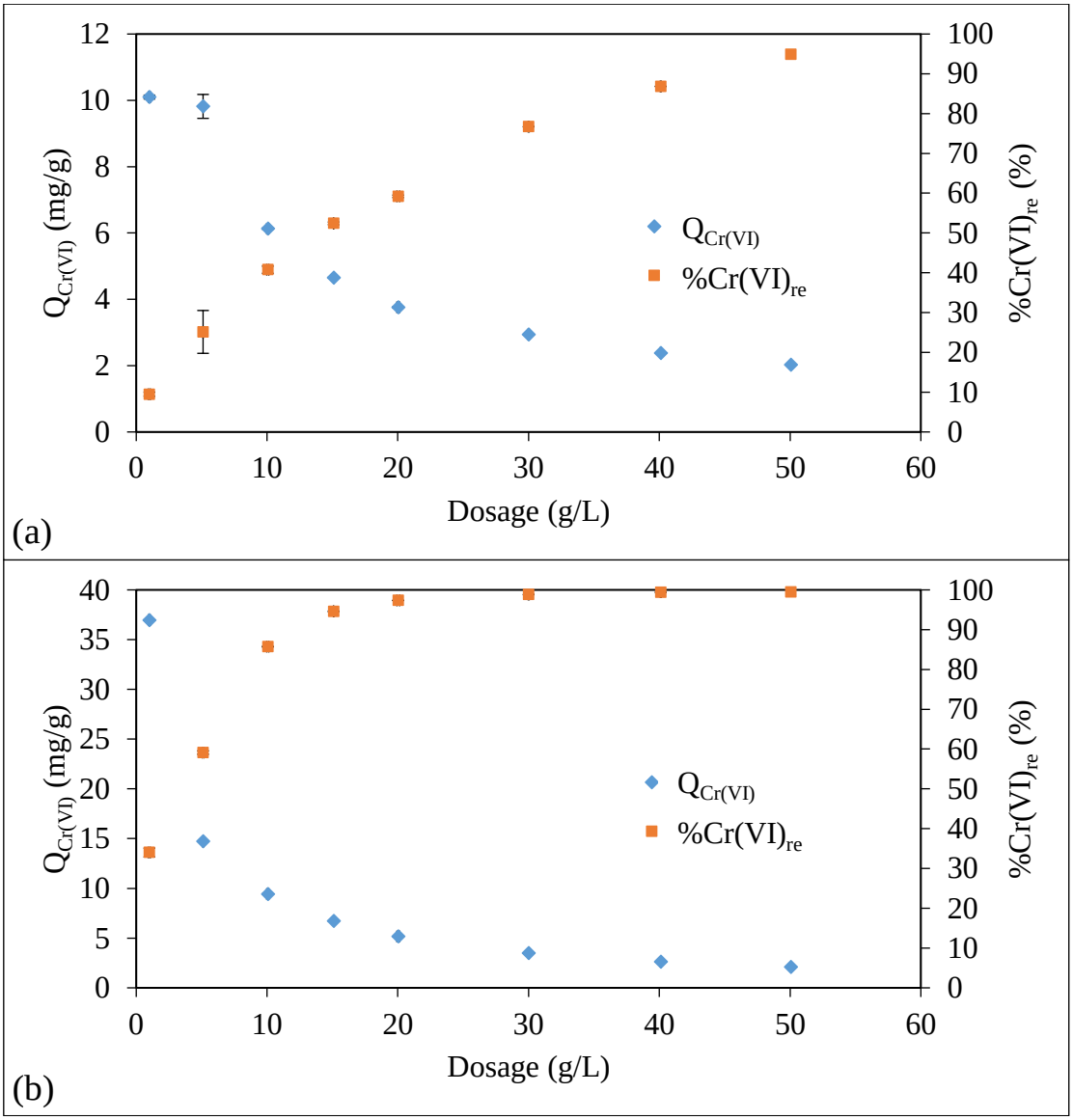


Figure 4-23 Effect of adsorbent dosage on the $Q_{Cr(VI)}$ and $\%Cr(VI)_{re}$ by (a) CA and (b) SCA. (Experimental conditions: $[Cr(VI)]_0$ = 100 ppm, adsorbent dosage = 1 - 50 g/L, t = 3 d, pH 2, temperature = 25°C and agitation = 250 rpm)

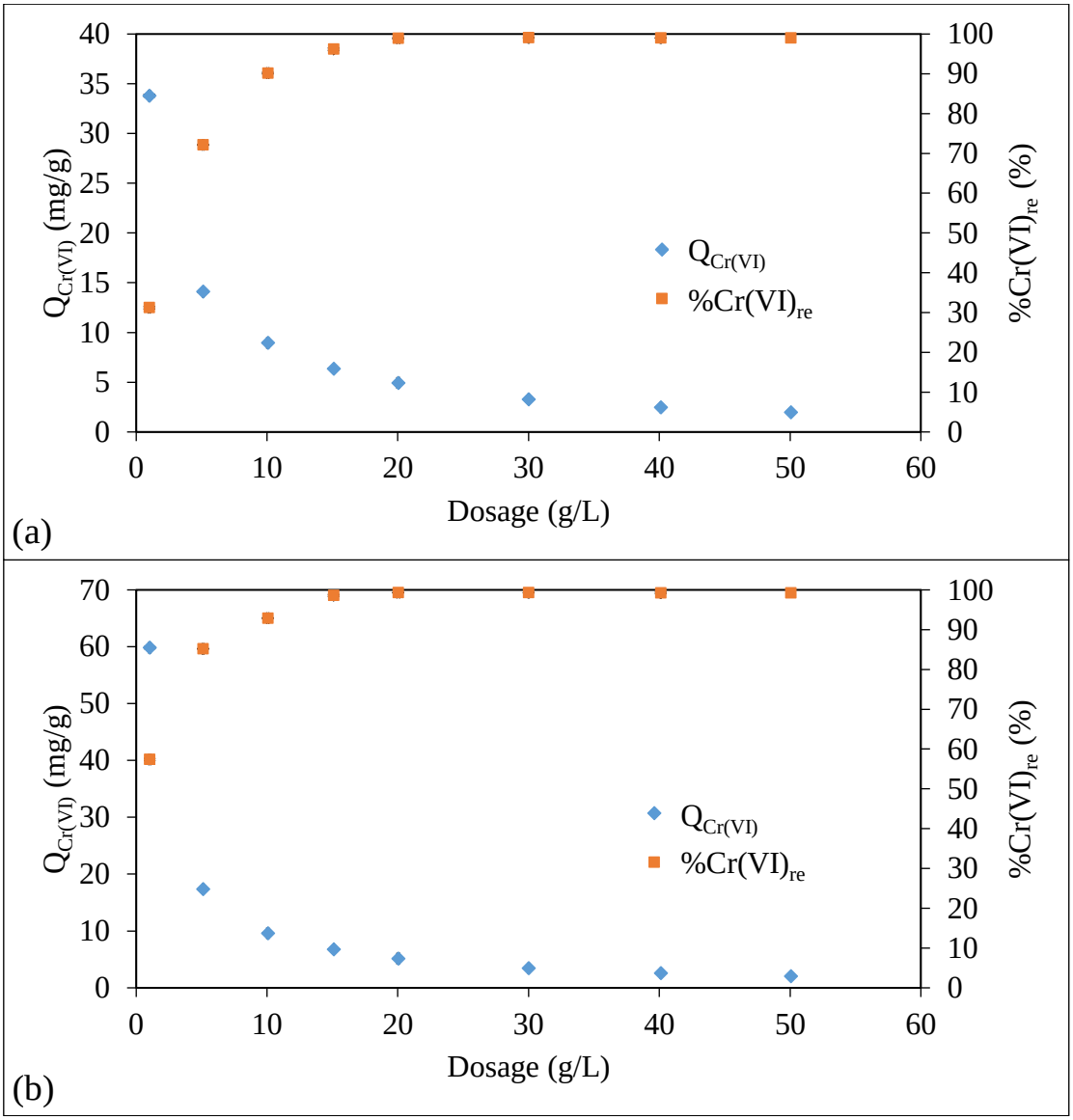


Figure 4-24 Effect of adsorbent dosage on the $Q_{Cr(VI)}$ and $\%Cr(VI)_{re}$ by (a) CAIM and (b) SCAIM. (Experimental conditions: $[Cr(VI)]_0$ = 100 ppm, adsorbent dosage = 1 - 50 g/L, t = 3 d, pH 2, temperature = 25°C and agitation = 250 rpm)

### 4.3.8 Effect of temperature

In this study, the Cr(VI) removal kinetics of SCAIM was investigated under a range of temperatures between 4 and 40°C. The results of MR were adopted from previous research (Lo, 2013) for comparison. Figure 4-25 shows that the $Q_{Cr(VI)}$ of MR and SCAIM increased sharply at the three different temperature points within the first 1 h due to the high availability of adsorption sites on the adsorbent surface. The Cr(VI) removal kinetics appeared to slow down and reached an equilibrium at a longer contact time since there was a decreasing number of binding sites available for the Cr(VI) adsorption. Figure 4-25a further shows that the $Q_{Cr(VI)}$ of the freely-suspended MR increased with rising temperature, indicating that the Cr(VI) removal by MR was kinetically controlled by an endothermic process. Similarly, the $Q_{Cr(VI)}$ of SCAIM increased with rising temperature from 1440 to 4320 min (Figure 4-25b). The increase in temperature resulted in an increase in the chance of collision between the Cr(VI) ions and the binding sites on the surface of the adsorbent.

The Cr(VI) removal kinetics of the SCAIM under different temperatures were best simulated by the fractional power kinetic model with the lowest RMSE values and the highest correlation coefficients. Figure 4-25 shows the Cr(VI) removal kinetic data and the modelling curves of the fractional power, while Table 4-6 summarizes the modelling parameters. It was found that the specific Cr(VI) removal rate at t = 1 min ($k_f v$) decreased from 0.569 ± 0.005 to 0.435 ± 0.012 mg/g-min when the temperature increased from 4 to 40°C.

Van't Hoff equation was employed to estimate the thermodynamic parameters, including Gibb's free energy change (ΔG), enthalpy change (ΔH), and entropy change (ΔS).

$$\ln\left(\frac{K_1}{K_2}\right) = \frac{-\Delta H}{R}\left(\frac{1}{T_1} - \frac{1}{T_2}\right)$$

$$\Delta G = \Delta H - T\Delta S$$

$$K = \frac{Q_{Cr(VI)}}{[Cr(VI)]_{eqm}}$$

where $K_1$ is the equilibrium constant at $T_1$, $K_2$ is the equilibrium constant at $T_2$, R is gas constant 8.314 J/mol-K, and $[Cr(VI)]_{eqm}$ is the equilibrium Cr(VI) concentration.

Table 4-7 summarizes the thermodynamic parameters of the Cr(VI) removal by MR and SCAIM. The enthalpy change (ΔH, J/mol) and the entropy change (ΔS, J/mol-K) of the Cr(VI) removal by MR and SCAIM were calculated from the linear plot of ln K versus 1/T. The ΔG for the Cr(VI) removal by MR was negative at every tested temperature, confirming the feasibility and the spontaneous nature of the Cr(VI) removal process. The ΔG value decreased from -9.754 to -10.61 J/mol with increasing temperature from 20 to 40°C, indicating that the Cr(VI) removal by the MR was more favorable at higher temperatures. The positive ΔH (+27.70 J/mol) implied that the Cr(VI) removal by MR was an endothermic process, while the positive ΔS (+42.74 J/mol-K) confirmed the increase in the randomness of the solid-solution system due to some structural changes of the biomass surface after the Cr adsorption.

The positive values of ΔH (+6.784 ± 0.065 J/mol) and ΔS (+49.07 ± 0.27 J/mol-K) were similarly found in the Cr(VI) removal process by the SCAIM. The Cr(VI) removal process by

the SCAIM was an endothermic process with increasing randomness. The negative ΔG value indicated that the Cr(VI) removal process by the SCAIM was a spontaneous process.

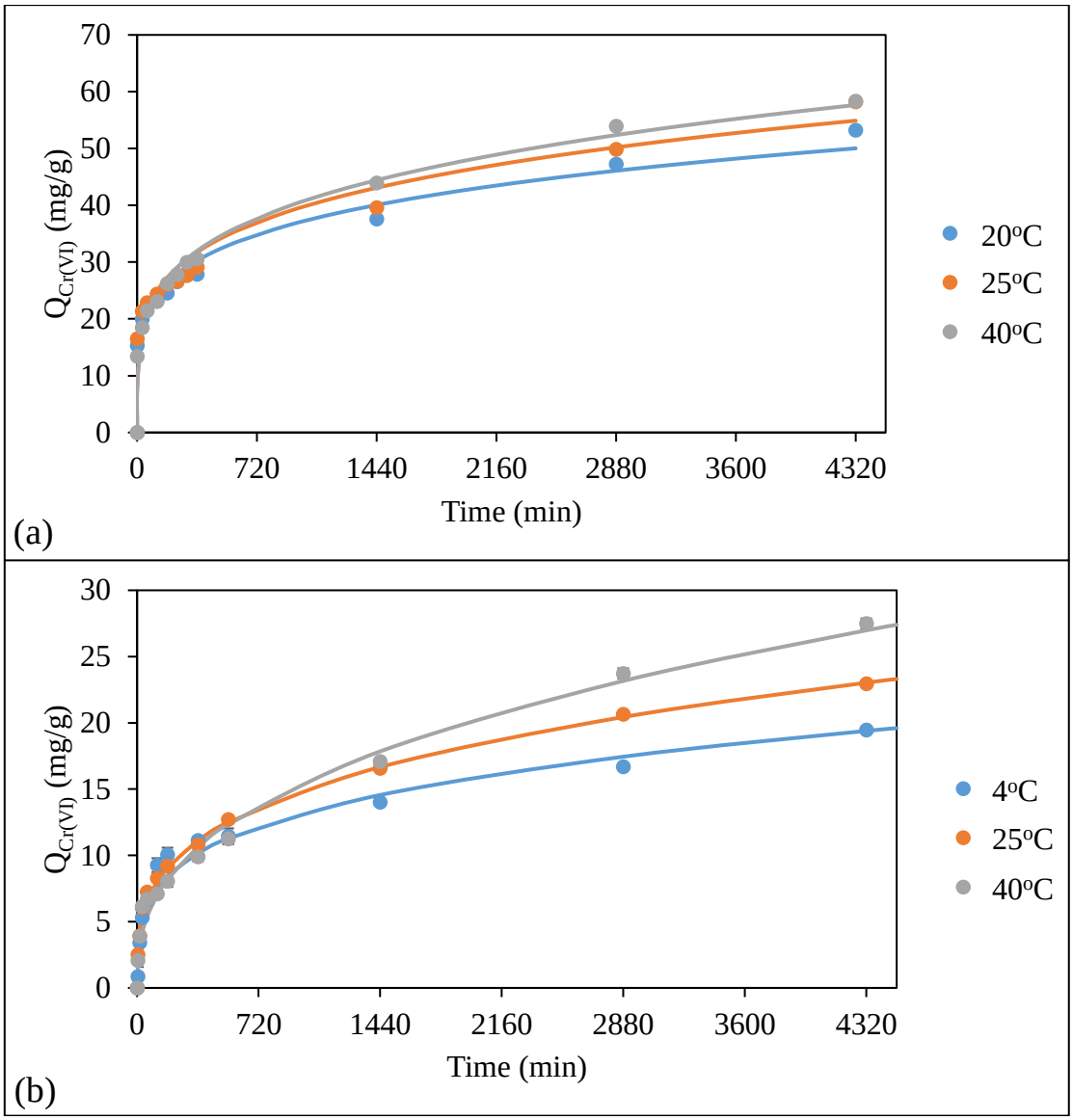


Figure 4-25 Effect of temperature on the Cr(VI) removal kinetics. (a) MR and (b) SCAIM. (Experimental conditions: **MR**, $[Cr(VI)]_0$ = 100 ppm, adsorbent dosage = 1 g/L, t = 24 h, pH 2, temperature = 20, 25 and 40ºC and agitation = 250 rpm; **SCAIM**, $[Cr(VI)]_0$ = 50 ppm, adsorbent dosage = 1 g/L, t = 3 d, pH 2, temperature = 4, 25 and 40ºC and agitation = 250 rpm)

Table 4-6 Modelling parameters of the fractional power model for the Cr(VI) removal by SCAIM at different temperatures.

| Temp. | $k_f$ (mg/g-min$^v$) | v | $k_f v$ (mg/g-min$^v$) | $R^2$ | RMSE |
|---|---|---|---|---|---|
| 4°C | 2.181 ± 0.020 | 0.261 ± 0.002 | 0.569 ± 0.005 | 0.962 ± 0.003 | 1.223 ± 0.008 |
| 25°C | 1.960 ± 0.009 | 0.294 ± 0.009 | 0.577 ± 0.001 | 0.996 ± 0.001 | 0.456 ± 0.082 |
| 40°C | 1.158 ± 0.038 | 0.376 ± 0.002 | 0.435 ± 0.012 | 0.987 ± 0.005 | 1.006 ± 0.085 |

Table 4-7 Thermodynamic parameters of Cr(VI) removal on MR and SCAIM.

| | Temp. (°C) | MR | Temp. (°C) | SCAIM |
|---|---|---|---|---|
| ΔG (J/mol) | 20 | -9.754 | 4 | -6.808 ± 0.009 |
| | 25 | -9.968 | 25 | -7.838 ± 0.015 |
| | 40 | -10.61 | 40 | -8.574 ± 0.019 |
| ΔH (J/mol) | | +27.70 | | +6.784 ± 0.065 |
| ΔS (J/mol-K) | | +42.74 | | +49.07 ± 0.27 |

### 4.3.9 Effect of agitation speed

The Cr(VI) removal kinetics by the silica-doped calcium-alginate-immobilized *M. rouxii* (SCAIM) was investigated at different agitation speeds (Figure 4-26). The results of MR were adopted from previous research (Lo, 2013) for comparison. With increasing agitation speed, the Cr(VI) removal rate and Cr(VI) removal capacity of the freely suspended MR were enhanced due to the reduced thickness of the boundary layer. The boundary layer diffusion could limit the Cr(VI) removal rate by MR at low agitation speed. However, the effect of agitation speed was less significant in the SCAIM.

In order to evaluate Cr(VI) removal rate under different agitation speeds, the Cr(VI) removal kinetic curves were simulated by the fractional power model (Table 4-8). The specific Cr(VI) removal rates at t = 1 min ($k_f v$) of SCAIM increased from 0.569 ± 0.005 to 0.705 ± 0.008 mg/g-min when the agitation speed increased from 100 rpm to 400 rpm. A higher agitation speed would enhance the external mass transfer rate and reduce the thickness of the boundary layer. Nonetheless, the initial stage (> 2 h) of the intra-particle diffusion plots of Cr(VI) removal by the SCAIM at 400 rpm (Figure 4-27) could pass through the origin, so the Cr(VI) removal rate should be predominantly controlled by the intra-particle diffusion rather than the external mass transfer.

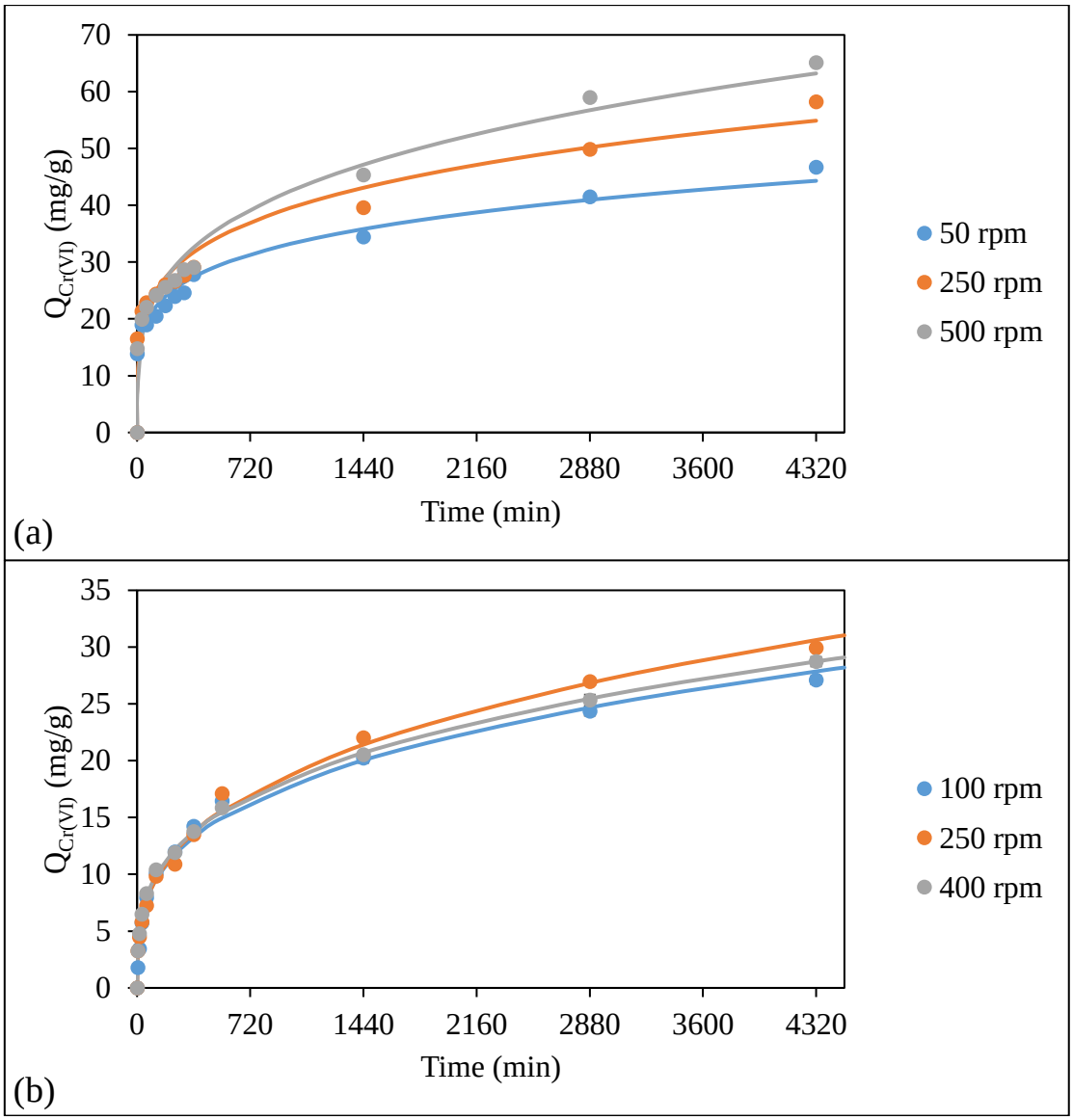


Figure 4-26 Effect of agitation speed on the Cr(VI) removal kinetics. (a) MR and (b) SCAIM. (Experimental conditions: **MR**, $[Cr(VI)]_0$ = 100 ppm, adsorbent dosage = 1 g/L, t = 3 d, pH 2, temperature = 25ºC, agitation = 50, 250 and 500 rpm; **SCAIM**, $[Cr(VI)]_0$ = 50 ppm, adsorbent dosage = 1 g/L, t = 3 d, pH 2, temperature = 25ºC, agitation = 100, 250 and 400 rpm)

Table 4-8 Modelling parameters of the fractional power model for the Cr(VI) removal by SCAIM at different agitation speeds.

| Agitation | $k_f$ (mg/g-min$^v$) | v | $k_f v$ (mg/g-min) | $R^2$ | RMSE |
|---|---|---|---|---|---|
| 100 rpm | 2.271 ± 0.087 | 0.300 ± 0.003 | 0.569 ± 0.005 | 0.987 ± 0.004 | 1.052 ± 0.005 |
| 250 rpm | 2.006 ± 0.024 | 0.326 ± 0.007 | 0.653 ± 0.006 | 0.995 ± 0.001 | 0.699 ± 0.003 |
| 400 rpm | 2.362 ± 0.021 | 0.299 ± 0.008 | 0.705 ± 0.008 | 0.999 ± 0.004 | 0.350 ± 0.040 |

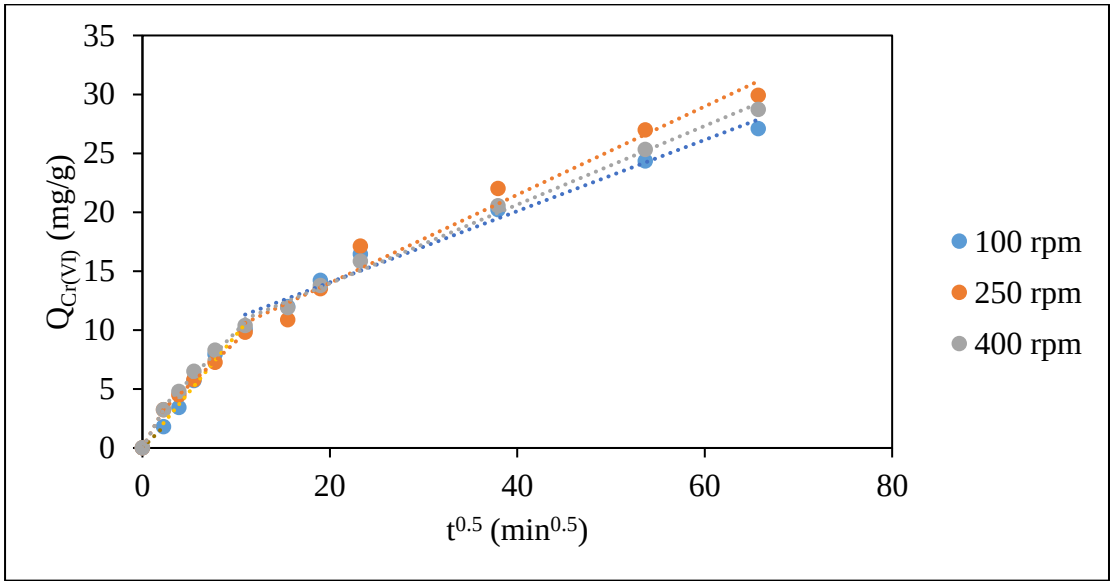


Figure 4-27 Intra-particle diffusion plot of Cr(VI) removal by SCAIM at different agitation speeds.

### 4.3.10 Cr desorption studies

Desorption is a crucial process for recovering the adsorbed metal ions and regenerating the adsorbent. Ten desorption agents were tested for their Cr desorption performance from the Cr-laden SCAIM (Figure 4-28). The percentage Cr(VI) desorption ($\%D_{Cr(VI)}$) and percentage Cr desorption ($\%D_{Cr}$) were calculated by the following equations.

$$\%D_{Cr(VI)} = \frac{Amount\ of\ Cr(VI)\ desorbed}{Amount\ of\ Cr\ adsorbed} \times 100\%$$

$$\%D_{Cr} = \frac{Amount\ of\ Cr\ desorbed}{Amount\ of\ Cr\ adsorbed} \times 100\%$$

All the desorbed Cr was determined to be in the form of Cr(III), so the $\%D_{Cr(VI)}$ values of the ten tested desorption agents were equal to zero. The result confirmed that the adsorbed Cr(VI) was reduced to Cr(III) on the adsorbent surface. The 2 M $HNO_3$ was the best desorption agent providing 86.14 ± 0.86% Cr desorption in 1 day. The acidic desorption agents ($HNO_3$, $H_2SO_4$, HCl and citric acid) were shown to be effective desorption agents since the cationic Cr(III) on the surface of SCAIM could be desorbed by a high concentration of protons through the ion-exchange mechanism. An increase in the concentration of acid showed a positive effect on the $\%D_{Cr}$. The higher the acid concentration was, the higher the $\%D_{Cr}$ would be. This result demonstrated that the concentration of protons affected the degree of Cr(III) desorption. In addition, the DDI water and the 4% $CaCl_2$ solution were unable to regenerate the Cr-laden SCAIM.

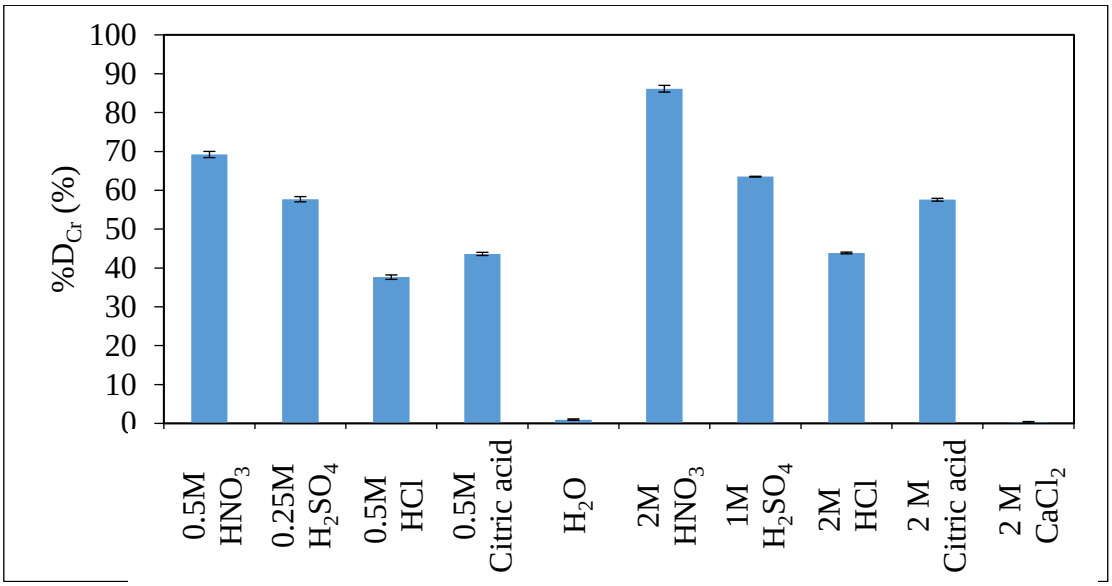


Figure 4-28 Percentage Cr desorption from Cr-laden SCAIM by different desorption agents. (Experimental conditions: **adsorption**, $[Cr(VI)]_0$ = 50 ppm, adsorbent dosage = 10 g/L, t = 3 d, pH 2, temperature = 25ºC and agitation = 250 rpm; **desorption**, adsorbent dosage = 20 g/L, t = 1 d, temperature = 25ºC and agitation = 250 rpm)

## 4.4 Continuous Cr(VI) removal by silica-doped calcium-alginate-immobilized *M. rouxii*

### 4.4.1 Column adsorption

Continuous Cr(VI) removal study was carried out using a fixed-bed column reactor packed with SCAIM at various inlet Cr(VI) concentrations (10 to 50 ppm) and flow rates (1.0 to 0.5 ml/min). The Cr(VI) removal performances of the fixed-bed column reactor at different column conditions were illustrated by the breakthrough curves (Figure 4-29), which were the plots of outlet Cr(VI) concentration ($C_t/C_0$) versus time. The breakthrough concentration was set at 4 ppm, which meets the standards for effluents discharged into the Victoria Harbor in Hong Kong (HKSAR, 1997). As shown in Figure 4-29, the steepness of the breakthrough curve changed under varied experimental conditions accordingly. Table 4-9 summarizes the breakthrough time ($t_b$) and breakthrough volume ($V_b$) of the 50 cm SCAIM column at various inlet Cr(VI) concentrations and flow rates. At a fixed inlet flow rate of 1.0 ml/min, the $t_b$ increased from 3400 to 18000 min when the inlet Cr(VI) concentration decreased from 50 to 10 ppm. The Cr(VI) breakthrough occurred faster, and the breakthrough curve was steeper at higher inlet Cr(VI) concentration. This could be explained by the fact that any increase in Cr(VI) concentration also increased the Cr(VI) concentration gradient. The greater concentration gradient led to a reduction in time required for the removal of a certain amount of Cr(VI) due to the overcrowding effect on the surface of the SCAIM beads.

The effect of inlet flow rate on the breakthrough curve was also investigated with the fixed initial Cr (VI) concentration of 10 ppm and a bed height of 50 cm, respectively. The $t_b$ increased from 18000 to 40000 min when the inlet Cr(VI) flow rate decreased from 1.0 to 0.5 ml/min. This phenomenon is attributed to the fact that the longer residence time achieved the higher Cr(VI) removal capacity of SCAIM. In addition, a decrease in inlet flow rate would reduce the sharpness of the breakthrough curve. At higher flow rates, a shorter breakthrough time was observed. The short breakthrough time was the result of the premature saturation of the column. The Cr(VI) removal ability of SCAIM column could be maintained for a longer period of time.

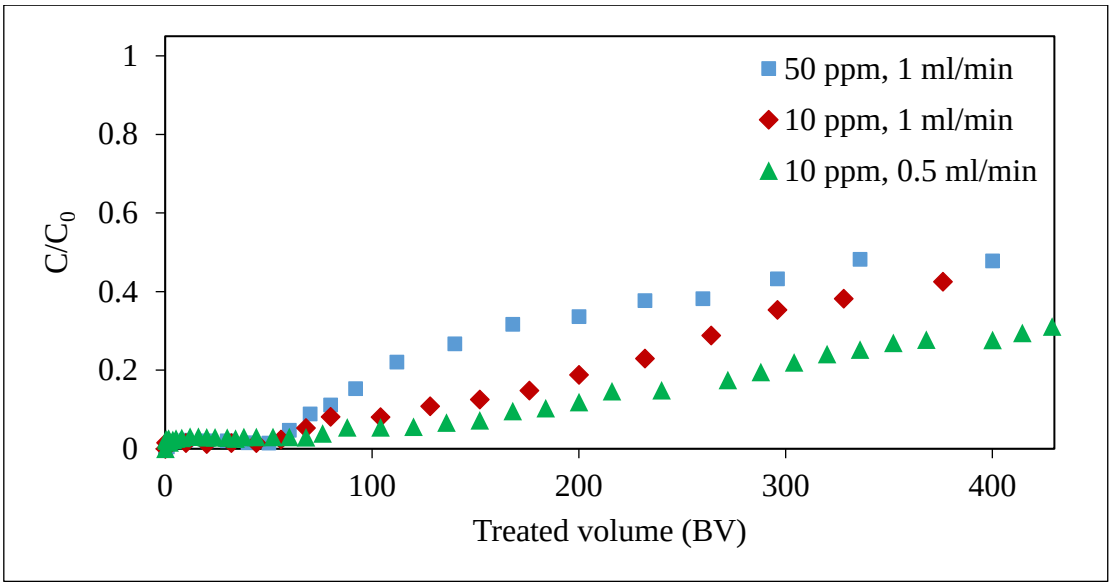


Figure 4-29 Breakthrough curves for different inlet Cr(VI) concentrations and flow rates. (Experimental conditions: $[Cr(VI)]_0$ = 10 - 50 ppm, bed height = 50 cm, pH 2.0, flow rate = 0.5 - 1.0 ml/min, temperature = 22.5°C)

Table 4-9 Cr(VI) removal by SCAIM in a fixed-bed column at different process conditions.

| Inlet Cr(VI) concentration (ppm) | Flow rate (ml/min) | Breakthrough volume / $V_b$ (BV) | Breakthrough time / $t_b$ (min) |
|---|---|---|---|
| 50 | 1.0 | 68 | 3400 |
| 10 | 1.0 | 360 | 18000 |
| 10 | 0.5 | 400 | 40000 |

### 4.4.2 Column desorption

The regeneration of the Cr-laden SCAIM column was performed by feeding it with 2 M $HNO_3$ solution which was found to be the best desorption agent in the batch study (Section 4.3.10). Prior to that, The Cr-laden SCAIM column was completely saturated with Cr after being treated with 50 ppm Cr(VI) at the inlet flow rate of 1.0 ml/min. In the column desorption study, the SCAIM column saturated with Cr was regenerated by having 2 M $HNO_3$ solution pass at a flow rate of 0.25 ml/min through the exhausted column, and the Cr(VI) and total Cr concentrations of the outlet samples from the column were analyzed by the ultraviolet-visible (UV-vis) spectrometry and inductive coupled plasma optical emission spectrometry (ICP-OES), respectively. The results of UV-vis spectrometry confirmed that all the desorbed Cr was in the form of Cr(III), so the Cr(III) concentrations of the outlet solutions were analyzed using the ICP-OES with suitable dilution. Figure 4-30 shows the Cr desorption profile from the Cr-laden SCAIM column. It can be seen that almost 100% of Cr desorption was achieved in 3000 $cm^3$ of the desorption solution. Extremely high (8490 ppm) Cr(III) concentration was obtained in the eluent at the 0.7 BV, so the SCAIM column could be used to remove and recover Cr from the Cr-laden wastewater. As discussed in the batch desorption study in Section 4.3.10, the 2 M $HNO_3$ solution was effective in Cr(III) desorption due to the low Cr(III) binding affinity in acidic conditions.

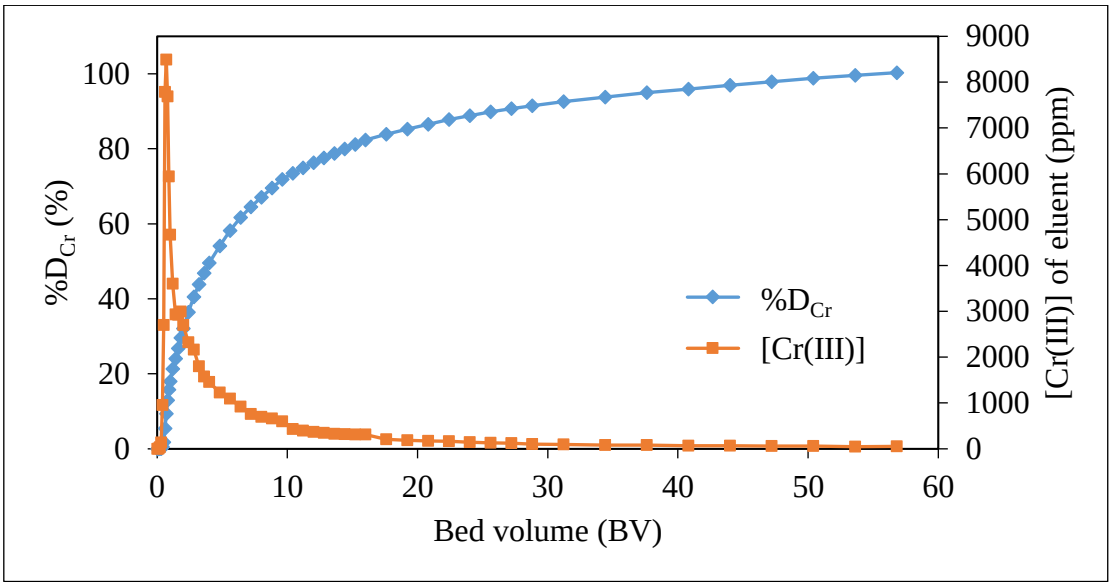


Figure 4-30 Cr desorption profile of Cr-laden SCAIM column using 2M $HNO_3$ solution. (Experimental conditions: **adsorption**, $[Cr(VI)]_0$ = 50 ppm, flow rate = 1.0 ml/min, pH 2, temperature = 22.5°C; **desorption**, desorption agent = 2 M $HNO_3$ solution, flow rate = 0.25 ml/min, temperature = 22.5°C)

# 4.5 Removal of Cr(VI) by silica-doped zirconium-alginate-immobilized *M. rouxii*

## 4.5.1 Screening of anionic pollutants

Silica-doped zirconium-alginate-immobilized *M. rouxii* (SZAIM) was prepared by immersing SCAIM in 4% zirconyl chloride solution for 24 h. The divalent Ca(II) ions in SCAIM were replaced by the tetravalent Zr(IV) ions through the ion-exchange mechanism. Tetravalent Zr(IV) cations in SZAIM beads would have a strong affinity towards anionic pollutants. In this study, the adsorption abilities of silica-doped zirconium-alginate-immobilized *M. rouxii* (SZAIM) to the five different anionic pollutants (Cr(VI), As(V), As(III), $PO_4^{3-}$ and $F^-$) were evaluated in batch adsorption mode. As shown in Figure 4-31, the adsorption capacity of SZAIM for removing Cr(VI), As(V), As(III), $PO_4^{3-}$ and $F^-$ was 169.6 ± 2.6, 52.39 ± 1.10, 10.39 ± 1.84, 21.67 ± 0.27 and 111.5 ± 17.7 mg/g, respectively. Generally, SZAIM exhibited improved adsorption capacity to the five tested anionic pollutants compared with SCAIM (Figure 4-5). It was because the anions possessed stronger affinity to the tetravalent Zr(IV) in the zirconium alginate than the divalent Ca(II) in calcium alginate. Based on the adsorption results, SZAIM showed preferential adsorption to Cr(VI) among the five tested anionic pollutants. In the following sections, the Cr(VI) removal performance of SZAIM was optimized with several factors including contact time, pH and initial Cr(VI) concentration. Furthermore, SZAIM beads exhibited high fluoride adsorption capacity of 111.5 ±17.7 mg/g,

but it was less effective in removing As(III), As(V) and phosphate from the aqueous phase.

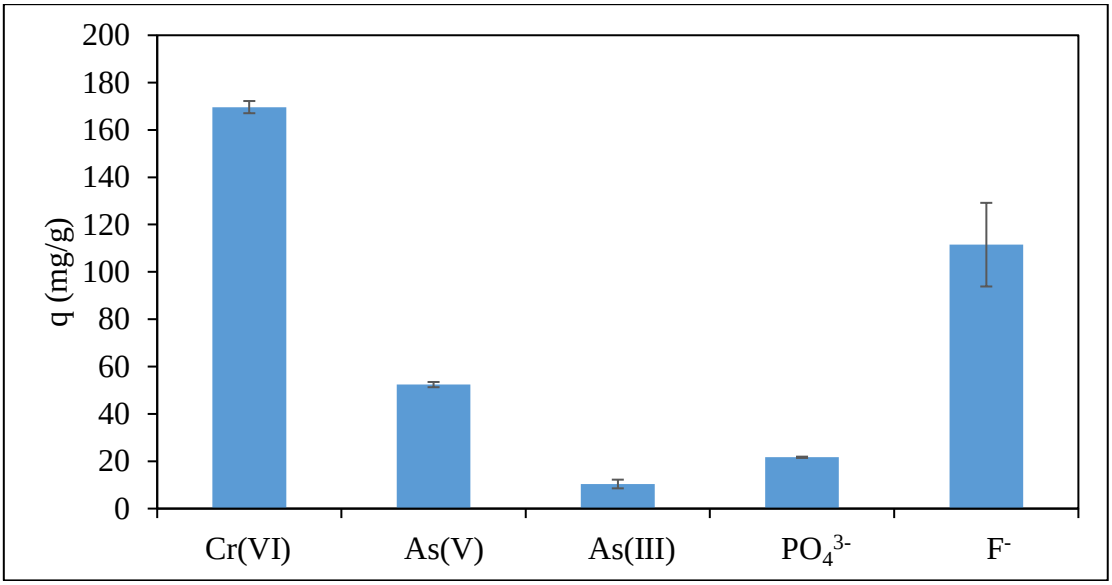


Figure 4-31 Screening results of five anionic pollutants by SZAIM. (Experimental conditions: $[Cr(VI)]_0$ = 500 ppm, adsorbent dosage = 1 g/L, t = 3 d, temperature = 25ºC and agitation = 250 rpm)

### 4.5.2 Effect of pH

Figure 4-32 illustrates the effect of solution pH on percentage Cr(VI) removal (%$Cr(VI)_{re}$) and percentage total Cr adsorption (%$Cr_{ads}$) of SZAIM. At pH 7.0, the %$Cr(VI)_{re}$ of SZAIM was only 37.47 ± 1.87%, however, it gradually increased with decreasing solution pH and reached a maximum of 92.28 ± 0.13% at pH 2.0. At the same time, the equilibrium Cr(VI) concentrations reduced from 68.01 ± 2.04 to 8.38 ± 0.09 ppm as the solution pH decreased from 7.0 to 2.0. The anionic Cr(VI) ions bound onto the tetravalent Zr(IV) cations in zirconium alginate, the protonated amine groups in the immobilized *M. rouxii* and the protonated ethylenediamine groups on the silica through the strong electrostatic attraction. In addition, the %$Cr_{ads}$ of SCAIM also increased with decreasing pH from 7.0 to 4.0 in the same manner, indicating the absence of Cr(III) release under neutral to a weakly acidic environment. The absence of Cr(III) release might be due to the low availability of protons for both adsorption-coupled reduction of Cr(VI) and desorption of Cr(III) through the ion-exchange mechanism. However, when pH further decreased from 4.0 to 1.0, the %$Cr_{ads}$ of SZAIM drastically dropped from 83.03 ± 0.08% to 33.77 ± 1.38%, while the concentration of Cr(III) increased from 8.34 ± 0.03 to 59.23 ± 1.26 ppm. This was because the acidic aqueous solution contained a high concentration of protons, which was favorable to the adsorption-coupled reduction of Cr(VI) and the subsequent release of the reduced Cr(III) from the adsorbent surface.

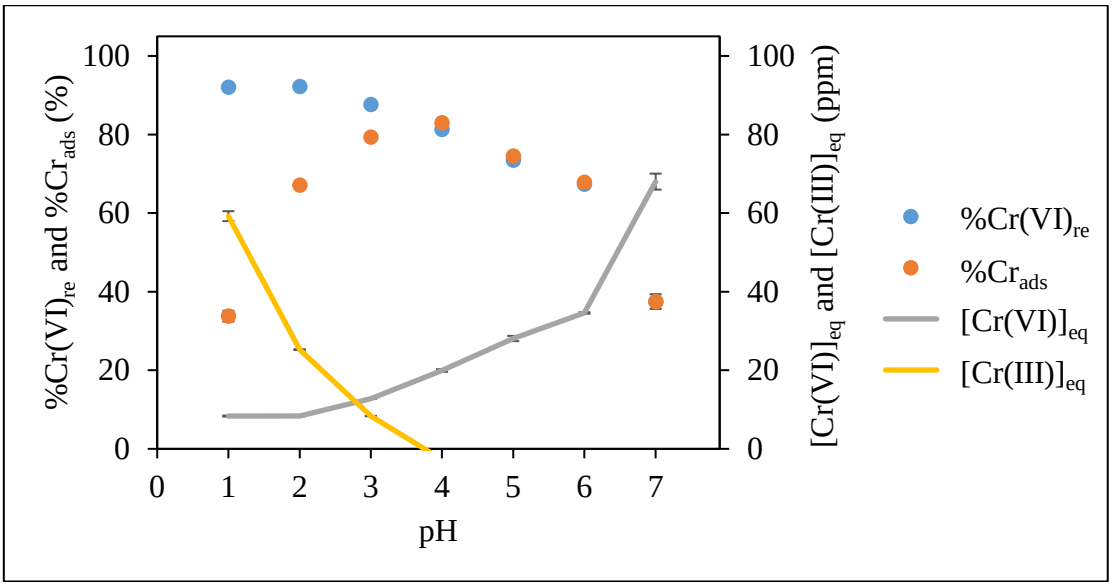


Figure 4-32 Effect of pH on the $\%Cr(VI)_{re}$ and $\%Cr_{ads}$ on SZAIM. (Experimental conditions: $[Cr(VI)]_0$ = 100 ppm, adsorbent dosage = 10 g/L, t = 3 d, pH 1 - 7, temperature = 25ºC and agitation = 250 rpm)

### 4.5.3 Effect of contact time and kinetic modelling

The effect of contact time on the percentage Cr(VI) removal ($\%Cr(VI)_{re}$) and percentage total Cr adsorption ($\%Cr_{ads}$) of SZAIM beads were investigated at pH 2.0, the adsorbent dosage of 10 g/L and initial Cr(VI) concentration of 100 ppm. Figure 4-33 shows the kinetic profiles of percentage Cr(VI) removal ($\%Cr(VI)_{re}$) and percentage Cr adsorption ($\%Cr_{ads}$) by SZAIM, as well as the concentration profiles of Cr(VI) and Cr(III). It can be observed that the $\%Cr(VI)_{re}$ and $\%Cr_{ads}$ values dramatically increased in the first 2 h, with over 70% of the $\%Cr(VI)_{re}$ and $\%Cr_{ads}$ achieved in 2 h, and the $\%Cr(VI)_{re}$ and $\%Cr_{ads}$ gradually increased afterward. Finally, the $\%Cr_{ads}$ reached a plateau at 9 h, while the $\%Cr(VI)_{re}$ could not attain equilibrium on Day 3.

Figure 4-33 also plotted the concentration profiles of Cr(VI) and Cr(III). The Cr(VI) was rapidly removed in the first 2 h, and the amount of Cr(III) release was insignificant during this period. The rapid removal of Cr(VI) in the initial period indicated the strong electrostatic interaction between the anionic Cr(VI) ions and the tetravalent cationic Zr(IV) in the SZAIM. Moreover, the positively-charged surface groups on the biomass surface and the ethylenediamine-functionalized silica also made an important contribution to the Cr(VI) adsorption as discussed in Section 4.3.1.

In addition, the Cr(VI) removal capacity ($Q_{Cr(VI)}$) and total Cr adsorption capacity ($q_{tot}$) of SZAIM were investigated as a function of time at pH 2.0, adsorbent dosage of 1 g/L and initial Cr(VI) concentration of 50 ppm. The experimental kinetic data are presented in Figure 4-34a.

It can be seen that the $Q_{Cr(VI)}$ and $q_{tot}$ values rapidly increased within the first 2 h. The rate of Cr adsorption decreased gradually, and the total Cr adsorption equilibrium was attained at 6 h. Additionally, no Cr(III) was released back to the solution phase within the first 6 h since the $Q_{Cr(VI)}$ and $q_{tot}$ values were almost the same within this period. A significant amount of Cr(III) was detected in the aqueous phase after 6 h, and the concentration of Cr(III) increased with increasing contact time. The Cr(III) was possibly desorbed from the SZAIM surface by high concentration of proton presenting in the acidic adsorption environment.

The Cr(VI) removal kinetics of SZAIM beads was simulated by five different nonlinear kinetic models, namely pseudo-first-order, pseudo-second-order, Elovich, fractional power and intra-particle diffusion models. The resulting kinetic modelling curves are illustrated in Figure 4-34b. Table 4-10 lists and compares the kinetic modelling results for the Cr(VI) removal by SZAIM with those by MR biomass and SCAIM. The modelling results show that the pseudo-second-order kinetics was the best-fit model to describe the Cr(VI) removal kinetics on SZAIM because of the lowest RMSE value (1.231 ± 0.008) and highest correlation coefficient (0.990 ± 0.003**)**. The pseudo-second-order kinetic constant, $k_2$, of SZAIM (7.05E-4 ± 4.27E-7 g/mg-min) was significantly larger than that of SCAIM (1.10E-4 ± 1.27E-6 g/mg-min). The fast Cr(VI) removal rate of SZAIM could be explained by the strong affinity between the anionic Cr(VI) and tetravalent Zr(IV) in zirconium alginate. In addition, the intra-particle diffusion model failed to simulate the Cr(VI) removal kinetics of SZAIM, indicating that the Cr(VI)

removal by SZAIM was not controlled only by the intra-particle diffusion.

The leaching of Zr(IV) from SZAIM to the aqueous phase was insignificant within the 3-day Cr(VI) removal experiment. The trivalent Cr(III) and the proton could not desorbed the tetravalent Zr(IV) in SZAIM, which strongly bound to the carboxylic acid groups of alginate. In fact, there is no study that reports the carcinogenic effect of zirconium in human, rat and mice. The SZAIM is a nontoxic and safe adsorbent for the removal Cr(VI) from wastewater.

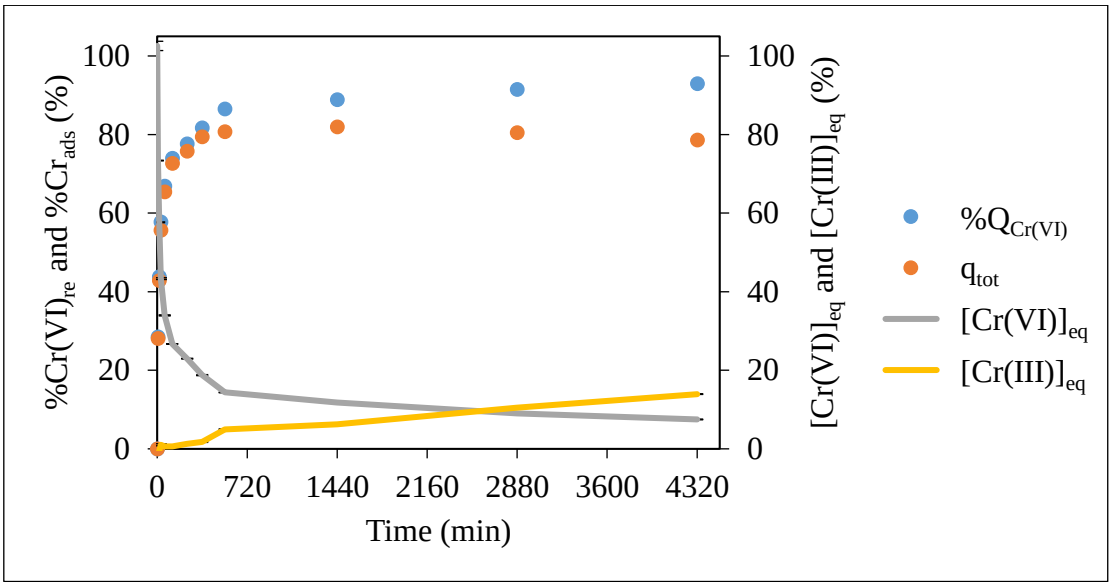


Figure 4-33 Cr(VI) removal kinetics and total Cr adsorption kinetics of SZAIM. (Experimental conditions: $[Cr(VI)]_0$ = 100 ppm, adsorbent dosage = 10 g/L, t = 3 d, pH 2, temperature = 25°C and agitation = 250 rpm)

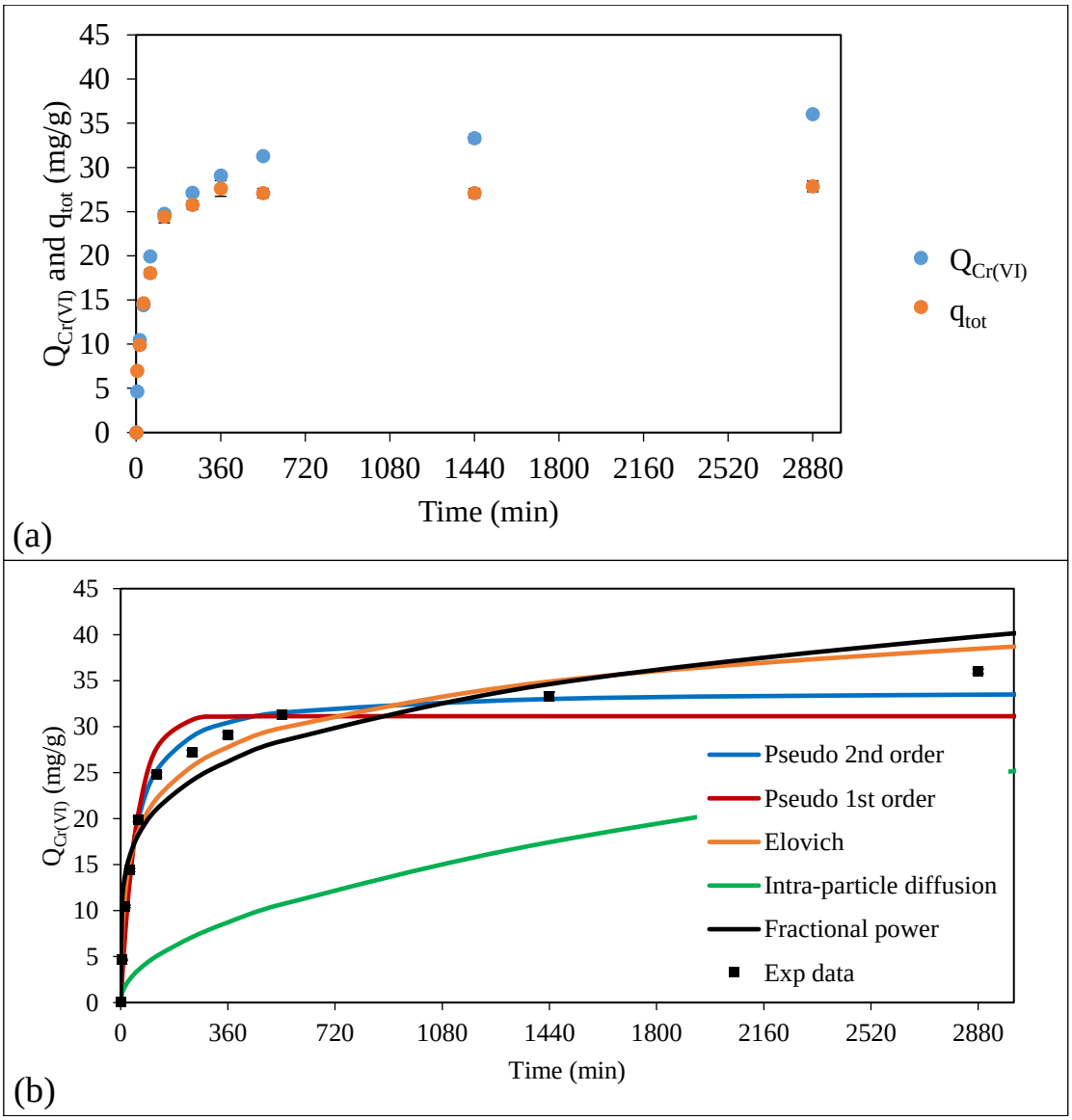


Figure 4-34 (a) Cr(VI) removal kinetics and total Cr adsorption kinetics of SZAIM; and (b) Cr(VI) removal kinetic modelling curves of SZAIM. (Experimental conditions: $[Cr(VI)]_0$ = 50 ppm, adsorbent dosage = 1 g/L, t = 3 d, pH 2, temperature = 25ºC and agitation = 250 rpm)

Table 4-10 Kinetic modelling parameters for Cr(VI) removal by MR, SCAIM and SZAIM.

| Pseudo 1st order | $k_1$ (1/min) | $q_e$ (mg/g) | $R^2$ | RMSE |
|---|---|---|---|---|
| MR* | 3.91E-3 | 47.52 | 0.691 | 10.45 |
| SCAIM* | 2.40E-3 ± 1.41E-6 | 26.09 ± 0.11 | 0.877 ± 0.004 | 3.453 ± 0.039 |
| SZAIM | 1.82E-2 ± 1.48E-4 | 31.13 ± 0.27 | 0.953 ± 0.004 | 2.626 ± 0.010 |
| Pseudo 2nd order | $k_2$ (g/mg-min) | $q_e$ (mg/g) | $R^2$ | RMSE |
| MR* | 1.15E-4 | 50.92 | 0.763 | 9.101 |
| SCAIM* | 1.10E-4 ± 1.27E-6 | 29.04 ± 0.16 | 0.923 ± 0.003 | 2.728 ± 0.041 |
| SZAIM | 7.05E-4 ± 4.27E-7 | 33.96 ± 0.28 | **0.990 ± 0.003** | **1.231 ± 0.008** |
| Elovich | b (g/mg) | a (mg/g-min) | $t_0$ (min) | $R^2$ | RMSE |
| MR* | 0.130 | 1.396 | 5.532 | 0.861 | 6.943 |
| SCAIM* | 0.188 ± 0.002 | 0.248 ± 0.005 | 21.43 ± 0.64 | 0.974 ± 0.001 | 1.583 ± 0.027 |
| SZAIM | 0.194 ± 0.001 | 3.098 ± 0.070 | 1.666 ± 0.027 | 0.978 ± 0.002 | 1.789 ± 0.005 |
| Fractional Power | $k_f$ (mg/g-min$^{vf}$) | v | $k_f v$ (mg/g-min) | $R^2$ | RMSE |
| MR* | 8.121 | 0.226 | 1.835 | **0.974** | **4.298** |
| SCAIM* | 2.123 ± 0.008 | 0.318 ± 0.001 | 0.630 ± 0.004 | **0.999 ± 0.003** | **0.340 ± 0.034** |
| SZAIM | 8.023 ± 0.108 | 0.201 ± 0.006 | 1.613 ± 0.022 | 0.923 ± 0.004 | 3.366 ± 0.020 |
| Intra-particle diffusion | $k_{diff}$ (mg/g-min$^{0.5}$) | | $R^2$ | RMSE | |
| MR* | 0.097 | | 0.615 | 21.97 | |
| SCAIM* | 0.280 ± 0.004 | | 0.893 ± 0.005 | 5.429 ± 0.020 | |
| SZAIM | 0.460 ± 0.004 | | 0.752 ± 0.006 | 16.20 ± 0.176 | |

* The simulation results of MR and SCAIM were presented in Section 4.3.3.

### 4.5.4 Effect of initial concentration and isotherm modelling

The effect of initial Cr(VI) concentration on the percentage Cr(VI) removal ($\%Cr(VI)_{re}$) and percentage total Cr adsorption ($\%Cr_{ads}$) of SZAIM are illustrated in Figure 4-35a. The $\%Cr(VI)_{re}$ and $\%Cr_{ads}$ values decrease with an increase of initial Cr(VI) concentration. Meanwhile, the total Cr adsorption isotherm was determined by plotting the total Cr adsorption capacity ($q_{tot}$) versus the equilibrium Cr concentration ($C_e$). Five isotherm models, namely Langmuir, Freundlich, Tempkin, Dubinin-Radushkevich and Sips isotherm models, were employed to simulate the experimental isotherm results. Figure 4-35b displays the isotherm modelling curves, and Table 4-11 reports the modelling parameters. Both the Sips and Langmuir isotherm models showed the lowest RMSE value (1.244 ± 0.083) and the highest correlation coefficient (0.998 ± 0.004). It was because the Sips exponent ($m_s$) was equal to 1, indicating that the Sips model was reduced to the Langmuir model. Therefore, the best-fit model was the Langmuir model, and the total maximum Cr adsorption capacity ($q_{max}$) was 90.62 ± 4.11 mg/g, which was higher than that of SCAIM (78.15 ± 4.79 mg/g). The improved $q_{max}$ value of SZAIM suggested that the Zr(IV) in SZAIM beads would take part in the Cr(VI) adsorption.

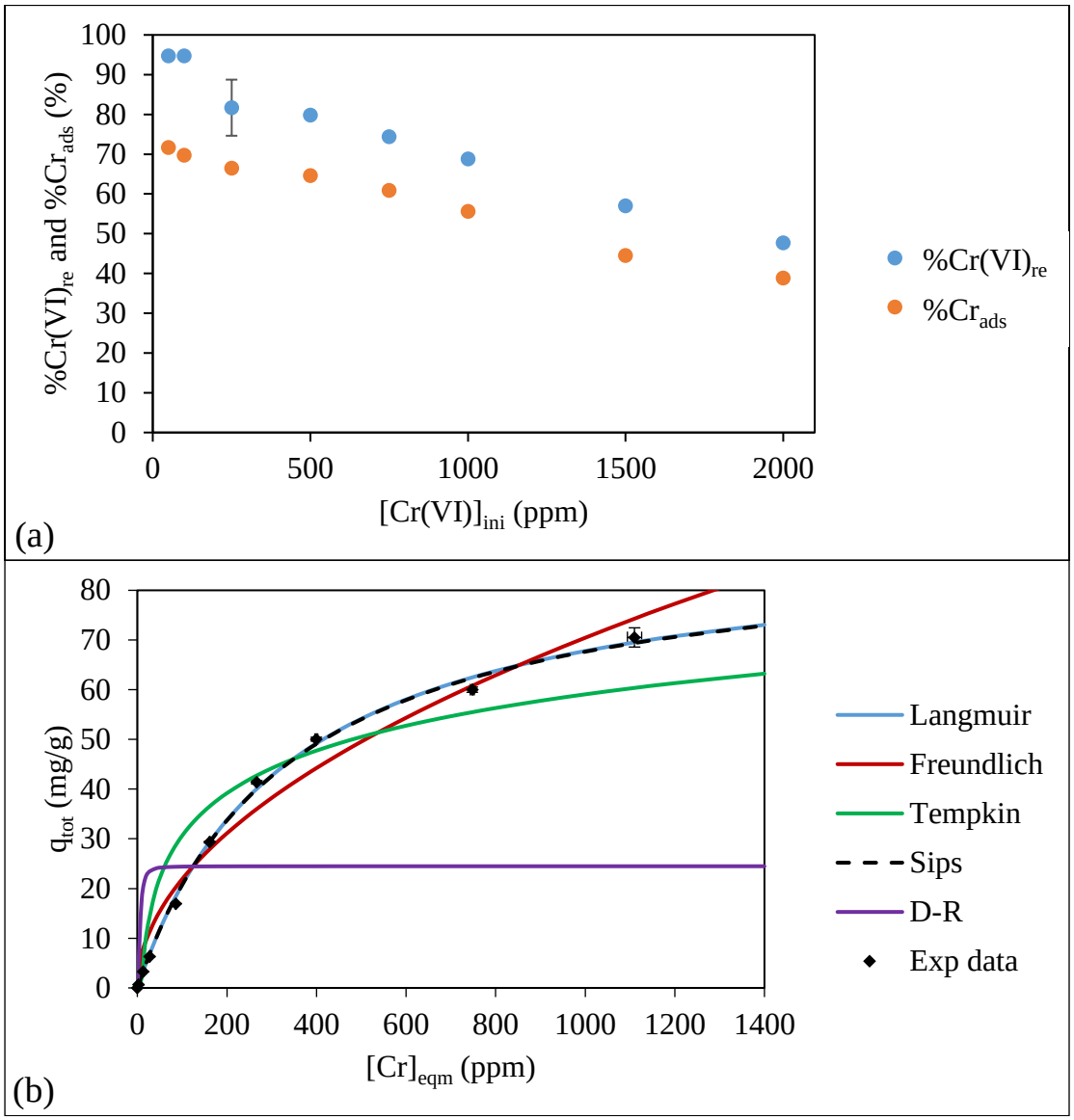


Figure 4-35 (a) Effect of initial Cr(VI) concentration on $\%Cr(VI)_{re}$ and $\%Cr_{ads}$ of SZAIM; and (b) total Cr adsorption isotherm modelling curves of SZAIM. (Experimental conditions: $[Cr(VI)]_0$ = 10 - 2000 ppm, adsorbent dosage = 10 g/L, t = 3 d, pH 2, temperature = 25°C and agitation = 250 rpm)

Table 4-11 Isotherm modelling parameters for total Cr adsorption on MR, SCAIM and SZAIM.

| Langmuir | $q_{max}$ (mg/g) | $K_L$ | $R^2$ | RMSE |
|---|---|---|---|---|
| MR* | 80.21 ± 6.05 | 5.76E-3 ± 5.72E-4 | 0.996 ± 0.002 | 1.207 ± 0.251 |
| SCAIM* | 78.15 ± 4.79 | 2.32E-3 ± 1.71E-4 | 0.995 ± 0.001 | 1.610 ± 0.029 |
| SZAIM | 90.62 ± 4.11 | 2.97E-3 ± 2.56E-4 | **0.998 ± 0.002** | **1.244 ± 0.083** |
| Freundlich | $K_F$ (mg/g) | n | $R^2$ | RMSE |
| MR* | 1.665 ± 0.136 | 1.640 ± 0.057 | 0.993 ± 0.002 | 1.709 ± 0.238 |
| SCAIM* | 1.594 ± 0.078 | 1.952 ± 0.049 | 0.988 ± 0.002 | 2.563 ± 0.136 |
| SZAIM | 2.110 ± 0.157 | 1.969 ± 0.055 | 0.977 ± 0.004 | 4.255 ± 0.291 |
| Tempkin | $b_T$ (J/mol) | $K_T$ (L/g) | $R^2$ | RMSE |
| MR* | 188.3 ± 7.6 | 0.112 ± 0.005 | 0.936 ± 0.004 | 4.230 ± 0.281 |
| SCAIM* | 276.8 ± 9.86 | 0.177 ± 0.005 | 0.850 ± 0.004 | 8.424 ± 0.408 |
| SZAIM | 200.5 ± 3.00 | 0.119 ± 0.002 | 0.891 ± 0.006 | 8.557 ± 0.405 |
| D-R | Q (mg/g) | $B_D$ ($mol^2/kJ^2$) | $R^2$ | RMSE |
| MR* | 37.98 ± 0.66 | 3.36E-6 ± 5.69E-8 | 0.854 ± 0.012 | 18.09 ± 0.57 |
| SCAIM* | 20.66 ± 0.36 | 1.48E-6 ± 7.30E-8 | 0.578 ± 0.001 | 21.15 ± 0.76 |
| SZAIM | 24.48 ± 0.09 | 5.43E-6 ± 2.14E-8 | 0.609 ± 0.002 | 24.97 ± 0.52 |
| Sips | $n_m$ (L/mg) | $K_s$ (L/g) | $m_s$ | $R^2$ | RMSE |
| MR* | 6.94E-3 ± 8.4E-4 | 0.652 ± 0.023 | 0.903 ± 0.003 | **0.997 ± 0.002** | **1.147 ± 0.259** |
| SCAIM* | 4.24E-3 ± 1.2E-4 | 0.400 ± 0.029 | 0.838 ± 0.017 | **0.997 ± 0.001** | **1.361 ± 0.043** |
| SZAIM | 2.97E-3 ± 2.55E-4 | 0.269 ± 0.010 | 1.000 ± 0.000 | **0.998 ± 0.004** | **1.244 ± 0.082** |

* The simulation results of SCAIM was presented in Section 4.3.6.

## 4.6 Characterizations of immobilized *M. rouxii*

### 4.6.1 Fourier-transform Infrared spectroscopy (FTIR)

Fourier-transform infrared (FTIR) spectra were obtained in order to identify the functional groups on the surface of adsorbents and elucidate their Cr(VI) removal mechanism. Figure 4-36 compares the FTIR spectra of the MR, Cr-MR, sodium alginate, CA, CAIM, SCAIM, Cr-SCAIM, ZA, ZAIM and SZAIM, while Table 4-12 lists the assignments of FTIR bands.

In the FTIR spectrum of the *M. rouxii* (MR), the broad signal at 3300 - 3400 $cm^{-1}$ represented the O-H stretching of the hydroxyl groups and the N-H stretching of the amine and amide groups (Ozer et al., 2012). The C-H stretching signal was observed at 2927 $cm^{-1}$, while the peak at 1650 $cm^{-1}$ was associated with the asymmetric stretching of carboxylate groups and the C=O stretching of amide groups (amide I) (Ramrakhiani et al., 2011). The vibrational frequency 1540 $cm^{-1}$ was assigned to the N-H bending of the amide groups (amide II) on the biomass materials (e.g., chitin, chitosan) (Smith, 1999). The signal at 1400 $cm^{-1}$ corresponded to the symmetric stretching of carboxylate groups (Costa et al., 2018). The peak at 1240 $cm^{-1}$ could be assigned to the C-N stretching of amide groups (amide III) and the C-O-C stretching of ether groups (Deng and Ting, 2005). The peak at 1150 $cm^{-1}$ could be attributed to the C-OH stretching of secondary alcohols, while the C-OH stretching of the primary alcohols appeared between 1080 to 1030 $cm^{-1}$ (Smith, 1999). The peak at 990 $cm^{-1}$ was assigned to the C-C-C stretching of secondary alcohols (Smith, 1999). The abovementioned FTIR signals suggested

the existence of hydroxyl, carboxyl, amine and amide groups in the MR. After Cr uptake, the asymmetric stretching of carboxylate groups in the MR shifted to lower wavenumber, suggesting the involvement of the carboxylate groups on the MR in the formation of a complex with Cr(III) ions. Moreover, the C-C-C stretching of the secondary alcohols at 990 $cm^{-1}$ disappeared after the Cr uptake. The secondary alcohols groups were consumed during the reduction of Cr(VI) and were oxidized to ketone groups.

The FTIR spectrum of CA also displayed the intense peak at 3400 ± 50 $cm^{-1}$, which corresponded to the O-H stretching of the hydroxyl groups in the alginate chains. The C-H stretching of aliphatic carbon was found at 2930 $cm^{-1}$. The peaks at 1600 and 1420 $cm^{-1}$ were assigned to the asymmetric and symmetric stretching bands of the carboxylate groups, respectively. The peaks at 1080 and 1030 $cm^{-1}$ were attributed to the C–O stretching vibration of the pyranosyl ring in the alginate (Daemi and Barikani, 2012). These signals indicated that the alginate chains contained a large number of carboxylate and hydroxyl groups.

After immobilizing the MR into the calcium alginate, the CAIM and SCAIM displayed similar spectra to that of CA. The characteristic peaks of hydroxyl, aliphatic carbon and carboxylate groups could be observed at 3410, 2920, 1640, 1420, 1080 and 1030 $cm^{-1}$. Meanwhile, there was an extra peak at 1540 $cm^{-1}$ in the spectrum of CAIM, which belonged to the N-H bending stretching signal of the amide groups in the immobilized MR. This signal affirmed the successful immobilization of MR in the calcium alginate. Moreover, the presence

of biomass in the SCAIM was confirmed by the shoulder at around 1540 $cm^{-1}$, which was shielded by the broad C=O stretching peak due to the carboxylate group from the alginate and the immobilized biomass. Nonetheless, the SCAIM should be rich in nitrogen functional groups, such as the amine and amide groups in the immobilized MR and the ethylenediamine groups in the doped silica. The existence of amine groups in the SCAIM was further confirmed by the XPS analysis (Section 4.6.3). The asymmetric stretching of carboxylate groups in the SCAIM displayed a negative shifting in wavenumber after Cr uptake, suggesting the interaction between the Cr(III) and the carboxylate groups on the immobilized MR and the alginate chains.

Zirconium-alginate-based adsorbents (i.e., ZA, ZAIM and SZAIM) were prepared by replacing the divalent Ca(II) ions in the corresponding calcium-alginate-based adsorbents (e.g. CA, CAIM and SCAIM) with the tetravalent Zr(IV) ions. The FTIR spectra revealed that the major functional groups present in the ZA, ZAIM and SZAIM were very similar to those in the CA, CAIM and SCAIM (Zhou et al., 2015).

The multivalent cations (e.g. Ca(II) and Zr(IV)) are crucial crosslinking agents that interacted with the carboxylate groups of the alginate chains. There are basically four binding configurations (Figure 4-37): (1) ionic interaction or uncoordinated form, (2) monodentate coordination, (3) bidentate coordination and (4) bidentate bridging coordination (Nakamoto, 2009; Papageorgiou et al., 2010). The separation of the asymmetric stretching and symmetric stretching vibrations of the carboxylate groups ($\Delta v = v_{asym} - v_{sym}$) is correlated to the binding

structure of the metal-carboxylate complex. If $\Delta v(COO^-)_{complex} << \Delta v(COO^-)_{Na}$, the bidentate chelating coordination is suggested. If $\Delta v(COO^-)_{complex} \approx \Delta v(COO^-)_{Na}$, the bidentate bridging coordination is suggested. If $\Delta v(COO^-)_{complex} << \Delta v(COO^-)_{Na}$, the monodentate coordination is suggested.

The $\Delta v(COO^-)_{complex}$ values of CA, CAIM, SCAIM, ZA, ZAIM and SZAIM were calculated to be 187.3, 221.9, 234.2, 181.9, 217.4 and 228.6 $cm^{-1}$, respectively, while the $\Delta v(COO^-)_{Na}$ was 187.9 $cm^{-1}$. It was found that the $\Delta v(COO^-)_{complex}$ values of CA and ZA were similar to the $\Delta v(COO^-)_{Na}$, which suggested the formation of a bidentate bridging complex of the Ca(II) and Zr(IV) ions with the carboxylate groups in the alginate chains. However, the $\Delta v(COO^-)_{complex}$ values of the immobilized adsorbents (CAIM, SCAIM, ZAIM and SZAIM) were much larger than the $\Delta v(COO^-)_{Na}$, so the asymmetric monodentate complex was suggested. The structure of metal-carboxylate complex in the metal-alginate immobilized *M. rouxii* would be different from that in the pure metal alginate because the carboxylate groups of the immobilized MR would also coordinate with the metal cations. In addition, the $\Delta v(COO^-)_{complex}$ values of the Cr-laden SCAIM and Cr-laden MR were 231.3 and 253.6 $cm^{-1}$, respectively, which were larger than the $\Delta v(COO^-)_{Na}$. These results suggested that the Cr(III) ions would also form a monodentate complex with the carboxylate groups on the alginate and biomass surface. The Ca(II) ions in the SCAIM were replaced by the Cr(III) ions through the ion-exchange mechanism because the carboxylate groups of alginate showed stronger binding

affinity to the trivalent Cr(III) than the divalent Ca(II) (Menakbi et al., 2016). That explained the observation of Ca(II) leakage from the SCAIM in the Cr(VI) removal studies.

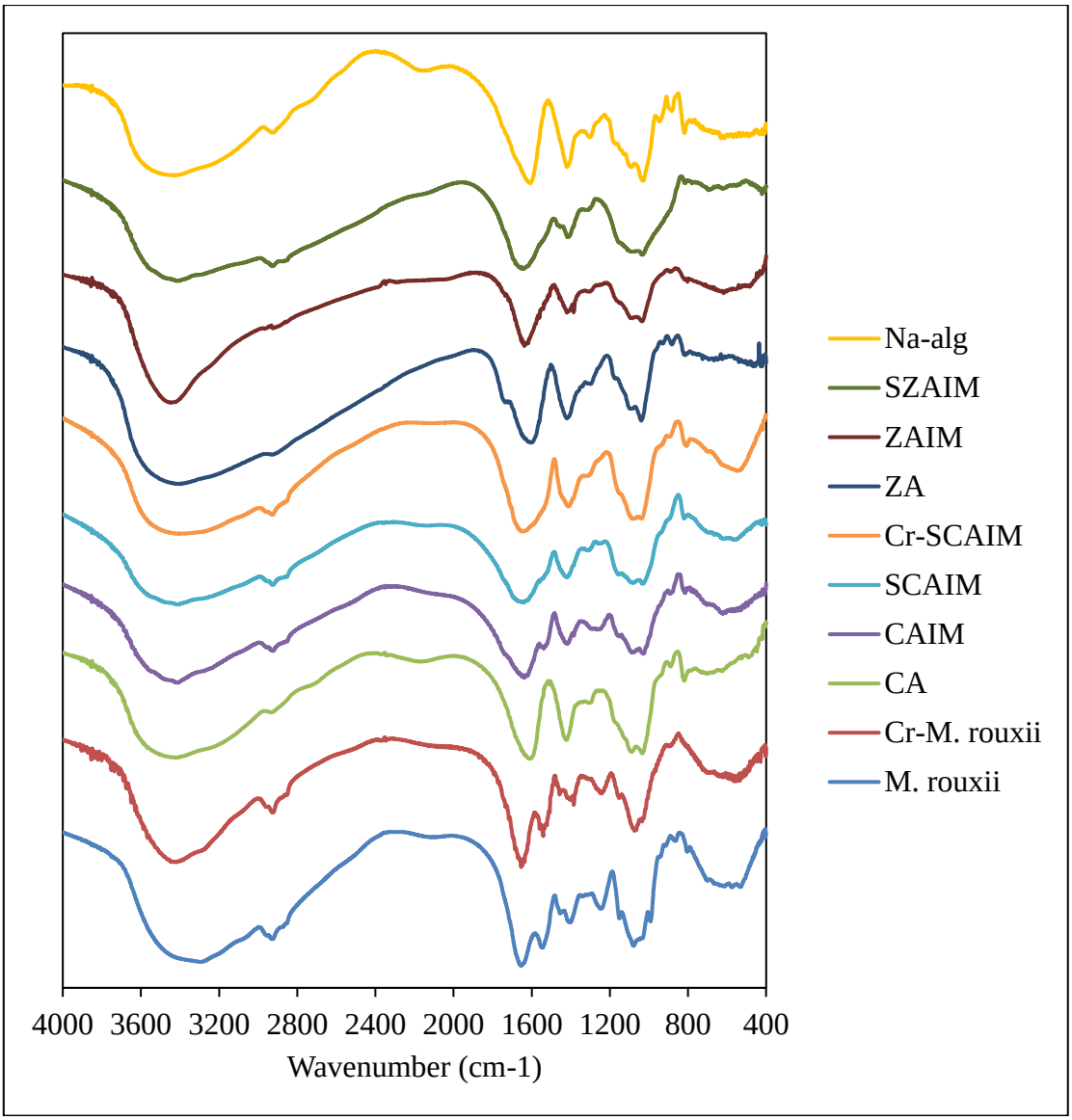


Figure 4-36 FTIR spectra of the freely suspended and immobilized *M. rouxii*.

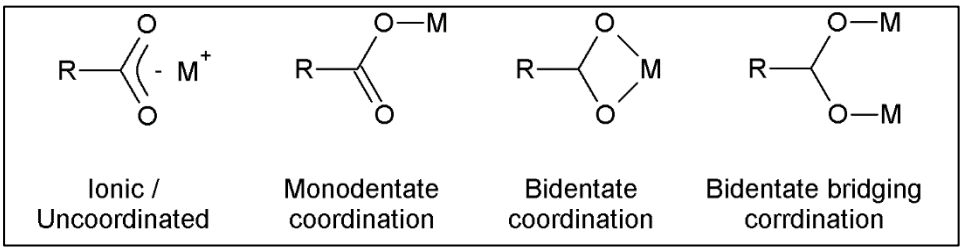


Figure 4-37 Possible binding structures of the metal-carboxylate complex.

Table 4-12 Assignment table of the FTIR signals of different adsorbents.

| *M. rouxii* | Cr-*M. rouxii* | CA | CAIM | SCAIM | Cr-SCAIM | ZA | ZAIM | SZAIM | Na-alg | Assignment |
|---|---|---|---|---|---|---|---|---|---|---|
| 3300.4 | 3421.6 | 3448.1 | 3412.7 | 3413.3 | 3404.7 | 3417.7 | 3448.4 | 3412.4 | 3430.5 | O-H stretching / N-H stretching* |
| 2927.7 | 2925.1 | 2932.9 | 2924.4 | 2924.8 | 2927.5 | 2914.0 | 2920.0 | 2926.1 | 2932.8 | C-H stretching |
| 1655.0 | 1653.7 | 1607.7 | 1639.2 | 1652.2 | 1644.0 | 1601.4 | 1637.0 | 1644.9 | 1607.2 | Asymmetric stretching of carboxylate / C=O stretching of amide (amide I)* |
| 1544.9 | 1541.3 | / | 1539.0 | / | / | / | / | / | | N-H bending (amide II) |
| 1404.2 | 1400.1 | 1420.4 | 1417.3 | 1418.0 | 1412.8 | 1419.5 | 1419.6 | 1416.2 | 1419.23 | Symmetric stretching of carboxylate |
| 1245.9 | 1241.0 | / | / | / | / | / | / | / | | C-N stretching of amide (amide III)/ C-O-C stretching of ether |
| 1150.3 | 1151.3 | / | / | / | / | / | / | / | / | C-OH stretching of secondary alcohol |
| 1080.7 | 1073.7 | 1087.5 | 1087.6 | 1083.7 | 1080.6 | 1083.9 | 1083.2 | 1086.8 | 1090.2 | C-O stretching of primary alcohol |
| 1034.2 | 1035.6 | 1034.2 | 1027.5 | 1031.1 | 1038.2 | 1039.0 | 1034.7 | 1034.0 | 1030.1 | |
| 992.7 | / | / | / | / | / | / | / | / | | $CH_3$-C-$CH_3$ stretching of secondary alcohol |

* Only occur in the free and immobilized *M. rouxii*.

### 4.6.2 Scanning electron microscopy (SEM)

The surface morphology and elemental composition of dried CA, SCA, CAIM and SCAIM were investigated by the scanning electron microscopy (SEM). Figure 4-38a-b shows that the hydrogel structure of CA, SCA shrank after the removal of water by the drying process. The CAIM and SCAIM could retain the round shape (Figure 4-38c-d) since the vacancies between the alginate chains were filled up by the immobilized biomass. A large number of small particles with a diameter of ~5μm were observed on the surface of SCA, and they were most likely silica particles (Figure 4-38e). The silica particles contained some ethylenediamine groups, which could contribute to Cr(VI) adsorption.

The energy dispersive X-ray (EDX) spectroscopy (Figure 4-41 to 4-41) was employed to identify the principal elements on the surfaces of CA, SCA, CAIM, SCAIM, Cr-laden CAIM and Cr-laden SCAIM. The surface of CA contained C, O, Cl and Ca which were attributed to the alginate chains and calcium chloride. The absence of Na signal indicated the complete replacement of sodium ions in sodium alginate by calcium ions. In the EDA spectrum of SCA, a new Si peak was identified, indicating the successful doping of silica on the surface of CA beads. The N signal of the ethylenediamine groups in the doped silica could not be observed since it was covered by the strong C signal. After the immobilization of *M. rouxii* by calcium alginate, the new P and S signals in CAIM were contributed by the immobilized biomass materials. *M. rouxii* was rich in nitrogen, but the weak N signal was easily overlapped by the

strong C signal.

As shown in Figure 4-40, the SCAIM beads contained C, O, P, S, Ca, Cl and Si. The C, O, P and S signals were contributed by the immobilized biomass materials and the alginate, while the Ca and Cl signals were introduced during the calcium alginate immobilization step. The Si signal confirmed the successful doping of the silica particles on the SCAIM beads. Additionally, the Cr signals were observed in the EDX spectrum of the Cr-loaded CAIM and SCAIM, revealing the adsorption of Cr ions on the surface of CAIM and SCAIM beads. The oxidation state of the adsorbed Cr was further identified by XPS analysis, as reported in Section 4.6.3. It should be noted that the Ca peak disappeared after Cr adsorption, suggesting that the Ca(II) ions in the calcium alginate was replaced by the Cr(III) ions through the ion-exchange mechanism.

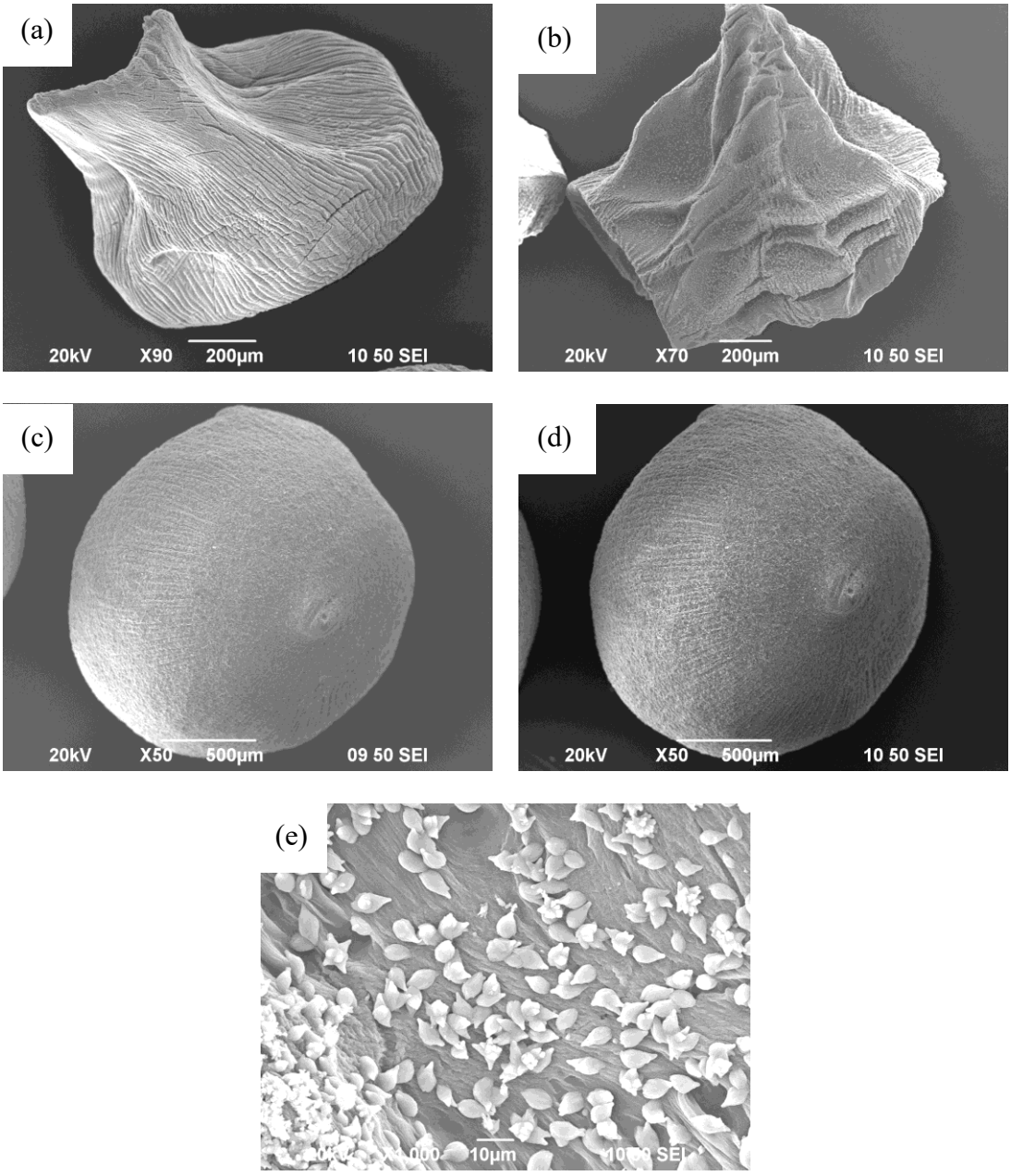


Figure 4-38 SEM images of (a) CA (x 90), (b) SCA (x 70), (c) CAIM (x 50), (d) SCAIM (x 50) and (e) the silica particles doped on SCA surface (x 1000).

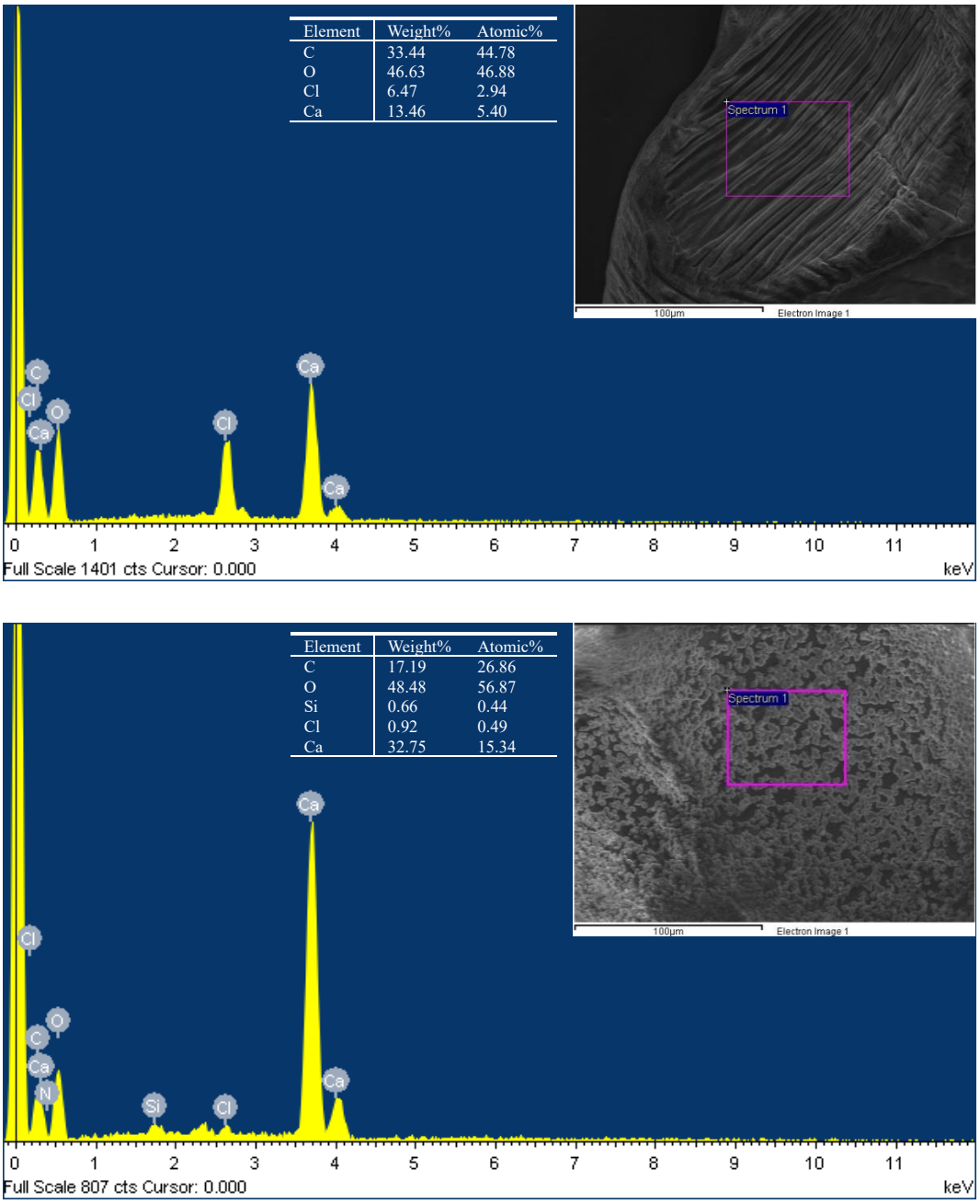


Figure 4-39 EDX spectra of pristine CA (Top) and SCA (Bottom).

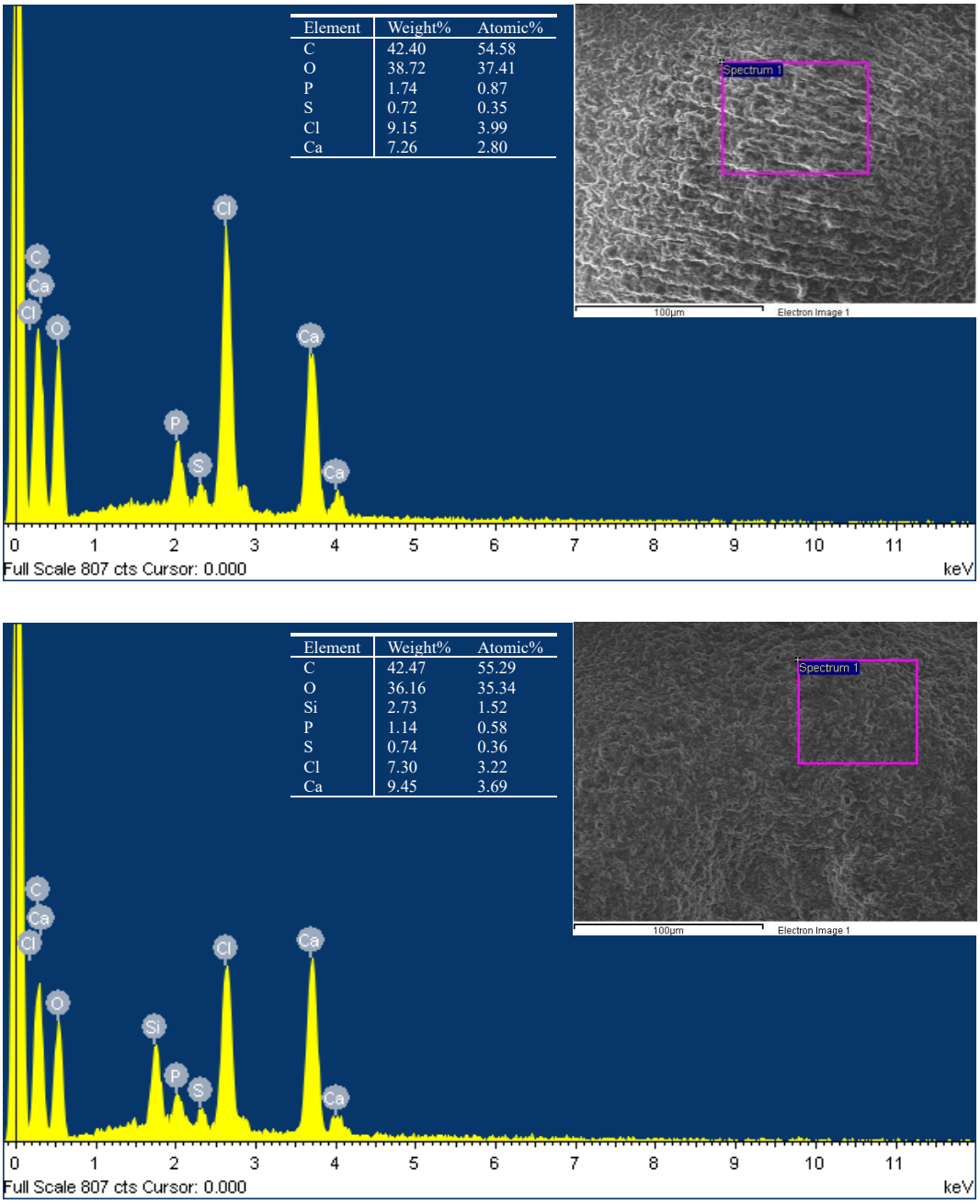


Figure 4-40 EDX spectra of pristine CAIM (Top) and SCAIM (Bottom).

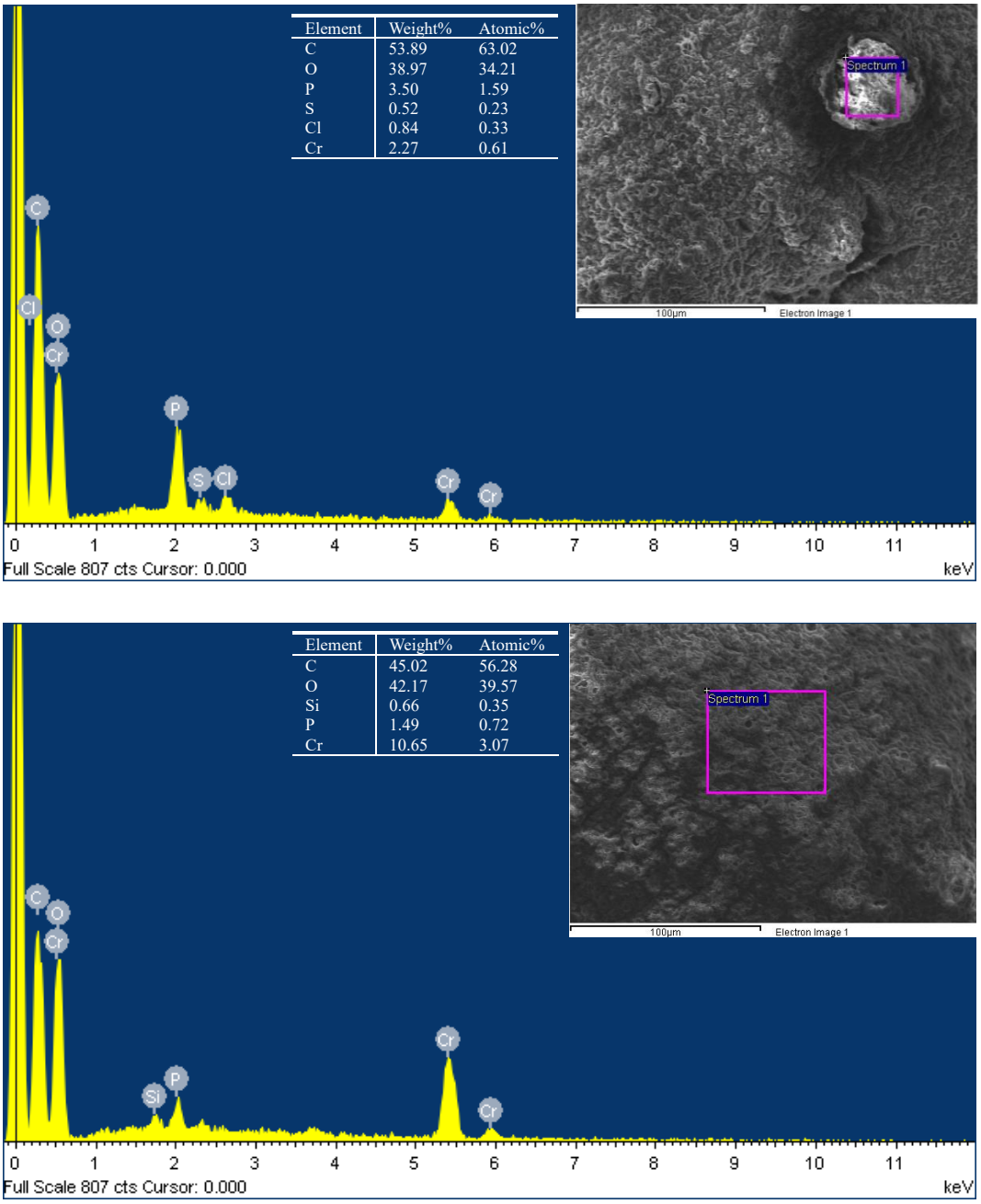


Figure 4-41 EDX spectra of pristine Cr-loaded CAIM (Top) and Cr-loaded SCAIM (Bottom).

### 4.6.3 X-ray photoelectron spectroscopy (XPS)

XPS is a powerful characterization technique to analyze the surface composition of adsorbents and determine the binding reaction between Cr(VI) and adsorbents. Figure 4-42 displays the wide scan XPS spectra of pristine and Cr-laden *M. rouxii*, while Table 4-13 summarizes the surface elemental compositions generated from the region information on the wide scan spectra. The wide scan XPS spectra of pristine *M. rouxii* (Figure 4-42a) confirmed the presence of C, N, O, and P on the surface of biomass. The Cr-laden *M. rouxii* was prepared by treating the biomass with pH 2.0 Cr(VI) solution for 3 days. A new peak at about 577 eV appeared in the Cr-laden *M. rouxii* (Figure 4-42b), which was attributed to the Cr 2p signal, proving that the chromium ions were adsorbed onto the surface of biomass under the acidic adsorption condition.

Figure 4-43 shows the high-resolution XPS spectra of the pristine MR, while Table 4-14 lists the binding energies of the samples and standard compounds. The high-resolution XPS spectra were then deconvoluted to identify the bonding configuration of C, N and O in the samples. The C1s spectrum of the pristine MR (Figure 4-43a) was resolved into four component peaks with the binding energies of 285.048, 286.524, 287.924 and 288.861 eV, which were assigned to the groups of C-C/H, C-O/N, C=O and O=C-O, respectively. The O1s spectrum (Figure 4-44a) could be divided into two components at 532.802 and 531.138 eV, representing the O-C and O=C, respectively. The deconvolution of C1s and O1s spectra

revealed the presence of hydroxyl, carbonyl and carboxyl groups on the surface of MR. The hydroxyl groups contributed to the Cr(VI)-reducing ability of MR, while the carboxyl acid groups would form a complex with the reduced Cr(III) ions. In addition, the high-resolution N1s spectrum revealed the presence of nitrogen atoms in two different configurations (Figure 4-43b). The resolved peaks at 400.114 and 401.920 eV were attributed to the $-NH_2$ (amine) and $-NH_3^+$ (protonated amine), respectively. The chitosan and proteins of the fungal biomass were rich in amine groups, which were partially protonated under acidic conditions. The protonated amine groups posed a positive charge and played an important role in the Cr(VI) adsorption through the electrostatic attraction. The P 2p spectra of pristine and Cr-laden *M. rouxii* (Figure 4-44b) displayed a distinct peak at 133.968 eV, which was assigned to the P-O group. No shifting in the binding energy was observed after Cr adsorption, indicating that the phosphate group would not participate in Cr adsorption.

Figure 4-45 displays the Cr2p3/2 and Cr2p1/2 signals of the Cr-laden MR at different contact time and solution pH. It could be seen that the Cr signals appeared after 1-minute contact with the Cr(VI) solution at pH 2, indicating a fast Cr adsorption on MR. The intensity of chromium signals increased with increasing contact time (Figure 4-45a), which indicated a continuous uptake of Cr on the biomass surface. The rapid Cr adsorption was the result of the strong electrostatic attraction between the anionic Cr(VI) ions and the protonated amine groups. In addition, the oxidation state of the adsorbed Cr was identified by comparing the binding

energies of the Cr-laden samples with those of standard Cr(III) and Cr(VI) compounds (e.g., $Cr(NO_3)_3$ and $Na_2CrO_4$). The binding energies of the Cr2p3/2 signal ranged from 577.7 to 578.1 eV, which was very close to the Cr(III) standards (578.408 eV). These results confirmed that all the adsorbed Cr on the MR surface was in the form of Cr(III). Moreover, the Cr(III) signal was even present in the sample was taken after 1-minute contact with Cr(VI) solution at pH 2, indicating that the adsorbed Cr(VI) ions were immediately reduced to Cr(III) ions once the Cr(VI) ions were adsorbed on MR surface. Furthermore, the Cr-laden MR samples were prepared under the weakly acidic (pH 4) and neutral (pH 7) environments (Figure 4-45b). The intensity of Cr2p signals in the pH 4 sample was lower than that in the pH 2 sample, whereas there was no Cr signal in the pH 7 sample. The mass concentrations of Cr on the surface of Cr-laden *M. rouxii* (Table 4-13) were consistent with the results of Cr(VI) removal studies that demonstrated the insignificant Cr adsorption on MR at pH 7 (Lo, 2013). It is worthy to note that the Cr(VI) reduction was also observed even at pH 4.

After the Cr adsorption on MR at pH 2, the O=C-O peak in the C1s spectrum and the O=C peak in the O1s spectrum shifted to higher binding energy (Table 4-14). The positive shifting indicated the complex formation between the reduced Cr(III) ions and the carboxyl groups on the MR surface. Additionally, there was no significant shifting in the $-NH_2$ and $-NH_3^+$ signals of the N1s spectrum after Cr adsorption since the nitrogen functional groups on the biomass surface did not interact with the Cr(III) ions. Under the typical acidic adsorption condition, the

protonated amine groups ($-NH_3^+$) formed an electrostatic interaction with the anionic Cr(VI) ions. However, the Cr(VI) ions were immediately reduced by electron-donor groups (such as hydroxyl and amine groups) (Tian et al., 2016; Luo et al., 2017; Yang et al., 2018). The reduced Cr(III) could no longer be adsorbed by the positively-charged $-NH_3^+$ groups and hence was released back to the solution phase due to the electrostatic repulsion.

Table 4-13 Surface compositions of pristine and Cr-laden *M. rouxii*.

| | Mass concentration (wt%) | | | | |
|---|---|---|---|---|---|
| | Cr2p | O1s | N1s | C1s | P2p |
| MR | 0 | 23.48 | 5.02 | 69.60 | 1.74 |
| Cr-MR (pH 2, 1 d) | 2.16 | 25.97 | 5.90 | 64.58 | 1.39 |
| Cr-MR (pH 4, 1 d) | 1.10 | 23.82 | 7.34 | 66.57 | 1.18 |
| Cr-MR (pH 7, 1 d) | 0.54 | 23.58 | 6.63 | 67.68 | 1.57 |

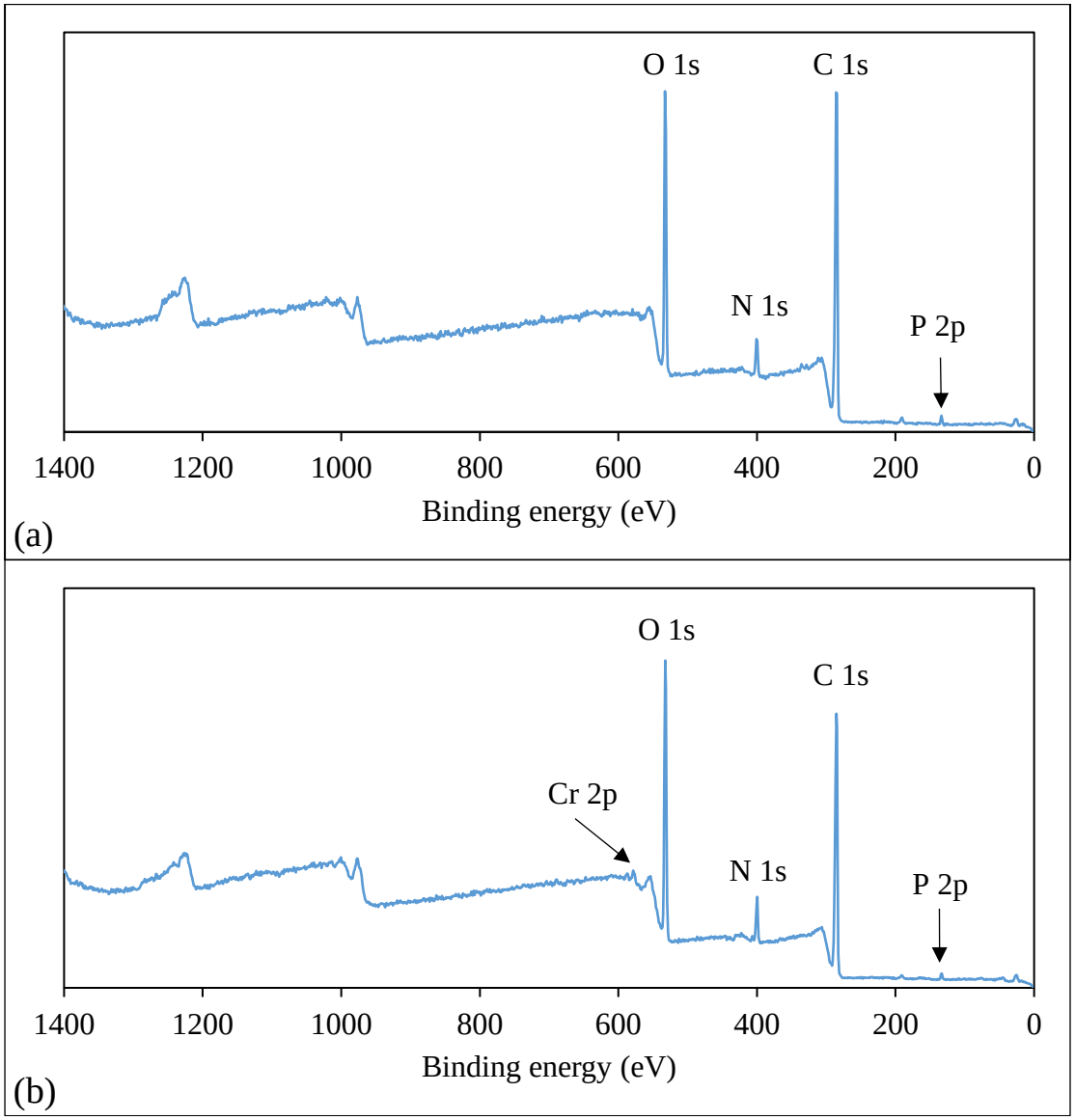


Figure 4-42 Wide scan XPS spectra of (a) pristine and (b) Cr-laden *M. rouxii* (pH 2, 1 day).

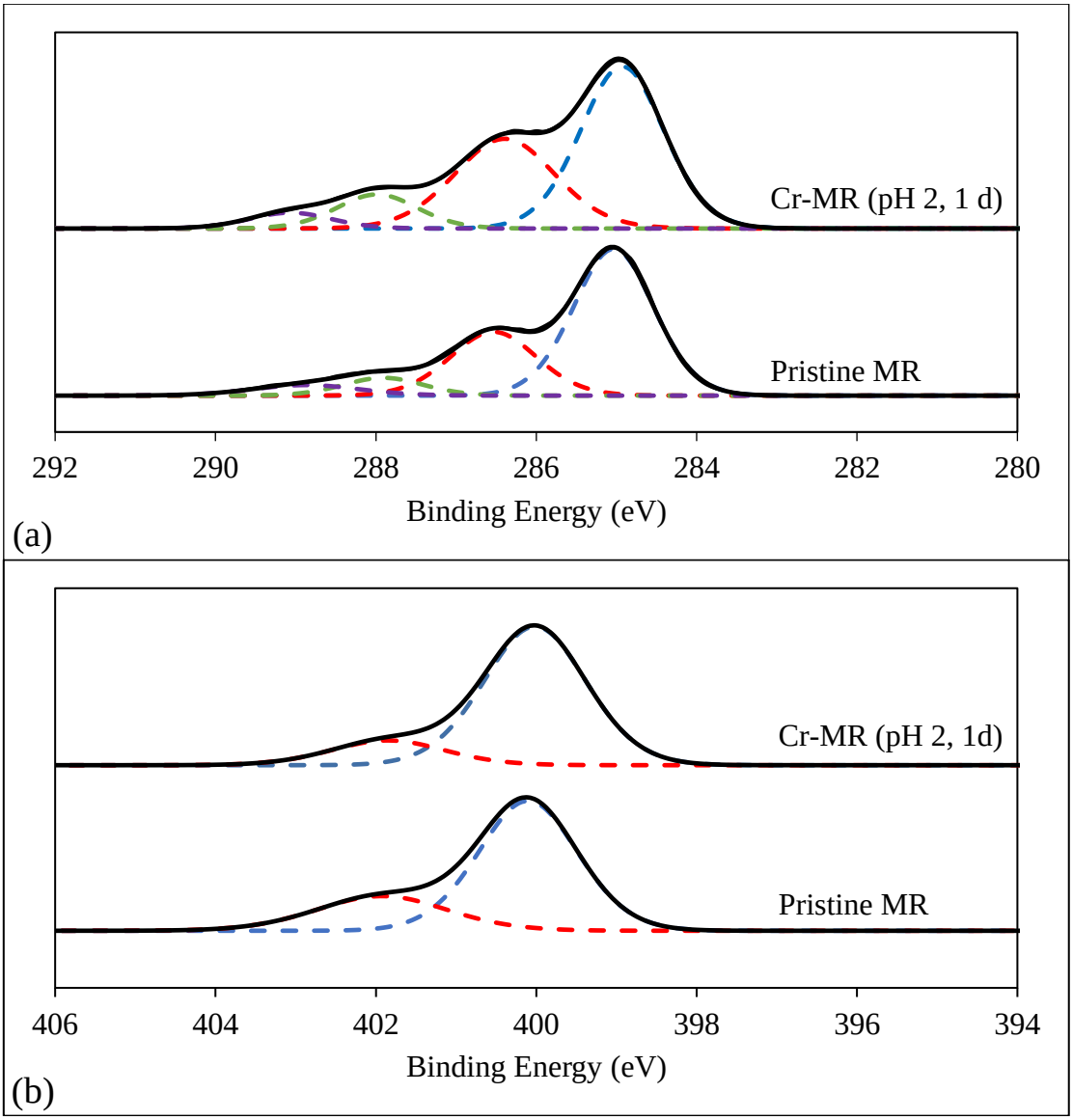


Figure 4-43 High-resolution XPS spectra of pristine and Cr-laden *M. rouxii*: (a) C1s and (b) N1s.

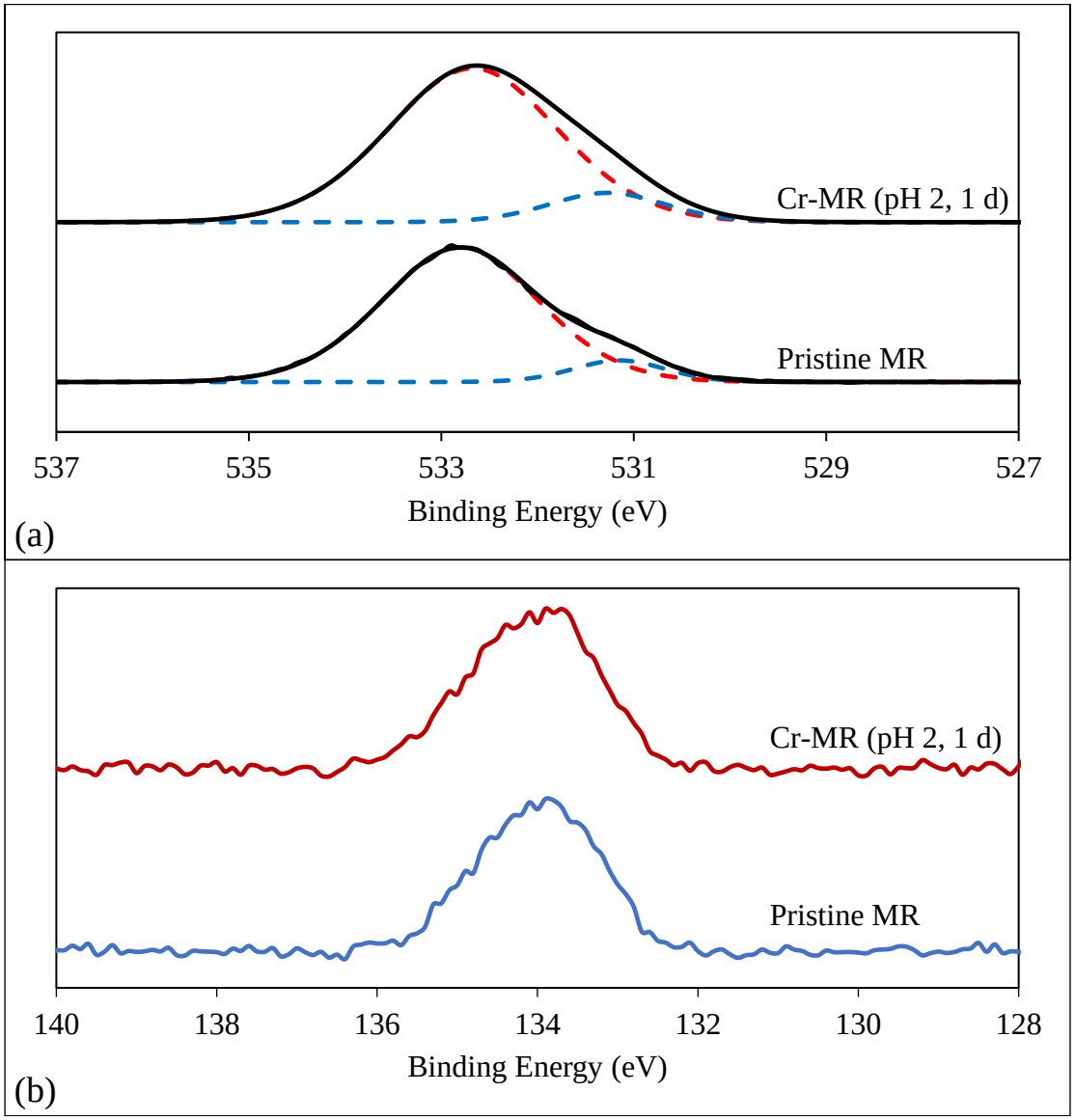


Figure 4-44 High-resolution XPS spectra of pristine and Cr-laden *M. rouxii*: (a) O1s and (b) P2p.

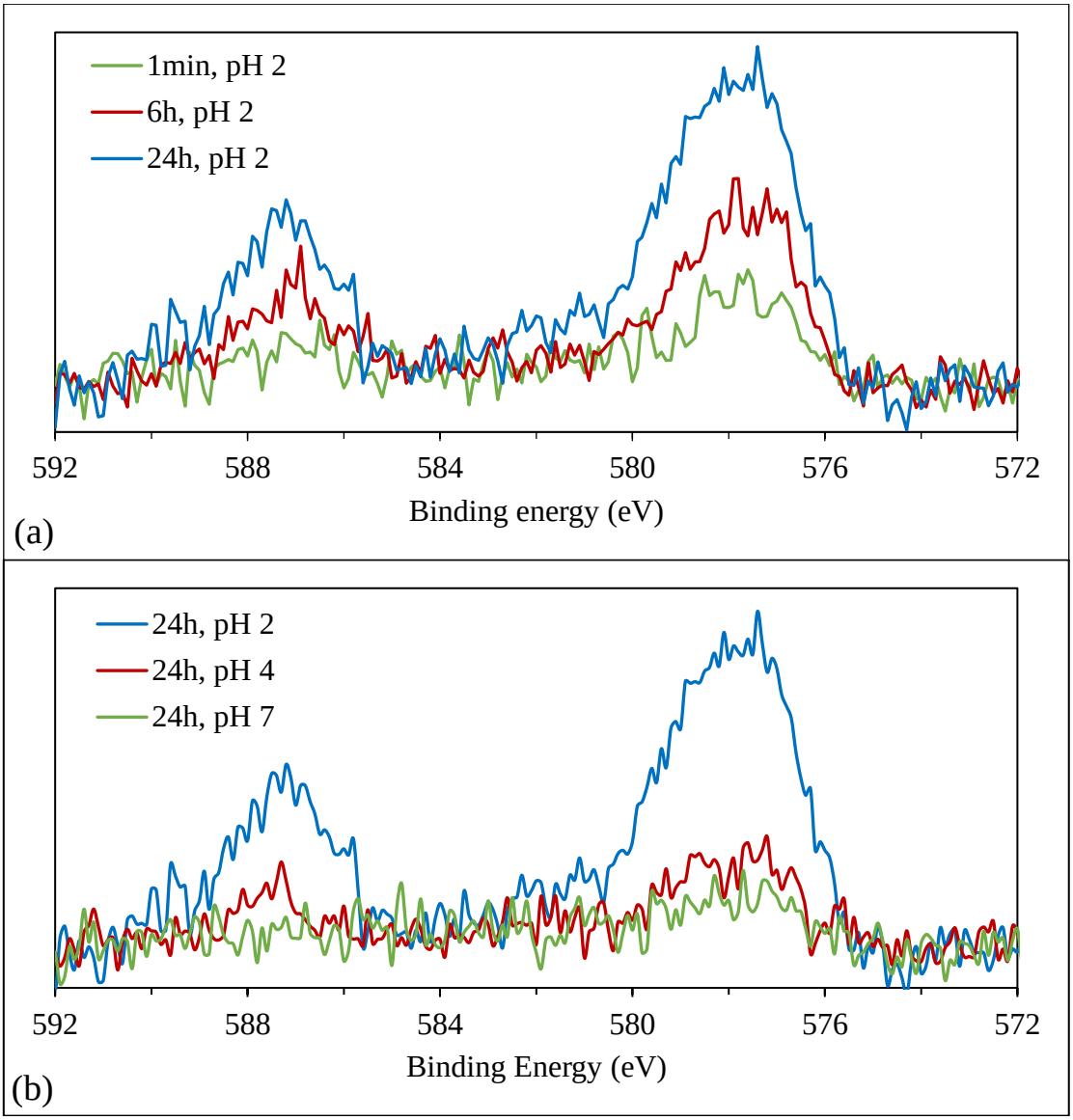


Figure 4-45 Cr2p spectra of Cr-laden *M. rouxii* at different (a) contact time and (b) solution pH.

Table 4-14 Binding energies, atomic concentrations and chemical shifts of pristine and Cr(VI)-laden *M. rouxii* and the standard compounds.

| Assignment | | | MR | Cr-MR | | | | | Cr(III) std | Cr(VI) std |
|---|---|---|---|---|---|---|---|---|---|---|
| | | | | pH 2 | | | pH 4 | pH 7 | | |
| | | | | 1 min | 6 h | 24 h | 24 h | 24 h | | |
| C1s | C-C, C-H | B.E. (eV) | 285.048 | 284.948 | 284.98 | 284.943 | 285.013 | 284.982 | / | / |
| | | A.C. (%) | 59.26% | 55.08% | 57.61% | 50.84% | 57.54% | 55.15% | / | / |
| | | Shift (eV) | / | -0.100 | -0.068 | -0.105 | -0.035 | -0.066 | / | / |
| | C-O, C-N | B.E. (eV) | 286.524 | 286.459 | 286.494 | 286.387 | 286.508 | 286.487 | / | / |
| | | A.C. (%) | 27.82% | 32.25% | 28.48% | 33.92% | 28.01% | 31.67% | / | / |
| | | Shift (eV) | / | -0.065 | -0.030 | -0.137 | -0.016 | -0.037 | / | / |
| | C=O | B.E. (eV) | 287.924 | 288.098 | 288.074 | 287.997 | 288.045 | 288.056 | / | / |
| | | A.C. (%) | 7.22% | 8.87% | 9.70% | 10.36% | 9.24% | 9.18% | / | / |
| | | Shift (eV) | / | +0.174 | +0.150 | +0.073 | +0.121 | +0.132 | / | / |
| | O=C-O | B.E. (eV) | 288.861 | 289.160 | 289.107 | 289.076 | 289.044 | 288.943 | / | / |
| | | A.C. (%) | 5.70% | 3.80% | 4.21% | 4.88% | 5.20% | 4.00% | / | / |
| | | Shift (eV) | / | +0.299 | +0.246 | +0.215 | +0.183 | +0.082 | / | / |

*B.E. = binding energy, A.C. = atomic concentration

Table 4-14 (con't) Binding energies, atomic concentrations and chemical shifts of pristine and Cr(VI)-laden *M. rouxii* and the standard compounds.

| Assignment | | | MR | Cr-MR | | | | | Cr(III) std | Cr(VI) std |
|---|---|---|---|---|---|---|---|---|---|---|
| | | | | pH 2 | | | pH 4 | pH 7 | | |
| | | | | 1 min | 6 h | 24 h | 24 h | 24 h | | |
| N1s | $NH_2$ | B.E. (eV) | 400.114 | 400.039 | 400.05 | 400.032 | 400.074 | 400.090 | / | / |
| | | A.C. (%) | 73.95% | 82.32% | 84.68% | 83.47% | 84.38% | 79.70% | / | / |
| | | Shift (eV) | / | -0.075 | -0.064 | -0.082 | -0.040 | -0.024 | / | / |
| | $NH_3^+$ | B.E. (eV) | 401.920 | 401.875 | 401.998 | 401.845 | 401.742 | 401.801 | / | / |
| | | A.C. (%) | 26.05% | 17.68% | 15.32% | 16.53% | 15.62% | 20.30% | / | / |
| | | Shift (eV) | / | -0.045 | +0.078 | -0.075 | -0.178 | -0.119 | / | / |
| O1s | O-C | B.E. (eV) | 532.802 | 532.685 | 532.665 | 532.654 | 532.573 | 532.735 | / | / |
| | | A.C. (%) | 91.36% | 89.70% | 90.06% | 88.40% | 90.63% | 87.06% | / | / |
| | | Shift (eV) | / | -0.117 | -0.137 | -0.148 | -0.229 | -0.067 | / | / |
| | O=C | B.E. (eV) | 531.138 | 531.177 | 531.227 | 531.278 | 531.263 | 531.242 | / | / |
| | | A.C. (%) | 8.64% | 10.30% | 9.94% | 11.60% | 9.37% | 12.94% | / | / |
| | | Shift (eV) | / | +0.039 | +0.089 | +0.140 | +0.125 | +0.104 | / | / |
| P2p | P-O | B.E. (eV) | 133.968 | 133.969 | 134.012 | 134.049 | 133.947 | 134.030 | / | / |
| | | A.C. (%) | / | +0.001 | +0.044 | +0.081 | -0.021 | +0.062 | / | / |
| Cr2p | 2p3/2 | B.E. (eV) | / | 577.700 | 577.885 | 578.100 | 578.224 | / | 578.408 | 579.808 |

*B.E. = binding energy, A.C. = atomic concentration

XPS analysis was also applied to investigate the surface functional groups on the calcium-alginate-based adsorbents and elucidate their Cr(VI) removal mechanism. Figure 4-46 and Figure 4-47 show the wide scan XPS spectra of CA, SCA, SCAIM and Cr-laden SCAIM, while the surface compositions were summarized in Table 4-15. The wide scan XPS spectrum of CA demonstrated the presence of C, N, O and Ca on the surface of CA. After doping silica on CA, the new Si2s and Si2p signals at around 150 and 100 eV indicated the successful doping of silica on the surface of calcium alginate. In the spectrum of SCAIM, the distinct P2p (~133 eV) and Si2p (~100 eV) signals were attributed to the phosphorous groups on the *M. rouxii* and the Si-O groups of the doped silica, respectively. After the Cr adsorption, an extra Cr2p peak at 577 eV was found in the Cr-laden CA, SCA and SCAIM, while the intensities of Ca2p peak were significantly reduced. These results indicated that the calcium ions in the calcium alginate were replaced by the Cr(III) ions through the ion-exchange mechanism.

Figure 4-48 and Figure 4-49 display the C1s, N1s, O1s and P2p XPS spectra of the silica-doped calcium alginate immobilized *M. rouxii* (SCAIM) before and after Cr(VI) removal, while Table 4-16 lists the binding energies of the CA, SCA, SCAIM and the standard compounds. As shown in Table 4-16, the C1s spectrum of CA was resolved into four peaks at 284.922, 286.608, 288.072 and 289.221 eV, which were assigned to the groups of C-C/H, C-O, C=O and O=C-O, respectively. The O 1s signals at 532.871 and 531.268 eV were attributed to O-C and O=C groups, respectively. These results indicated the presence of hydroxyl and

carboxyl groups in the alginate, which were responsible for the Cr(VI) reduction and Cr(III) complexation, respectively. The small N 1s signal at 400.128 eV belonged to the -$NH_2$ (amine groups) of the impurities in the alginate (e.g., proteins).

After doping of silica on the calcium alginate, the SCA displayed similar C1s and O1s spectra to those of CA. The intense N1s spectrum could be resolved into two peaks at 400.142 and 401.695 eV, which were associated with the -$NH_2$ and -$NH_3^+$ signals of the ethylenediamine groups in the doped silica. Concerning the silica-doped calcium alginate immobilized *M. rouxii* (SCAIM), the similar characteristic C1s peaks of C-C/H, C-O/N, C=O and O=C-O were observed at 284.968, 286.367, 287.849 and 288.677 eV, respectively (Figure 4-48a). The typical signals of O-C and O=C appeared at 532.787 and 530.971 eV, respectively, in the O1s spectrum of SCAIM (Figure 4-49a). These results demonstrated that the immobilized MR and the alginate chains contained a large amount of hydroxyl, carbonyl and carboxyl groups. Moreover, the N1s spectrum of SCAIM (Figure 4-48b) resulted in two resolved peaks at 400.109 and 402.143 eV, which corresponded to the -$NH_2$ (amine) and -$NH_3^+$ (protonated amine). These signals were contributed by the amine groups in the immobilized MR and the ethylenediamine groups of the doped silica. A new peak at 407.195 eV corresponded to the $NO_x$ signal of nitrate ions, which was introduced in the pre-condition step. In P2p spectrum of SCAIM (Figure 4-49b), the peak at 133.747 eV was assigned to the P-O groups of the immobilized *M. rouxii*.

In the Cr2p XPS spectra of Cr-CA, Cr-SCA and Cr-SCAIM (Figure 4-50a), the peak at ~578.4 eV was assigned to the Cr2p3/2 signal of Cr(III) by comparing the binding energies with those of the Cr(III) and Cr(VI) standards. Moreover, the Cr(III) signals were detected on the SCAIM surface after 1-minute contact with the Cr(VI) solution (Figure 4-50b). No Cr(VI) signal was found in the Cr-laden immobilized adsorbents, so the Cr(VI) ions were rapidly adsorbed on the surface of SCAIM and then immediately reduced to Cr(III). It was concluded that the Cr(VI) ions were removed by the SCAIM through the adsorption-reduction mechanism as similar to MR. It should be noted that the Cr(III) signal was also observed in the Cr2p spectra of Cr-CA and Cr-SCA, confirming the Cr(VI) reducing ability of calcium alginate.

In order to investigate the functional groups involving in the Cr adsorption, the high-resolution C1s, N1s and O1s XPS spectra of Cr-CA, Cr-SCA and Cr-SCAIM were deconvoluted and were compared with the pristine adsorbents (Figure 4-48 and Figure 4-49). After Cr adsorption, there was no noticeable shifting in the binding energy of C-C, C-O and C=O signals in the C1s spectra of CA and SCA, indicating that the alkyl carbon, hydroxyl, carbonyl groups did not involve in the Cr adsorption on the CA and SCA. On the contrary, the O=C-O signal in the C1s spectra displayed significant positive shifts in binding energy (+0.224 eV) after Cr adsorption, suggesting that the carboxyl groups in the alginate chains played an important role in the binding of Cr. Furthermore, the C-O, C=O and O=C-O signals in the SCAIM exhibited appreciable change in binding energy after Cr adsorption. The Cr would also

bind to the hydroxyl and carbonyl groups in the immobilized biomass, not only the carboxyl groups in the alginate. The involvement of carboxyl groups in the Cr adsorption supported the finding from FTIR analysis (Section 4.6.1) which confirmed the formation of Cr(III)-carboxylate complex in the alginate-based adsorbents. In addition, there was no significant shifting in binding energy of the $NH_2$ and $NH_3^+$ signals in the SCAIM after Cr adsorption, implying that the nitrogen-functional groups in the SCAIM had no interaction to the cationic Cr(III).

In the pristine CA, SCA and SCAIM, there was a strong Ca2p signals (Figure 4-51) at 347.8 and 351.4 eV, which were attributed to the Ca2p 3/2 and Ca2p 1/2 signals of the Ca(II) ions in calcium alginate, respectively. The Ca2p signals of Cr-CA and Cr-SCA significantly dropped after a 3-day contact with Cr(VI) solution, whereas the Ca2p signal of Cr-SCAIM even disappeared after 1 day. These results were consistent with the result of Cr(VI) removal studies that the Ca(II) ions on the SCAIM surface were displaced by the reduced Cr(III) ions through the ion-exchange mechanism.

Table 4-15 Surface compositions of pristine and Cr-laden CA, SCA and SCAIM beads.

| | Mass concentration (wt%) | | | | | | | |
|---|---|---|---|---|---|---|---|---|
| | Cr2p | O1s | N1s | Ca2p | C1s | Cl2p | P2p | Si2p |
| CA | 0 | 39.50 | 3.14 | 1.19 | 55.48 | 0.65 | 0 | 0 |
| Cr-CA | 1.22 | 39.51 | 3.36 | 0.47 | 54.65 | 0.74 | 0 | 0 |
| SCA | 0 | 37.13 | 4.19 | 1.78 | 54.45 | 0.41 | 0 | 2.03 |
| Cr-SCA | 4.10 | 42.74 | 2.31 | 0.66 | 47.91 | 0.12 | 0 | 2.15 |
| SCAIM | 0 | 24.25 | 2.53 | 7.65 | 62.20 | 0 | 2.10 | 1.26 |
| Cr-SCAIM | 6.25 | 31.52 | 6.94 | 0.12 | 53.90 | 0 | 0.71 | 0.56 |

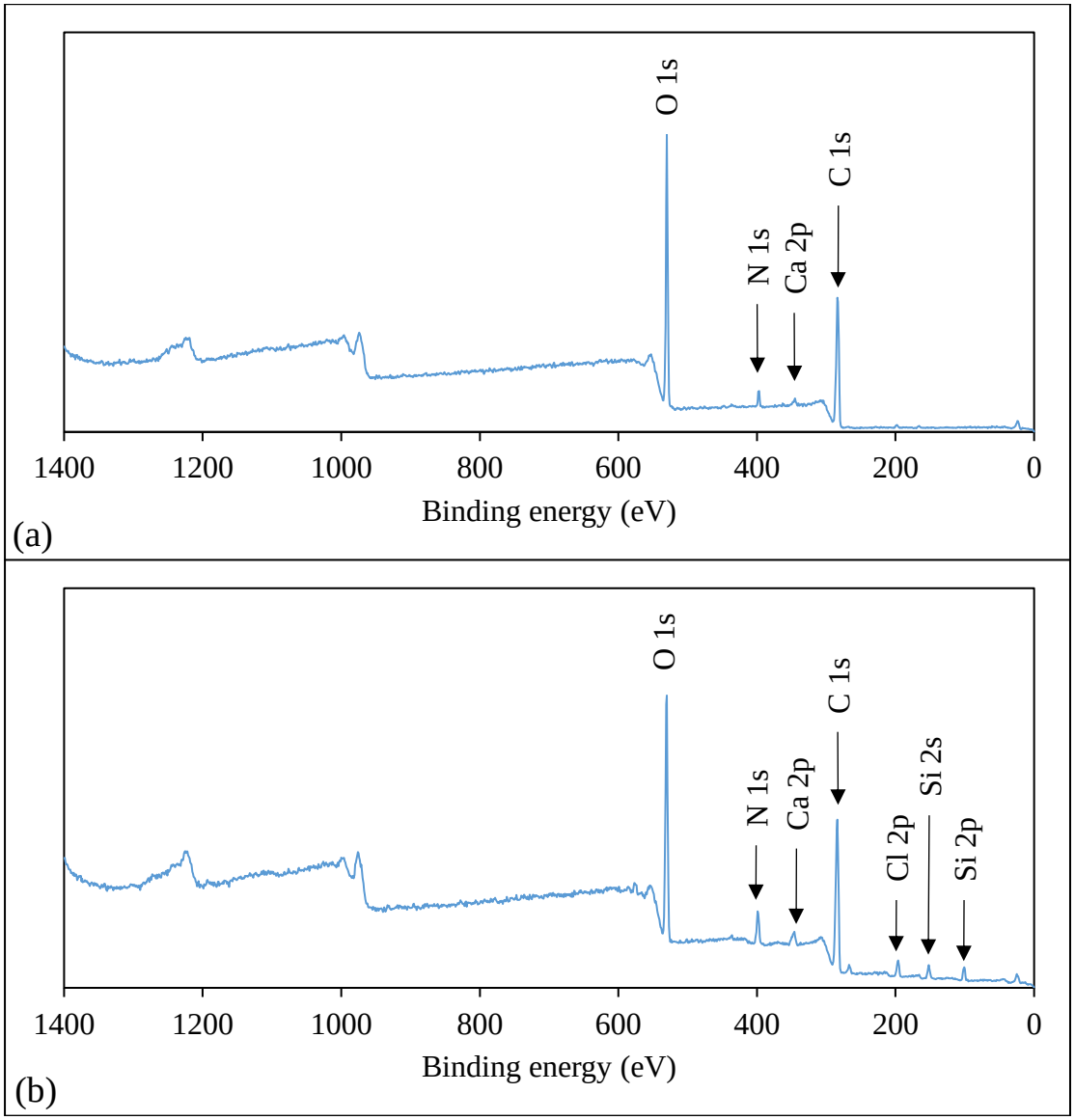


Figure 4-46 Wide scan XPS spectra of (a) CA and (b) SCA.

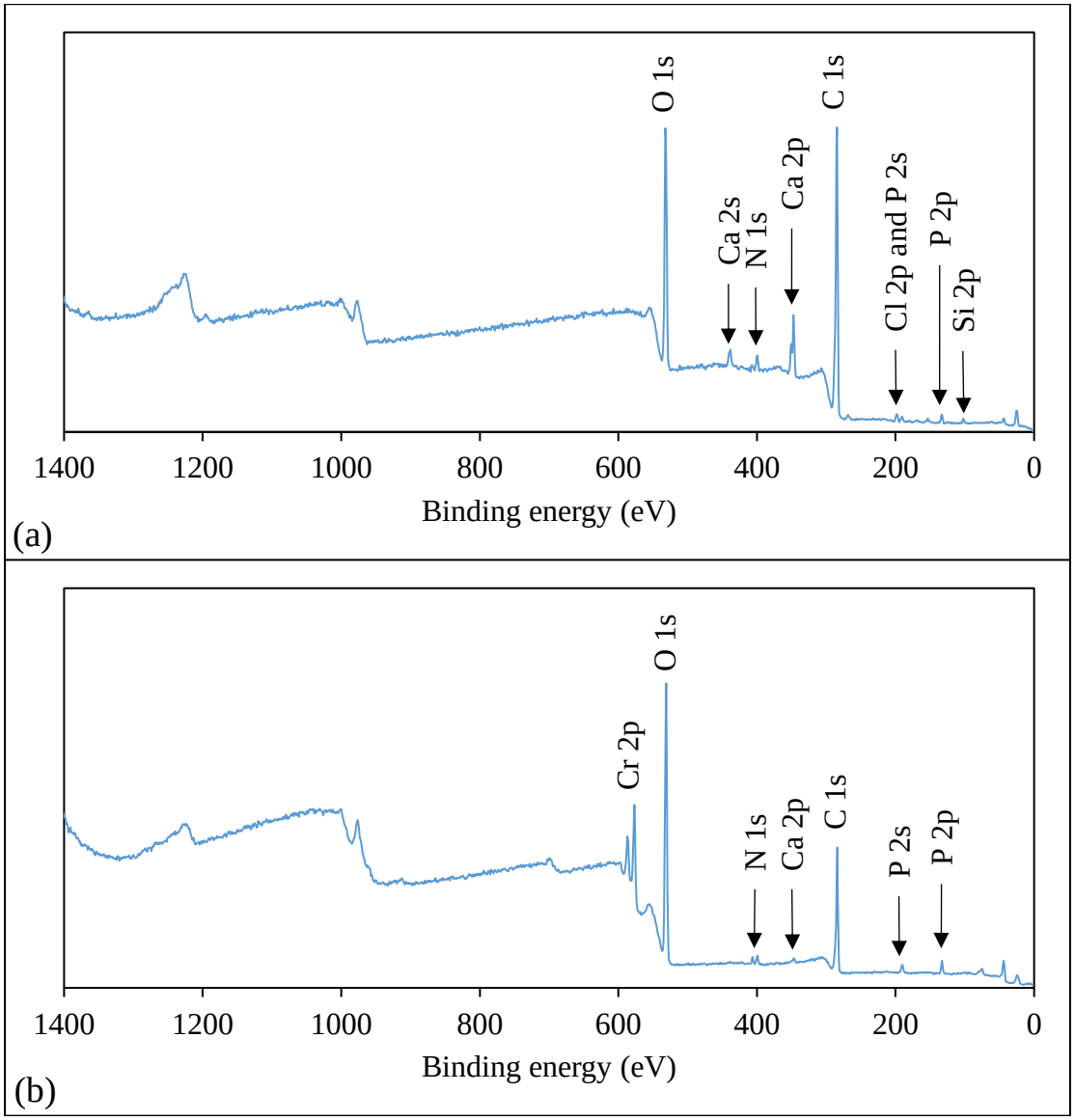


Figure 4-47 Wide scan XPS spectra of (a) SCAIM and (b) Cr-laden SCAIM.

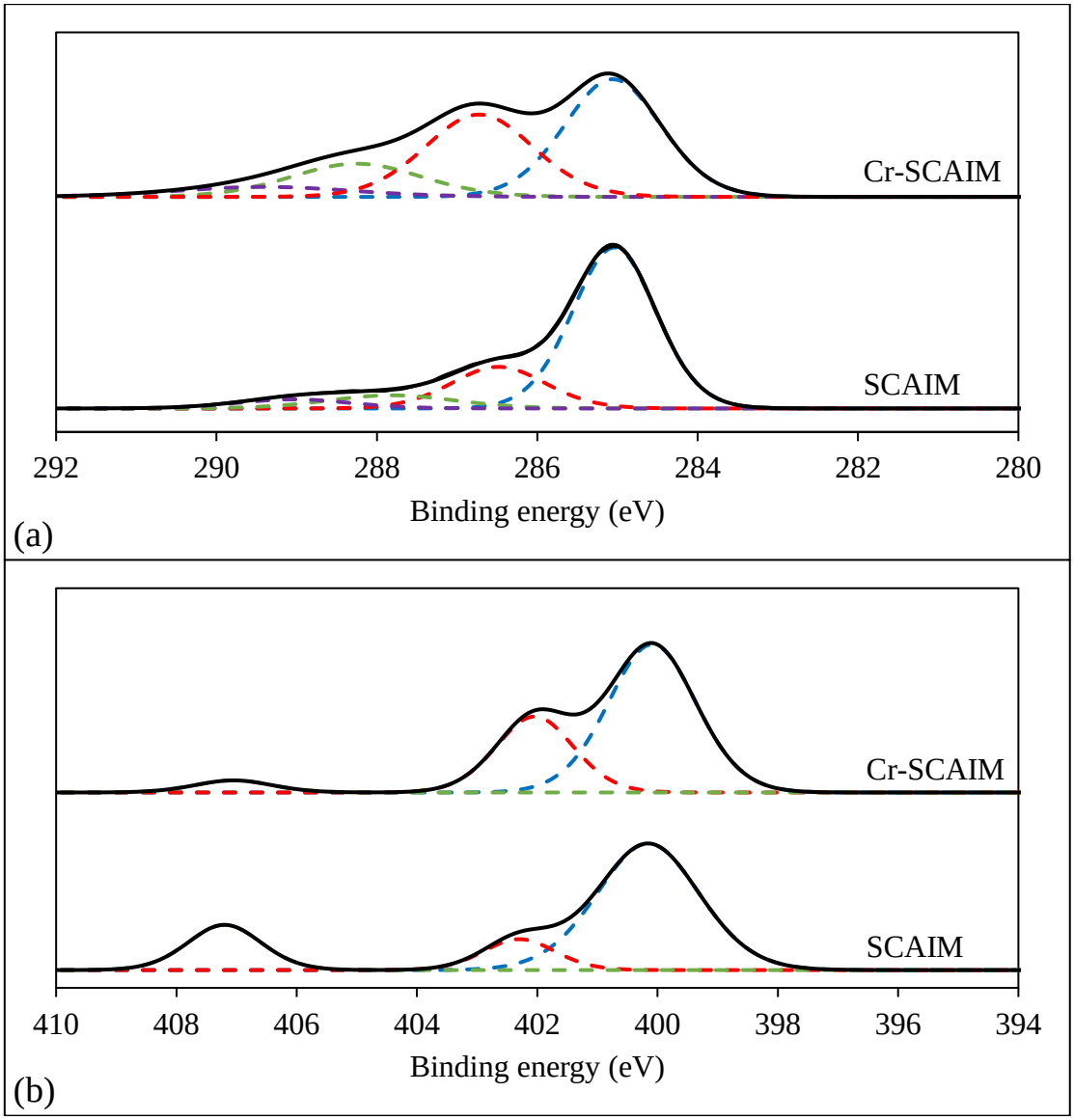


Figure 4-48 High-resolution XPS spectra of the pristine and Cr-laden SCAIM: (a) C1s and (b) N1s.

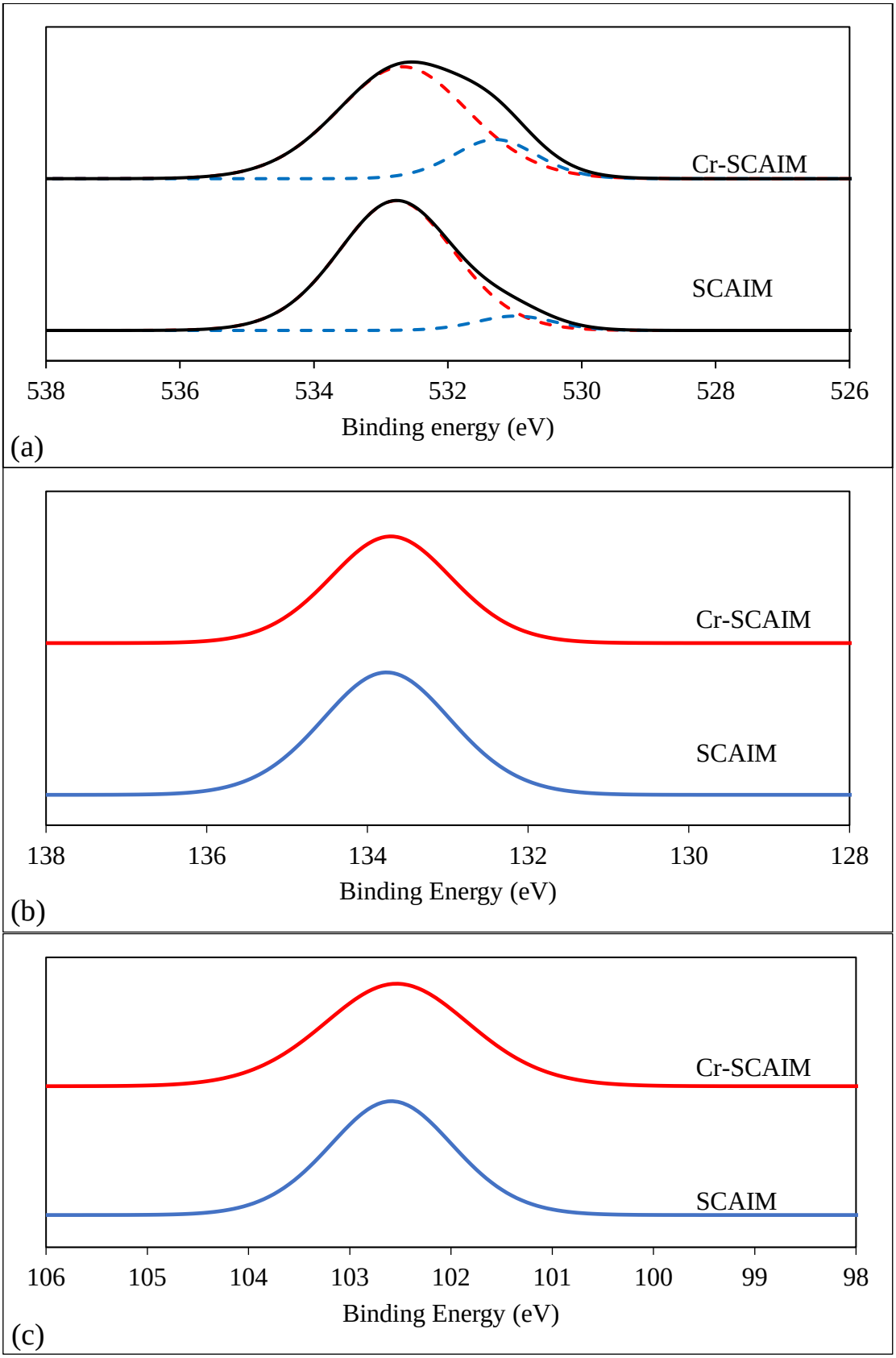


Figure 4-49 High-resolution XPS spectra of the pristine and Cr-laden SCAIM: (a) O1s (b) P2p and (c) Si2p.

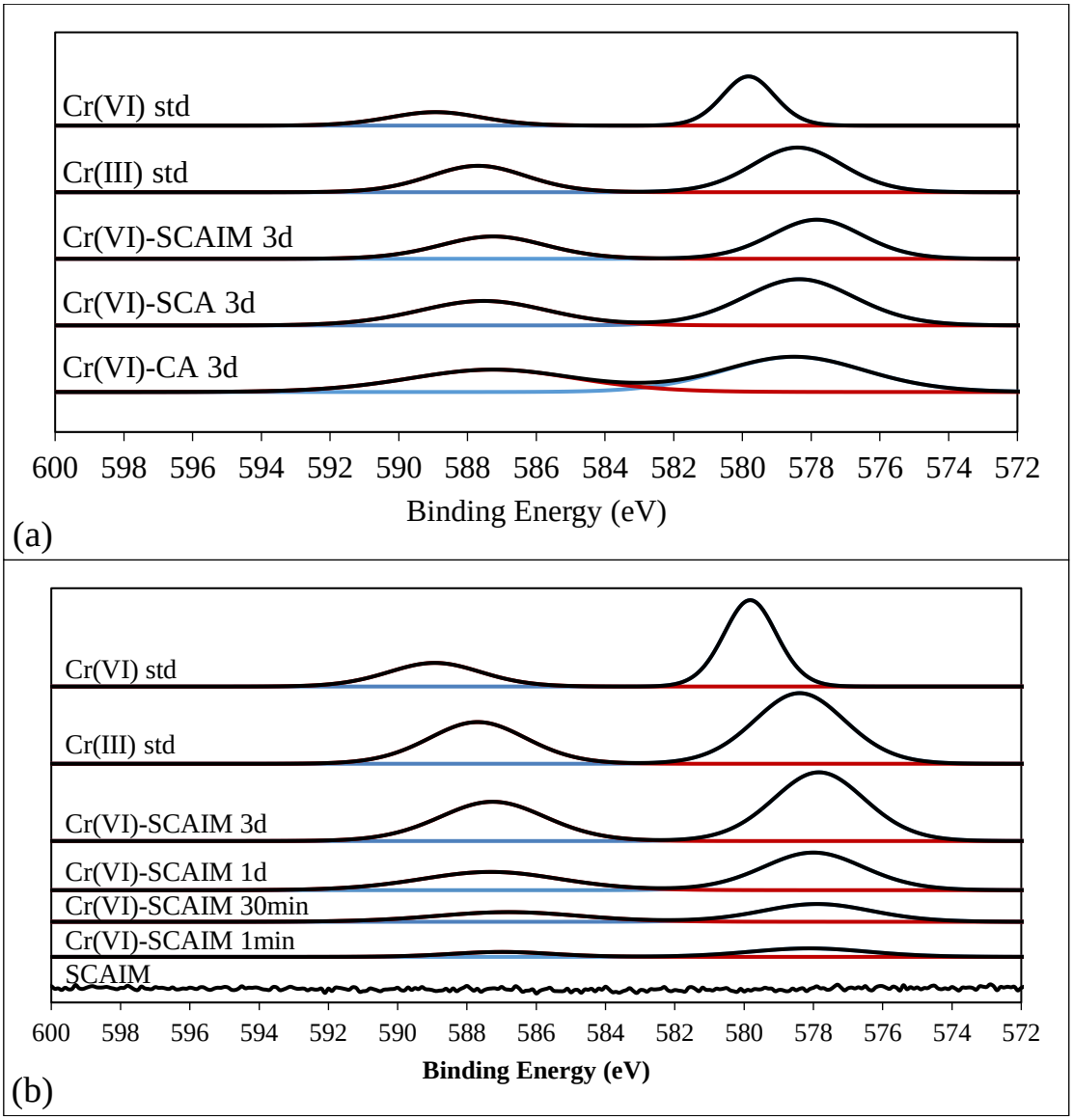


Figure 4-50 Cr2p spectra of (a) the different Cr-loaded bead adsorbents and (b) the Cr-loaded SCAIM with different contact times.

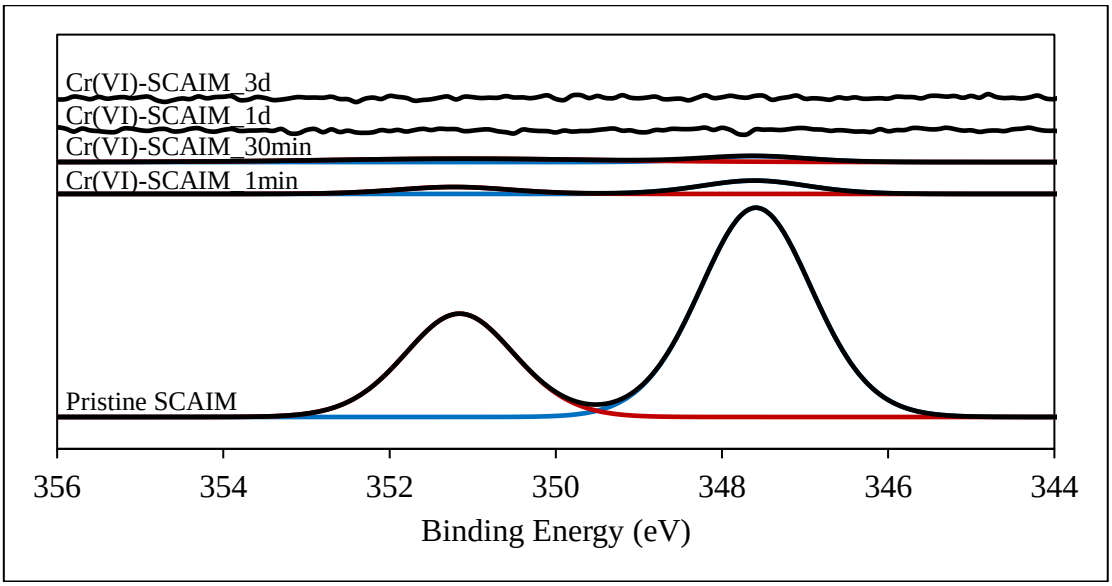


Figure 4-51 Ca2p spectra of pristine and Cr-loaded SCAIM with different contact times.

Table 4-16 Binding energies, atomic concentrations and chemical shifts of pristine and Cr(VI)-laden calcium-alginate-based adsorbents and the standard compounds.

| Assignment | | | CA | Cr-CA pH 2, 3 d | SCA | Cr-SCA pH 2, 3 d | SCAIM | Cr-SCAIM pH 2, 3 d | Cr(III) std | Cr(VI) std |
|---|---|---|---|---|---|---|---|---|---|---|
| C1s | C-C, C-H | B.E. (eV) | 284.922 | 285.002 | 285.003 | 285.001 | 284.968 | 285.052 | / | / |
| | | A.C. (%) | 30.34% | 26.30% | 31.28% | 21.93% | 56.84% | 43.67% | / | / |
| | | Shift (eV) | / | +0.08 | / | -0.002 | / | +0.084 | / | / |
| | C-O, C-N | B.E. (eV) | 286.608 | 286.643 | 286.518 | 286.631 | 286.367 | 286.596 | / | / |
| | | A.C. (%) | 44.97% | 44.48% | 41.46% | 46.52% | 30.99% | 31.05% | / | / |
| | | Shift (eV) | / | +0.035 | / | +0.113 | / | +0.229 | / | / |
| | C=O | B.E. (eV) | 288.072 | 288.155 | 287.889 | 287.999 | 287.849 | 288.064 | / | / |
| | | A.C. (%) | 14.20% | 20.43% | 14.48% | 20.63% | 5.84% | 18.39% | / | / |
| | | Shift (eV) | / | +0.083 | / | +0.110 | / | +0.215 | / | / |
| | O=C-O | B.E. (eV) | 289.221 | 289.445 | 288.820 | 289.064 | 288.677 | 288.931 | / | / |
| | | A.C. (%) | 10.48% | 8.79% | 12.78% | 10.92% | 6.33% | 6.88% | / | / |
| | | Shift (eV) | / | +0.224 | / | +0.244 | / | +0.254 | / | / |
| P2p | P-O | B.E. (eV) | / | / | / | / | 133.747 | 133.713 | / | / |
| | | Shift (eV) | / | / | / | / | / | -0.034 | / | / |
| Ca2p | 2p3/2 | B.E. (eV) | 347.894 | 347.955 | 347.796 | 347.870 | 347.737 | / | / | / |
| | | Shift (eV) | / | +0.061 | / | +0.074 | / | / | / | / |
| Cr2p | 2p3/2 | B.E. (eV) | / | 578.440 | / | 578.350 | / | 577.858 | 578.408 | 579.808 |

*B.E. = binding energy, A.C. = atomic concentration

Table 4-17 (con't) Binding energies, atomic concentrations and chemical shifts of pristine and Cr(VI)-laden calcium-alginate-based adsorbents and the standard compounds.

| Assignment | | | CA | Cr-CA pH 2, 3 d | SCA | Cr-SCA pH 2, 3 d | SCAIM | Cr-SCAIM pH 2, 3 d | Cr(III) std | Cr(VI) std |
|---|---|---|---|---|---|---|---|---|---|---|
| N1s | $NH_2$ | B.E. (eV) | 400.128 | 400.228 | 400.142 | 400.299 | 400.109 | 400.106 | / | / |
| | | A.C. (%) | / | / | 38.44% | 52.10% | 68.94% | 65.67% | / | / |
| | | Shift (eV) | / | +0.100 | / | +0.157 | / | -0.003 | / | / |
| | $NH_3^+$ | B.E. (eV) | / | / | 401.695 | 401.931 | 402.143 | 402.058 | / | / |
| | | A.C. (%) | / | / | 61.56% | 47.90% | 14.06% | 29.62% | / | / |
| | | Shift (eV) | / | / | / | +0.236 | / | -0.085 | / | / |
| | $NO_x$ | B.E. (eV) | / | / | / | / | 407.195 | 407.075 | / | / |
| | | A.C. (%) | / | / | / | / | 17.00% | 4.71% | / | / |
| | | Shift (eV) | / | / | / | / | / | -0.120 | / | / |
| O1s | O-C | B.E. (eV) | 532.871 | 532.957 | 532.792 | 532.812 | 532.787 | 532.844 | / | / |
| | | A.C. (%) | 93.90% | 96.37% | 94.98% | 98.37% | 93.13% | 70.83% | / | / |
| | | Shift (eV) | / | +0.086 | / | +0.020 | / | +0.057 | / | / |
| | O=C | B.E. (eV) | 531.268 | 531.217 | 531.156 | 530.864 | 530.971 | 531.373 | / | / |
| | | A.C. (%) | 6.10% | 3.63% | 5.02% | 1.63% | 6.87% | 29.17% | / | / |
| | | Shift (eV) | / | -0.051 | / | -0.292 | / | +0.402 | / | / |
| Si2p | Si-O | B.E. (eV) | / | / | 102.495 | 102.462 | 102.567 | 102.519 | / | / |
| | | Shift (eV) | / | / | / | -0.033 | / | -0.048 | / | / |

*B.E. = binding energy, A.C. = atomic concentration

Silica-doped zirconium alginate immobilized *M. rouxii* (SZAIM) exhibited a higher total Cr adsorption capacity and a faster Cr adsorption rate than SCAIM (Section 4.5), so the surface characteristics and Cr(VI) removal mechanism of the zirconium-alginate-based adsorbents were further analyzed using XPS. Figure 4-52 presents the wide scan XPS spectrum of pristine and Cr-laden SZAIM. The Ca2p signal could not be observed in all zirconium-alginate-based adsorbents (Table 4-17). The zirconium-alginate-based adsorbents (i.e., ZA and SZAIM) were prepared by immersing the corresponding calcium alginate materials (i.e., CA and SCAIM) in the zirconium oxychloride solution for 24 hours. The absence of Ca2p signal in all the zirconium-alginate-based materials indicated the complete replacement of the Ca(II) ions in the calcium alginate structure by the Zr(IV) ions through the ion-exchange mechanism.

As shown in Figure 4-53a, the high-resolution C1s spectrum of SZAIM was deconvoluted into four component peaks at 285.0, 286.7, 287.9 and 289.2 eV, which corresponded to the groups of C-C/H, C-O/N, C=O and O=C-O, respectively. The N1s spectrum of SZAIM (Figure 4-53b) confirmed the presence of two different nitrogen functionalities, $-NH_2$ (amine) and $-NH_3^+$ (protonated amine), on the surface of SZAIM. The O1s spectrum of SZAIM (Figure 4-53c) was resolved into two component peaks at 533.3 and 532.5 eV, representing O-C (hydroxyl and ether) and O=C (carbonyl), respectively. In addition, the Zr3d signals appeared in the all the zirconium-alginate-based adsorbents. Moreover, the Zr3d spectrum of SZAIM (Figure 4-54a) could be resolved into two component peaks at 183.028 and 185.389 eV, which

were assigned to the Zr3d 5/2 and Zr3d 3/2 signals, respectively. The binding energies were comparable to the literature values of zirconium alginate (Zhou et al., 2015).

The external surface and the cross-section of Cr-laden SZAIM beads were analyzed using XPS. It was found that the Cr2p signal appeared on the surface and in the interior of SZAIM beads. The Cr(VI) ions could diffuse inside the SZAIM beads and reached the binding sites in the interior of SZAIM beads, such as surface groups of the immobilized *M. rouxii* and Zr(IV) of zirconium alginate. Furthermore, the Cr2p 3/2 signal of Cr-laden SZAIM beads was deconvoluted into two component peaks at 577 and 579 eV (Figure 4-54b), indicating that both Cr(III) and Cr(VI) ions were present on the surface and in the interior of Cr-laden SZAIM beads. Based on the peak area of the resolved peaks, 54.72% of the adsorbed Cr on the external surface of SZAIM was in the form of Cr(III), while the remaining 45.28% was Cr(VI). Similar Cr(III)/Cr(VI) ratio could be observed in the interior of SZAIM beads, so the adsorption sites and reducing groups were evenly distributed throughout the SZAIM beads. It should be noted that the signals of Cr(III) and Cr(VI) were also detected on the surface of Cr-laden ZA, with similar Cr(III)/Cr(VI) ratio (Cr(III): 55.89% and Cr(VI): 44.11%).-As mentioned before, all the adsorbed Cr(VI) on SCAIM beads and raw *M. rouxii* was reduced to Cr(III). Therefore, the Zr(IV) should be the key component leading to the partial reduction of the adsorbed Cr(VI) in the Cr-laden SZAIM.

The presence of Cr(VI) and Cr(III) signals on the Cr-laden ZA confirmed that the

zirconium alginate was able to remove the Cr(VI) ions by two different mechanisms: (1) electrostatic adsorption and (2) adsorption-coupled reduction. The cationic tetravalent Zr(IV) in zirconium alginate would serve as the adsorption sites for the anionic Cr(VI) due to the strong electrostatic attraction. After Cr(VI) adsorption, the Zr3d 3/2 signals of ZA showed a negative shifting in binding energy (Table 4-18), suggesting the interaction between the anionic Cr(VI) ions and the Zr(IV) ions in the zirconium-alginate based adsorbents. The binding would be so strong that the adsorbed Cr(VI) could not be transferred to the adjacent electron-donor groups for the reduction reaction. On the other hand, the hydroxyl groups on the alginate chains also played an important role in the adsorption-coupled reduction mechanism. The hydroxyl groups could be protonated under the acidic adsorption environment, so the Cr(VI) was adsorbed by the protonated hydroxyl group. Moreover, the hydroxyl groups also acted as electron-donor groups that reduced the adsorbed Cr(VI) ions to Cr(III). After adsorption of Cr, the mass concentration of Zr3d in ZA reduced from 13.86 to 8.80%. The Zr(IV) ions were displaced from zirconium alginate by the Cr(III) ions through the ion-exchange mechanism. The reduced Cr(III) ions would then form complex with the carboxylate groups on the alginate chains.

For the case of SZAIM, both the direct adsorption and adsorption-coupled reduction mechanism involved in the Cr(VI) removal as similar to the case of SCAIM. Part of the adsorbed Cr(VI) strongly bound to the Zr(IV) through the electrostatic attraction. Meanwhile,

another part of the adsorbed Cr(VI) was adsorbed by the amine groups of the immobilized *M. rouxii*, the ethylenediamine groups of the silica particles and the protonated hydroxyl groups. The adsorbed Cr(VI) anions were then reduced to Cr(III) by the electron-donor groups (e.g., hydroxyl groups). That could explain the presence of Cr(III) and Cr(VI) on the Cr-laden SZAIM.

Table 4-17 Surface compositions of pristine and Cr-laden ZA and SZAIM beads.

| | Mass concentration (wt%) | | | | | | | | | |
|---|---|---|---|---|---|---|---|---|---|---|
| | Cr2p | O1s | N1s | Ca2p | C1s | Zr3d | Cl2p | S2p | P2p | Si2p |
| ZA | 0 | 41.51 | 0.60 | 0 | 41.64 | 13.86 | 0.98 | 1.23 | 0.13 | 0 |
| Cr-ZA | 0.74 | 34.11 | 2.53 | 0 | 51.92 | 8.80 | 0.39 | 1.07 | 0.24 | 0 |
| SZAIM | 0 | 30.26 | 1.97 | 0 | 32.67 | 27.75 | 5.32 | 0.19 | 0.19 | 1.65 |
| Cr-SZAIM | 4.35 | 31.79 | 2.35 | 0 | 38.09 | 21.58 | 0 | 0.25 | 0.20 | 1.41 |
| Cr-SZAIM* | 4.84 | 32.93 | 2.43 | 0 | 34.35 | 22.83 | 0.37 | 0.4 | 0.23 | 1.62 |

*Cross section of SZAIM

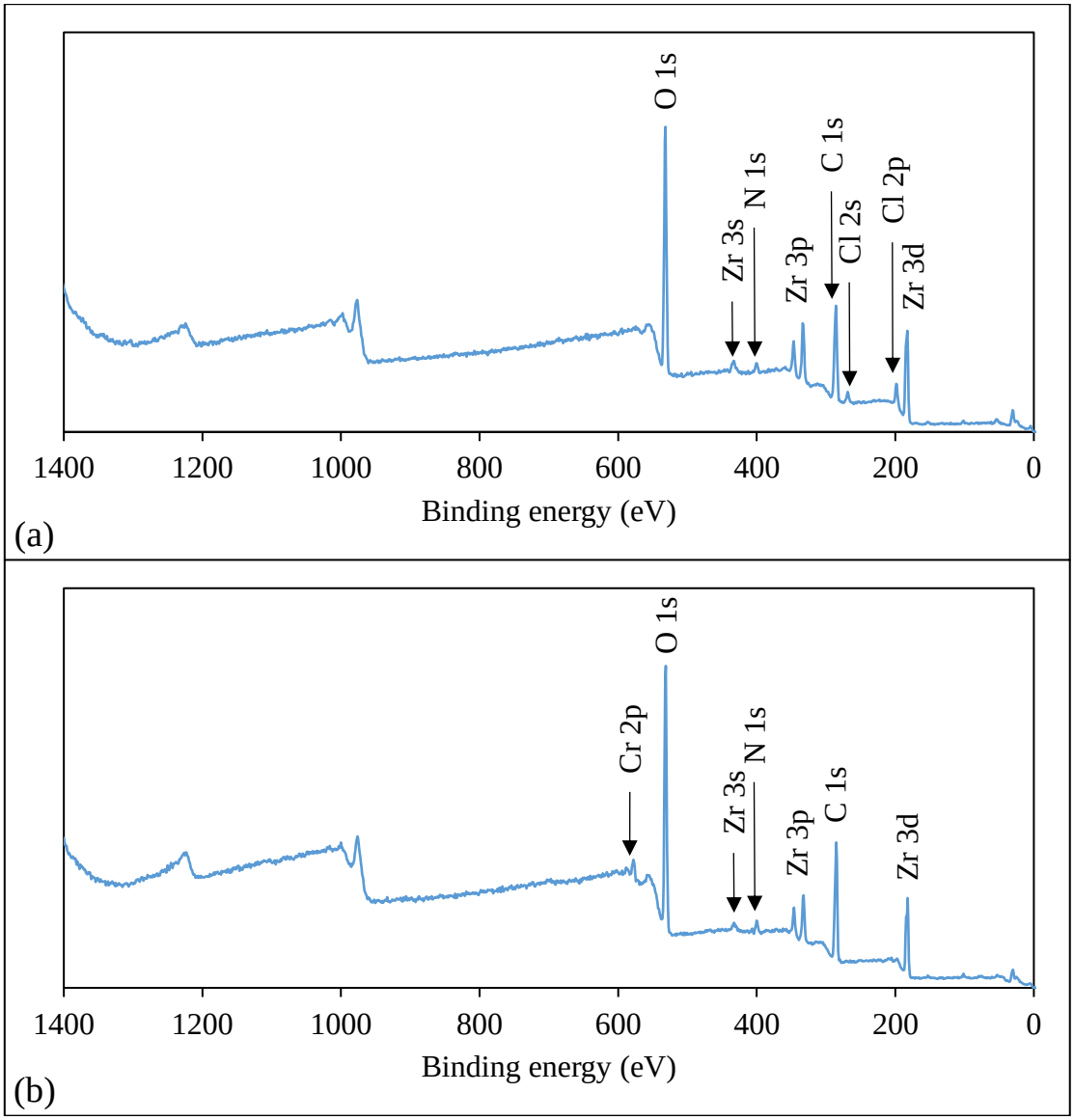


Figure 4-52 Wide scan XPS spectra of (a) SZAIM and (b) Cr-laden SZAIM.

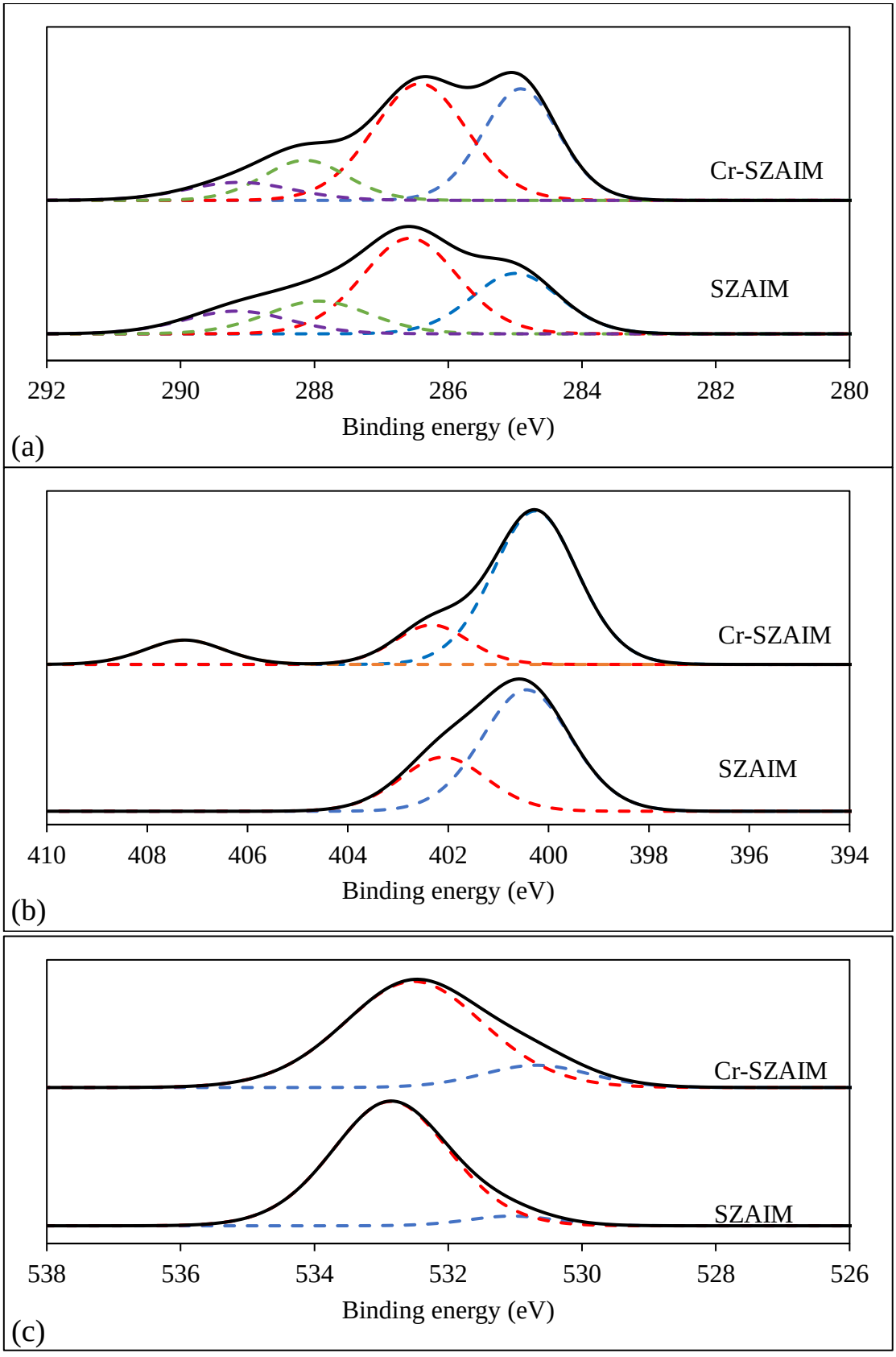


Figure 4-53 High-resolution XPS spectra of the pristine and Cr-laden SZAIM: (a) C1s, (b) N1s and (c) O1s.

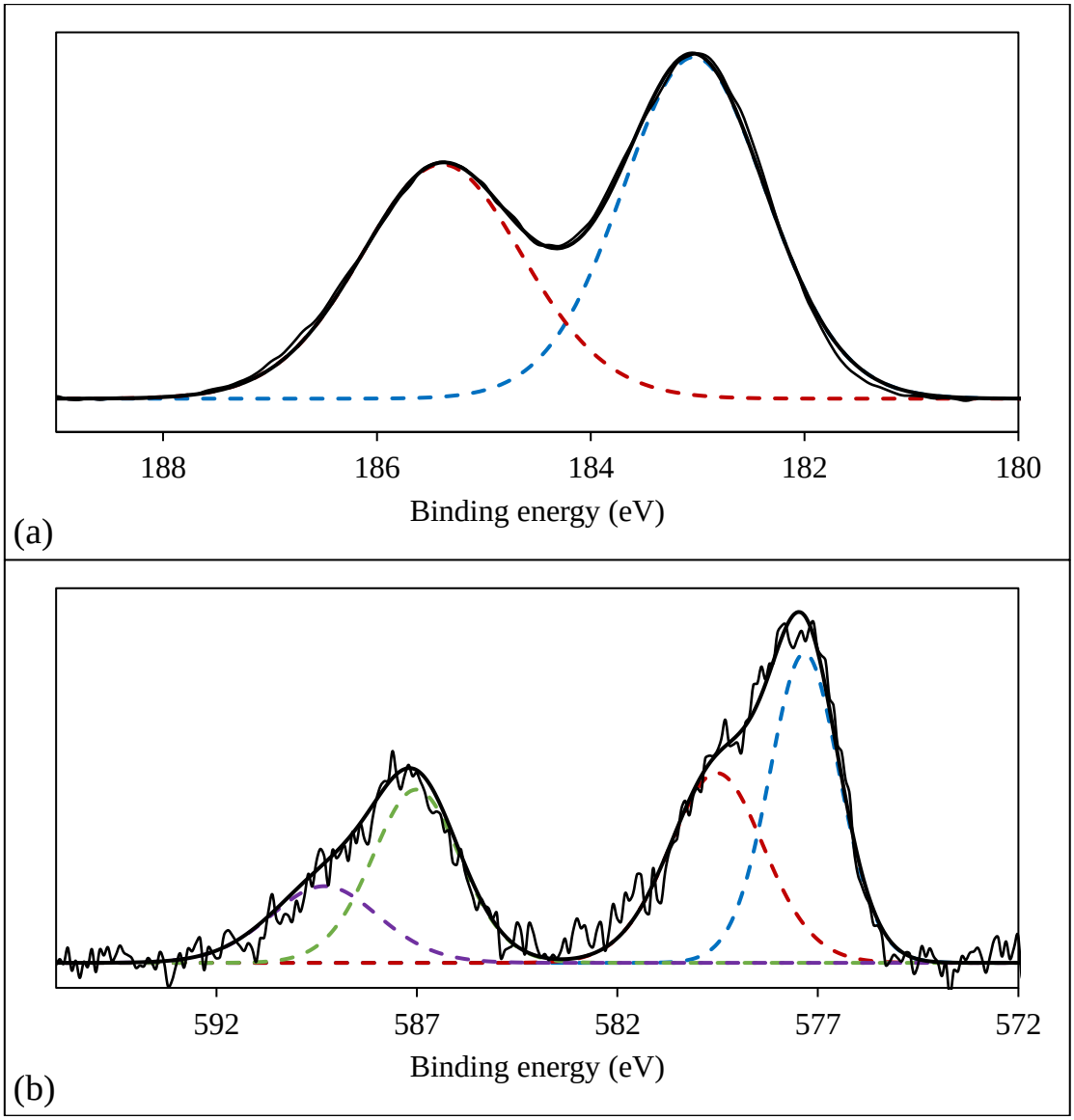


Figure 4-54 High-resolution XPS spectra of the Cr-laden SZAIM with 3-day contact with Cr(VI) solution: (a) Zr3d and (b) Cr2p.

Table 4-18 Binding energies, atomic concentrations and chemical shifts of Cr(VI)-laden SZAIM.

| Assignment | | | ZA | Cr-ZA | SZAIM | Cr-SZAIM | Cr-SZAIM* | Cr(III) std | Cr(VI) std |
|---|---|---|---|---|---|---|---|---|---|
| C1s | C-C, C-H | B.E. (eV) | 284.998 | 284.995 | 284.998 | 284.996 | 285.000 | / | / |
| | | A.C. (%) | 24.22% | 21.05% | 26.28% | 34.27% | 33.78% | / | / |
| | | Shift (eV) | / | -0.003 | / | -0.002 | +0.002 | / | / |
| | C-O, C-N | B.E. (eV) | 286.749 | 286.437 | 286.571 | 286.515 | 286.568 | / | / |
| | | A.C. (%) | 43.21% | 38.33% | 45.17% | 44.35% | 41.40% | / | / |
| | | Shift (eV) | / | -0.312 | / | -0.056 | -0.003 | / | / |
| | C=O | B.E. (eV) | 287.909 | 287.907 | 287.948 | 288.217 | 288.194 | / | / |
| | | A.C. (%) | 13.12% | 28.47% | 16.58% | 13.58% | 16.22% | / | / |
| | | Shift (eV) | / | -0.002 | / | +0.269 | +0.246 | / | / |
| | O=C-O | B.E. (eV) | 289.247 | 289.633 | 289.153 | 289.202 | 289.241 | / | / |
| | | A.C. (%) | 19.45% | 12.16% | 11.97% | 7.80% | 8.61% | / | / |
| | | Shift (eV) | / | +0.386 | / | +0.049 | +0.088 | / | / |
| O1s | O-C | B.E. (eV) | 533.305 | 533.376 | 532.833 | 532.542 | 532.527 | / | / |
| | | A.C. (%) | 51.00% | 52.68% | 94.45% | 86.16% | 84.32% | / | / |
| | | Shift (eV) | / | +0.071 | / | -0.291 | -0.306 | / | / |
| | O=C | B.E. (eV) | 532.563 | 532.505 | 531.059 | 530.672 | 530.647 | / | / |
| | | A.C. (%) | 49.00% | 47.32% | 5.55% | 13.84% | 15.68% | / | / |
| | | Shift (eV) | / | -0.058 | / | -0.387 | -0.412 | / | / |

*Cross section of SZAIM B.E. = binding energy, A.C. = atomic concentration

Table 4-18 (con't) Binding energies, atomic concentrations and chemical shifts of Cr(VI)-laden SZAIM.

| Assignment | | | ZA | Cr-ZA | SZAIM | Cr-SZAIM | Cr-SZAIM* | Cr(III) std | Cr(VI) std |
|---|---|---|---|---|---|---|---|---|---|
| N1s | $NH_2$ | B.E. (eV) | 401.023 | 401.051 | 400.420 | 400.288 | 400.279 | / | / |
| | | A.C. (%) | / | / | 69.74% | 72.80% | 72.30% | / | / |
| | | Shift (eV) | / | +0.028 | / | -0.132 | -0.141 | / | / |
| | $NH_3^+$ | B.E. (eV) | / | / | 402.430 | 402.340 | 402.388 | / | / |
| | | A.C. (%) | / | / | 30.26% | 16.35% | 14.95% | / | / |
| | | Shift (eV) | / | / | / | -0.090 | -0.042 | / | / |
| | $NO_x$ | B.E. (eV) | / | / | / | 407.276 | 407.120 | / | / |
| | | A.C. (%) | / | / | / | 10.85% | 12.75% | / | / |
| Zr3d | Zr 3d 1/2 | B.E. (eV) | 183.278 | 183.193 | 183.028 | 182.707 | 182.771 | / | / |
| | | A.C. (%) | 52.62% | 20.20% | 46.40% | 57.56% | 58.76% | / | / |
| | | Shift (eV) | / | -0.085 | / | -0.321 | -0.257 | / | / |
| | Zr 3d 3/2 | B.E. (eV) | 185.667 | 184.688 | 185.389 | 185.104 | 185.109 | / | / |
| | | A.C. (%) | 40.01% | 48.76% | 35.89% | 42.44% | 41.24% | / | / |
| | | Shift (eV) | / | -0.979 | / | -0.285 | -0.280 | / | / |
| Cr2p | Cr 2p 3/2 of Cr(III) | B.E. (eV) | / | 577.641 | / | 577.342 | 577.500 | 578.408 | / |
| | | A.C. (%) | / | 55.89% | / | 54.72% | 64.88% | / | / |
| | Cr 2p 3/2 of Cr(VI) | B.E. (eV) | / | 580.139 | / | 579.541 | 579.772 | / | 579.808 |
| | | A.C. (%) | / | 44.11% | / | 45.28% | 35.12% | / | / |

*Cross section of SZAIM, B.E. = binding energy, A.C. = atomic concentration

## 4.7 Cr(VI) removal mechanisms

Based on the results of Cr(VI) removal studies, the silica-doped calcium-alginate-immobilized *M. rouxii* (SCAIM) beads has demonstrated the best Cr(VI) removal performance with the highest $\%Cr(VI)_{re}$ among the four tested alginate-based adsorbents. The Cr(VI) removal ability of SCAIM was pH-dependent that the $\%Cr(VI)_{re}$ increased as pH decreased from 7.0 to 1.0. The highest Cr(VI) removal was observed at solution pH 1.0. Moreover, the Cr(VI) removal kinetics indicated that the Cr(VI) concentration in the solution phase sharply decreased after a 2-hour contact with the SCAIM at pH 2.0. The adsorption of Cr(VI) was due to the electrostatic interactions between the anionic Cr(VI) and the protonated surface of SCAIM. A significant amount of Cr(III) was also detected in the solution phase after 2 h, indicating the involvement of Cr(VI) reduction in the whole Cr(VI) removal process. Some of the reduced cationic Cr(III) was desorbed from the positively-charged adsorbent surface due to the electrostatic repulsion.

The SEM-EDX spectrum of Cr-laden SCAIM indicated the presence of chromium, and the oxidation state of the chromium bound on the surface of SCAIM was further confirmed by the high-resolution Cr2p XPS spectrum. The Cr2p 3/2 peak at ~578.0 eV was assigned to the Cr(III) species, so only Cr(III) could be found on the surface of SCAIM. In addition, the results of Cr(VI) removal studies revealed that the dissolved organics released from the MR had neither adsorption nor reducing properties to the Cr(VI). The Cr(VI) reduction only occurred

on the surface of the adsorbent. Furthermore, the Cr2p XPS spectrum showed that only Cr(III) ions were found on the surface of SCAIM after 1-minute contact with the Cr(VI) solution. Thus, it can be concluded that the Cr(VI) ions were rapidly adsorbed onto the protonated surface group and were then promptly reduced to Cr(III) ions on the adsorbent surface under acidic conditions.

FTIR and XPS analyses were employed to identify the surface functional groups on SCAIM participating in the adsorption and reduction of Cr(VI), as well as the adsorption of Cr(III). The characteristic FTIR peaks at 3400, 2900, 1640, 1420, 1030 $cm^{-1}$ affirmed the presence of hydroxyl, aliphatic carbon, carboxylate groups in the SCAIM beads. The N-H bending signal at 1550 $cm^{-1}$ demonstrated that the SCAIM beads were rich in nitrogen functional groups. The SCAIM was a composite adsorbent consisting of a fungal biomass (*M. rouxii*) immobilized in a silica-doped calcium-alginate hydrogel matrix. Consequently, the nitrogen functional groups came from the amine and amide groups in the cell wall of *M. rouxii*, which was reported to contain significant amounts of chitosan and chitin in its cell wall, reaching as high as 35% of its dry weight (Sudarshan et al., 1992). Secondly, the nitrogen functional groups could also come from the ethylenediamine groups in the doped silica. Moreover, the N1s XPS spectrum of SCAIM was resolved into two peaks at 400.109 and 402.143 eV, which belonged to the uncharged ($-NH_2$) and protonated ($-NH_3^+$) amine groups, respectively. Under acidic conditions, the nitrogen functional groups would be protonated.

Additionally, the C1s and O1s XPS spectra illustrated the presence of hydroxyl groups in the polysaccharide-based alginate matrix, which would be protonated too under acidic conditions.

$$-\mathrm{NH_2} + \mathrm{H^+} \rightarrow -\mathrm{NH_3^+}$$

$$-\mathrm{NHCH_2CH_2NH_2} + \mathrm{H^+} \rightarrow -\mathrm{NHCH_2CH_2NH_3^+}$$

$$-\mathrm{OH} + \mathrm{H^+} \rightarrow -\mathrm{OH_2^+}$$

In the pH range of 1.0 to 5.0, the Cr(VI) species mainly exists in the forms of $HCrO_4^-$ and $Cr_2O_7^{2-}$ with $HCrO_4^-$ as the predominant species. These Cr(VI) anions ($HCrO_4^-$ and $Cr_2O_7^{2-}$) would be actively adsorbed by the positively-charged amine, ethylenediamine and hydroxyl groups on the SCAIM beads through the electrostatic interactions.

$$-\mathrm{NH_3^+} + \mathrm{HCrO_4^-} \rightarrow -\mathrm{NH_3^+} \cdots \mathrm{HCrO_4^-}$$

$$2(-\mathrm{NH_3^+}) + \mathrm{Cr_2O_7^{2-}} \rightarrow -\mathrm{NH_3^+} \cdots \mathrm{Cr_2O_7^{2-}} \cdots \mathrm{NH_3^+} -$$

$$-\mathrm{NHCH_2CH_2NH_3^+} + \mathrm{HCrO_4^-} \rightarrow -\mathrm{NHCH_2CH_2NH_3^+} \cdots \mathrm{HCrO_4^-}$$

$$2(-\mathrm{NHCH_2CH_2NH_3^+}) + \mathrm{Cr_2O_7^{2-}} \rightarrow -\mathrm{NHCH_2CH_2NH_3^+} \cdots \mathrm{Cr_2O_7^{2-}} \cdots \mathrm{NH_3^+CH_2CH_2NH} -$$

$$-\mathrm{OH_2^+} + \mathrm{HCrO_4^-} \rightarrow -\mathrm{OH_2^+} \cdots \mathrm{HCrO_4^-}$$

$$2(-\mathrm{OH_2^+}) + \mathrm{Cr_2O_7^{2-}} \rightarrow -\mathrm{OH_2^+} \cdots \mathrm{Cr_2O_7^{2-}} \cdots \mathrm{OH_2^+}$$

The hydroxyl groups in the alginate matrix could act as the electron-donor groups for reducing Cr(VI) (Ramrakhiani et al., 2011; Yang et al., 2018). It was important to mention that the adsorption-coupled reduction preferably occurred in the acidic environment (pH ≤ 4). The proton played a crucial role in protonating the surface groups and catalyzing the Cr(VI)

reduction.

$$4(-NH_3^+ \cdots HCrO_4^-) + 3(-CH_2OH) + 16H^+ \rightarrow 4(-NH_3^+) + 4Cr(III) + 3(-COOH) + 13H_2O$$

$$4(-NH_3^+ \cdots Cr_2O_7^{2-} \cdots NH_3^+ -) + 3(-CH_2OH) + 16H^+ \rightarrow 4(-NH_3^+) + 4Cr(III) + 3(-COOH) + 11H_2O$$

As mentioned before, the Cr 2p XPS spectrum of Cr-laden SCAIM confirmed that all the adsorbed Cr on the surface of the fungal biomass was in the form of Cr(III). The binding configuration of Cr(III) ions on the surface of SCAIM was investigated using XPS and FTIR. After the adsorption of Cr on SCAIM, the O=C-O peak in the C1s spectrum and the O=C peak in the O1s spectrum showed a positive shifting in binding energy, indicating that the reduced Cr(III) ions formed a coordination complex with the carboxylate groups of the alginate matrix and biomass materials. The FTIR spectrum of the Cr-laden SCAIM also confirmed the formation of monodentate Cr(III)-carboxylate complex with the carboxylate groups in the SCAIM beads.

$$Cr(III) + 3(-COOH) \rightarrow (-COO)_3Cr(III) + 3H^+$$

The monodentate Cr(III)-carboxylate complexation structure was supported by the works of Menakbi et al. (2016) which studied the hydrated structure complexation of trivalent metal cations to mannuronate type alginate using the quantum chemical density functional theory (DFT) based method. The computation results suggested that the monodentate binding mode

was found to be energetically more stable for trivalent cation since the $–(COO^-)\cdots M^{3+}$ bond in alginate was shorter than the $–OH\cdots M^{3+}$ bond in water molecules.

Apart from the complexation, the ion-exchange mechanism also involved in the Cr(III) adsorption. The results of Cr(VI) removal studies revealed the continuous release of Ca(II) ions from the SCAIM to the solution phase during the Cr(VI) removal process. Comparison of EDX spectra and XPS spectra before and after Cr adsorption established that Ca(II) ions in the calcium alginate were replaced by the Cr(III) ions through the ion-exchange mechanism.

Based on the computation results (Menakbi et al., 2016), the mannuronate groups of alginate were shown to exhibit significantly stronger binding to the trivalent cations than the divalent cations. The Cr(III) and protons would exchange with Ca(II) ions via ion exchange mechanism. The results of Ca(II) leaching reported that 85.5% of Cr(III) was adsorbed through the complexation, while the remaining 14.5% was due to the ion-exchange mechanism.

$$2\mathrm{Cr(III)} + 3[(-\mathrm{COO})_2\mathrm{Ca(II)}] \rightarrow 2[(-\mathrm{COO})_3\mathrm{Cr(III)}] + 3\mathrm{Ca(II)}$$

On the basis of these findings, the adsorption-coupled reduction mechanism of Cr(VI) by the SCAIM was proposed (Figure 4-55). First, the Cr(VI) anions were adsorbed onto the protonated functional groups (e.g., amine groups on the surface of *M. rouxii*, hydroxyl groups of the alginate chains, and ethylenediamine groups in the silica particles) on the adsorbent surface through electrostatic interactions. Second, the adsorbed Cr(VI) ions were transferred to the adjacent electron-donor groups (e.g., hydroxyl groups) and reduced to Cr(III) ions. Third,

the reduced Cr(III) ions were adsorbed on the carboxylate groups by either complexation or ion-exchange mechanism. Some of the Cr(III) ions were repelled from the positively-charged adsorbent surface due to the electrostatic repulsion. After the Cr(VI) reduction, the Cr(VI) adsorption sites were free to adsorb new Cr(VI) ions.

For the case of SZAIM beads, the Cr2p spectrum demonstrated that both Cr(VI) and Cr(III) ions were found on the surface after the Cr(VI) removal. The presence of Cr(III) indicated that the immobilized *M. rouxii*, alginate chains and silica particles in the SZAIM could remove the Cr(VI) ions through the adsorption-coupled reduction mechanism as discussed previously. In addition, the Cr(III) ions were adsorbed by the carboxylate groups on the surface of the biomass through the complexation mechanism. The ion-exchange mechanism was not involved in the Cr(III) adsorption since there was insignificant Zr(IV) leaching during the 3-day Cr adsorption process. The trivalent Cr(III) could not replace the tetravalent Zr(IV) ions in zirconium alginate since the Zr(IV) exhibited significantly stronger affinity to the mannuronate groups of alginate.

The occurrence of Cr(VI) could be explained by the electrostatic interaction between the anionic Cr(VI) and the cationic tetravalent Zr(IV) in the zirconium alginate, which was suggested by the negative shifting in the binding energy of Zr3d signals in the Cr-laden SZAIM.

$$-(\mathrm{COO})_4\mathrm{Zr(IV)} + \mathrm{HCrO_4^-} \rightarrow -(\mathrm{COO})_4\mathrm{Zr(IV)} \cdots \mathrm{HCrO_4^-}$$

Such binding interactions were so strong that the adsorbed Cr(VI) ions could not be transferred to the adjacent electron-donor groups for the subsequent reduction reaction.

Therefore, there are two possible Cr(VI) removal mechanisms: (i) direct adsorption of Cr(VI) anions without reduction; and (ii) adsorption-coupled reduction.

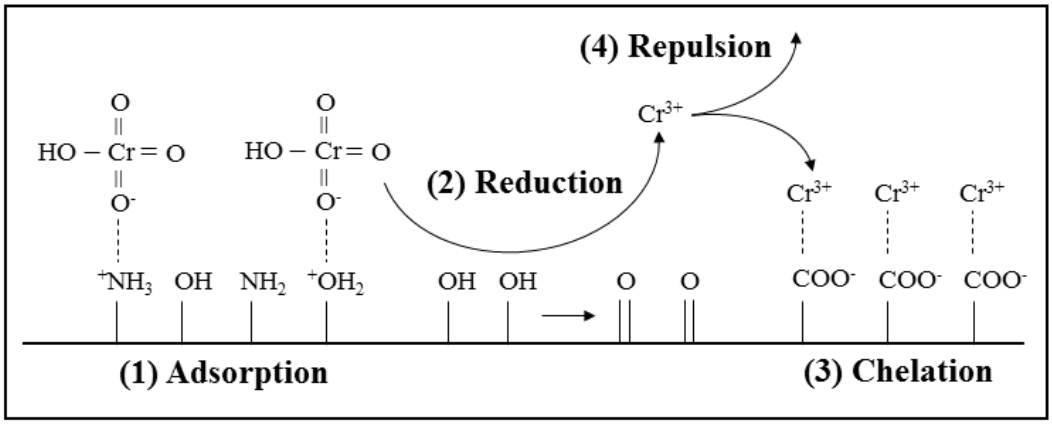


Figure 4-55 The Cr(VI) adsorption-coupled reduction mechanism

# 5. Removal of Cr(VI) by Hydrothermal Carbonized *M. rouxii*

# 5.1 Physical and basic chemical properties of hydrothermal carbonized *M. rouxii*

## 5.1.1 $N_2$ adsorption/desorption isotherm

The surface area and porosity of MR, HTC-MR, HTC-MR-CaFe, 0.5DEA-HTC-MR and 0.5PEI-HTC-MR were investigated by the $N_2$ adsorption/desorption isotherm analysis. The porosity characteristics of the adsorbents are tabulated in Table 5-1. As expected, the raw MR showed a small total BET surface area of 10.11 ± 0.33 $m^2/g$ and a total pore volume of 2.43E-2 ± 6.17E-4 $cm^3/g$. The total BET surface area of the HTC-MR was 35.84 ± 1.65 $m^2/g$, which was 3.5 times as high as that of the raw MR. The polymeric cell components (e.g., chitosan, protein and polysaccharide) were depolymerized into small monomeric molecules under the hydrothermal condition. Those monomers were then re-polymerized randomly through the dehydration and condensation reaction, so the hydrochars would have a loose structure. Moreover, the direct solid conversion of the biomaterial into carbonaceous materials would involve in the formation of the primary hydrochars. Some dissolved materials might leach out from the solid biomaterials, so the HTC-MR showed a larger total pore volume of 2.43E-2 ± 6.17E-4 $cm^3/g$ than that of MR (0.191 ± 0.009 $cm^3/g$).

A reduction in the surface area of HTC-MR was observed in the hydrochars coupled with different amine-containing modifying agents (e.g., DEA, PEI). The total BET surface areas of 0.5DEA-HTC-MR and 0.5PEI-HTC-MR was 27.78 ± 0.90 and 27.63 ± 0.23 $m^2/g$, respectively,

which was lower than that of HTC-MR. This was because the DEA molecules would act as a cross-linker facilitating the aggregation of the small hydrochars particles. The particle size of the HTC materials was confirmed by the dynamic light scattering technique. It will be discussed in Section 5.1.2. The highly cross-linked structure of 0.5DEA-HTC-MR would result in a low total pore volume (7.75E-2 ± 2.98E-4 $cm^3/g$).

The hydrothermal carbonized *M. rouxii* was also prepared in the presence of a eutectic salt mixture of $CalCl_2$ and $FeCl_3$. The obtained hydrochars (HTC-MR-CaFe) was expected to have a microporous characteristic. However, the total BET surface area of HTC-MR-CaFe (25.96 ± 0.05 $m^2/g$) was smaller than that of HTC-MR (35.84 ± 1.65 $m^2/g$). The HTC-MR-CaFe exhibited even smaller total pore volume (0.191 ± 0.009 $cm^3/g$) than that of HTC-MR (5.31E-2 ± 5.40E-4 $cm^3/g$). The low degree of porosity in HTC-MR-CaFe would be attributed to the high degree of carbonization under the drastic hypersaline condition.

The pore surface areas of different pore size ranges were obtained from the Barrett-Joyner-Halenda (BJH) analysis. The results showed that the pore area of HTC materials was mainly contributed by the mesopore with the mean pore radius of 2.870 to 3.105 nm. The mesopore areas of MR, HTC-MR, HTC-MR-CaFe, 0.5DEA-HTC-MR and 0.5PEI-HTC-MR were 10.85 ± 0.35, 43.01 ± 1.44, 26.38 ± 0.19, 34.06 ± 0.86 and 34.68 ± 0.03 $m^2/g$, respectively. The HTC-MR-CaFe showed a negligible micropore area of 0.758 ± 0.056 $m^2/g$, which was much smaller than that of HTC-MR (7.228 ± 0.367 $m^2/g$). The microporous characteristic could not be introduced

to HTC-MR under hypersaline condition.

Table 5-1 BET surface area and BJH pore volume of MR, HTC-MR, HTC-MR-CaFe, 0.5DEA-HTC-MR and 0.5PEI-HTC-MR.

| | | MR | HTC-MR | HTC-MR-CaFe | 0.5DEA-HTC-MR | 0.5PEI-HTC-MR |
|---|---|---|---|---|---|---|
| Particle Size (nm) | | 4995 ± 511 | 2314 ± 356 | 2082 ± 360 | 4213 ± 185 | 2036 ± 42 |
| Total BET surface area[a] ($m^2/g$) | | 10.11 ± 0.33 | 35.84 ± 1.65 | 25.96 ± 0.05 | 27.78 ± 0.90 | 27.63 ± 0.23 |
| External surface area[b] ($m^2/g$) | | 1.201 ± 0.012 | 2.593 ± 0.017 | 2.882 ± 0.017 | 1.424 ± 0.032 | 2.947 ± 0.143 |
| Total pore volume[c] ($cm^3/g$) | | 2.43E-2 ± 6.17E-4 | 0.191 ± 0.009 | 5.31E-2 ± 5.40E-4 | 7.75E-2 ± 2.98E-4 | 0.134 ± 0.003 |
| Pore Volume[d] ($cm^3/g$) | Micropore (< 2 nm) | 1.20E-3 ± 9.55E-5 | 9.45E-3 ± 1.09E-3 | 2.63E-3 ± 7.85E-5 | 5.04E-3 ± 4.25E-4 | 6.82E-3 ± 6.77E-4 |
| | Mesopore (2 - 50 nm) | **1.68E-2 ± 5.98E-4** | **8.51E-2 ± 2.93E-3** | **3.99E-2 ± 2.89E-4** | **5.52E-2 ± 9.88E-4** | **6.67E-2 ± 3.66E-4** |
| | Macropore[e] (> 50 nm) | 6.73E-3 ± 4.31E-5 | **0.1032 ± 0.006** | **1.16E-2 ± 8.03E-4** | 1.99E-2 ± 7.62E-4 | **6.96E-2 ± 1.66E-3** |
| Pore Area[d] ($m^2/g$) | Micropore (< 2 nm) | 0.995 ± 0.039 | 3.504 ± 0.235 | 2.345 ± 0.145 | 3.098 ± 0.064 | 1.383 ± 0.083 |
| | Mesopore (2 - 50 nm) | **10.85 ± 0.35** | **43.01 ± 1.44** | **26.38 ± 0.19** | **34.06 ± 0.86** | **34.68 ± 0.03** |
| | Macropore (> 50 nm) | 0.438 ± 0 | 7.228 ± 0.367 | 0.758 ± 0.056 | 1.311 ± 0.045 | 4.894 ± 0.070 |
| Mean pore radius (nm) | | 2.965 ± 0.007 | 3.105 ± 0.007 | 2.870 ± 0.099 | 2.880 ± 0.184 | 3.090 ± 0.368 |

[a]Specific surface area was calculated with the Brunauer-Emmett-Teller (BET) analysis; [b]The external surface area was calculated based on the particle size; [c]Total pore volume was calculated from single point adsorption at $P/P_0$ =0.99; [d]The pore volumes of mesopore and macropore, and pore surface areas in each pore size range were obtained from Barrett-Joyner-Halenda (BJH) analysis; and [e]The micropore volume was obtained from the Horvath-Kawazoe (Original HK) method.

### 5.1.2 Dynamic light scattering

The particle size of HTC materials was measured using Nano ZS zetasizer (Malvern Panalytical, UK), and the results are listed in Table 5-1. The particle sizes of MR, HTC-MR, 0.5DEA-HTC-MR, 0.5PEI-HTC-MR and $Fe_3O_4$-0.5PEI-HTC-MR were 4995 ± 511, 2314 ± 356, 4213 ± 185, 2036 ± 42 and 1403 ± 503 nm, respectively. The fungal biomass (MR) was pulverized using a laboratory blender following by sieving using 180 μm sieve, so its size was relatively large. The hydrothermal carbonization of fungal biomass led to a great reduction in particle size because the structural components of MR were degraded into small molecules under hydrothermal condition. The small molecules then polymerized to form hydrochars. The size of hydrochars depended on the growth rate of hydrochars and duration of the hydrothermal process. Besides, co-carbonization of MR with DEA resulted in an increase in the size of HTC-MR, since the DEA molecule had two hydroxyl groups which would act as a cross-linker of the growing hydrochars particles. Meanwhile, the 0.5PEI-HTC-MR showed similar particle size to HTC-MR so the PEI molecules would be coated on the surface of HTC-MR and did not affect the size of HTC-MR. The incorporation of iron oxide nanoparticles would reduce the size of 0.5PEI-HTC-MR because the $Fe_3O_4$ particles provided extra nucleation sites for the growth of hydrochars.

### 5.1.3 Elemental analysis (EA)

The elemental compositions of HTC materials are listed in Table 5-2. The carbon contents of MR and HTC-MR were 41.69 ± 0.03% and 51.24 ± 0.12%, respectively. It was found that the hydrothermal carbonization process increased the carbon content of MR, while the nitrogen content remained unchanged. Besides, the oxygen content of MR was reduced after the hydrothermal process due to the dehydration and decarboxylation reactions of the biomass materials. After the HTC treatment, the pale-yellow MR became a brown hydrochars, indicating the partial carbonization of biomass materials. The yield of HTC-MR was 40.64%, so nearly 60% of the organic materials were lost in the HTC solution residue or as gas. As shown in Section 5.2.1, the Cr(VI) removal capacity ($Q_{Cr(VI)}$) of HTC-MR (158.4 ± 0.8 mg/g) was 2 times of that of MR (79.54 ± 1.19 mg/g). A portion of the biomass materials, which was not responsible for Cr(VI) removal, was removed in the hydrothermal process.

Six different amine-containing modifying agents including acrylamide (AA), diethanolamine (DEA), polyethyleneimine (PEI), urea, ammonium hydroxide ($NH_4OH$) and triethylenetetramine (TETA), were co-carbonized with *M. rouxii* in order to enhance the Cr(VI) removal capacity of HTC-MR. The results showed that most of the modifying agents could not enhance the nitrogen content of HTC-MR, except the ammonium hydroxide. It should be noted that the 0.5DEA-HTC-MR and 0.5PEI-HTC-MR exhibited an improved Cr(VI) removal capacity ($Q_{Cr(VI)}$) over HTC-MR, however, the 0.5DEA-HTC-MR and 0.5PEI-HTC-MR

showed a lower nitrogen content than the HTC-MR. This meant that the Cr(VI) removal capacity of HTC-MR was not directly proportional to the nitrogen content, but was dependent on the nature of nitrogen groups. The speciation of the nitrogen groups on the adsorbents would be further investigated by the XPS analysis (Section 5.5.3). Apart from the nitrogen functional groups, the oxygen functional groups would also participate in the Cr(VI) adsorption. The results of Cr(VI) removal studies (Section 5.2.1) showed that the 0.5DEA-HTC-MR and 0.5PEI-HTC-MR exhibited excellent Cr(VI) removal capabilities ($Q_{Cr(VI)}$) of 209.5 ± 2.5 and 239.3 ± 2.7 mg/g, respectively, so the hydrothermal carbonization processes for the preparation of HTC-MR, 0.5DEA-HTC-MR and 0.5PEI-HTC-MR were optimized with different hydrothermal reaction parameters, such as temperature, time and dosage of modifying agent.

Temperature is a crucial parameter that determines the reaction type and controls the reaction rate of the hydrothermal process. The HTC-MR, 0.5DEA-HTC-MR and 0.5PEI-HTC-MR were prepared under various hydrothermal temperatures (160, 200 and 240ºC). As the hydrothermal temperature increased from 160ºC to 240ºC, the carbon content of HTC-MR increased from 47.48 ± 0.06% to 62.21 ± 0.25%, while the nitrogen content decreased from 8.96 ± 0.01% to 7.37 ± 0.16%. Meanwhile, the oxygen content of HCT-MR decreased from 35.76 ± 0.14% to 22.77 ± 0.31%. The increased carbon content confirmed the increase in the degree of carbonization under elevated temperature. The oxygen functional groups and nitrogen functional groups in the HTC-MR were decomposed at a higher temperature, leading

to a decrease in the oxygen and nitrogen content. Similarly, the nitrogen content of 0.5PEI-HTC-MR decreased from 8.48 ± 0.13% to 7.17 ± 0.01% with increasing temperature from 160ºC to 240ºC (Section 5.2.2). At the same time, the carbon content increased from 47.88 ± 0.71% to 50.34 ± 0.07%. The reduction in nitrogen content could be explained by the deamination of the polyethyleneimine and biomass materials at high temperature (Joo-Hee et al., 2009). It is worth mentioning that the nitrogen and oxygen contents of 0.5DEA-HTC-MR remained unchanged with different hydrothermal temperatures. The loss of nitrogen functional groups and oxygen functional groups at the higher temperature was compensated by the functionalization of amine and hydroxyl groups due to the intermolecular dehydration between the diethanolamine and hydrochars.

Hydrothermal reaction time affects the extent of reaction and hence controls the composition of HTC materials. A longer reaction time resulted in small changes in the nitrogen, carbon and oxygen contents of the HTC-MR and 0.5PEI-HTC-MR. The nitrogen content of 0.5DEA-HTC-MR was even unchanged with the increase in the hydrothermal reaction time. However, the $Q_{Cr(VI)}$ value of HTC-MR, 0.5DEA-HTC-MR and 0.5PEI-HTC-MR was greatly influenced by the reaction time (Section 5.2.3). The $Q_{Cr(VI)}$ was in fact related to the number of effective adsorption sites rather than directly proportional to the total amount of nitrogen and oxygen functional groups. Moreover, 0.5DEA-HTC-MR and 0.5PEI-HTC-MR showed the maximum $Q_{Cr(VI)}$ at 12 h reaction time. The excessive dehydration and carbonization of

hydrochars would result in the formation of stable oxygen from reactive surface groups (He et al., 2013).

The diethanolamine modified HTC-MR (DEA-HTC-MR) was prepared with different DEA dosages of 0.1, 0.25, 0.5 and 1.0 g DEA/g MR. The oxygen content of 0.1DEA-HTC-MR, 0.25DEA-HTC-MR, 0.5DEA-HTC-MR and 1.0DEA-HTC-MR was 33.07 ± 0.36, 38.13 ± 0.37, 45.04 ± 0.28 and 42.77 ± 0.20%, respectively. The highest oxygen content was obtained in 0.5DEA-HTC-MR, which showed the highest Cr(VI) removal capacity of 219.2 ± 1.9 mg/g. Meanwhile, the trend of nitrogen content was opposite to the trend of $Q_{Cr(VI)}$. These results proposed that the oxygen functional groups (e.g., hydroxyl and carbonyl groups) would also participate in the Cr(VI) adsorption apart from the nitrogen functional groups. The amount of oxygen functional groups was generally much higher than nitrogen groups, so the oxygen functional groups would be the main Cr(VI) adsorption sites on HTC materials.

The oxygen content of DEA-HTC-MR increased with the increase in DEA dosage from 0.1 to 0.5 g DEA/g MR. This could be explained by the reaction mechanism of DEA towards the HTC-MR. There are two hydroxyl groups in a DEA molecule, and the surface of hydrochars particles (primary and secondary char) are often rich in hydroxyl groups. Therefore, the DEA molecules would be grafted onto the surface of HTC-MR through the intermolecular dehydration. After dehydration reaction, there is a remaining hydroxyl group in the grafted DEA molecules, which would be active for successive dehydration reactions as well as the

Cr(VI) adsorption. In addition, the DEA could act as a cross-linking agent of the growing polymers or secondary chars. This would introduce some ether groups to the DEA-HTC-MR. Moreover, the deamination reaction of hydrochars would be accelerated in the alkaline condition. The nitrogen content of DEA-HTC-MR decreased with the increase of DEA dosage.

The effect of polyethyleneimine (PEI) dosage on the nitrogen content of PEI-HTC-MR was also investigated by varying the PEI dosage from 0.1 to 1.0 g PEI/g MR. The surface of hydrochars was functionalized with the amine groups by the grafting of PEI molecules on HTC-MR. In the proposed reaction mechanism, the amine groups of PEI molecules would react with the aldehyde groups on the surface of hydrochars. However, the nitrogen content of PEI-HTC-MR decreased when the PEI dosage increased from 0.1 to 0.5 g DEA/g MR. It is surprising that the lowest nitrogen content was achieved in 0.5PEI-HTC-MR, which however showed the highest $Q_{Cr(VI)}$ of 243.9 ± 1.2 mg/g. The 0.5PEI-HTC-MR exhibited the highest oxygen contents (36.70 ± 0.19%), so Cr(VI) would be also adsorbed onto the oxygen functional groups (e.g., hydroxyl and carboxylic acid groups) on the 0.5PEI-HTC-MR.

To investigate the effect of molecular weight of PEI on the performance of Cr(VI) removal, the 0.5PEI(800)-HTC-MR and 0.5PEI(25000)-HTC-MR were prepared using the PEI with weight average molecular weight of ~800 and ~25000 g/mol, respectively. The nitrogen content of 0.5PEI(25000)-HTC-MR (12.16 ± 1.03%) was significantly higher than that of 0.5PEI(800)-HTC-MR (7.24 ± 0.03%). However, the 0.5PEI(25000)-HTC-MR (23.72 ± 4.87%) showed

lower oxygen content than 0.5PEI(800)-HTC-MR (36.70 ± 0.19%). Both the nitrogen functional groups and oxygen functional groups would participate in the Cr(VI) removal, so 0.5PEI(25000)-HTC-MR showed very similar Cr(VI) removal capacity to 0.5PEI(800)-HTC-MR. Increasing the molecular weight of PEI had no effect on the Cr(VI) removal performance of PEI-HTC-MR. The PEI with weight average molecular weight of 800 g/mol was used as the amine-containing modifying agent throughout the study.

The HTC-MR-CaFe was prepared through the hydrothermal carbonization of *M. rouxii* in the presence of eutectic salt of $CaCl_2/FeCl_3$. The nitrogen content of HTC-MR-CaFe (2.42 ± 0.01%) was lower than that of HTC-MR (8.49 ± 0.17%), while the oxygen content of HTC-MR-CaFe was comparable to the HTC-MR. However, the HTC-MR-CaFe (70.35 ± 2.96 mg/g) showed a much lower Cr(VI) removal capacity than the HTC-MR (158.4 ± 0.8 mg/g). The low nitrogen content in HTC-MR-CaFe could be explained by the fact that the decomposition of nitrogen-containing functional groups (e.g., amine, amide and pyridine groups) was favored in the hypersaline condition. Dehydration reaction was also favored under hypersaline condition. The reactive oxygen functional groups, such as hydroxyl and carboxylic acid, were removed, while the stable oxygen functional groups (e.g. ether) were formed. In addition, the high carbon content of 57.11 ± 0.60% was obtained in HTC-MR-CaFe, suggesting the high degree of carbonization in the hypersaline condition.

The N, C and H contents of $Fe_3O_4$-0.5PEI-HTC-MR were significantly reduced after the

incorporation of $Fe_3O_4$. Moreover, the $Q_{Cr(VI)}$ 0.5PEI-HTC-MR was reduced after the incorporation of $Fe_3O_4$ since the $Fe_3O_4$ showed lower Cr(VI) removal ability than the 0.5PEI-HTC-MR. The O content of $Fe_3O_4$-0.5PEI-HTC-MR could not be estimated since it had a high content of $Fe_3O_4$. The Fe content of $Fe_3O_4$-0.5PEI-HTC-MR could be determined by the microwave digestion followed by the ICP-OES measurement.

Table 5-2 Elemental composition of HTC materials.

| Adsorbent | N (%) | C (%) | H (%) | S (%) | O (%) | $Q_{Cr(VI)}$ (mg/g) |
|---|---|---|---|---|---|---|
| MR | 8.49 ± 0.01 | 41.69 ± 0.03 | 6.65 ± 0.07 | 0.45 ± 0.04 | 42.84 ± 0.33 | 79.54 ± 1.19 |
| HTC-MR | 8.49 ± 0.17 | 51.24 ± 0.12 | 7.41 ± 0.02 | 0.11 ± 0.02 | 32.47 ± 0.21 | 158.4 ± 0.8 |
| 0.5AA-HTC-MR | 7.33 ± 0.07 | 50.80 ± 0.02 | 7.60 ± 0.03 | 0.41 ± 0.03 | 33.86 ± 0.08 | 165.8 ± 4.0 |
| 0.5DEA-HTC-MR | 6.82 ± 0.09 | 40.70 ± 0.21 | 7.28 ± 0.16 | 0.16 ± 0.05 | 45.04 ± 0.28 | 209.5 ± 2.5 |
| 0.5PEI-HTC-MR | 7.24 ± 0.03 | 47.78 ± 0.07 | 8.22 ± 0.16 | 0.06 ± 0.07 | 36.70 ± 0.19 | 239.3 ± 2.7 |
| 0.5Urea-HTC-MR | 6.34 ± 0.23 | 41.76 ± 0.25 | 7.74 ± 0.17 | 0.17 ± 0.07 | 43.99 ± 0.39 | 125.0 ± 3.1 |
| $NH_4OH$-HTC-MR | 9.33 ± 0.11 | 50.57 ± 1.06 | 7.18 ± 0.11 | 0.41 ± 0.03 | 32.50 ± 0.83 | 208.9 ± 2.3 |
| 0.5TETA-HTC-MR | 7.10 ± 0.04 | 45.33 ± 0.21 | 7.35 ± 0.09 | 0.10 ± 0.05 | 40.13 ± 0.28 | 193.8 ± 7.9 |
| 160C-HTC-MR | 8.96 ± 0.01 | 47.48 ± 0.06 | 7.57 ± 0.12 | 0.23 ± 0.03 | 35.76 ± 0.14 | 121.4 ± 1.9 |
| 240C-HTC-MR | 7.37 ± 0.16 | 62.21 ± 0.25 | 7.54 ± 0.02 | 0.11 ± 0.09 | 22.77 ± 0.31 | 207.5 ± 1.7 |
| 160C-0.5DEA-HTC-MR | 7.03 ± 0.05 | 41.94 ± 0.07 | 7.54 ± 0.07 | 0.00 ± 0.00 | 43.49 ± 0.11 | 169.7 ± 0.2 |
| 240C-0.5DEA-HTC-MR | 7.01 ± 0.21 | 45.80 ± 1.01 | 7.43 ± 0.12 | 0.03 ± 0.04 | 39.73 ± 1.04 | 180.8 ± 0.7 |
| 160C-0.5PEI-HTC-MR | 8.48 ± 0.13 | 47.88 ± 0.71 | 8.26 ± 0.08 | 0.01 ± 0.01 | 35.37 ± 0.73 | 200.2 ± 2.7 |
| 240C-0.5PEI-HTC-MR | 7.17 ± 0.01 | 50.34 ± 0.07 | 8.37 ± 0.11 | 0.00 ± 0.00 | 34.12 ± 0.13 | 230.0 ± 1.7 |
| 6h-HTC-MR | 8.37 ± 0.04 | 51.09 ± 0.36 | 7.67 ± 0.28 | 0.67 ± 0.39 | 32.20 ± 0.60 | 145.4 ± 4.4 |
| 18h-HTC-MR | 7.99 ± 0.16 | 55.49 ± 0.03 | 7.38 ± 0.20 | 0.33 ± 0.04 | 28.81 ± 0.26 | 173.4 ± 6.3 |
| 6h-0.5DEA-HTC-MR | 7.09 ± 0.01 | 42.30 ± 0.08 | 7.54 ± 0.07 | 0.00 ± 0.00 | 43.09 ± 0.11 | 183.4 ± 1.5 |
| 18h-0.5DEA-HTC-MR | 7.18 ± 0.08 | 44.36 ± 0.23 | 7.63 ± 0.07 | 0.01 ± 0.01 | 40.82 ± 0.25 | 180.6 ± 5.4 |
| 6h-0.5PEI-HTC-MR | 7.57 ± 0.07 | 48.32 ± 0.11 | 7.75 ± 0.44 | 0.00 ± 0.00 | 36.36 ± 0.46 | 209.7 ± 8.8 |
| 18h-0.5PEI-HTC-MR | 7.24 ± 0.09 | 49.57 ± 0.22 | 8.37 ± 0.01 | 0.00 ± 0.00 | 34.82 ± 0.24 | 226.0 ± 4.4 |
| 0.1DEA-HTC-MR | 8.25 ± 0.12 | 50.43 ± 0.33 | 7.91 ± 0.08 | 0.34 ± 0.02 | 33.07 ± 0.36 | 148.6 ± 2.2 |
| 0.25DEA-HTC-MR | 7.57 ± 0.07 | 46.42 ± 0.32 | 7.68 ± 0.17 | 0.20 ± 0.01 | 38.13 ± 0.37 | 167.6 ± 2.9 |
| 1.0DEA-HTC-MR | 7.06 ± 0.03 | 42.54 ± 0.20 | 7.62 ± 0.01 | 0.01 ± 0.01 | 42.77 ± 0.20 | 186.9 ± 1.7 |
| 0.1PEI-HTC-MR | 8.12 ± 0.04 | 49.78 ± 0.19 | 8.16 ± 0.13 | 0.22 ± 0.01 | 33.72 ± 0.23 | 198.5 ± 3.4 |
| 0.25PEI-HTC-MR | 7.44 ± 0.04 | 48.99 ± 0.13 | 8.36 ± 0.01 | 0.29 ± 0.15 | 34.92 ± 0.20 | 225.5 ± 1.2 |
| 1.0PEI-HTC-MR | 7.69 ± 0.12 | 50.19 ± 0.94 | 8.59 ± 0.26 | 0.00 ± 0.00 | 33.53 ± 0.19 | 206.2 ± 1.9 |
| 0.5PEI(25000)-HTC-MR | 12.16 ± 1.03 | 54.04 ± 4.67 | 10.08 ± 0.93 | 0.00 ± 0.00 | 23.72 ± 4.87 | 255.5 ± 0.7 |
| HTC-MR-CaFe | 2.42 ± 0.01 | 57.11 ± 0.60 | 5.64 ± 0.14 | 0.89 ± 0.08 | 33.95 ± 0.67 | 70.35 ± 2.96 |
| $Fe_3O_4$-0.5PEI-HTC-MR | 5.27 ± 0.13 | 33.62 ± 0.35 | 5.78 ± 0.09 | 0.07 ± 0.06 | / | 178.2 ± 2.8 |

## 5.2 Preparation of hydrothermal carbonized *M. rouxii*

### 5.2.1 Effect of the modifying agent

Hydrothermal carbonized *M. rouxii* (HTC-MR) was successfully prepared by hydrothermal treatment of 50 g/L *M. rouxii* (MR) suspension at 200ºC for 12 h, and its Cr(VI) removal performance was evaluated. Figure 5-1 shows the Cr(VI) removal capacity ($Q_{Cr(VI)}$), total Cr adsorption capacity ($q_{tot}$) and amount of Cr(III) release ($Cr(III)_{rel}$) of the raw *M. rouxii*, hydrothermal carbonized *M. rouxii* (HTC-MR) and amino-functionalized HTC-MR. The $Q_{Cr(VI)}$ value of HTC-MR was 158.4 ± 0.7 mg/g, which was double to that of the pristine MR (79.54 ± 1.19 mg/g), so the Cr(VI) removal capacity of biomass material could be greatly enhanced by a simple one-pot hydrothermal treatment.

Amine group is known to be an effective functional group for the Cr(VI) adsorption (Huang and Chen, 2009; Sun et al., 2014; Luo et al., 2017). In order to enhance the Cr(VI) removal capacity of HTC-MR, different amino-functionalized HTC-MRs were fabricated by the co-carbonization of *M. rouxii* with various amine-containing modifying agents, including acrylamide (AA), diethanolamine (DEA), polyethyleneimine (PEI), urea, ammonium hydroxide ($NH_4OH$) and triethylenetetramine (TETA). The obtained products were designated as 0.5AA-HTC-MR, 0.5DEA-HTC-MR, 0.5PEI-HTC-MR, 0.5Urea-HTC-MR, $NH_4OH$-HTC-MR and 0.5TETA-HTC-MR, respectively. As shown in Figure 5-1, the $Q_{Cr(VI)}$ values of 0.5AA-HTC-MR, 0.5DEA-HTC-MR, 0.5PEI-HTC-MR, 0.5Urea-HTC-MR, $NH_4OH$-HTC-MR and

0.5TETA-HTC-MR were 165.8 ± 4.0, 209.5 ± 2.5, 239.3 ± 2.7, 125.0 ± 3.1, 208.9 ± 2.3 and 193.9 ± 7.9 mg/g, respectively. The results show that the six tested modifying agents displayed different effect on the $Q_{Cr(VI)}$ values of HTC-MR. The DEA, PEI, $NH_4OH$ and TETA enhanced the Cr(VI) removal capacity of HTC-MR, and the highest $Q_{Cr(VI)}$ value was obtained with the 0.5PEI-HTC-MR. The amine groups on the modifying agents, especially PEI, could functionalize the HTC-MR with amine groups which could participate in the Cr(VI) adsorption. However, the AA showed very little improvement on $Q_{Cr(VI)}$, and the 0.5Urea-HTC-MR exhibited even lower $Q_{Cr(VI)}$ value than the HTC-MR.

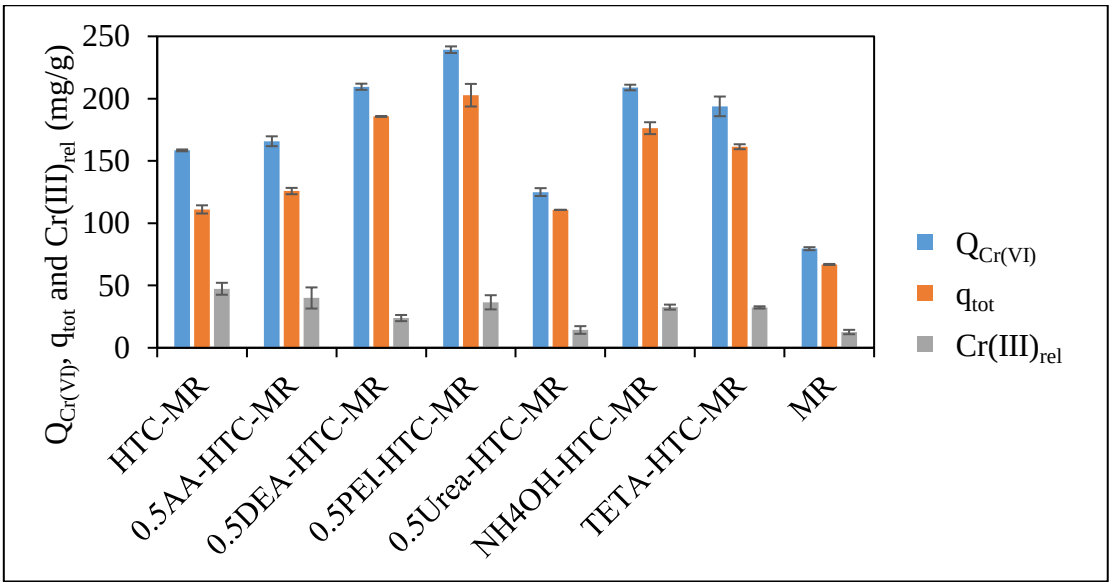


Figure 5-1 $Q_{Cr(VI)}$, $q_{tot}$ and $Cr(III)_{rel}$ of raw MR and HTC materials. (Experimental conditions: [Cr(VI)] = 500 ppm, adsorbent dosage = 1 g/L, t = 1 d, pH 2, temperature = 25°C and agitation = 250 rpm)

### 5.2.2 Effect of temperature

In the following sections, the three different HTC materials, HTC-MR, 0.5DEA-HTC-MR and 0.5PEI-HTC-MR, were prepared in hydrothermal conditions with varying reaction time, temperatures and dosages of the modifying agent. The $Q_{Cr(VI)}$ was plotted as a function of reaction temperature, reaction time and dosage of the modifying agent. These data were important for designing the hydrothermal carbonization process.

At a constant reaction time of 12 h, the yield of HTC-MR gradually decreased from 49.1% to 22.2% when the reaction temperature was increased from 160°C to 240°C (Figure 5-2a). This could be attributed to the increase in the degree of carbonization, as well as increased extents of liquefaction and gasification of the biomass at a higher temperature (Falco et al., 2011). This could explain why the HTC-MR with darker color was obtained at a higher reaction temperature. Meanwhile, the $Q_{Cr(VI)}$ value of HTC-MR was increased from 121.4 ± 1.9 to 207.5 ± 1.7 mg/g as the hydrothermal reaction temperature was increased from 160°C to 240°C. The biomass materials that were not responsible for the Cr(VI) removal were eliminated during the hydrothermal treatment. Therefore, 200°C was chosen as the optimal temperature for the preparation of HTC-MR in order to obtain a high $Q_{Cr(VI)}$ and reasonable product yield.

Figure 5-2Figure 5-2b and Figure 5-25-2c show that the $Q_{Cr(VI)}$ values of DEA-HTC-MR and PEI-HTC-MR reached the highest at 200°C. The optimal hydrothermal temperature was observably found at 200°C. It should be noted that the yield of PEI-HTC-MR increased with

the increase in hydrothermal temperature (Figure 5-2c). The polyethyleneimine would co-carbonize with MR to form hydrochars at a higher temperature, which compensated the loss of product due to the liquefaction and gasification.

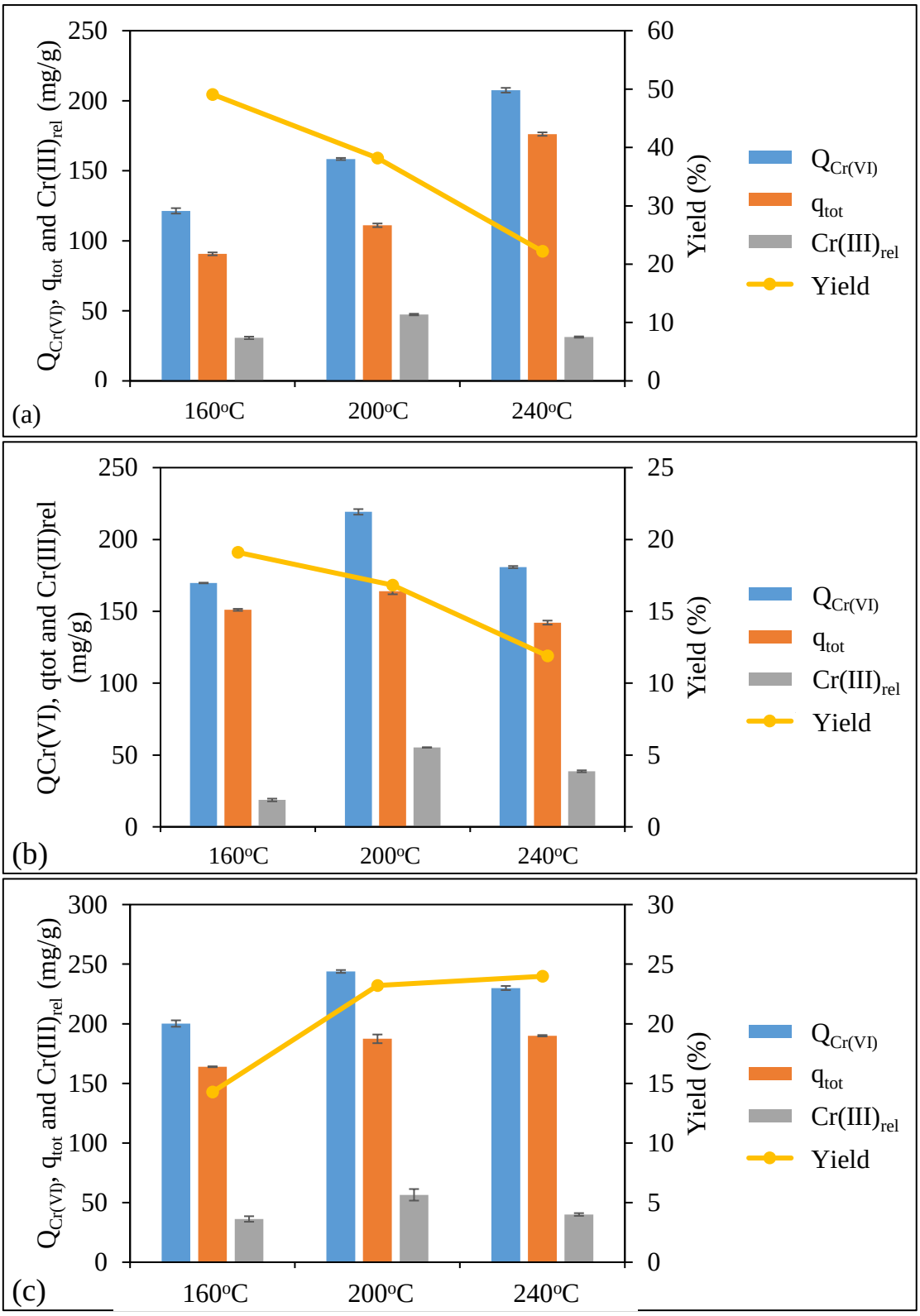


Figure 5-2 $Q_{Cr(VI)}$, $q_{tot}$ and $Cr(III)_{rel}$ of (a) HTC-MR, (b) 0.5DEA-HTC-MR and (c) 0.5PEI-HTC-MR prepared in different reaction temperature. (Experimental conditions: [Cr(VI)] = 500 ppm, adsorbent dosage = 1 g/L, t = 1 d, pH 2, temperature = 25°C and agitation = 250 rpm)

### 5.2.3 Effect of time

Reaction time determines the completeness of the hydrothermal reaction. The $Q_{Cr(VI)}$ of HTC-MR value increased from 145.4 ± 4.4 to 173.4 ± 6.3 mg/g when the hydrothermal reaction time was increased from 6 h to 18 h (Figure 5-3a). However, the yield of HTC-MR decreased from 33.44% to 25.22% with the increase in reaction time. As the hydrothermal process time increased, the extensive liquefaction and gasification of biopolymer resulted in the weight loss of hydrochars. The lost materials seemed less likely to participate in the Cr(VI) removal, so the $Q_{Cr(VI)}$ of HTC-MR increased with hydrothermal reaction time. Moreover, a longer reaction time led to extensive dehydration and condensation of the hydrochars. With the increase in the reaction time, the obtained hydrochars showed a higher degree of carbonization and was darker in color. Therefore, 12 h was selected as the optimal hydrothermal reaction time in order to strike a balance between the Cr(VI) removal capacity and the yield of hydrochars. Likewise, the 0.5PEI-HTC-MR and 0.5DEA-HTC-MR showed the highest $Q_{Cr(VI)}$ at 12-h hydrothermal reaction time with the optimal hydrochars yield or yield close to the optimal value, respectively (Figure 5-3b and 5-3c).

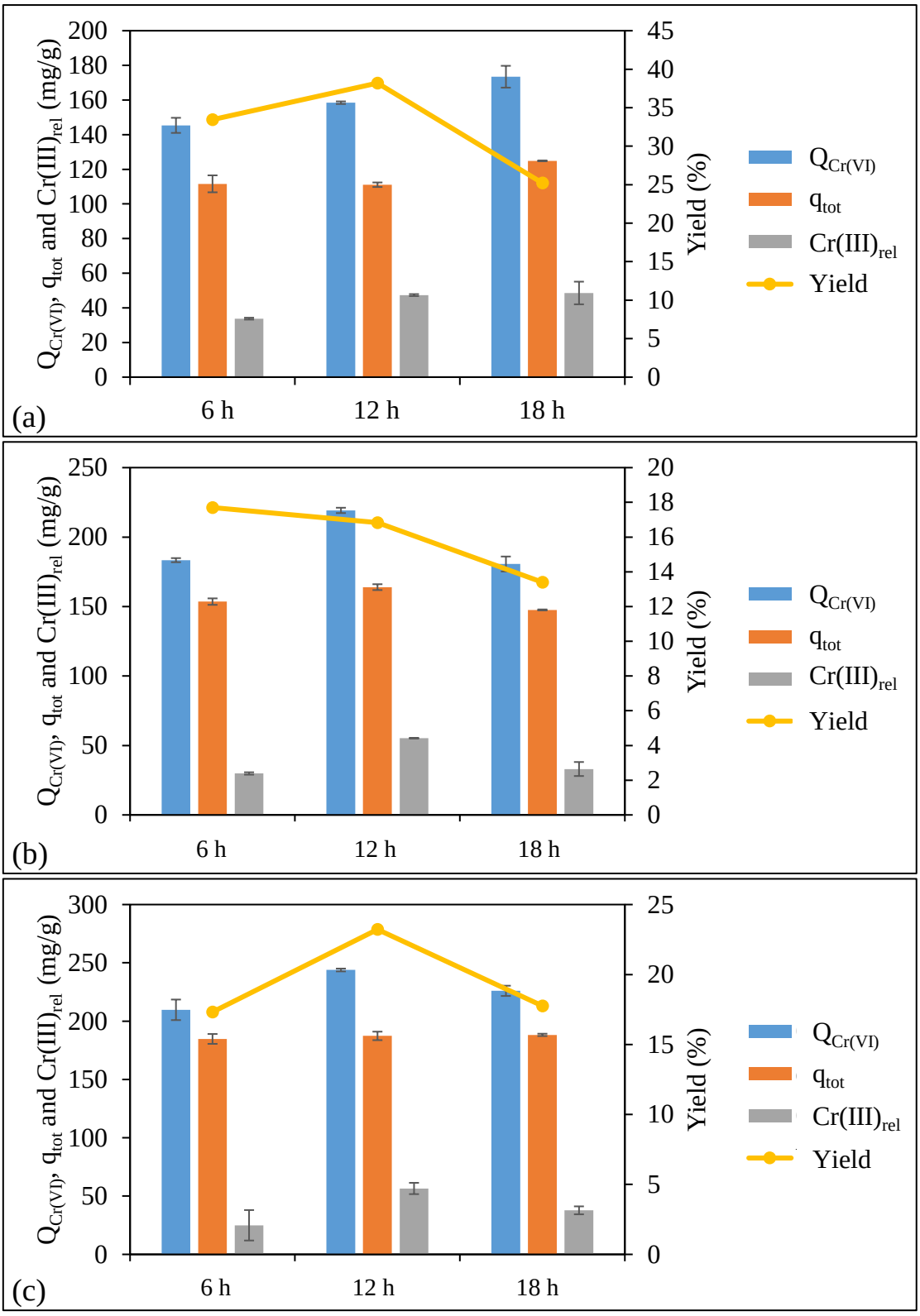


Figure 5-3 $Q_{Cr(VI)}$, $q_{tot}$ and $Cr(III)_{rel}$ of (a) HTC-MR, (b) 0.5DEA-HTC-MR and (c) 0.5PEI-HTC-MR prepared in different reaction time. (Experimental conditions: [Cr(VI)] = 500 ppm, adsorbent dosage = 1 g/L, t = 1 d, pH 2, temperature = 25°C and agitation = 250 rpm)

### 5.2.4 Effect of modifying agent dosage

Two different amine-containing modifying agents (DEA, MW = 105.14; and PEI, MW = 800) were introduced in the hydrothermal carbonization process in order to functionalize the HTC-MR surface with amine groups, which provided extra binding sites for Cr(VI). Section 5.2.1 demonstrated that the amino-functionalized HTC-MR gave higher Cr(VI) removal capacity than the HTC-MR. In this section, the aim was to explore the influence of the modifying agent dosage (0.1 - 1.0 g/g biomass) on the $Q_{Cr(VI)}$ value and the yield of hydrochars, and hence to optimize the dosage of the amine-containing modifying agents added in the hydrothermal carbonization.

As shown in Figure 5-4a, the $Q_{Cr(VI)}$ values of HTC-MR, 0.1DEA-HTC-MR, 0.25DEA-HTC-MR, 0.5DEA-HTC-MR and 1.0DEA-HTC-MR at 1-day contact time were 166.0 ± 0.7, 148.6 ± 2.2, 167.6 ± 2.9, 219.2 ± 1.9 and 186.9 ± 1.7 mg/g, respectively. The $Q_{Cr(VI)}$ values of 0.1PEI-HTC-MR, 0.25PEI-HTC-MR, 0.5PEI-HTC-MR and 1.0PEI-HTC-MR at 1-day contact time were 198.5 ± 3.4, 225.5 ± 1.2, 243.9 ± 1.2 and 206.2 ± 1.9 mg/g, respectively (Figure 5-4b). The $Q_{Cr(VI)}$ values of DEA-HTC-MR and PEI-HTC-MR increased when the dosages of DEA and PEI increased from 0.1 to 0.5 g/g biomass. It could be observed that the $Q_{Cr(VI)}$ values were not linearly proportional to the amount of modifying agents added. This observation indicated that not all the modifying agents had been incorporated into the HTC-MR. Furthermore, when the DEA and PEI dosages were further increased from 0.5 to 1.0 g/g

biomass, the $Q_{Cr(VI)}$ values of DEA-HTC-MR and PEI-HTC-MR reduced. Therefore, the optimum dosage of DEA and PEI was 0.5 g per g of MR.

As the dosage of modifying agent increased, the yield of hydrochars generally decreased. In the hydrothermal carbonization of sugar such as glucose, organic acids (e.g., acetic, lactic, propenoic, levulinic and formic acids) were formed by the decomposition of sugar and intermediates (Weingarten et al., 2012; Pileidis and Titirici, 2016). The hydronium ions from the organic acids served as a catalyst for the formation of 5-(hydroxymethyl)furfural (5-HMF), which then polymerized through the inter-molecular dehydration or the aldol condensation to form a soluble polymeric material. According to the LaMer model, small nuclei were formed until the molecular weight of the polymers increased to a certain point. The nuclei finally grew into a hydrochars microspheres by the inter-particle dehydration of the oxygen-containing functional groups (e.g., hydroxyl, carbonyl and carboxylic acid groups) presented on the surface of the clusters (Sevilla and Fuertes, 2009; Brun et al., 2013). However, both the DEA and PEI are alkaline (pH around 10 to 11) and would neutralize part of the hydronium ions. The alkaline condition would reduce the production of 5-HMF in the hydrothermal reaction and hence the yield of hydrochars (Huang et al., 2017b).

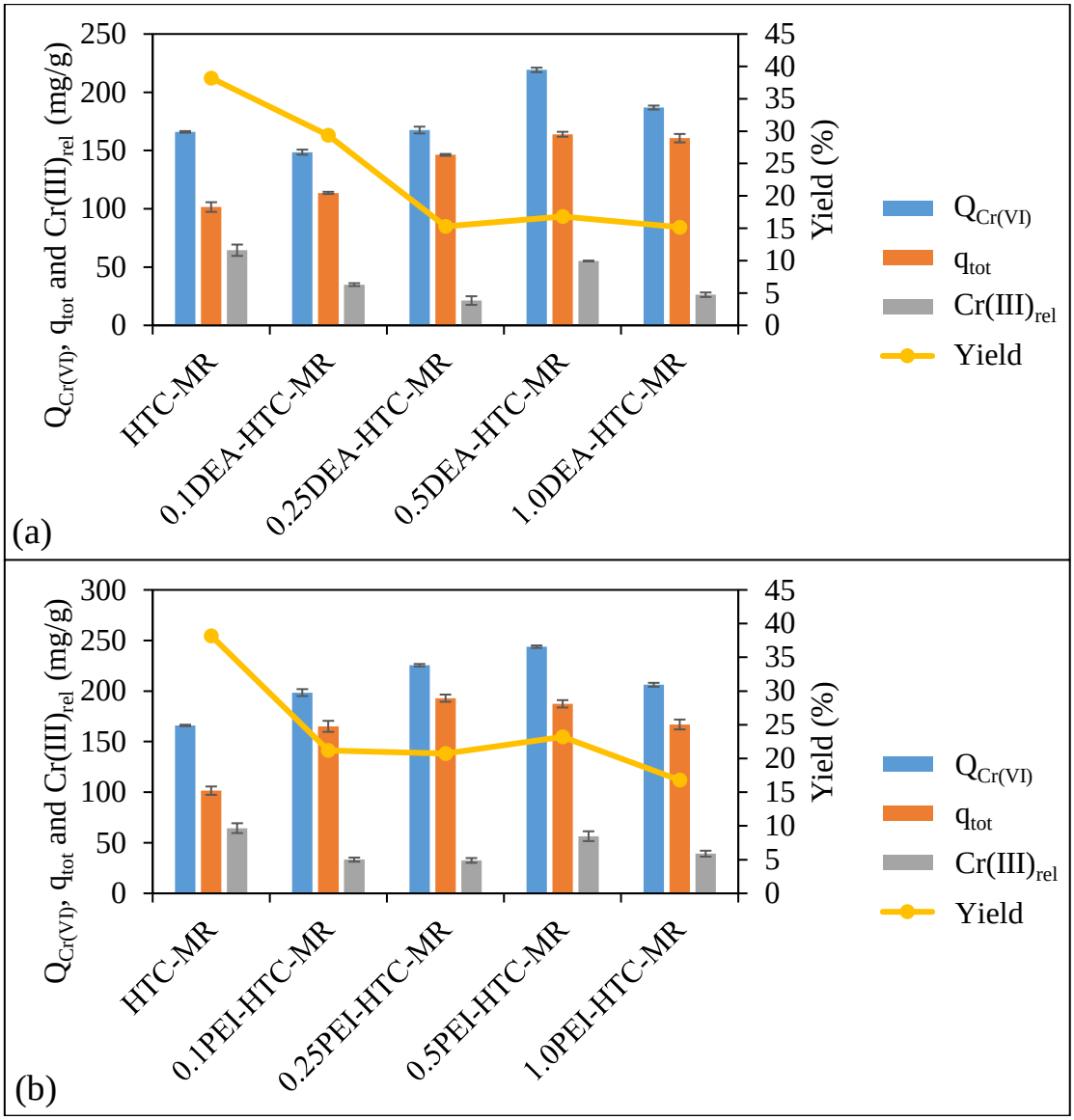


Figure 5-4 $Q_{Cr(VI)}$, $q_{tot}$ and $Cr(III)_{rel}$ of (a) 0.5DEA-HTC-MR and (b) 0.5PEI-HTC-MR prepared in different dosages of modifying agent. (Experimental conditions: [Cr(VI)] = 500 ppm, adsorbent dosage = 1 g/L, t = 1 d, pH 2, temp = 25°C)

The 0.5PEI-HTC-MR was prepared with the PEI of two different molecular weights, 800 and 25,000 g/mol. Figure 5-5 illustrates the Cr(VI) removal kinetics of 0.5PEI(800)-HTC-MR and 0.5PEI(25000)-HTC-MR. Similar Cr(VI) adsorption kinetic curves were obtained, regardless of the molecular weight of PEI. Moreover, all the PEI-modified HTC-MRs appeared in yellow, suggesting that the carbonization reaction of the biomaterials was inhibited by the PEI molecules regardless of the reaction time (6 to 18 h) and reaction temperature (160 to 240°C), dosage and molecular weight of PEI. The PEI molecules were less likely to be carbonized at the typical hydrothermal conditions. Instead, the PEI molecules were chemically grafted onto the surface of hydrochars (Wang et al., 2015a). During the hydrothermal process, the amino groups from the PEI molecules underwent the condensation reaction with the carboxylic acid groups from the biomass materials.

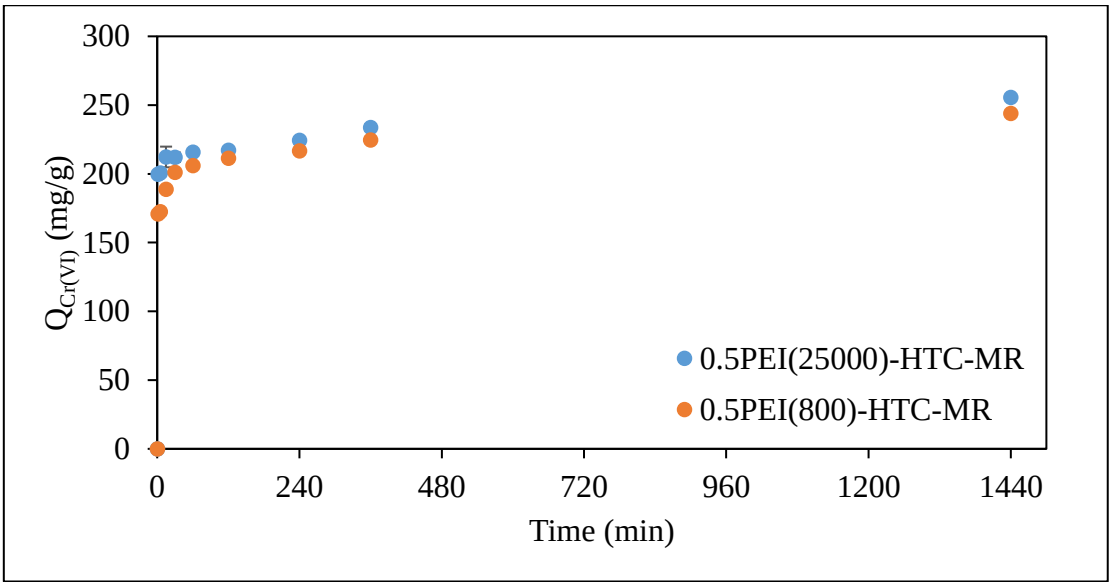


Figure 5-5 Cr(VI) removal kinetics of 0.5PEI-HTC-MR with different molecular weights of PEI. (Experimental conditions: [Cr(VI)] = 500 ppm, adsorbent dosage = 1 g/L, t = 1 d, pH 2, temperature = 25ºC and agitation = 250 rpm)

### 5.2.5 Incorporation of zirconium oxide in HTC-MR

The $ZrO_2$-$NH_4$-HTC-MR was prepared by incorporating $ZrO_2$ particles into the $NH_4$-HTC-MR with the one-pot hydrothermal synthesis as mentioned in Section 3.5.2. The $ZrO_2$ particles would act as the nucleation sites for the hydrothermal carbonization reaction, so the $ZrO_2$-$NH_4$-HTC-MR showed a higher degree of carbonization with a dark brown color. As shown in Figure 5-6, the $Q_{Cr(VI)}$ value of $ZrO_2$-$NH_4$-HTC-MR was 179.9 ± 3.1 mg/g, which was lower than that of the $NH_4$-HTC-MR (208.9 ± 2.3 mg/g). This was because the $ZrO_2$ showed a low $Q_{Cr(VI)}$ of 67.28 ± 3.26 mg/g. Hence, the incorporation of $ZrO_2$ into $NH_4$-HTC-MR could not improve the Cr(VI) removal capacity of HTC-MR.

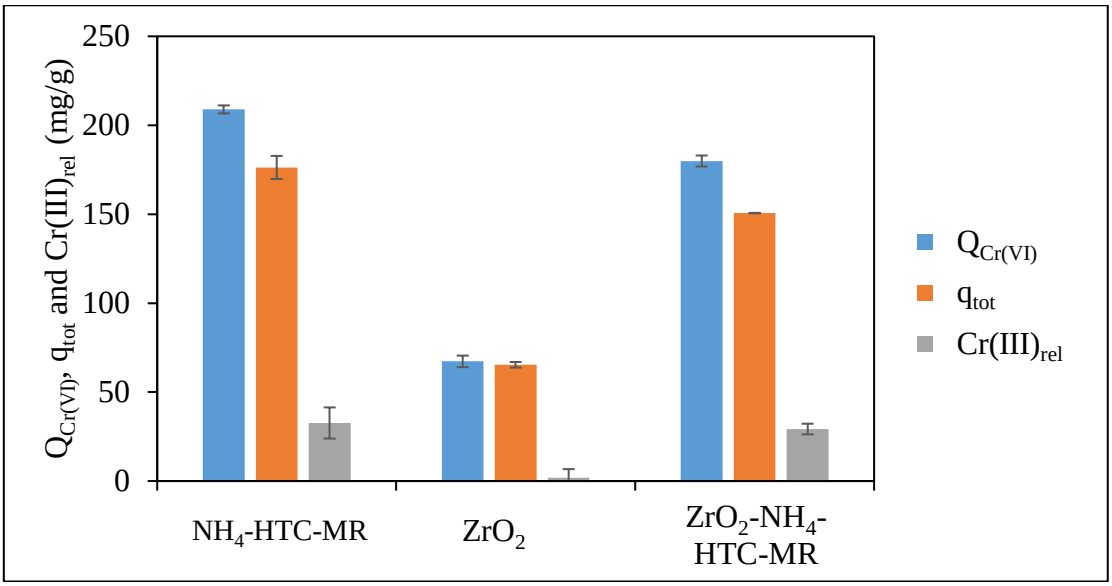


Figure 5-6 The $Q_{Cr(VI)}$, $q_{tot}$ and $Cr(III)_{rel}$ values of $NH_4$-HTC-MR, $ZrO_2$ and $ZrO_2$-$NH_4$-HTC-MR. (Experimental conditions: [Cr(VI)] = 500 ppm, adsorbent dosage = 1 g/L, t = 1 d, pH 2, temperature = 25ºC and agitation = 250 rpm)

### 5.2.6 Preparation of HTC-MR in the eutectic salt template

Porous carbon materials can be prepared via the soft-template technique, in which the eutectic salt is applied as a "soft template" to the hydrothermal carbonization process. The eutectic salt template is non-carbonizable and has a low melting point comparable to the hydrothermal temperature, so the eutectic salt melts at the hydrothermal conditions and acts as a "soft template" for the formation of hydrothermal carbon. After the hydrothermal treatment, the salt template in the hydrochars can be easily removed by rinsing the hydrochars with DDI water. The obtained carbon material would show a microporous characteristic. Alatalo et al. (2016) demonstrated the use of the LiCl-$ZnCl_2$ eutectic salt mixture as a soft template for hydrothermal carbonization of D-fructose. The prepared carbon material exhibited a high surface area of 554 $m^2/g$, which was much higher than those of the traditional hydrothermal carbon materials without any activation processes (normally < 100 $m^2/g$). The highly porous hydrothermal carbon materials could also be prepared with the hydrothermal carbonization followed by the thermal or chemical activation (Braghiroli et al., 2012; Brun et al., 2013). The eutectic salt method took advantage of the one-pot synthetic route without further activation step.

In this study, the hydrothermal carbonized *M. rouxii* was prepared in the presence of a eutectic salt mixture of $CalCl_2$ and $FeCl_3$. The obtained hydrochars (HTC-MR-CaFe) was black in color, indicating complete carbonization of the biomass materials. Fechler et al. (2013) could

not synthesize complete-carbonized hydrochars in the absence of eutectic salt. The eutectic salt provided a drastic condition and hence enhanced the carbonization rate. As shown in Figure 5-8, the yield of HTC-MR-CaFe (40.64%) was lower than that of HTC-MR (16.01%) due to the more complete carbonization of biomaterials with the salt catalyst. The melting point of $CaCl_2$/$FeCl_3$eutectic salt (Figure 5-7) was comparable to the hydrothermal temperature (200°C), so the salt mixture melts at the hydrothermal condition and acts as a "soft-template" for the carbonization reaction. The prepared HTC-MR-CaFe was expected to have a microporous characteristic.

Nonetheless, the $Q_{Cr(VI)}$ of HTC-MR-CaFe was 70.35 ± 2.96 mg/g, which was lower than that of HTC-MR (158.4 ± 0.7 mg/g). The significant reduction in Cr(VI) adsorption capacity could be explained by the results of the elemental analysis (Section 5.1.3). The nitrogen content of HTC-MR was significantly reduced from 8.49 ± 0.17 to 2.42 ± 0.01% (Table 5-2) after the addition of a eutectic salt mixture of $CaCl_2$ and $FeCl_3$. The nitrogen-containing functional groups were lost as a result of the high degree of carbonization. Additionally, the total Brunauer–Emmett–Teller (BET) surface area of HTC-MR-CaFe (25.96 ± 0.05 $m^2$/g) was even smaller than that of HTC-MR (35.84 ± 1.65 $m^2$/g) (Table 5-1).

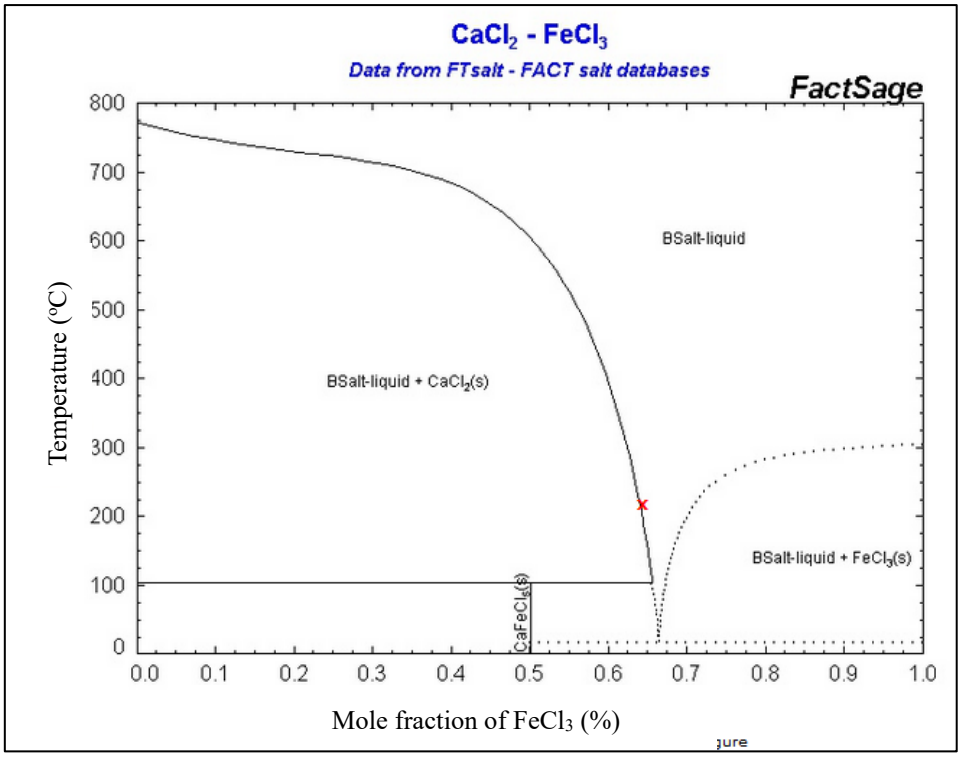


Figure 5-7 Temperature-composition phase diagram of $CaCl_2$ and $FeCl_3$ binary system (CRCT, 2015).

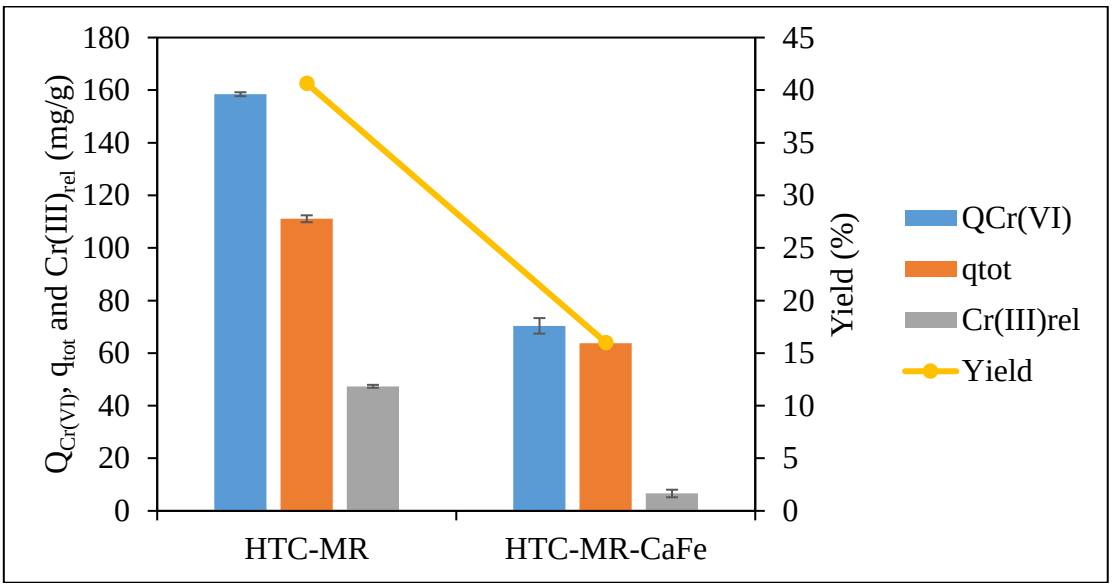


Figure 5-8 $Q_{Cr(VI)}$ values of HTC-MR and HTC-MR-CaFe. (Experimental conditions: [Cr(VI)] = 500 ppm, adsorbent dosage = 1 g/L, t = 1 d, pH 2, temperature = 25°C and agitation = 250 rpm)

## 5.3 Removal of Cr(VI) by hydrothermal carbonized *M. rouxii*

### 5.3.1 Screening of cationic and anionic pollutants

Figure 5-9 compares the removal capacities of HTC materials toward different cationic and anionic pollutants. The HTC-MR showed excellent removal capacity to Cr(VI) as compared to other cationic and anionic pollutants. The $Q_{Cr(VI)}$ values of HTC-MR, 0.5DEA-HTC-MR and 0.5PEI-HTC-MR were 166.0 ± 0.7, 219.2 ± 1.9 and 243.9 ± 1.2 mg/g, respectively. In the acidic adsorption condition (pH 2.0), the amine groups on the HTC materials surface were protonated and positive-charged, so that it could participate in the Cr(VI) adsorption through the electrostatic interaction. The Cr(VI) adsorption mechanism will be discussed in Section 5.3.4.

The HTC materials, however, exhibited a low adsorption capacity for removing other anionic pollutants, such as As(V), As(III), phosphate and fluoride. The adsorption studies for As(V), phosphate and fluoride were performed at pH 4.0 so that the As(V), phosphate and fluoride were in the anionic form of $H_2AsO_4^-$, $H_2PO_4^-$ and $F^-$. Indeed, the HTC-MR showed zero surface charge at this condition (Figure 5-14), so the adsorptions of As(V), phosphate and fluoride were not favored at pH 4.0. The As(III) adsorption was also not favored on HTC-MR since the HTC-MR showed a negative surface charge at pH 7.0. Besides, the 0.5DEA-HTC-MR and 0.5PEI-HTC-MR exhibited positive charge at pH 4.0 and 7.0, but they also showed poor adsorption capacities to As(III), As(III), phosphate and fluoride.

Amine group was demonstrated as an effective functional group for heavy metals adsorption. The adsorption capacities of the HTC materials to the cationic pollutants, Cd(II), Cr(III), Cu(II), Ni(II), Pb(II) and Zn(II), were also investigated. The HTC-MR, 0.5DEA-HTC-MR and 0.5PEI-HTC-MR all exhibited good Cd(II) adsorption capacity of 105.3 ± 1. 4, 109.6 ± 1.6 and 118.9 ± 2.3 mg/g, respectively. Demir-Cakan et al. (2009) prepared a carboxylate-rich carbonaceous material that exhibited an experimental Cd(II) adsorption capacity of 88.8 mg/g. Our amino-functionalized HTC materials showed higher Cd(II) adsorption capacity than the carboxylate-rich carbonaceous materials. The amine, carbonyl and hydroxyl groups were demonstrated as effective functional groups for the adsorption process (Sayyadi et al., 2018).

The Pb(II) adsorption capacities of HTC-MR, 0.5DEA-HTC-MR and 0.5PEI-HTC-MR were 80.43 ± 5.15, 44.14 ± 1.55 and 52.94 ± 3.07 mg/g, respectively. Demir-Cakan et al. (2009) reported that the carboxylate-rich carbonaceous material showed a high Pb(II) adsorption of 351.4 mg/g at pH 6.0. Chen et al. (2011) also reported that the attapulgite clay@carbon (ATP@C) nanocomposite adsorbent possessed a high Pb(II) adsorption capacity of 263.83 mg/g at pH 6.0. However, these results were doubtful since Pb(II) ions would precipitate at pH 6.0, which was the pH value Demir-Cakan et al. and Chen et al. used for their Pb(II) adsorption study.

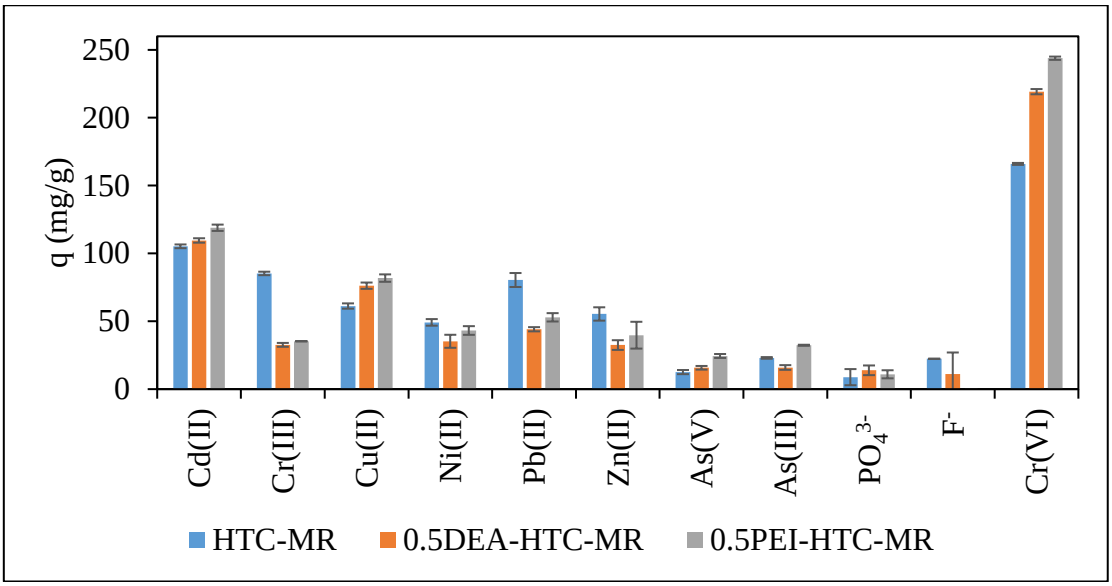


Figure 5-9 Screening results of six cationic and five anionic pollutants by HTC-MR, 0.5DEA-HTC-MR and 0.5PEI-HTC-MR. (Experimental conditions: [Cr(VI)] = 500 ppm, adsorbent dosage = 1 g/L, t = 1 d, temperature = 25°C and agitation = 250 rpm)

### 5.3.2 Effect of contact time

Figure 5-10 and Figure 5-11 display the kinetic profiles of $Q_{Cr(VI)}$, $q_{tot}$ and $Cr(III)_{rel}$ on MR, HTC-MR, 0.5AA-HTC-MR, 0.5DEA-HTC-MR, 0.5PEI-HTC-MR and 0.5Urea-HTC-MR. In general, the Cr(VI) was rapidly removed in the first 1 h, and the rate of Cr(VI) removal was gradually reduced afterward. Most systems did not reach equilibrium within 1 day. The fast Cr(VI) initial removal rate was contributed by the strong interaction between anionic Cr(VI) and the positively-charged surface, while the slow removal rate at the later stage was due to the slow diffusion of adsorbate into the interior of the adsorbent.

Figure 5-10 and Figure 5-11 show that the $Q_{Cr(VI)}$ values of MR, HTC-MR, 0.5AA-HTC-MR, 0.5DEA-HTC-MR, 0.5PEI-HTC-MR and 0.5Urea-HTC-MR at 1-day contact time were 63.38 ± 2.55, 166.0 ± 0.7, 150.3 ± 1.2, 219.2 ± 1.9, 243.9 ± 1.2 and 145.2 ± 2.2 mg/g, respectively. Hydrothermal carbonization treatment removed the biomass materials that were not responsible for the Cr(VI) removal, and hence significantly improved the Cr(VI) removal capacity of MR. In addition, the Cr(VI) removal capacity of HTC-MR could be further enhanced by co-carbonization of MR with the modifying agents. The $Q_{Cr(VI)}$ values of 0.5DEA-HTC-MR and 0.5PEI-HTC-MR were higher than that of HTC-MR, so the DEA and PEI were effective in increasing the Cr(VI) removal ability of HTC-MR (Figure 5-11a and Figure 5-11b). The DEA and PEI could functionalize the HTC-MR with amine groups that were responsible for the Cr(VI) adsorption. Besides, the $Q_{Cr(VI)}$ of HTC-MR could not be improved by the

acrylamide and urea (Figure 5-10c and Figure 5-11c).

A significant amount of Cr(III) was detected in the solution phase after a 1-minute contact with the tested adsorbents. The adsorbed Cr(VI) was immediately reduced to Cr(III) by the adjacent reducing groups on the surface of the HTC materials, and the reduced Cr(III) was released back to the solution phase due to the electrostatic repulsion between the cationic Cr(III) and the protonated adsorbent surface. The $Cr(III)_{rel}$ of HTC-MR was higher than that of raw MR. This result suggested that the amount of Cr(VI)-reducing groups of MR was "concentrated" after the hydrothermal carbonization, as a result, more Cr(VI) was reduced per unit mass of the HTC materials. In addition, the Cr-laden HTC materials were yellowish-brown in color, suggesting that the Cr(VI) would be present on the surface of Cr-laden adsorbents. Section 5.5.3 will report the oxidation state of the adsorbed Cr on HTCs surface as determined by XPS analysis.

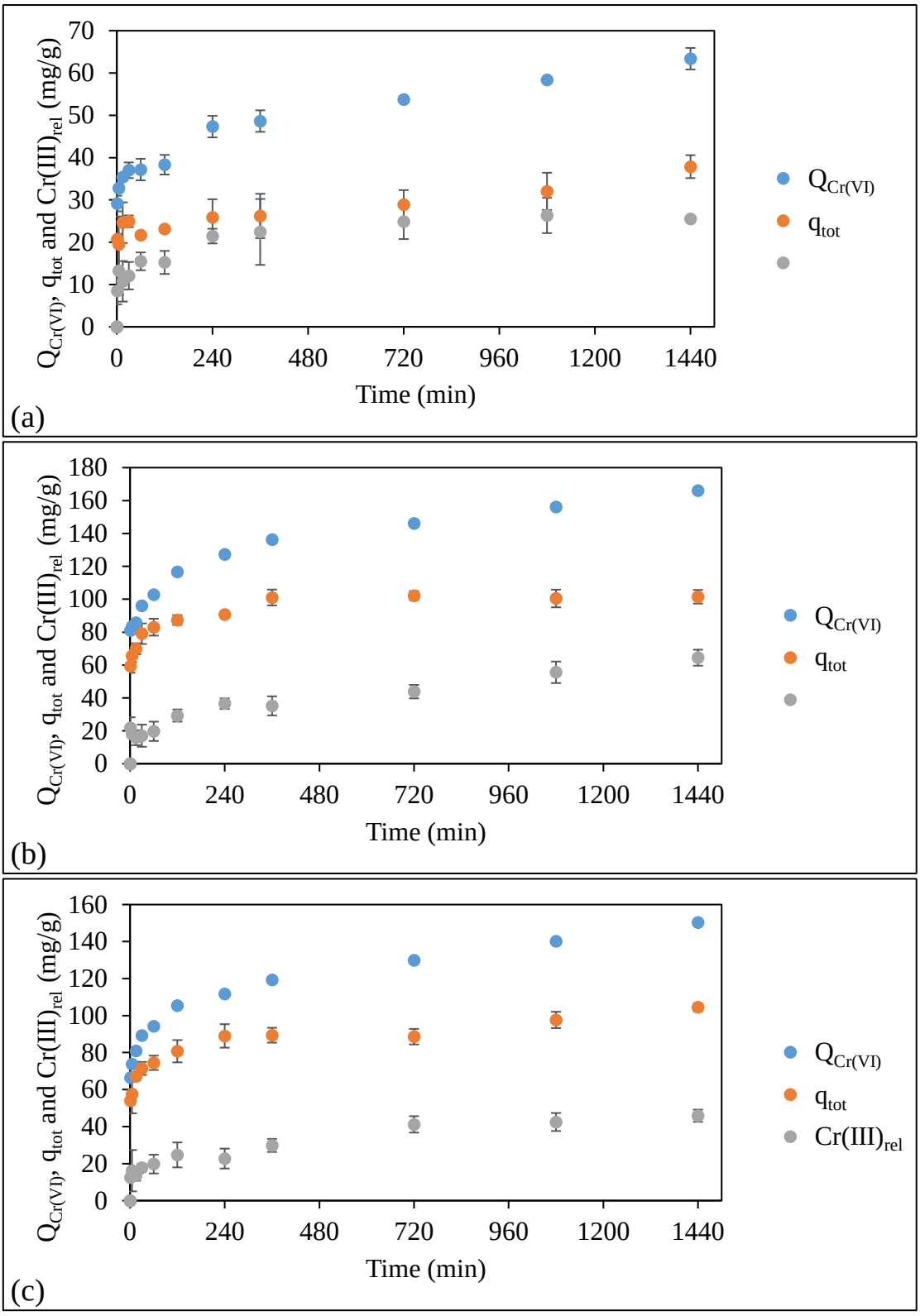


Figure 5-10 Effect of contact time on the $Q_{Cr(VI)}$, $q_{tot}$ and $Cr(III)_{rel}$ by (a) MR, (b) HTC-MR and (c) 0.5AA-HTC-MR. (Experimental conditions: [Cr(VI)] = 500 ppm, adsorbent dosage = 1 g/L, t = 1 d, pH 2, temperature = 25°C and agitation = 250 rpm)

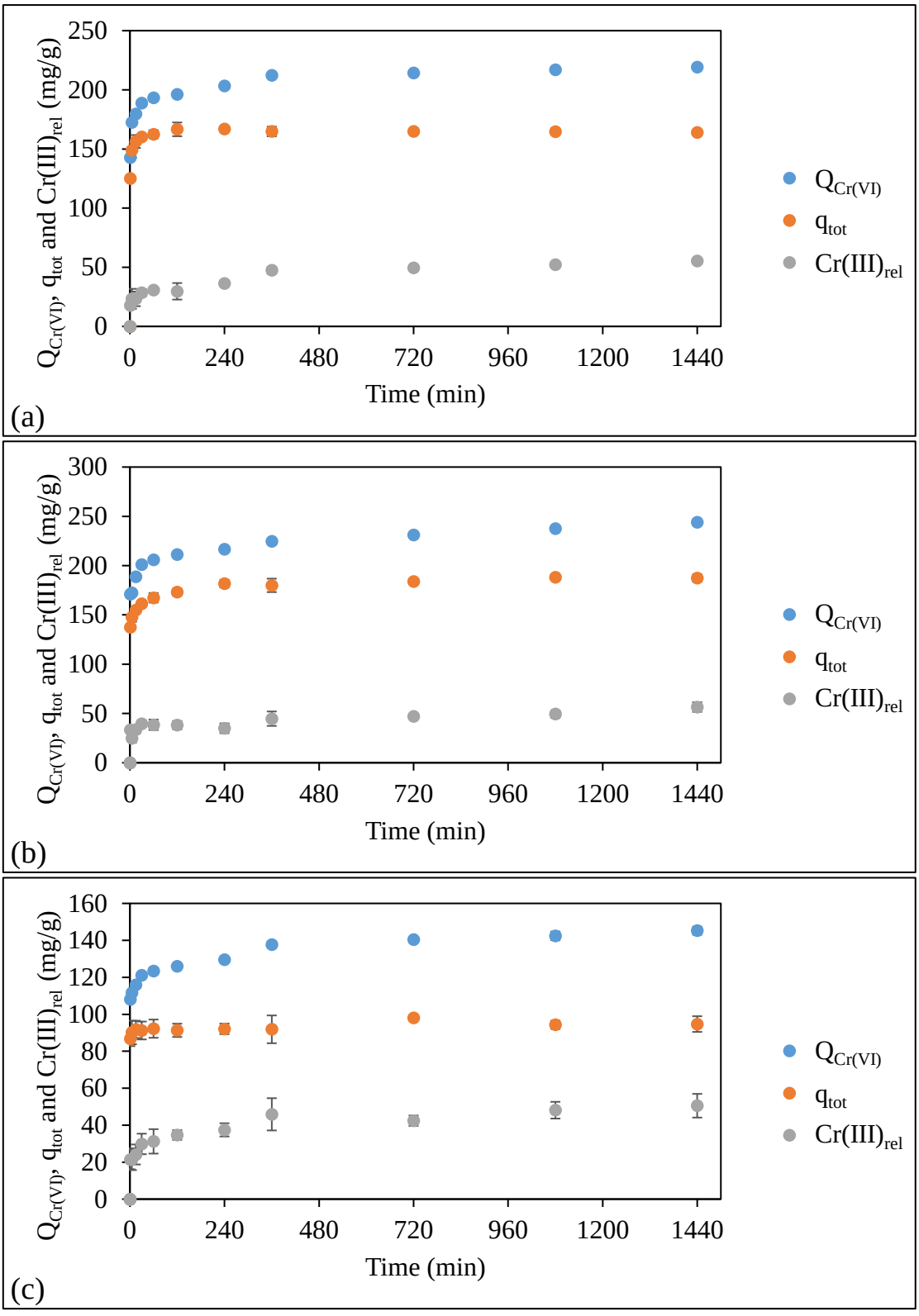


Figure 5-11 Effect of contact time on the $Q_{Cr(VI)}$, $q_{tot}$ and $Cr(III)_{rel}$ by (a) 0.5DEA-HTC-MR, (b) 0.5PEI-HTC-MR and (c) 0.5Urea-HTC-MR. (Experimental conditions: [Cr(VI)] = 500 ppm, adsorbent dosage = 1 g/L, t = 1 d, pH 2, temperature = 25°C and agitation = 250 rpm)

### 5.3.3 Kinetic modelling

The Cr(VI) removal kinetics on HTC-MR, 0.5DEA-HTC-MR and 0.5PEI-HTC-MR were simulated by various nonlinear kinetic models, namely pseudo-second-order, pseudo-first-order, Elovich, intra-particle diffusion and fractional power kinetic models Figure 5-12 presents the experimental kinetic data and the modelling curves, while Table 5-3 summarizes the kinetic modelling parameters. The Cr(VI) removal kinetics on HTC-MR, 0.5DEA-HTC-MR and 0.5PEI-HTC-MR could not reach the equilibrium within 12 h, so the fractional power model and the Elovich model could well describe the gradual rise of $Q_{Cr(VI)}$ at the later stage of the kinetic curves. The fractional power model was the best-fit model to simulate the Cr(VI) removal kinetics on HTC-MR and 0.5PEI-HTC-MR with the lowest RMSE values and the highest correlation coefficients. Meanwhile, the Elovich model fitted the Cr(VI) removal kinetics of 0.5DEA-HTC-MR with the lowest RMSE and the highest correlation coefficient, better than the fractional power model. The specific Cr(VI) removal rate ($k_fv$) from the fractional power model estimated the specific Cr(VI) removal rate by the adsorbents at t = 1 min. As summarized in Table 5-3, the calculated $k_fv$ values of Cr(VI) removal kinetics by HTC-MR, 0.5DEA-HTC-MR and 0.5PEI-HTC-MR were 8.042 ± 0.279, 7.828 ± 0.480 and 8.568 ± 0.063 mg/g-min, respectively. As previously reported (Table 4-3), the $k_fv$ value of MR was 1.835 mg/g-min. The hydrothermal carbons displayed a higher specific Cr(VI) removal rate than the raw MR, while the 0.5PEI-HTC-MR exhibited the highest specific Cr(VI) removal

rate among the tested adsorbents.

The approaching equilibrium parameters ($R_E$) of Cr(VI) removal kinetics on the three HTC-based materials, which were calculated from the Elovich model, ranged from 4.28E-2 to 7.49E-2, so the Cr(VI) removal kinetics on HTC-based materials were classified as a rapid rising curve (Wu et al., 2009). The Cr(VI) was rapidly adsorbed on the HTC-based materials owing to the strong electrostatic attraction between the anionic Cr(VI) ions and the positively-charged adsorbent surfaces. The calculated initial adsorption rates (a) of HTC-MR, 0.5DEA-HTC-MR and 0.5PEI-HTC-MR were 1.94E3 ± 9.31E1, 7.20E7 ± 6.52E6 and 6.33E7 ± 8.20E6 mg/g-min, respectively. Furthermore, the Cr(VI) removal kinetics of HTC materials was poorly fitted by the intra-particle diffusion model. The intra-particle diffusion plots of Cr(VI) removal on HTC materials were neither linear nor pass through the origin, so the Cr(VI) removal kinetics on HTC materials were not solely controlled by the intra-particle diffusion. Based on the results of dynamic light scattering (Section 5.1.2), the particle sizes of HTC-MR and 0.5PEI-HTC-MR were 2036 and 2314 nm, respectively. The BJH pore size and pore size distribution analysis shows that the 0.5DEA-HTC-MR exhibited a low total pore volume of 7.75E-2 ± 2.98E-4 $cm^3/g$. Therefore, the Cr(VI) adsorption predominantly occurred on the external surfaces of the HTC particles.

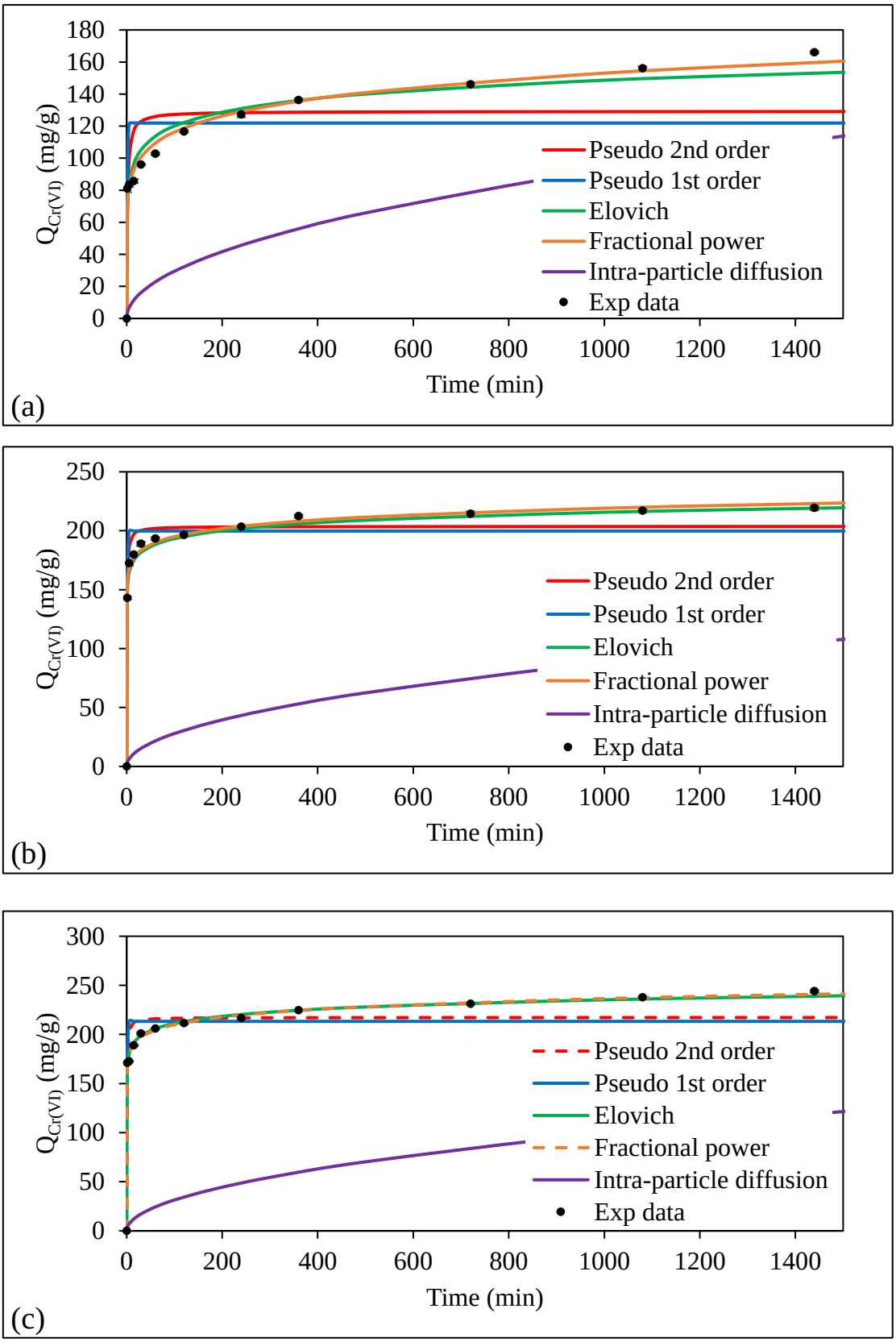


Figure 5-12 Cr(VI) removal kinetic modelling curves of (a) HTC-MR, (b) 0.5DEA-HTC-MR and (c) 0.5PEI-HTC-MR.

Table 5-3 Cr(VI) removal kinetic modelling parameters of HTC-MR, 0.5DEA-HTC-MR and 0.5PEI-HTC-MR.

| Pseudo 2nd order | $q_e$ (mg/g) | $k_2$ (g/mg-min) | $R^2$ | RMSE |
|---|---|---|---|---|
| HTC-MR | 129.2 ± 0.7 | 5.03E-3 ± 1.15E-4 | 0.729 ± 0.006 | 24.42 ± 0.44 |
| 0.5DEA-HTC-MR | 203.7 ± 0.6 | 9.59E-3 ± 6.15E-4 | 0.965 ± 0.006 | 11.80 ± 1.11 |
| 0.5PEI-HTC-MR | 217.3 ± 0.9 | 1.21E-2 ± 1.84E-4 | 0.929 ± 0.001 | 18.10 ± 0.22 |
| Pseudo 1st order | $q_e$ (mg/g) | $k_1$ (1/min) | $R^2$ | RMSE |
| HTC-MR | 121.9 ± 0.7 | 1.020 ± 0.055 | 0.649 ± 0.006 | 27.79 ± 0.42 |
| 0.5DEA-HTC-MR | 199.8 ± 3.5 | 1.240 ± 0.029 | 0.941 ± 0.009 | 15.39 ± 1.30 |
| 0.5PEI-HTC-MR | 213.4 ± 0.8 | 1.607 ± 0.004 | 0.904 ± 0.002 | 21.11 ± 0.28 |

| Elovich | b (g/mg) | a (mg/g-min) | $t_0$ (min) | $R_E$ | $R^2$ | RMSE |
|---|---|---|---|---|---|---|
| HTC-MR | 0.080 ± 0.001 | 1.94E3 ± 9.31E1 | 6.43E-3 ± 2.91E-4 | 7.49E-2 ± 1.08E-4 | 0.959 ± 0.002 | 9.522 ± 0.280 |
| 0.5DEA-HTC-MR | 0.225 ± 0.011 | 7.20E7 ± 6.52E6 | 2.35E-7 ± 2.21E-7 | 4.44E-2 ± 2.18E-3 | **0.996 ± 0.001** | **4.052 ± 0.360** |
| 0.5PEI-HTC-MR | 0.137 ± 0.005 | 6.33E7 ± 8.20E6 | 1.67E-7 ± 2.33E-8 | 4.28E-2 ± 2.45E-4 | 0.996 ± 0.002 | 4.154 ± 0.174 |

| Fractional Power | v | k (mg/g-min$^v$) | $k_f$v (mg/g-min) | $R^2$ | RMSE |
|---|---|---|---|---|---|
| HTC-MR | 0.120 ± 0.004 | 67.02 ± 0.64 | 8.042 ± 0.279 | **0.983 ± 0.001** | **6.084 ± 0.268** |
| 0.5DEA-HTC-MR | 5.07E-2 ± 3.03E-3 | 154.4 ± 2.1 | 7.828 ± 0.480 | 0.994 ± 0.001 | 4.998 ± 0.268 |
| 0.5PEI-HTC-MR | 5.18E-2 ± 3.68E-4 | 165.4 ± 0.3 | 8.568 ± 0.063 | **0.997 ± 0.003** | **3.507 ± 0.210** |

| Intra-particle diffusion | $k_{diff}$ (mg/g- min$^{0.5}$) | $R^2$ | RMSE |
|---|---|---|---|
| HTC-MR | 2.944 ± 0.017 | 0.727 ± 0.002 | 78.44 ± 0.71 |
| 0.5DEA-HTC-MR | 2.792 ± 0.092 | 0.360 ± 0.018 | 161.8 ± 1.2 |
| 0.5PEI-HTC-MR | 3.145 ± 0.022 | 0.394 ± 0.002 | 171.8 ± 0.5 |

### 5.3.4 Effect of pH

Solution pH is an important factor affecting the speciation of Cr(VI) and the surface charge of adsorbent and hence influencing the Cr(VI) adsorption. The Cr(VI) removal capacities ($Q_{Cr(VI)}$), total Cr adsorption capacities ($q_{tot}$) and amounts of Cr(III) released ($Cr(III)_{rel}$) of HTC-MR, 0.5DEA-HTC-MR and 0.5PEI-HTC-MR were examined at different solution pH (1.0 - 7.0). As shown in Figure 5-13a, the $Q_{Cr(VI)}$ and $q_{tot}$ values of HTC-MR gradually increased from 17.56 ± 5.71 to 171.2 ± 3.2 mg/g and from 5.632 ± 0.690 to 106.2 ± 1.1 mg/g, respectively, when the solution pH decreased from 7.0 to 1.0. This could be explained by the strong electrostatic interaction between the anionic Cr(VI) and the protonated HTC-MR surface. The release of Cr(III) mainly occurred in the acidic environment. The $Cr(III)_{rel}$ of HTC-MR increased from 9.838 ± 3.454 to 64.96 ± 2.13 mg/g as the solution pH decreased from 4.0 to 1.0. The Cr(III) release was much more significant in the acidic condition because the reduction of Cr(VI) was catalyzed in the presence of proton. The cationic Cr(III) ions were then repelled from the adsorbent surface to aqueous phase by electrostatic repulsion. Therefore, the $Cr(III)_{rel}$ values were higher at the acidic condition.

The trends of Cr(VI) removal of 0.5DEA-HTC-MR and 0.5PEI-HTC-MR were different from that of HTC-MR (Figure 5-13). Figure 5-13b indicates that the $Q_{Cr(VI)}$ and $q_{tot}$ of 0.5DEA-HTC-MR increased sharply from 10.88 ± 2.73 to 140.6 ± 3.2 mg/g and from 25.09 ± 0.46 to 146.7 ± 2.7 mg/g, respectively, when the solution pH decreased from 7.0 to 5.0. A plateau was

observed between pH 4.0 and 2.0, so the optimum pH for Cr(VI) removal and total Cr adsorption ranged from pH 4.0 to 2.0. When the solution pH was further decreased from 2.0 to 1.0, the $q_{tot}$ slightly decreased. A similar observation was made in the 0.5PEI-HTC-MR, where the $Q_{Cr(VI)}$ and $q_{tot}$ dramatically increased when the solution pH decreased from 7.0 to 5.0 (Figure 5-13c). The optimum pH for Cr(VI) removal was found as pH 2.0.

The zeta-potential analysis was crucial to elucidate the Cr(VI) adsorption mechanism on the HTC materials. The zeta potential analysis of HTC materials was carried out over the pH range from 1.0 to 7.0. As shown in Figure 5-14, the zeta-potential of HTC materials generally increased with the decrease in solution pH due to the protonation of surface functional groups. When the solution pH decreased from 7.0 to 3.0, the zeta-potential of HTC-MR increased from -32.33 ± 1.32 to +13.73 ± 0.80 mV. The increase in zeta-potential was contributed by the protonation of surface functional groups (e.g., amine group) on HTC-MR. The point of zero charge (pzc) of HTC-MR was pH 4.0. At this condition, the overall net surface charge was zero, but the $Q_{Cr(VI)}$ of HTC-MR at pH 4.0 was not zero. In fact, both the positively-charged and negatively-charged surface groups were present on the HTC-MR surface in this situation. The positively charged surface groups could still adsorb Cr(VI).

Figure 5-15 displays the speciation diagram of Cr(VI). More than 66% of Cr(VI) was in the form of $HCrO_4^-$ at pH < 6.0, and the remaining part of Cr(VI) was $CrO_4^{2-}$. The trend of zeta-potential could correlate to the $Q_{Cr(VI)}$ of HTC-MR. The higher the zeta-potential of the

HTC material was, the higher the Cr(VI) removal capacity would be. It was concluded that, at pH < 6.0, the anionic Cr(VI) ions were adsorbed onto the positively-charged functional groups by the electrostatic attraction.

By co-carbonizing the MR with a modifying agent (e.g., DEA and PEI), the zeta-potential values of 0.5DEA-HTC-MR and 0.5PEI-HTC-MR were more positive than of HTC-MR in the entire pH range from 1.0 to 7.0. This could be explained by the successful amine functionalization of the HTC-MR. The amine group had a $pK_a$ value at around 10 - 11, so the functionalized amine groups were protonated at pH 1.0 - 7.0. Protonation of the functionalized amine groups resulted in positive zeta-potential values of 0.5DEA-HTC-MR and 0.5PEI-HTC-MR in the range of pH 1.0 - 7.0 so the pzc of 0.5DEA-HTC-MR and 0.5PEI-HTC-MR could not be observed in the tested pH range.

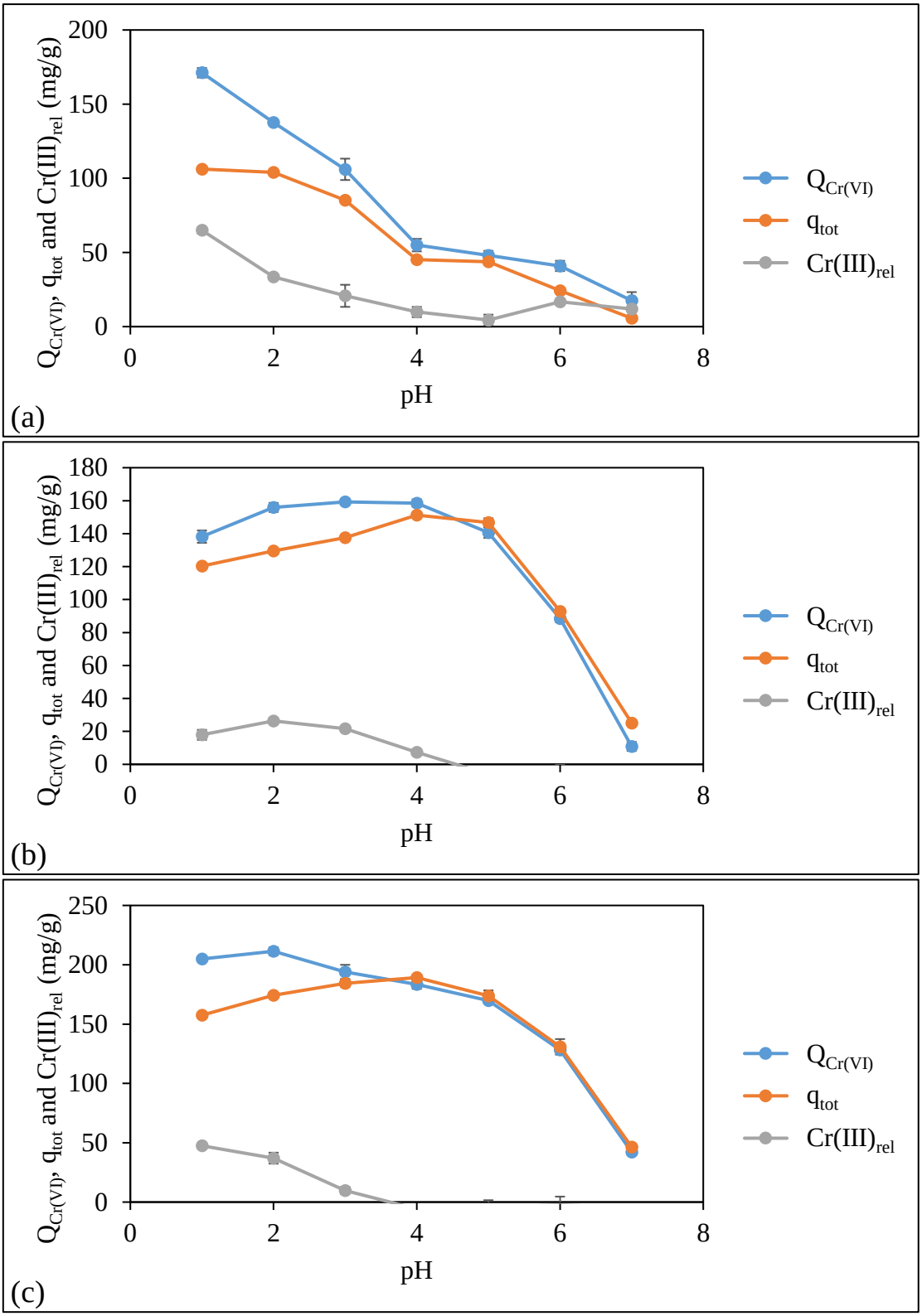


Figure 5-13 Effect of pH on $Q_{Cr(VI)}$, $q_{tot}$ and $Cr(III)_{rel}$ of (a) HTC-MR, (b) 0.5DEA-HTC-MR and (c) 0.5PEI-HTC-MR. (Experimental conditions: [Cr(VI)] = 500 ppm, adsorbent dosage = 1 g/L, t = 1 d, pH 1- 7, temperature = 25°C and agitation = 250 rpm)

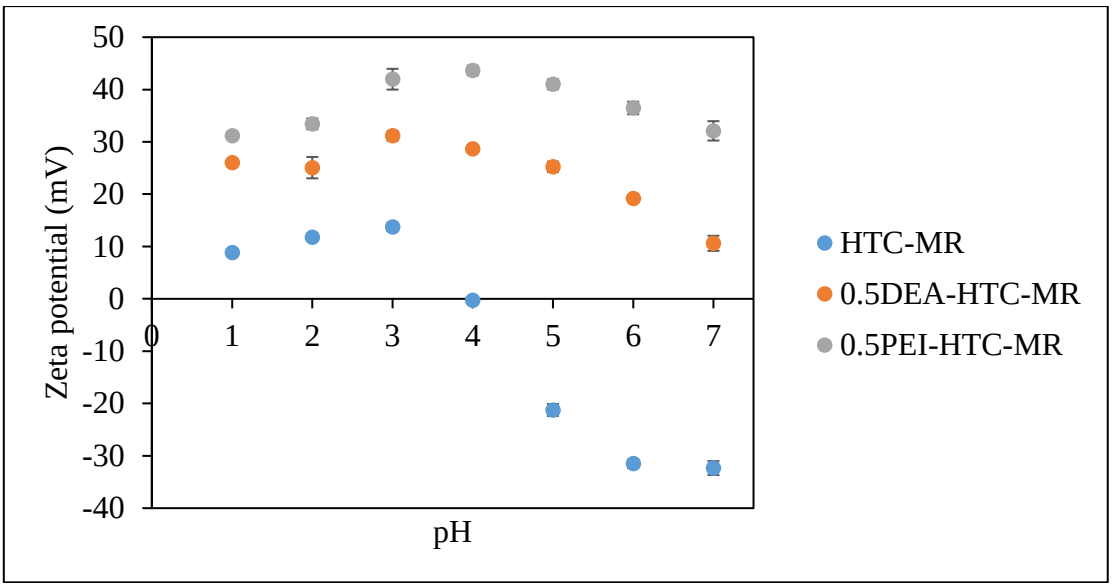


Figure 5-14 Effect of pH on zeta-potential of HTC-MR, 0.5DEA-HTC-MR and 0.5PEI-HTC-MR.

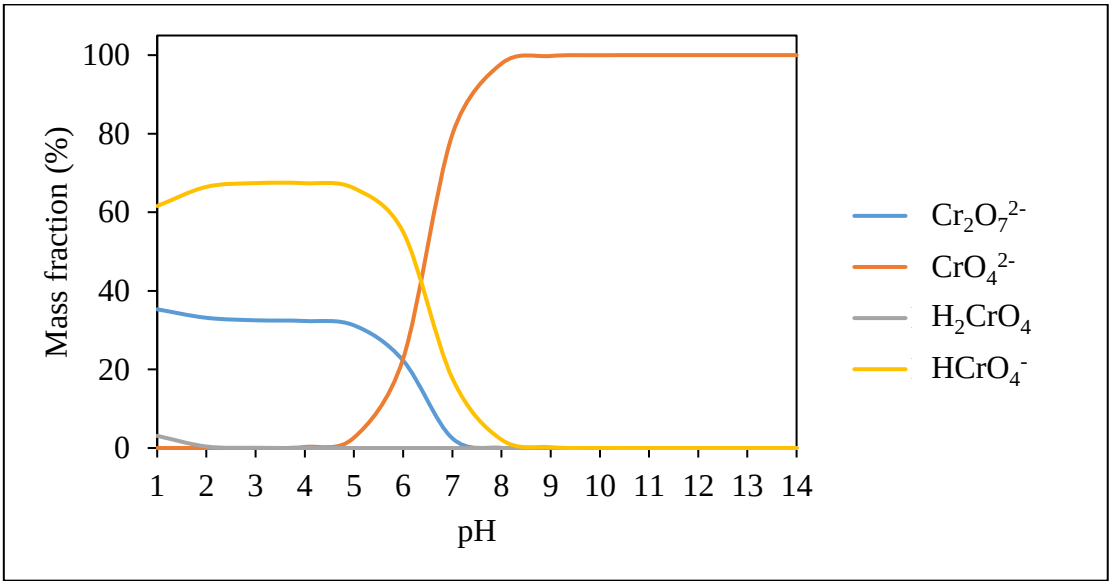


Figure 5-15 Speciation diagram of 500 ppm Cr(VI) solution simulated by Visual MINTEQ.

### 5.3.5 Effect of initial Cr(VI) concentration

Figure 5-16 illustrates the effect of initial Cr(VI) concentration on $Q_{Cr(VI)}$, $q_{tot}$ and $Cr(III)_{rel}$ of HTC-MR, 0.5DEA-HTC-MR and 0.5PEI-HTC-MR. It clearly showed that the $Q_{Cr(VI)}$, $q_{tot}$ and $Cr(III)_{rel}$ of HTC materials increased as the initial Cr(VI) concentration increased from 10 to 500 ppm. The $Q_{Cr(VI)}$, $q_{tot}$ and $Cr(III)_{rel}$ of HTC-MR reached the highest values of 168.5 ± 2.5, 103.6 ± 8.8 and 64.83 ± 11.28 mg/g at the initial Cr(VI) concentration of 500 ppm. The $Q_{Cr(VI)}$ values of 0.5DEA-HTC-MR reached a plateau at the initial Cr(VI) concentration of 750 ppm. However, the $Q_{Cr(VI)}$ values of 0.5PEI-HTC-MR could not reach a plateau even if 750 ppm Cr(VI) solution was used. The highest $Q_{Cr(VI)}$ values of 0.5DEA-HTC-MR and 0.5PEI-HTC-MR were 196.9 ± 3.6 and 234.9 ± 2.8 mg/g, respectively.

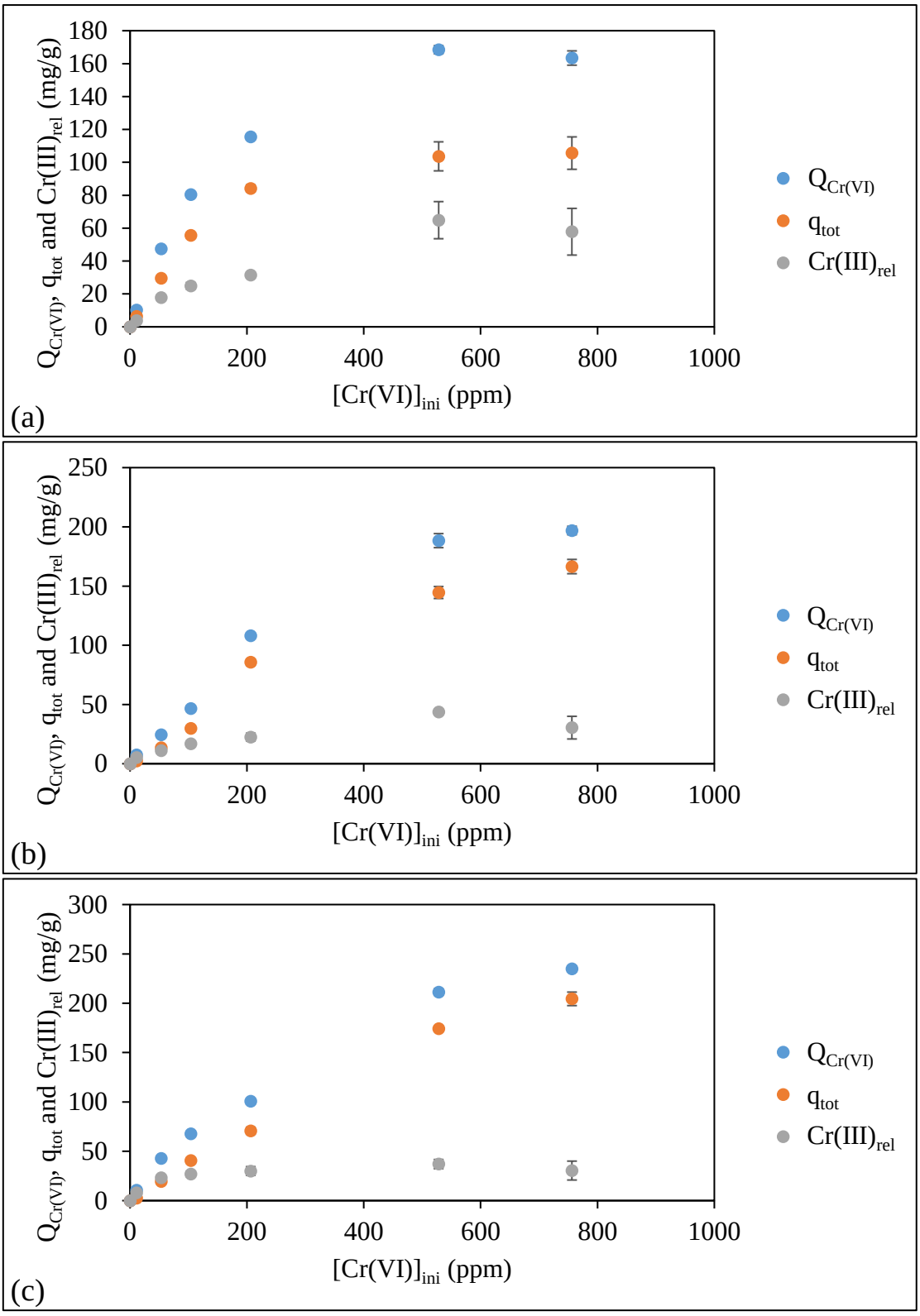


Figure 5-16 Effect of initial Cr(VI) concentration on $Q_{Cr(VI)}$, $q_{tot}$ and $Cr(III)_{rel}$ of (a) HTC-MR, (b) 0.5DEA-HTC-MR and (c) 0.5PEI-HTC-MR. (Experimental conditions: [Cr(VI)] = 10 - 500 ppm, adsorbent dosage = 1 g/L, t = 1 d, pH 2, temperature = 25°C and agitation = 250 rpm)

### 5.3.6 Isotherm modelling

The previous section investigated the total Cr adsorption capacities ($q_{tot}$) of HTC-MR, 0.5DEA-HTC-MR and 0.5PEI-HTC-MR, which represented the amount of Cr adsorbed on adsorbents. In order to understand the adsorption equilibrium and the maximum total Cr adsorption capacity of adsorbent, isotherm data were simulated with different adsorption isotherm models, namely Langmuir, Freundlich, Tempkin, Sips and Dubinin-Radushkevich (D-R) isotherm (Figure 5-17). As shown in Table 5-4, the Sips and Langmuir isotherm models showed the lowest RMSE value and the highest correlation coefficient. The Sips exponent ($m_s$) of HTC-MR, 0.5DEA-HTC-MR and 0.5PEI-HTC-MR was equal to 1, indicating that the Sips model was reduced to the Langmuir model. Therefore, the Langmuir model was the best-fit model to describe the Cr adsorption on the HTC materials. The excellent simulation of the isotherm data by the Langmuir model suggested homogeneous adsorption on the surface of HTC materials. The maximum total Cr adsorption capacities ($q_{max}$) of HTC-MR, 0.5DEA-HTC-MR and 0.5PEI-HTC-MR were 115.7 ± 10.8, 269.8 ± 5.9 and 414.6 ± 11.5 mg/g, respectively. The 0.5DEA-HTC-MR and 0.5PEI-HTC-MR showed higher Cr adsorption capacity than HTC-MR. Both the diethanolamine and polyethyleneimine were the effective modifying agents to functionalize the HTC-MR with amine groups and improve the Cr adsorption capacity of HTC-MR. The Langmuir constants, b, of HTC-MR, 0.5DEA-HTC-MR and 0.5PEI-HTC-MR were 2.14E-2 ± 2.24E-3, 3.06E-3 ± 1.48E-4 and 1.98E-3 ± 2.83E-6,

respectively. The lower b value of HTC-MR indicated that Cr(VI) exhibited a higher affinity to the HTC-MR than the 0.5DEA-HTC-MR and the 0.5PEI-HTC-MR. Therefore, at low initial Cr(VI) concentration (≤ 200 ppm), the total Cr adsorption capacity of HTC-MR should be higher than those of 0.5DEA-HTC-MR and 0.5PEI-HTC-MR. In addition, the Freundlich, Tempkin and D-R models did not simulate well the isotherm data.

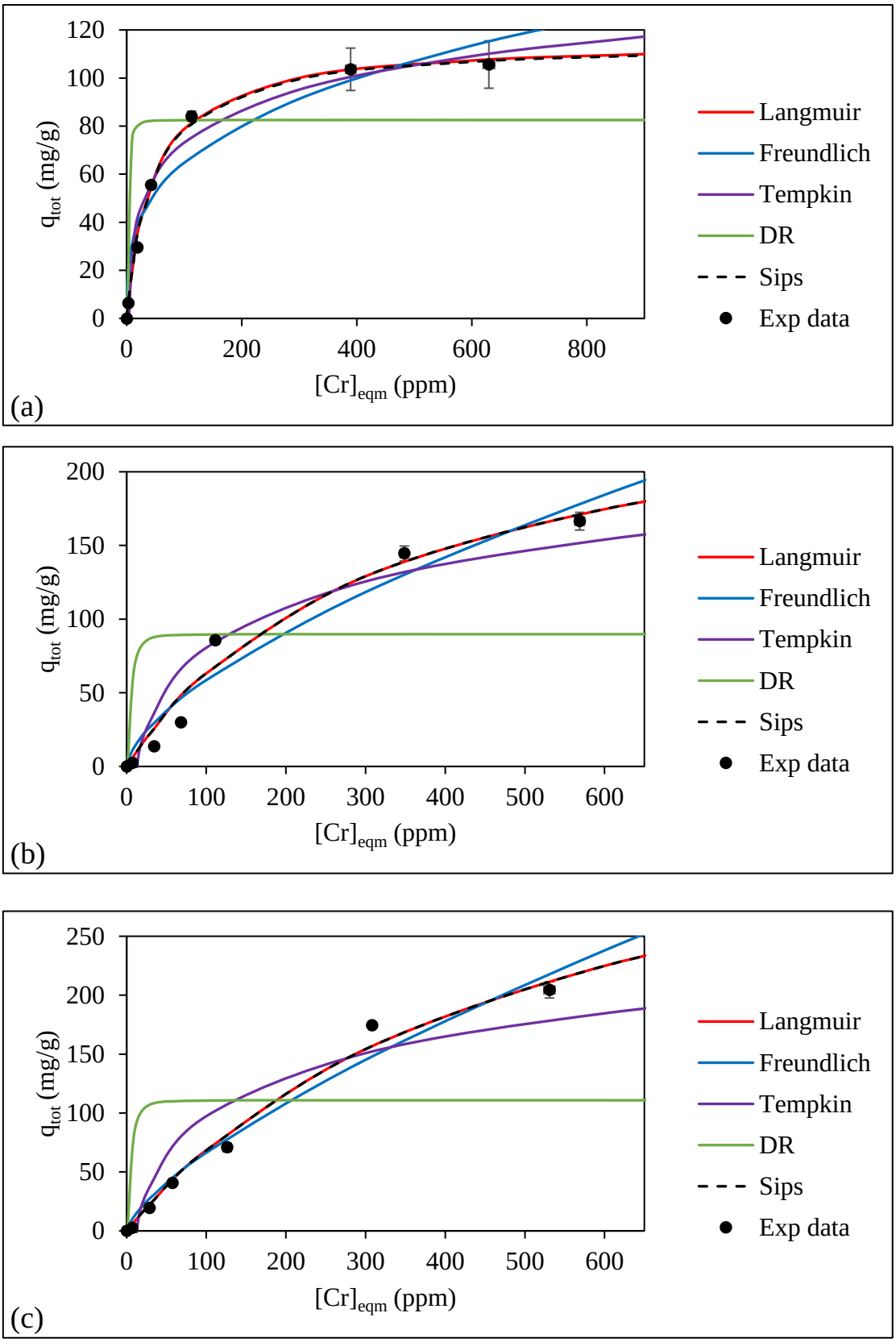


Figure 5-17 Total Cr adsorption isotherm of (a) HTC-MR, (b) 0.5DEA-HTC-MR and (c) 0.5PEI-HTC-MR.

Table 5-4 Isotherm modelling parameter of HTC-MR, 0.5DEA-HTC-MR and 0.5PEI-HTC-MR.

| Langmuir | $q_{max}$ | b | $R^2$ | RMSE |
|---|---|---|---|---|
| HTC-MR | 115.7 ± 10.8 | 2.14E-2 ± 2.24E-3 | **0.998 ± 0.002** | **2.176 ± 1.066** |
| 0.5DEA-HTC-MR | 269.8 ± 5.9 | 3.06E-3 ± 1.48E-4 | **0.973 ± 0.002** | **12.49 ± 0.10** |
| 0.5PEI-HTC-MR | 414.6 ± 11.5 | 1.98E-3 ± 2.83E-6 | **0.987 ± 0.007** | **10.25 ± 2.759** |
| Freundlich | $K_F$ | n | $R^2$ | RMSE |
| HTC-MR | 15.30 ± 0.24 | 3.193 ± 0.168 | 0.936 ± 0.015 | 12.20 ± 0.47 |
| 0.5DEA-HTC-MR | 3.082 ± 0.291 | 1.564 ± 0.021 | 0.950 ± 0.002 | 17.02 ± 0.15 |
| 0.5PEI-HTC-MR | 2.491 ± 0.088 | 1.403 ± 0.001 | 0.974 ± 0.010 | 14.59 ± 2.55 |
| Tempkin | $K_T$ | $b_T$ | $R^2$ | RMSE |
| HTC-MR | 0.382 ± 0.028 | 123.4 ± 11.33 | 0.973 ± 0.009 | 6.655 ± 0.477 |
| 0.5DEA-HTC-MR | 7.16E-2 ± 4.54E-3 | 60.51 ± 1.18 | 0.874 ± 0.003 | 24.76 ± 0.80 |
| 0.5PEI-HTC-MR | 7.38E-2 ± 3.64E-3 | 50.88 ± 0.44 | 0.857 ± 0.005 | 31.85 ± 0.11 |
| Sips | $K_s$ | $m_s$ | $n_m$ | $R^2$ | RMSE |
| HTC-MR | 2.459 ± 0.029 | 1.000 ± 0.000 | 2.14E-2 ± 2.24E-3 | **0.998 ± 0.002** | **2.176 ± 1.067** |
| 0.5DEA-HTC-MR | 0.825 ± 0.057 | 1.000 ± 0.000 | 3.06E-3 ± 1.48E-4 | **0.973 ± 0.002** | **12.49 ± 0.10** |
| 0.5PEI-HTC-MR | 0.819 ± 0.024 | 1.000 ± 0.000 | 1.98E-3 ± 2.83E-6 | **0.987 ± 0.007** | **10.25 ± 2.76** |
| D-R | $Q_D$ | E | $B_D$ | $R^2$ | RMSE |
| HTC-MR | 82.52 ± 4.77 | 575.1 ± 1.8 | 1.51E-6 ± 9.57E-9 | 0.918 ± 0.005 | 32.61 ± 3.06 |
| 0.5DEA-HTC-MR | 89.79 ± 2.18 | 321.9 ± 16.6 | 4.84E-6 ± 5.00E-7 | 0.821 ± 0.011 | 64.07 ± 1.78 |
| 0.5PEI-HTC-MR | 110.8 ± 1.3 | 324.4 ± 12.2 | 4.76E-6 ± 3.59E-7 | 0.875 ± 0.006 | 78.32 ± 0.75 |

### 5.3.7 Effect of adsorbent dosage

In order to examine the effect of adsorbent dosage, Cr(VI) removal study was carried out with various adsorbent dosages from 0.1 to 2.0 g/L and two different initial Cr(VI) concentrations (100 and 500 ppm). As shown in Figure 5-18, the percentage Cr(VI) removal generally increased with increasing adsorbent dosage since there were more adsorption functional groups available for Cr(VI) removal.

At low initial Cr(VI) concentration (100 ppm), the HTC-MR showed higher Cr(VI) affinity than the 0.5DEA-HTC-MR and the 0.5PEI-HTC-MR. More than 94% of Cr(VI) was removed by HTC-MR at 2.0 g/L adsorbent dosage in 1-day contact time. This was in agreement with the isotherm modelling results which showed that the HTC-MR had the largest Langmuir constant (b). Besides, the $Q_{Cr(VI)}$ of HTC materials decreased with increasing adsorbent dosage since the Cr(VI) removal capacity was limited by the low concentration of Cr(VI). The amount of Cr(III) released also decreased when the adsorbent increased from 0.1 to 0.5 g/L. The release of Cr(III) remained unchanged or only increased slightly when the adsorbent dosage was further increased to 2.0 g/L.

Under high concentration of Cr(VI) (500 ppm), the 0.5PEI-HTC-MR showed higher $\%Cr(VI)_{re}$ (71%) than HTC-MR (57%) and 0.5DEA-HTC-MR (64%) at the adsorbent dosage of 2.0 g/L. These results agreed with previous isotherm modelling results (Section 5.3.6) that the 0.5PEI-HTC-MR had the highest $q_{max}$ value.

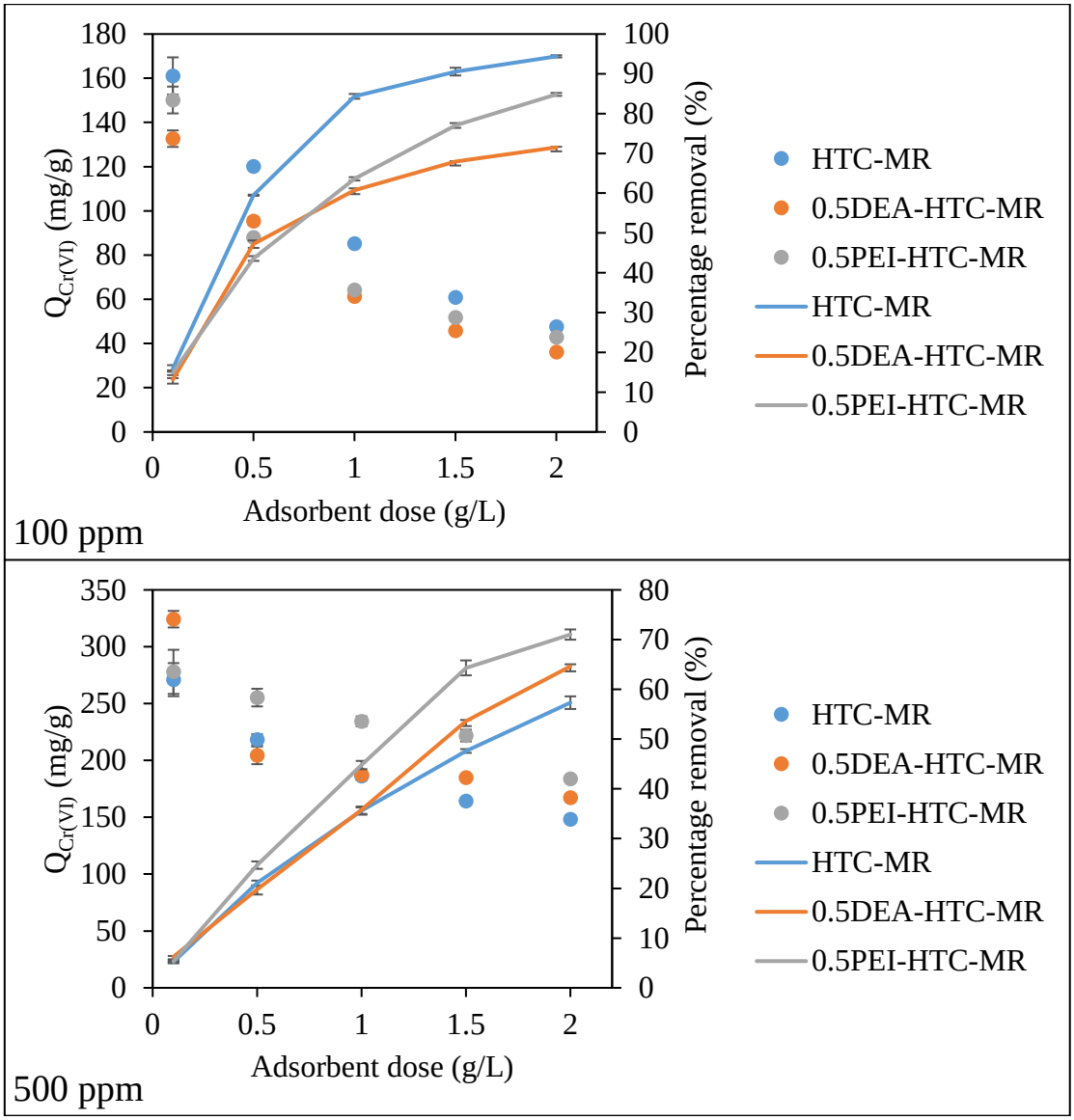


Figure 5-18 Effect of adsorbent dose on the Cr(VI) removal capacity and the percentage Cr(VI) removal. (Experimental conditions: [Cr(VI)] = 100 - 500 ppm, adsorbent dosage = 0.1 - 2.0 g/L, t = 1 d, pH 2, temperature = 25°C and agitation = 250 rpm)

### 5.3.8 Effect of temperature

Temperature is an important factor that affects the Cr(VI) removal on HTC materials. The Cr(VI) removal kinetics of the HTC materials was investigated under different temperatures (4ºC, 25ºC and 40ºC), and the Cr(VI) removal kinetic curves are shown in Figure 5-19. Higher Cr(VI) removal capacity and faster Cr(VI) removal rate were obtained at a higher temperature. The Cr(VI) removal capacity ($Q_{Cr(VI)}$) of HTC-MR increased from 159.4 ± 2.2 to 225.1 ± 9.2 mg/g when the temperature increased from 4ºC to 40ºC. A similar observation was made in 0.5DEA-HTC-MR and 0.5PEI-HTC-MR, where the $Q_{Cr(VI)}$ increased with the increase in temperatures. The higher $Q_{Cr(VI)}$ values at the higher temperature suggested the physisorption nature of Cr(VI) adsorption on the HTC-materials. In addition, by fitting the kinetic data to the fractional power kinetic model, the obtained $k_fv$ value represents the specific Cr(VI) removal rate at t = 1 min. The modelling curves were displayed in Figure 5-19, while the modelling parameters were summarized in Table 5-5. The $k_fv$ value of HTC-MR increased from 7.782 ± 0.027 to 10.59 ± 0.33 mg/g-min with increasing temperature from 4ºC to 40ºC. However, a lower $k_fv$ value was obtained with 0.5DEA-HTC-MR at a higher temperature. Meanwhile, there was no obvious relationship between the $k_fv$ values of 0.5PEI-HTC-MR and the temperatures.

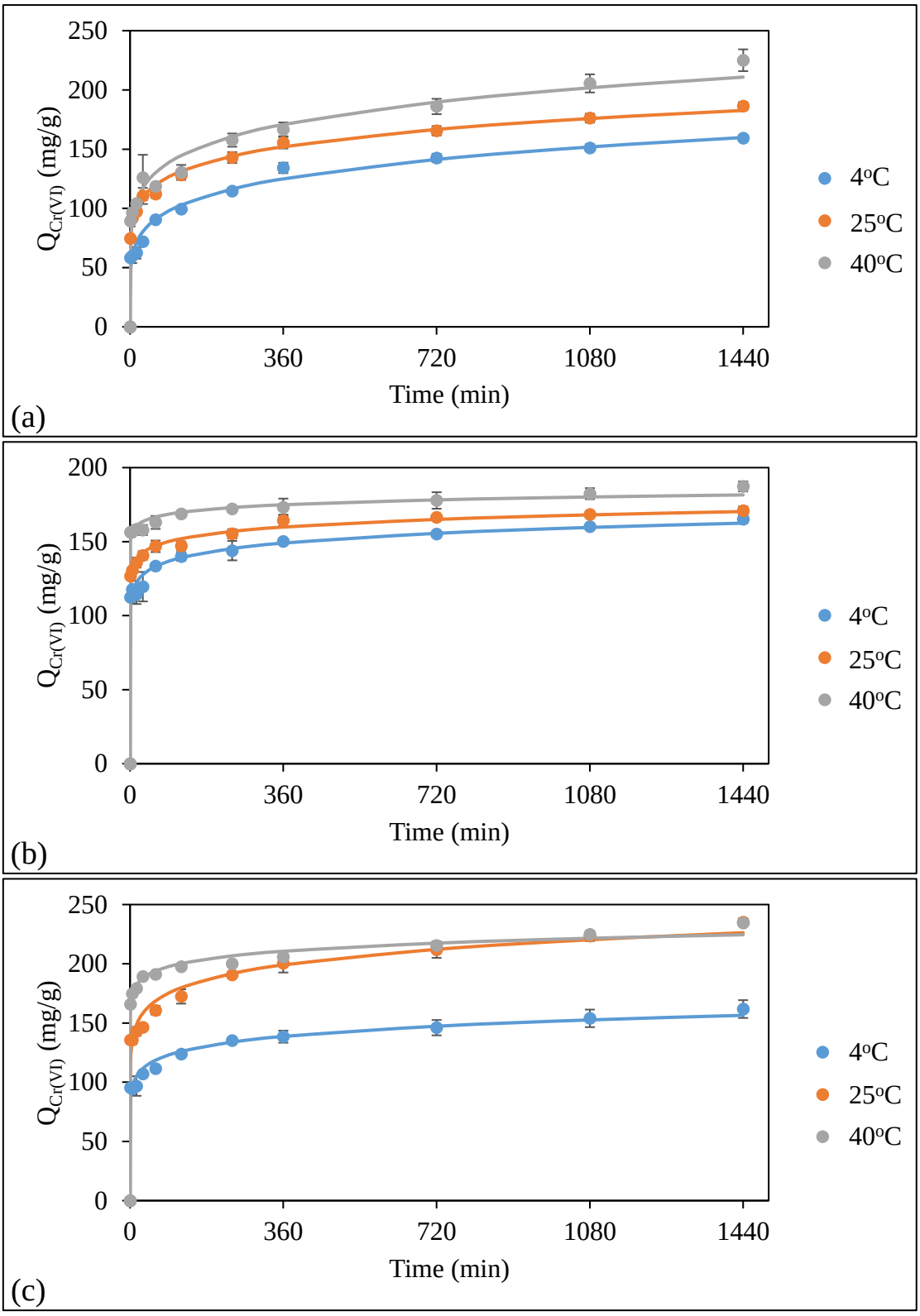


Figure 5-19 Cr(VI) removal kinetics at different temperature. (a) HTC-MR, (b) 0.5DEA-HTC-MR and (c) 0.5PEI-HTC-MR. (Experimental conditions: [Cr(VI)] = 500 ppm, adsorbent dosage = 1 g/L, t = 1 d, pH 2, temperature = 4, 25, 40ºC and agitation = 250 rpm)

Table 5-5 Modelling parameters from fractional power model for the Cr(VI) removal by HTC-MR, 0.5DEA-HTC-MR and 0.5PEI-HTC-MR at different temperatures.

| | Temperature | $k_f$ (mg/g-min$^v$) | v | $k_f v$ (mg/g-min) | $R^2$ | RMSE |
|---|---|---|---|---|---|---|
| HTC-MR | 4ºC | 43.92 ± 3.67 | 0.179 ± 0.015 | 7.782 ± 0.027 | 0.901 ± 0.027 | 6.903 ± 0.260 |
| | 25ºC | 69.54 ± 0.45 | 0.133 ± 0.005 | 9.233 ± 0.256 | 0.994 ± 0.006 | 4.418 ± 0.152 |
| | 40ºC | 69.94 ± 3.66 | 0.152 ± 0.013 | 10.59 ± 0.33 | 0.974 ± 0.012 | 11.53 ± 1.19 |
| 0.5DEA-HTC-MR | 4ºC | 103.2 ± 6.3 | 6.25E-2 ± 8.25E-3 | 6.426 ± 0.458 | 0.987 ± 0.008 | 5.266 ± 1.867 |
| | 25ºC | 122.1 ± 0.8 | 4.58E-2 ± 1.47E-3 | 5.592 ± 0.144 | 0.994 ± 0.001 | 3.849 ± 0.386 |
| | 40ºC | 149.3 ± 2.3 | 2.69E-2 ± 4.84E-3 | 4.010 ± 0.663 | 0.993 ± 0.005 | 4.223 ± 1.846 |
| 0.5PEI-HTC-MR | 4ºC | 82.95 ± 0.01 | 8.72E-2 ± 5.45E-3 | 7.232 ± 0.453 | 0.987 ± 0.003 | 6.133 ± 0.701 |
| | 25ºC | 115.6 ± 4.7 | 9.24E-2 ± 9.44E-3 | 10.65 ± 0.65 | 0.980 ± 0.004 | 9.162 ± 0.207 |
| | 40ºC | 160.5 ± 0.8 | 4.62E-2 ± 2.05E-3 | 7.407 ± 0.293 | 0.993 ± 0.003 | 5.143 ± 1.353 |

### 5.3.9 Cr desorption study

The desorption of Cr from the Cr-laden HTC-MR, 0.5DEA-HTC-MR and 0.5PEI-HTC-MR was investigated with four different desorption agents (e.g., 0.5 M $HNO_3$, 2.0 M $HNO_3$, 0.5 M NaOH and 2.0 M NaOH). The desorbed solutions were examined with UV-vis and ICP-OES analysis to determine the concentration of Cr(VI) and total Cr, respectively. The %Cr(VI) desorption ($\%D_{Cr(VI)}$) and %Cr desorption ($\%D_{Cr}$) were calculated by the following equations.

$$\%D_{Cr(VI)} = \frac{Amount\ of\ Cr(VI)\ desorbed}{Amount\ of\ Cr\ adsorbed} \times 100\%$$

$$\%D_{Cr} = \frac{Amount\ of\ Cr\ desorbed}{Amount\ of\ Cr\ adsorbed} \times 100\%$$

The $\%D_{Cr(VI)}$ and $\%D_{Cr}$ of different adsorbents using various desorption agents are illustrated in Figure 5-20. Considering the total Cr desorption ($\%D_{Cr}$), over 60% of Cr desorption was obtained with the four tested desorption agents. The adsorbed Cr could be removed from the adsorbent surface by using either acidic or alkaline solution, but their desorption mechanism and the ionic form of the desorbed Cr would be totally different.

With the use of NaOH solution as desorption agent, around 80% of the adsorbed Cr was desorbed from the Cr-laden 0.5DEA-HTC-MR and 0.5PEI-HTC-MR. Nearly all the desorbed Cr was Cr(VI) since the $\%D_{Cr(VI)}$ was approximately equal to $\%D_{Cr}$. These results suggested that the Cr(VI) adsorbed on 0.5DEA-HTC-MR and 0.5PEI-HTC-MR would not be reduced into Cr(III) during the desorption step. The NaOH could effectively desorb the Cr(VI) through

the ion-exchange mechanism, which the hydroxide ions from NaOH would replace the Cr(VI) from the adsorption sites. It is worth mentioning that the remaining 20% undesorbed Cr would be cationic Cr(III) which could not be desorbed from the adsorbent surface in the alkaline condition. These Cr(III) ions were the result of Cr(VI) reduction taking place in an acidic adsorption environment. The adsorbed Cr(VI) would not be reduced in the alkaline desorbing solution since Cr(VI) reduction was catalyzed by proton ions. The 0.5 M and 2.0 M NaOH showed similar desorption efficiency, so the effect of NaOH concentration was insignificant. In addition, the sodium hydroxide solution was less efficient in desorbing Cr from HTC-MR. The $\%D_{Cr}$ values of 0.5 and 2.0 M of NaOH were 55.9 and 63.3%, respectively.

Apart from the NaOH solution, the nitric acid could also effectively desorb Cr from the HTC materials. However, the Cr desorption mechanism of the $HNO_3$ solution was different from that of the NaOH solution. The $\%D_{Cr}$ values of Cr-laden HTC-MR in the 0.5 M $HNO_3$ and 2.0 M $HNO_3$ were 57.5% and 63.3%, respectively, which was similar to that in the 0.5 M NaOH and 2.0 M NaOH. For the Cr-laden 0.5DEA-HTC-MR and 0.5PEI-HTC-MR, the $\%D_{Cr}$ values of $HNO_3$ were even higher than that of NaOH. However, only 5.3 - 12.9% of the desorbed Cr from HTC-MR was Cr(VI) so the adsorbed Cr(VI) was reduced into Cr(III) on the adsorbent surface under acidic desorption condition. The reduced Cr(III) was then desorbed from the adsorbent by the high concentration of proton through the ion-exchange mechanism. The acid catalyzed Cr(VI) reduction was also observed in the Cr(VI)-laden 0.5DEA-HTC-MR

and 0.5PEI-HTC-MR. Moreover, the Cr(VI) reduction was more significant at the high concentration of acid. Nitric acid provided a high concentration of proton that enhanced the rate of Cr(VI) reduction, as well as the ion-exchange rate of Cr(III). Besides, there was a significant amount of Cr(VI) desorbed from HTC materials, implying that there was a portion of Cr(VI) being directly desorbed from the adsorbent surface without reduction. The ion-exchange reaction between the adsorbed Cr(VI) anions and the nitrate ions might account for the direct Cr(VI) desorption. Nevertheless, literature rarely applies acid as desorption agent for Cr(VI). There was no reported research that detail discussed the ionic form of the desorbed Cr. This study revealed the Cr desorption mechanism by the acid and alkaline solutions and also confirmed the acid-catalyzed Cr(VI) reduction in a new approach.

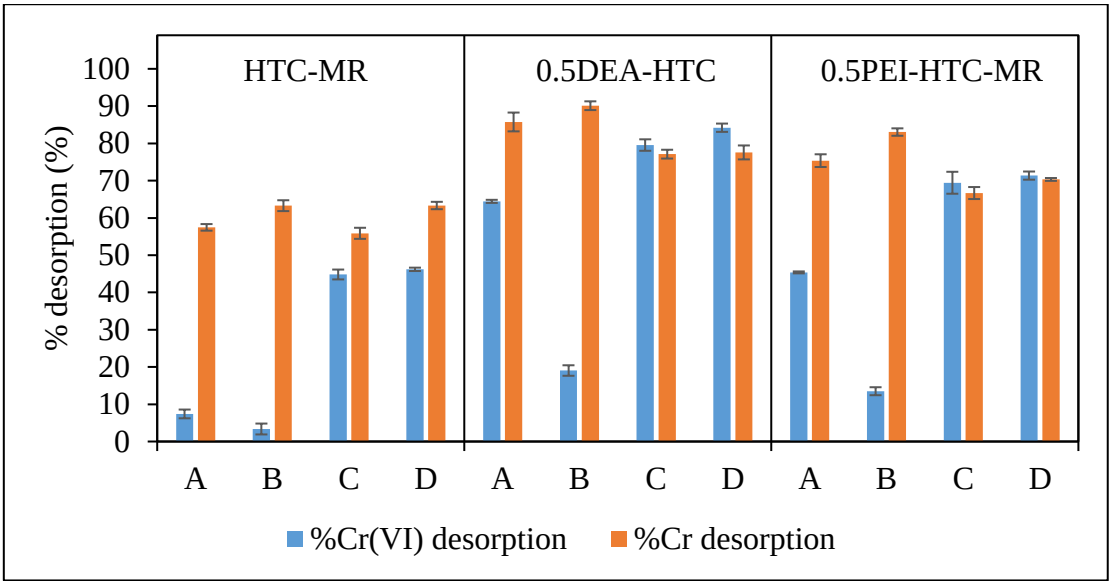


Figure 5-20 Percentage Cr(VI) desorption and percentage Cr desorption from Cr-laden HTC materials by different desorption agents: A = 0.5 M $HNO_3$, B = 2.0 M $HNO_3$, C = 0.5 M NaOH and D = 2.0 M NaOH. (Experimental conditions: **adsorption**, [Cr(VI)] = 500 ppm, adsorbent dosage = 1 g/L, t = 1 d, pH 2, temperature = 25ºC and agitation = 250 rpm; **desorption**, adsorbent dosage = 2 g/L, t = 1 d, temperature = 25ºC and agitation = 250 rpm)

Figure 5-21 compares the $Q_{Cr(VI)}$ value of HTC materials in the two-cycle adsorption. In the 2nd cycle adsorption, the $Q_{Cr(VI)}$ value of HTC materials was significantly reduced. Both the acidic and alkaline treatment would severely damage the Cr(VI) adsorption sites on the HTC materials. A lower concentration of NaOH could be applied in order to reduce the damage to the HTC materials with effective Cr(VI) desorption.

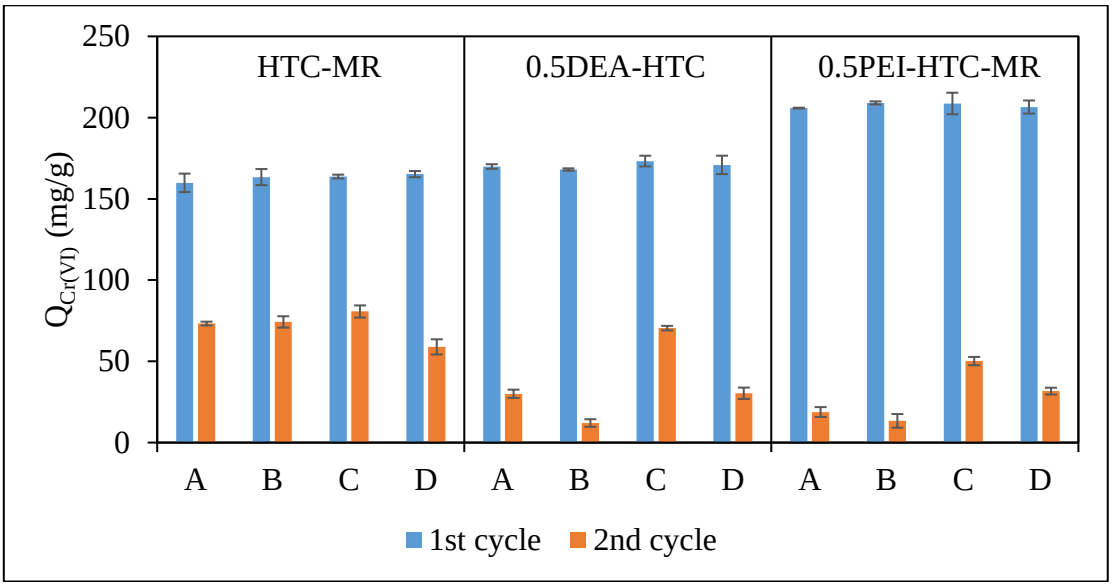


Figure 5-21 Adsorption-desorption cycle (A: 0.5 M $HNO_3$, B: 2.0 M $HNO_3$, C: 0.5 M NaOH and D: 2.0 M NaOH).

## 5.4 Removal of Cr(VI) by magnetic hydrothermal carbonized *M. rouxii* ($Fe_3O_4$-0.5PEI-HTC-MR)

### 5.4.1 Effect of contact time and kinetic modelling

The Cr(VI) removal kinetics of the $Fe_3O_4$, $Fe_3O_4$-0.5PEI-HTC-MR and 0.5PEI-HTC-MR are compared in Figure 5-22. A fast Cr(VI) removal was observed in the tested adsorbents and the equilibrium time was around 1 hour. The equilibrium Cr(VI) removal capacities ($Q_{Cr(VI)}$) of the $Fe_3O_4$, $Fe_3O_4$-0.5PEI-HTC-MR and 0.5PEI-HTC-MR was 32.26 ± 1.62, 162.3 ± 3.5 and 224.7 ± 0.5 mg/g, respectively. The $Fe_3O_4$-0.5PEI-HTC-MR showed lower equilibrium $Q_{Cr(VI)}$ than the 0.5PEI-HTC-MR since the $Fe_3O_4$ showed a lower Cr(VI) removal capacity than the 0.5PEI-HTC-MR.

Five kinetic models were applied to simulate the Cr(VI) removal kinetics of $Fe_3O_4$-0.5PEI-HTC-MR (Figure 5-23). The modelling parameters are summarized in Table 5-6. Both the Elovich and fractional power models could well describe the Cr(VI) removal kinetics of $Fe_3O_4$-0.5PEI-HTC-MR, but the fractional power model was the best-fit model with the lowest RMSE and the highest correlation coefficient. From the fractional power model, the specific Cr(VI) removal rate at t = 1 min ($k_fv$) of $Fe_3O_4$-0.5PEI-HTC-MR was 4.774 ± 0.300 mg/g-min, which was smaller than that of 0.5PEI-HTC-MR (8.568 ± 0.063 mg/g-min). The Cr(VI) removal rate of 0.5PEI-HTC-MR was reduced after the incorporation of $Fe_3O_4$ nanoparticles.

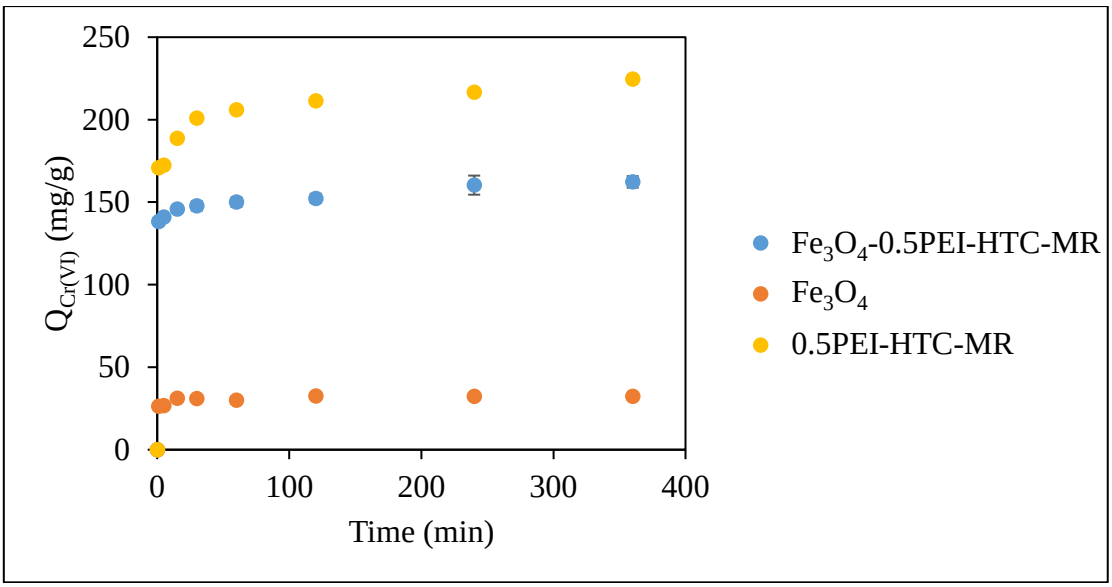


Figure 5-22 Cr(VI) removal kinetics of $Fe_3O_4$, $Fe_3O_4$-0.5PEI-HTC-MR and 0.5PEI-HTC-MR. (Experimental conditions: [Cr(VI)] = 500 ppm, adsorbent dosage = 1 g/L, t = 1 d, pH 2, temperature = 25ºC and agitation = 250 rpm)

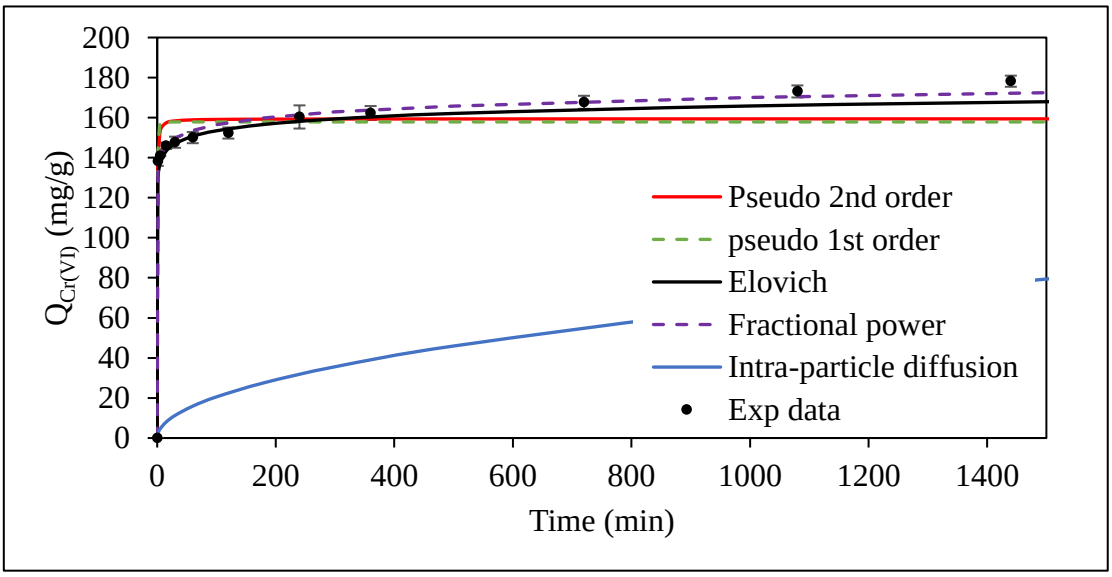


Figure 5-23 Modelling curves and experimental data of Cr(VI) removal kinetics of $Fe_3O_4$-0.5PEI-HTC-MR.

Table 5-6 Cr(VI) removal kinetic modelling parameters of $Fe_3O_4$-0.5PEI-HTC-MR and 0.5PEI-HTC-MR.

| Pseudo 2nd order | $q_e$ (mg/g) | $k_2$ (g $mg^{-1}$ $min^{-1}$) | $R^2$ | RMSE |
|---|---|---|---|---|
| $Fe_3O_4$-0.5PEI-HTC-MR | 159.4 ± 2.7 | 3.19E-2 ± 1.83E-3 | 0.951 ± 0.006 | 10.86 ± 0.85 |
| 0.5PEI-HTC-MR | 217.3 ± 0.9 | 1.21E-2 ± 1.84E-4 | 0.929 ± 0.001 | 18.10 ± 0.22 |
| Pseudo 1st order | $q_e$ (mg/g) | $k_1$ ($min^{-1}$) | $R^2$ | RMSE |
| $Fe_3O_4$-0.5PEI-HTC-MR | 157.9 ± 2.5 | 2.084 ± 0.005 | 0.942 ± 0.007 | 11.84 ± 0.96 |
| 0.5PEI-HTC-MR | 213.4 ± 0.8 | 1.607 ± 0.004 | 0.904 ± 0.002 | 21.11 ± 0.28 |

| Elovich | b (g $mg^{-1}$) | a (mg $g^{-1}$ $min^{-1}$) | $t_0$ (min) | $R_E$ | $R^2$ | RMSE |
|---|---|---|---|---|---|---|
| $Fe_3O_4$-0.5PEI-HTC-MR | 0.186 ± 0.014 | 4.46E11 ± 5.25E10 | 4.14E-11 ± 4.97E-12 | 3.03E-2 ±1.87E-3 | 0.993 ± 0.001 | 4.115 ± 0.102 |
| 0.5PEI-HTC-MR | 0.137 ± 0.005 | 6.33E7 ± 8.20E6 | 1.67E-7 ± 2.33E-8 | 4.28E-2 ± 2.45E-4 | 0.996 ± 0.002 | 4.154 ± 0.174 |

| Fractional Power | v | $k_f$ (mg/g-$min^v$) | $k_fv$ (mg/g-min) | $R^2$ | RMSE |
|---|---|---|---|---|---|
| $Fe_3O_4$-0.5PEI-HTC-MR | 3.60E-2 ± 2.25E-3 | 132.6 ± 0.8 | 4.774 ± 0.300 | **0.994 ± 0.001** | **3.678 ± 0.188** |
| 0.5PEI-HTC-MR | 5.18E2 ± 3.68E4 | 165.4 ± 0.3 | 8.568 ± 0.063 | **0.997 ± 0.003** | **3.507 ± 0.210** |

| Intra-particle diffusion | $k_{diff}$ (mg/g- $min^{0.5}$) | $R^2$ | RMSE |
|---|---|---|---|
| $Fe_3O_4$-0.5PEI-HTC-MR | 2.055 ± 0.073 | 0.324 ± 0.010 | 132.4 ± 1.5 |
| 0.5PEI-HTC-MR | 3.145 ± 0.022 | 0.394 ± 0.002 | 171.8 ± 0.5 |

### 5.4.2 Effect of pH

Figure 5-24 illustrates the effect of pH on $Q_{Cr(VI)}$, $q_{tot}$ and $Cr(III)_{rel}$ of $Fe_3O_4$-0.5PEI-HTC-MR. The Cr(VI) removal capacity was very low at pH of 7.0. It dramatically increased from 22.07 ± 1.44 to 133.3 ± 0.7 mg/g when the solution pH was increased from 7.0 to 4.0. The Cr(VI) removal was favored in the acidic pH (1.0 to 3.0). The highest $Q_{Cr(VI)}$ value was achieved at pH 2.0. The anionic Cr(VI) ions were adsorbed onto the protonated surface groups at $Fe_3O_4$-0.5PEI-HTC-MR. The trend of $q_{tot}$ value was similar to that of $Q_{Cr(VI)}$, and only small amounts of Cr(III) were detected in the solution phase at every tested pH values. The adsorbed Cr strongly bound to the $Fe_3O_4$-0.5PEI-HTC-MR surface, and the amounts of Cr(III) release was a bit larger in acidic pH. The Cr(III) might be desorbed by the proton ions through the ion-exchange mechanism.

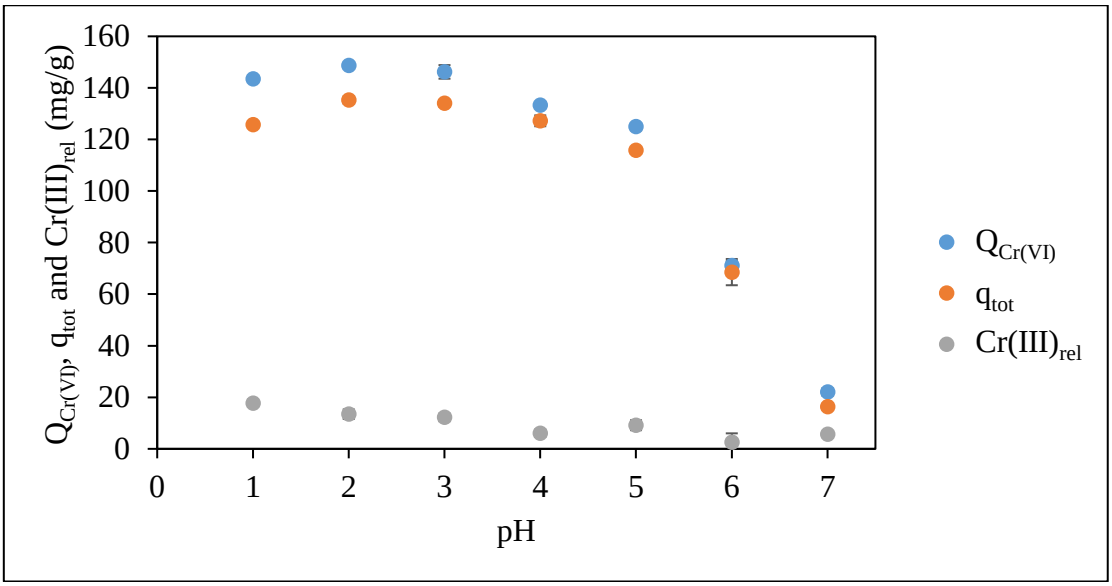


Figure 5-24 Effect of pH on Cr(VI) removal capacity, total Cr adsorption capacity and Cr(III) release by $Fe_3O_4$-0.5PEI-HTC-MR. (Experimental conditions: [Cr(VI)] = 500 ppm, adsorbent dosage = 1 g/L, t = 1 d, pH 1 - 7, temperature = 25°C and agitation = 250 rpm)

### 5.4.3 Effect of initial Cr(VI) concentration and isotherm modelling

The effect of initial Cr(VI) concentration on the Cr(VI) removal performance of $Fe_3O_4$-0.5PEI-HTC-MR was also investigated (Figure 5-25). The $Q_{Cr(VI)}$ and $q_{tot}$ values increased from 11.34 ± 0.14 to 163.0 ± 8.0 mg/g and from 6.158 ± 0.148 to 157.0 ± 3.88 mg/g, respectively, as the initial Cr(VI) concentration increased from 10 to 1000 ppm. Meanwhile, the percentage Cr(VI) removal reduced from 94.01 ± 1.1 to 15.89 ± 0.78%. Less than 15 ppm of the adsorbed Cr was released back to the solution phase in the form of Cr(III). The reduced Cr(III) would strongly bind to the $Fe_3O_4$-0.5PEI-HTC-MR.

The total Cr adsorption isotherm data were simulated with different isotherm models (Figure 5-26). By comparing the RMSE value of different models (Table 5-7), it was found that the Langmuir isotherm model was the best-fit model with the lowest RMSE and the highest correlation coefficient. It is worth noting that the $m_s$ value of the Sips model was equal to 1, which means the Sips model was reduced to the Langmuir model. This suggested the occurrence of monolayer Cr(VI) adsorption on the $Fe_3O_4$-0.5PEI-HTC-MR. The maximum total Cr adsorption capacity of $Fe_3O_4$-0.5PEI-HTC-MR was 220.5 ± 5.9 mg/g, which was smaller than that of 0.5PEI-HTC-MR (414.6 ± 11.5 mg/g). The Freundlich, Tempkin and Dubinin–Radushkevich (D-R) isotherm models failed to describe the isotherm data.

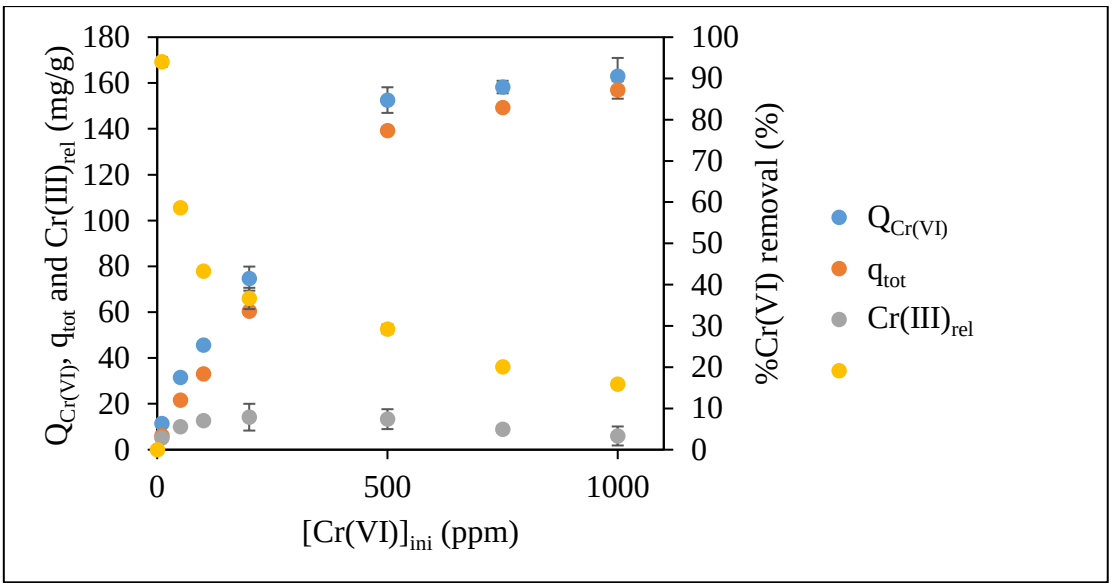


Figure 5-25 Effect of initial Cr(VI) concentration on Cr(VI) removal capacity ($Q_{Cr(VI)}$), total Cr adsorption capacity ($q_{tot}$) and Cr(III) release ($Cr(III)_{rel}$) by $Fe_3O_4$-0.5PEI-HTC-MR. (Experimental conditions: [Cr(VI)] = 10 - 500 ppm, adsorbent dosage = 1 g/L, t = 1 d, pH 2, temperature = 25°C and agitation = 250 rpm)

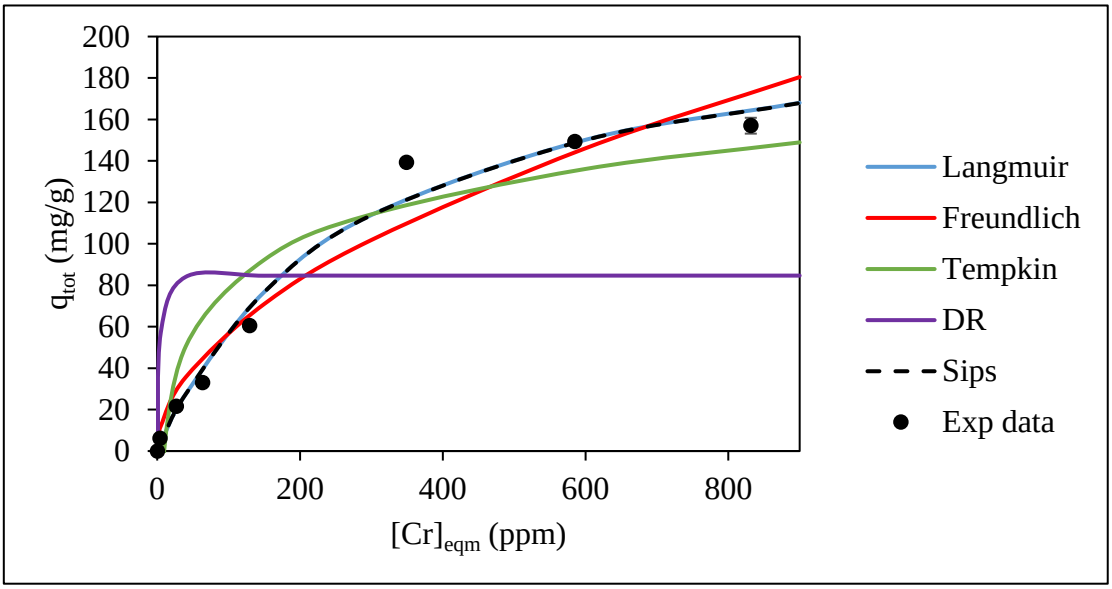


Figure 5-26 Total Cr adsorption isotherm of $Fe_3O_4$-0.5PEI-HTC-MR.

Table 5-7 Isotherm modelling parameters of $Fe_3O_4$-0.5PEI-HTC-MR and 0.5PEI-HTC-MR.

| Langmuir | $q_{max}$ | b | $R^2$ | RMSE |
|---|---|---|---|---|
| $Fe_3O_4$-0.5PEI-HTC-MR | 220.5 ± 5.9 | 3.56E-3 ± 1.58E-4 | **0.984 ± 0.004** | **9.240 ± 1.105** |
| 0.5PEI-HTC-MR | 414.6 ± 11.5 | 1.98E-3 ± 2.83E-6 | **0.987 ± 0.007** | **10.25 ± 2.759** |
| Freundlich | $K_F$ | n | $R^2$ | RMSE |
| $Fe_3O_4$-0.5PEI-HTC-MR | 5.220 ± 0.201 | 1.920 ± 0.030 | 0.956 ± 0.008 | 15.20 ± 1.24 |
| 0.5PEI-HTC-MR | 2.491 ± 0.088 | 1.403 ± 0.001 | 0.974 ± 0.010 | 14.59 ± 2.55 |
| Tempkin | $K_T$ | $b_T$ | $R^2$ | RMSE |
| $Fe_3O_4$-0.5PEI-HTC-MR | 0.124 ± 0.003 | 78.37 ± 0.28 | 0.856 ± 0.005 | 24.85 ± 0.29 |
| 0.5PEI-HTC-MR | 7.38E-2 ± 3.64E-3 | 50.88 ± 0.44 | 0.857 ± 0.005 | 31.85 ± 0.11 |
| Sips | $K_s$ | $m_s$ | $n_m$ | $R^2$ | RMSE |
| $Fe_3O_4$-0.5PEI-HTC-MR | 0.785 ± 0.014 | 1.000 ± 0.000 | 3.56E-3 ± 1.58E-4 | **0.984 ± 0.004** | **9.240 ± 1.105** |
| 0.5PEI-HTC-MR | 0.819 ± 0.024 | 1.000 ± 0.000 | 1.98E-3 ± 2.83E-6 | **0.987 ± 0.007** | **10.25 ± 2.76** |
| D-R | $Q_D$ | E | $B_D$ | $R^2$ | RMSE |
| $Fe_3O_4$-0.5PEI-HTC-MR | 84.65 ± 0.18 | 510.2 ± 11.3 | 1.92E-6 ± 8.55E-8 | 0.710 ± 0.007 | 58.91 ± 0.61 |
| 0.5PEI-HTC-MR | 110.8 ± 1.3 | 324.4 ± 12.2 | 4.76E-6 ± 3.59E-7 | 0.875 ± 0.006 | 78.32 ± 0.75 |

## 5.5 Characterization of hydrothermal carbonized *M. rouxii*

### 5.5.1 Fourier-transform Infrared spectroscopy (FTIR)

The Fourier-transform Infrared (FTIR) spectra of the raw MR and the HTC materials in the region between 4000 and 400 $cm^{-1}$ are illustrated in Figure 5-27. In the FTIR spectrum of HTC-MR, the board band at 3300 $cm^{-1}$ was the stretching vibration of O-H (Huang et al., 2017a). The intensity of O-H stretching was also observed in MR and was reduced after the HTC process, indicating the hydroxyl groups on the biomass materials were removed through the dehydration reaction. The signal at 3450 $cm^{-1}$ was assigned to the N–H stretching of amine groups (Xiao et al., 2013), while the peaks at 2920 to 2950 $cm^{-1}$ were attributed to the C-H stretching (Kumar et al., 2014; Li et al., 2014b). In the raw MR, the signal of the N–H stretching was masked by the O-H stretching.

Besides, the intensive peak at 1650 $cm^{-1}$ was associated with the asymmetric C=O stretching of carboxylate groups, the C=O stretching of amide (amide I) and the aromatic C=C stretching (Kumar et al., 2014). The peak at 1550 $cm^{-1}$ was attributed to the N-H bending and the C-N stretching of amide groups (Kumar et al., 2014; Li et al., 2014b). The signals of unsaturated carbon indicated the hydrothermal carbon was produced from aromatization of monomer (e.g., 5-hydroxymethylfurfural). The vibration frequency at 1410 $cm^{-1}$ was assigned to the symmetric C=O stretching of carboxylate groups. Meanwhile, the sharp peaks at 1380 to 1320 $cm^{-1}$ were the C-N stretching (Huang et al., 2017a). The peak at 1250 $cm^{-1}$ represented

the C-H stretching of amide (amide III) and the C-O stretching of phenol (Kumar et al., 2011; Kumar et al., 2014). The intensities of these peaks declined after the hydrothermal treatment. The peak at 1150 $cm^{-1}$ was the C–H vibrations associated with the pyranose (Xiao et al., 2013). The intensity of this peak was reduced after the hydrothermal treatment, but the pyranose structure did not completely disappear. This result suggested an incomplete decomposition of the pyranose ring through dehydration during the hydrothermal process. The peaks at 1080 to 1030 $cm^{-1}$ corresponded to C-O stretching of the hydroxyl group (Kumar et al., 2011; Kumar et al., 2014).

After amino-functionalization by modifying agents, the N-H stretching signal at 3450 $cm^{-1}$ became easier to be identified in the 0.5DEA-HTC-MR and 0.5PEI-HTC-MR. The modifying agents could functionalize the HTC-MR with amine groups. Moreover, the C-N stretching signal at 1320 to 1380 $cm^{-1}$ became more intense after the amino-functionalization. The carboxylic acid groups on the biomass materials would form an amide bonding with the amine groups of the modifying agents.

After Cr adsorption, the N–H stretching and C-N stretching signals exhibited a shift in wavenumber indicating the interaction between the adsorbed Cr(VI) ions and the amine groups. Moreover, the asymmetric C=O stretching peak was slightly shifted after Cr adsorption, suggesting the formation of Cr(III)-carboxylate complex. The $\Delta v(COO^-)_{complex}$ of the Cr-HTC-MR, Cr-0.5DEA-HTC-MR and Cr-0.5PEI-HTC-MR were 235.03, 237.03 and 234.7 $cm^{-1}$,

respectively, which were much larger than the $\Delta v(COO^-)_{Na}$ of 187.92 $cm^{-1}$. The reduced Cr(III) ions would form a monodentate complex with the carboxylate groups on the surface of adsorbents.

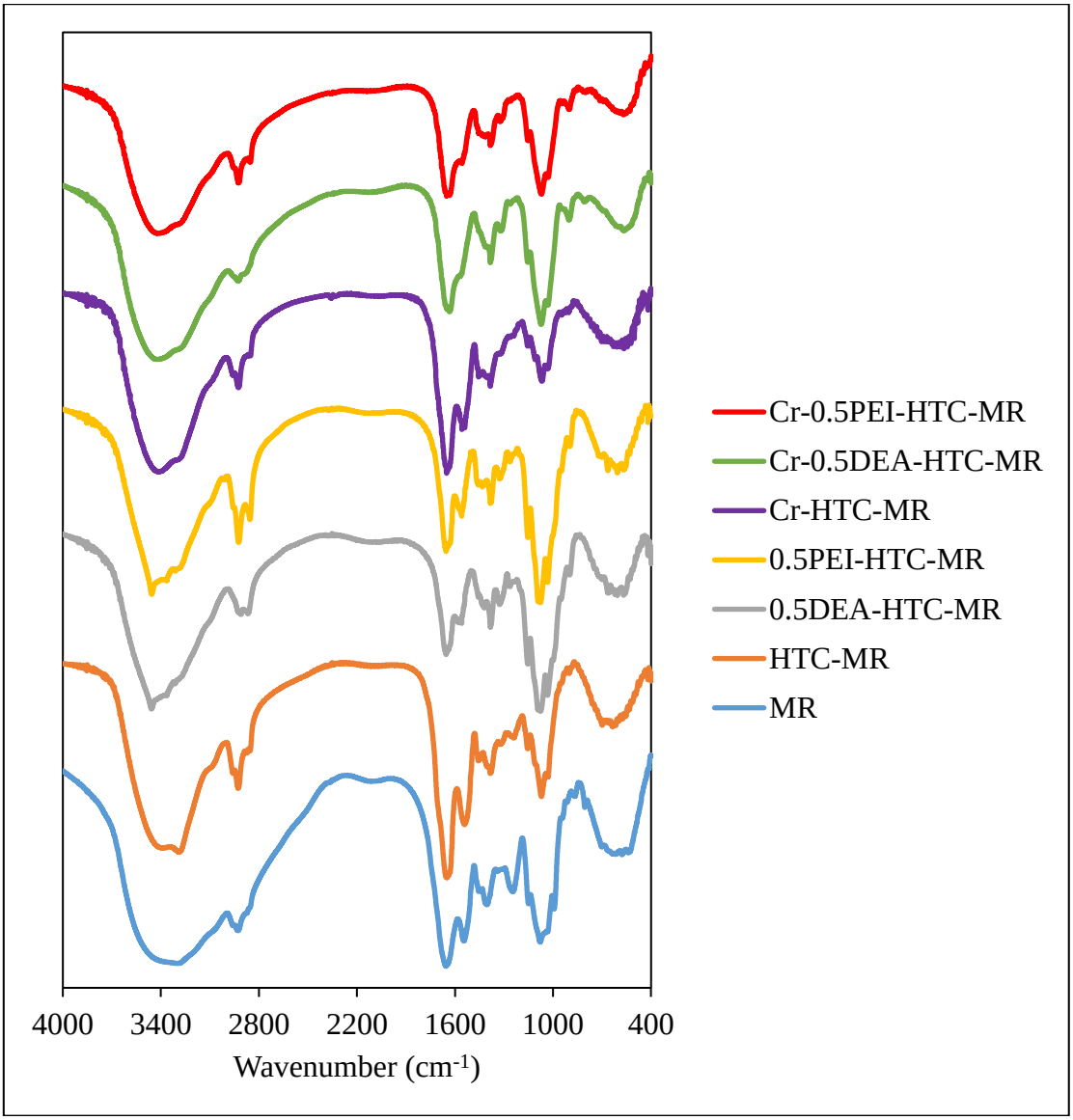


Figure 5-27 FTIR spectra of MR and HTC materials.

Table 5-8 Assignment table of the FTIR signals of MR and HTC materials.

| MR | HTC-MR | 0.5DEA-HTC-MR | 0.5PEI-HTC-MR | Cr-HTC-MR | Cr-0.5DEA-HTC-MR | Cr-0.5PEI-HTC-MR | Assignment |
|---|---|---|---|---|---|---|---|
| / | 3450.77 | 3457.19 | 3456.21 | 3411.62 | 3419.07 | 3418.83 | N–H stretching |
| 3300.42 | 3289.20 | 3313.22 | 3313.22 | 3286.89 | 3298.32 | 3294.99 | O-H stretching |
| 2927.74 | 2926.51 | 2926.28 | 2923.80 | 2925.11 | 2927.06 | 2924.73 | C-H stretching |
| 1655.02 | 1657.96 | 1654.32 | 1654.57 | 1652.02 | 1652.00 | 1651.87 | C=O asymmetric stretching of carboxyl / C=O stretching of amide (amide I) / aromatic C=C stretching |
| 1544.86 | 1541.46 | 1559.69 | 1559.70 | 1558.00 | 1558.23 | 1556.95 | C=C stretching of alkene / N-H bending of amide (amide II) |
| 1404.19 | 1402.81 | 1419.02 | 1433.20 | 1416.99 | 1414.97 | 1417.17 | C=O symmetric stretching |
| / | 1383.48 | 1383.20 | 1382.74 | 1384.15 | 1383.68 | 1383.68 | C−N stretching of amine |
| / | 1321.78 | 1326.37 | 1325.42 | 1322.95 | 1319.19 | 1323.88 | |
| 1245.93 | 1240.74 | 1265.61 | 1264.41 | 1264.61 | 1263.03 | 1261.17 | C-O stretching of phenol / C-N stretching of amide (amide III) |
| / | 1154.92 | 1154.41 | 1153.71 | 1154.39 | 1154.45 | 1154.25 | C–H vibrations of pyranose |
| 1079.99 | 1071.08 | 1076.97 | 1077.07 | 1067.82 | 1079.09 | 1072.86 | C-O stretching |
| 1034.10 | 1030.05 | 1033.63 | 1033.65 | 1034.16 | 1031.49 | 1031.49 | |

### 5.5.2 Nuclear magnetic resonance spectroscopy (NMR)

Figure 5-28 shows the $^{13}C$ solid-state MAS NMR spectra of MR, HTC-MR, 0.5DEA-HTC-MR and 0.5PEI-HTC-MR. The $^{13}C$ NMR spectra of HTC-MR were similar to those of the raw MR, indicating the incomplete carbonization of the MR. The observed peaks between 53 and 100 ppm are assigned to the C1-C6 carbons of N-acetylglucosamine monomeric unit of chitin, while the band at 24 ppm was attributed to the methyl carbon of chitin (Fukamizo et al., 1990; Younes et al., 2012). The signals of chitin could be observed in every tested sample which indicated a high structural homogeneity of MR, HTC-MR, 0.5DEA-HTC-MR and 0.5PEI-HTC-MR. The intensity of chitin peaks reduced after hydrothermal treatment, suggesting that some of the chitin was degraded under hydrothermal condition.

Besides, the peaks at 111 and 140 ppm were related to the furan β- and α-carbons (Falco et al., 2012; Alatalo et al., 2016). Furanic compounds such as 5-(hydroxymethyl) furfural (5-HMF) could be generated by the intramolecular dehydration of glucosamine (Figure 5-29) (Shu, 1998). The presence of $sp^2$ aromatic carbons, including the graphitic structures and the long-range conjugated double bonds, was confirmed by the peak at 126 ppm, while the peak at 150 ppm was contributed by the oxygen-substituted protonated and non-protonated C=C bonds (Titirici et al., 2008). Moreover, the peaks of carbonyl groups, such as amide, ketone/aldehyde and carboxylic acid, were observed at 170, 200 and 230 ppm, respectively (Zhao et al., 2010). Co-carbonization of MR with DEA led to a reduction in the intensity of the $sp^2$ aromatic carbon

and the furanic carbon peaks, so the DEA would inhibit the aromatization of hydrochars as well as the 5-HMF formation. When the PEI was co-carbonized with MR, the furanic carbon peaks disappeared, so the PEI hindered the formation of furanic compounds.

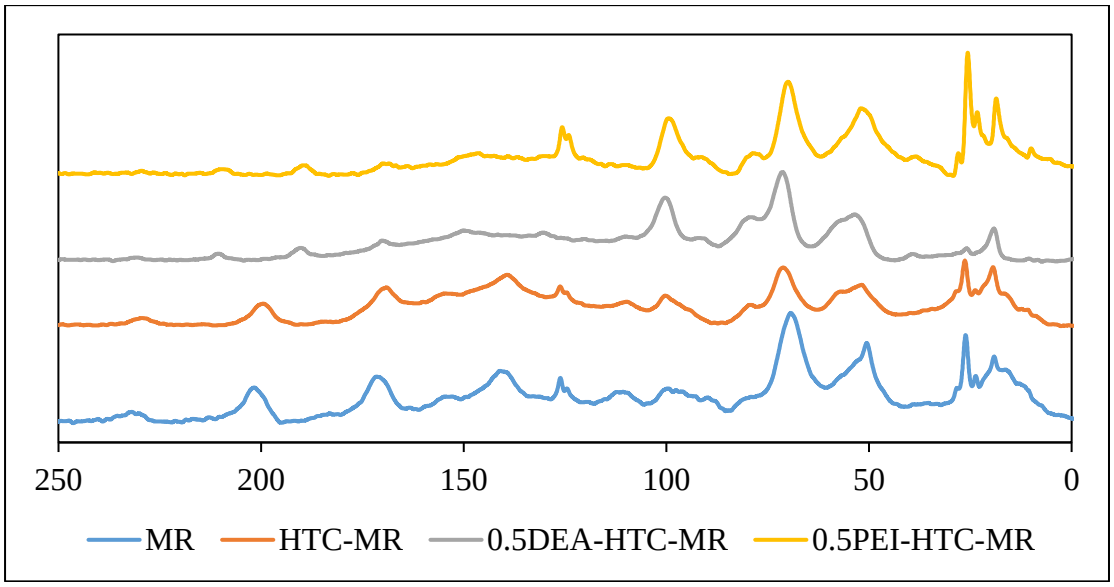


Figure 5-28 NMR spectra of the adsorbents.

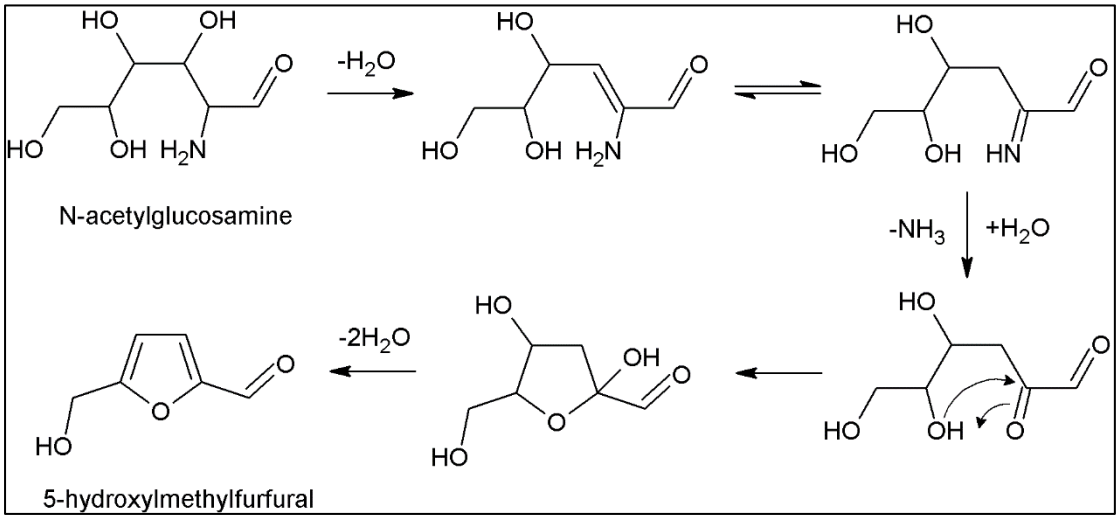


Figure 5-29 Formation mechanism of 5-hydroxylmethylfurfural from N-acetyl-glucosamine (Shu, 1998).

### 5.5.3 X-ray photoelectron spectroscopy (XPS)

The surface compositions of the pristine and Cr-laden adsorbents (MR, HTC-MR, 0.5DEA-HTC-MR and 0.5PEI-HTC-MR) were characterized by XPS techniques. The XPS results showed that the HTC materials consisted of C, O, N, S and P (Table 5-9). More than 18% of oxygen was incorporated in the HTC materials, suggesting that the HTC materials contained large amounts of oxygen functional groups (Wu et al., 2015). The nitrogen content of HTC-MR was significantly higher than that of the raw MR. The HTC-MR exhibited higher $Q_{Cr(VI)}$ than the MR, so the nitrogen functional groups would be responsible for Cr(VI) adsorption. The nitrogen content of HTC-MR could not be further increased by co-carbonization of amine-containing modifying agents (DEA and PEI). However, the $Q_{Cr(VI)}$ value was improved by co-carbonization of MR with DEA and PEI. Not only the nitrogen groups but also the oxygen functional groups could be responsible adsorption site for Cr(VI) (Wang et al., 2017). Also, the $Q_{Cr(VI)}$ value depended on the number of effective adsorption sites rather than the total amount of nitrogen functional groups.

The Cr 2p signals were observed in the HTC materials after treatment of Cr(VI). As shown in Table 5-9, 2.16, 6.19, 10.90 and 12.23% of Cr was introduced to MR, HTC-MR, 0.5DEA-HTC-MR and 0.5PEI-HTC-MR, respectively, after Cr(VI) adsorption, indicating the Cr was adsorbed on the surface of HTC materials. The trend of Cr atomic concentration in Cr-laden HTC materials was in agreement with the trend of total Cr adsorption capacity of 0.5PEI-HTC-

MR > 0.5DEA-HTC-MR > HTC-MR > MR. Meanwhile, the oxygen content of the Cr-laden HTC materials was higher than that of the pristine adsorbents, indicating the successful adsorption of Cr(VI) ions ($HCrO_4^-$) on the surface of HTC materials. Direct Cr(VI) adsorption would be one of the possible Cr(VI) removal mechanisms of HTC materials. The elemental compositions obtained from XPS analysis showed good agreement to those determined by elemental analysis (Section 5.1.3). These results demonstrated that the oxygen and nitrogen groups were evenly present on the surface and in the core of the hydrochars microsphere.

Table 5-9 Surface composition of pristine and Cr-laden adsorbents.

| Adsorbent | Mass concentration (wt%) | | | | | |
|---|---|---|---|---|---|---|
| | Cr2p | O1s | N1s | C1s | S2p | P2p |
| MR | 0 | 19.11 | 4.67 | 75.45 | 0 | 0.73 |
| HTC-MR | 0 | 19.37 | 8.60 | 71.48 | 0.49 | 0.05 |
| 0.5DEA-HTC-MR | 0 | 29.96 | 7.01 | 62.41 | 0.16 | 0.46 |
| 0.5PEI-HTC-MR | 0 | 18.87 | 7.11 | 73.53 | 0.04 | 0.44 |
| Cr-MR | 2.16 | 25.97 | 5.90 | 64.58 | 0 | 1.39 |
| Cr-HTC-MR | 6.19 | 24.07 | 8.04 | 61.16 | 0.51 | 0.03 |
| Cr-0.5DEA-HTC-MR | 10.90 | 34.92 | 6.23 | 47.72 | 0.18 | 0.05 |
| Cr-0.5PEI-HTC-MR | 12.23 | 29.50 | 4.89 | 53.08 | 0.10 | 0.19 |

XPS measurement was a powerful characterization method to investigate the surface functional groups on adsorbents. The high-resolution XPS spectra of C1s, N1s, O1s and Cr2p are displayed in Figure 5-30 to Figure 5-36. Those signals were deconvoluted into several component peaks, representing the elements in different chemical environments (Table 5-10). The C1s spectrum of MR could be resolved into four peaks: 285.0 (C-C/C-H/C=C), 286.5 (C-O-H/C-O-C/C-N), 287.9 (C=O/N-C=O/C=N) and 288.9 eV (O-C=O) (Wohlgemuth et al., 2012; Alatalo et al., 2016; Lei et al., 2016). As compared with the C1s spectrum of HTC-MR, the peaks at 285.0, 286.5 and 287.9 eV were retained in the hydrothermal carbonized MR. It is worthy to note that there was a new peak at 285.9 eV in HTC-MR, while the peak at 288.9 eV (O=C-O) disappeared after hydrothermal treatment (Hua et al., 2017). Lei et al. (2016) also reported the loss of the O-C=O peak after hydrothermal carbonization of corn stalk, as the oxygen functional groups took part in the linkage of hydrochars. Besides, the new peak at 285.9 eV was assigned to the C=C-O/C=C-N. The $sp^2$ hybridized carbon was formed by the aromatization. The intensity of the peak at 287.9 eV (C=O/N-C=O/C=N) increased after hydrothermal treatment of raw MR. Considering the formation mechanism of hydrochars, the small nuclei were linked together via dehydration reaction of reactive oxygen functional groups (e.g., hydroxyl group) in the growing step. As a result, large amounts of stable oxygen groups, such as ether, quinone and pyrone, were formed (Sevilla and Fuertes, 2009). Also, amide was formed by the condensation reaction between the amino group ($-NH_2$) and the carboxylic acid

group (−COOH). Besides, the carboxylic acid and ester groups were removed by decarboxylation and dehydration reaction. Similar to HTC-MR, four deconvoluted peaks were also present in the C1s spectrum of 0.5DEA-HTC-MR and 0.5PEI-HTC-MR. The relative intensity of C-O/C-N peak increased, suggesting that the hydroxyl, ether and amine groups were successfully functionalized on HTC-MR by the co-carbonization with DEA and PEI.

As shown in Figure 5-32a, the N1s deconvoluted peak of HTC-MR at 400.078 eV was actually the nitrogen species overlapping in a very narrow binding energy range (e.g., pyridine at ~398.5 eV, pyrrole at ~ 400.5 eV, pyridone at ~400.5 eV, pyrrolidone at ~399.6 eV, amide at ~399.9 eV, amine at ~399.3 eV) (Wohlgemuth et al., 2012; Wang et al., 2015b; Huang et al., 2017a; Huang et al., 2017b). These nitrogen-containing functional groups were considered to be responsible for the Cr(VI) adsorption at the acidic environment. Meanwhile, a new peak at 401.166 eV was generated after the hydrothermal treatment of MR, which was the graphitic-type quaternary-N structure (Gao et al., 2014; Wang et al., 2015b). This result was consistent with that obtained from the C1s spectrum which revealed the $sp^2$ hybridized carbon in the HTC-MR.

The O1s XPS spectra are compared in Figure 5-34 and Figure 5-35. A strong O1s signal in the O1s spectrum of HTC-MR showed that the hydrochars obtained was rich in oxygen-containing groups. The broad peak envelop indicated that oxygen atoms were under different chemical environments. The O1s component peaks at 531.7 and 533.0 eV represented the O=C

and O-C/C-O-C, respectively (Sevilla and Fuertes, 2009; Wang et al., 2012a; Zhao et al., 2016). The intensity of the O=C peak increased after the hydrothermal treatment because of the overlapping signal of C=C-O. By adding modifying agents, the relative intensity of O-C peak of 0.5DEA-HTC-MR and 0.5PEI-HTC-MR was higher than that of HTC-MR. The 0.5DEA-HTC-MR and 0.5PEI-HTC-MR appeared yellow instead of the brown-like HTC-MR. The modifying agents inhibited the aromatization of biochar, so the signal of C=C-O reduced.

Cr2p signals appeared in the HTC materials after treating Cr(VI) for 1 day, indicating the successful adsorption of Cr on the HTC surface. The anionic Cr(VI) ions were adsorbed electrostatically on the protonated hydrochars surface in the acidic environment. In the Cr2p spectra of Cr-laden HTC materials (Figure 5-36), two individual peaks were observed at 577.4 and 586.8 eV, which corresponded to the 2p3/2 and 2p1/2 signals, respectively. Moreover, each signal could be resolved into two component peaks, indicating that two oxidation states of Cr presented on the Cr-laden HTC materials. The peaks of 577.257 and 586.632 eV were contributed by Cr(III), while the peaks at 579.301 and 588.839 eV were related to Cr(VI) (Qiu et al., 2015). Both Cr(VI) and Cr(III) were found on the surface of HTC materials, suggesting that the adsorbed Cr(VI) ions were partially reduced to Cr(III) by the oxidation of hydroxyl groups (Chen et al., 2011; Wang et al., 2017). Moreover, the Cr signals were observed in the Cr-laden samples with 1-minute contact time, indicating the rapid Cr(VI) adsorption and reduction on the surface of 0.5DEA-HTC-MR and 0.5PEI-HTC-MR.

After adsorption of Cr(VI) on HTC materials, the peaks of C=C-O/C=C-N, C-O/C-N, and C=O/N-C=O/C=N showed positive shifting in binding energy, suggesting oxygen groups and nitrogen groups would participate in the Cr adsorption. The peak of C-C/C-H/C=C had no shifting because the $sp^3$ hybridized carbon had no interaction with Cr. The role of the aromatic amine groups on the Cr adsorption was further confirmed by the positive shifting of N1s signal of C=C-N. The positive shifting of binding energy indicated the protonation of aromatic amines, which would form an electrostatic interaction with the anionic Cr(VI) ions. Furthermore, the binding energy of O=C and O-C in the O1s spectrum of HTC materials increased after adsorption of Cr(VI), so the Cr would also be adsorbed on the hydroxyl and carbonyl groups in hydrochars. The intensity of O=C peak in the O1s spectrum of Cr-laden materials increased after Cr(VI) adsorption because of the O1s signal of chromate ($HCrO_4^-$) on the HTC surface. On the other hand, the increase in the intensity of the O=C peak was also contributed by the oxidation of hydroxyl groups in the Cr(VI) adsorption-coupled reduction mechanism (Qiu et al., 2015).

Fe2p signal was observed in the $Fe_3O_4$-0.5PEI-HTC-MR and could be resolved into two peaks (Figure 5-37a). The resolved peaks at 710.9 and 715.6 eV corresponded to Fe2p3/2 peaks of Fe(II) and Fe(III), respectively. The presence of Fe(II) and Fe(III) suggested that the $Fe_3O_4$ nanoparticles were incorporated into 0.5PEI-HTC-MR. Moreover, extra peaks were found at 530.0 and 535.3 eV in the O1s spectrum of Cr-laden $Fe_3O_4$-0.5PEI-HTC-MR, which were the

oxide (O-Fe) and hydroxide (O-H) peaks of $Fe_3O_4$. Hydroxide signal was absent in $Fe_3O_4$-0.5PEI-HTC-MR (Figure 5-37b) due to the deprotonation in the alkaline hydrothermal condition. The hydroxide functional groups on $Fe_3O_4$ were then protonated to form $-OH_2^+$ groups because of the acidic adsorption environment.

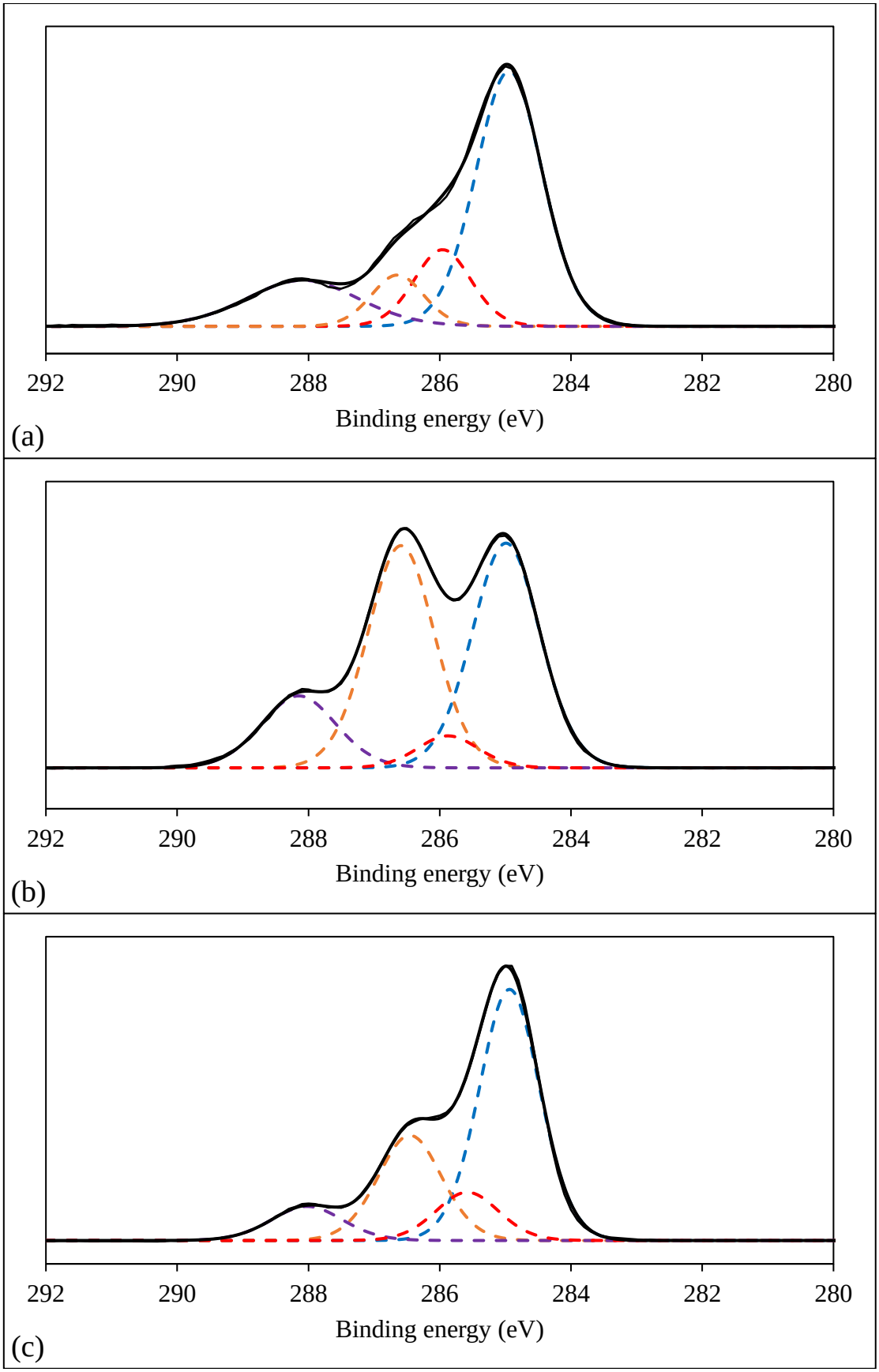


Figure 5-30 C1s spectra of (a) HTC-MR, (b) 0.5DEA-HTC-MR and (c) 0.5PEI-HTC-MR.

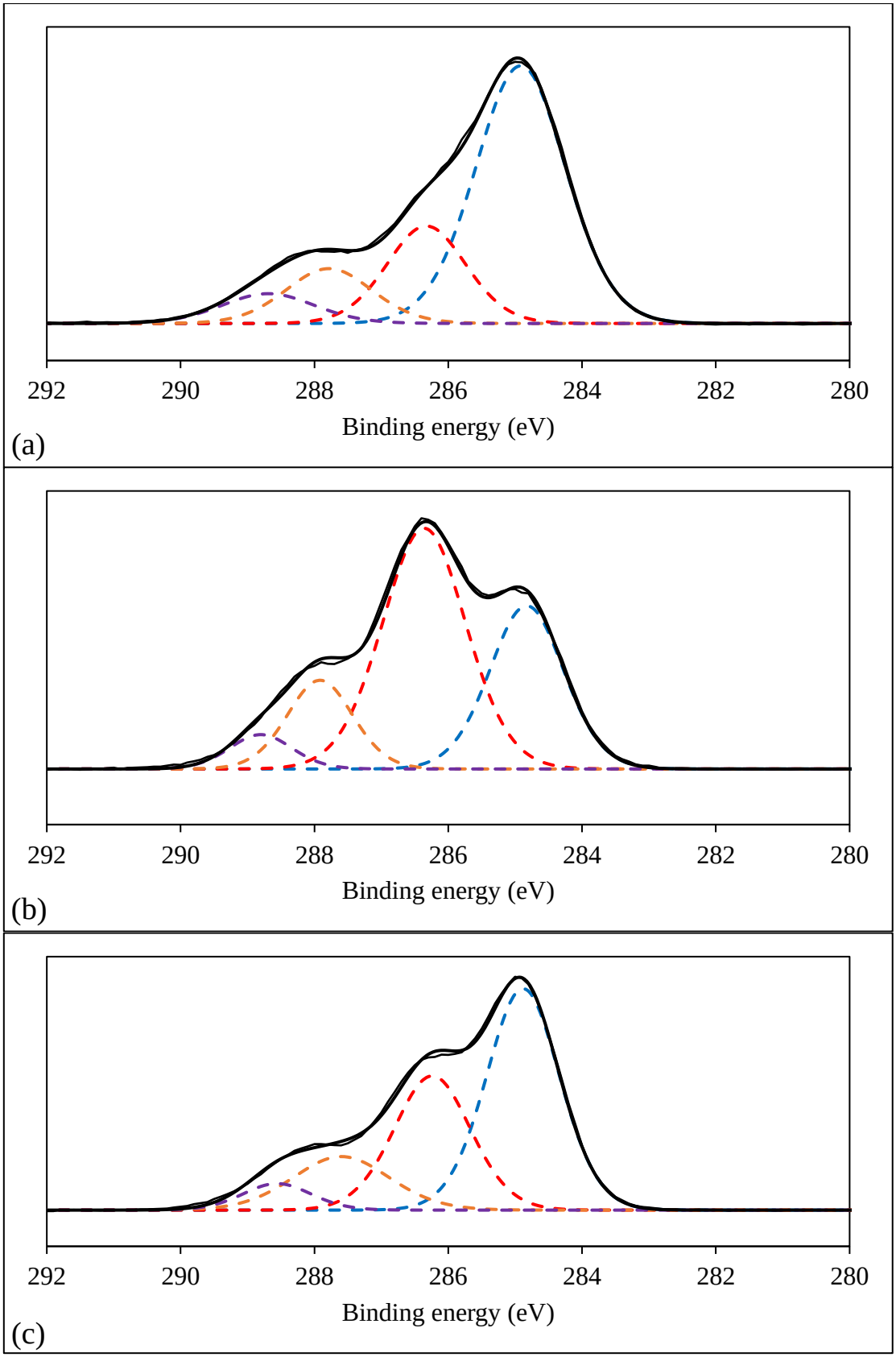


Figure 5-31 C1s spectra of (a) Cr-HTC-MR, (b) Cr-0.5DEA-HTC-MR and (c) Cr-0.5PEI-HTC-MR.

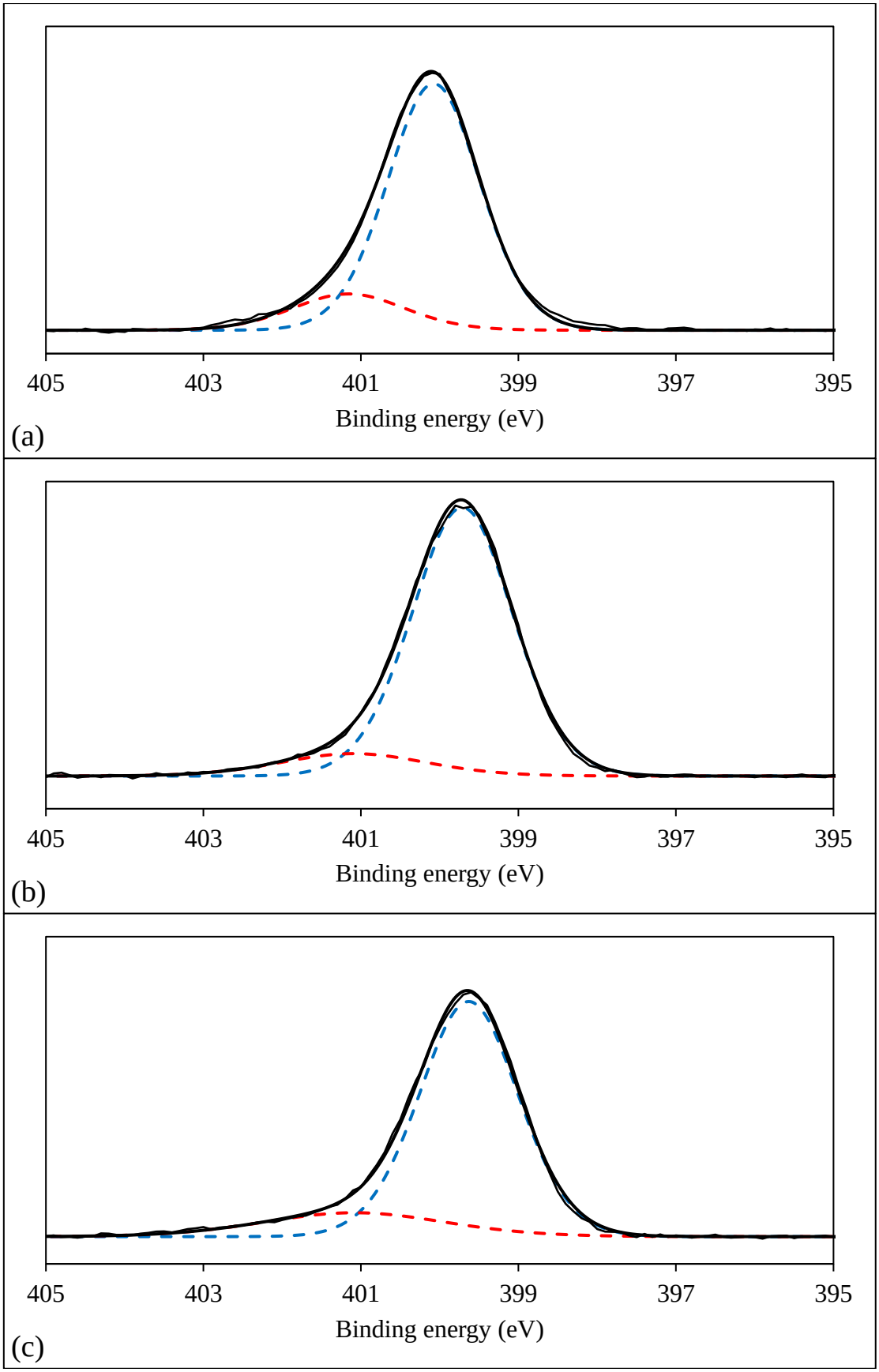


Figure 5-32 N1s spectra of (a) HTC-MR, (b) 0.5DEA-HTC-MR and (c) 0.5PEI-HTC-MR.

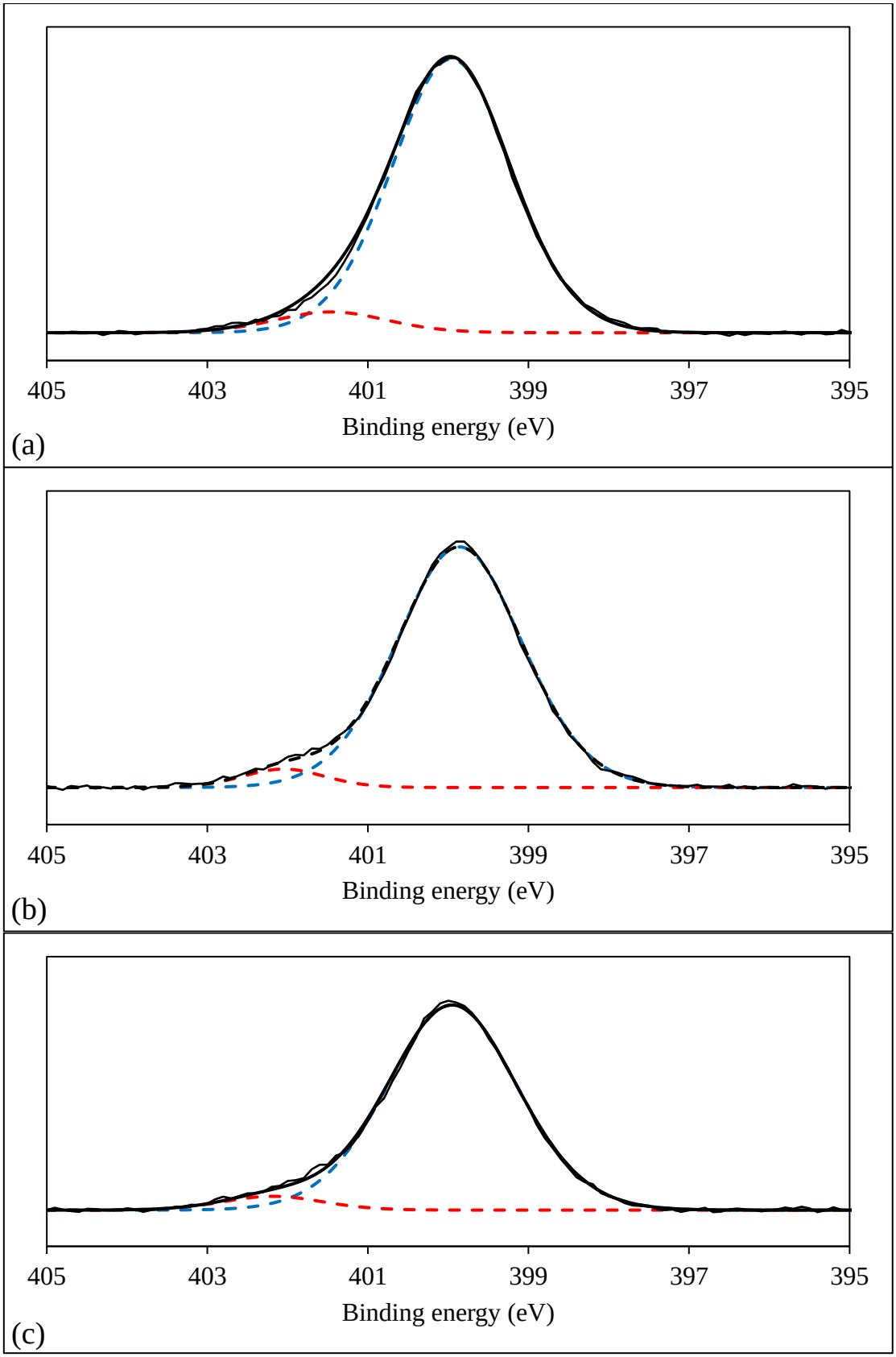


Figure 5-33 N1s spectra of (a) Cr-HTC-MR, (b) Cr-0.5DEA-HTC-MR and (c) Cr-0.5PEI-HTC-MR.

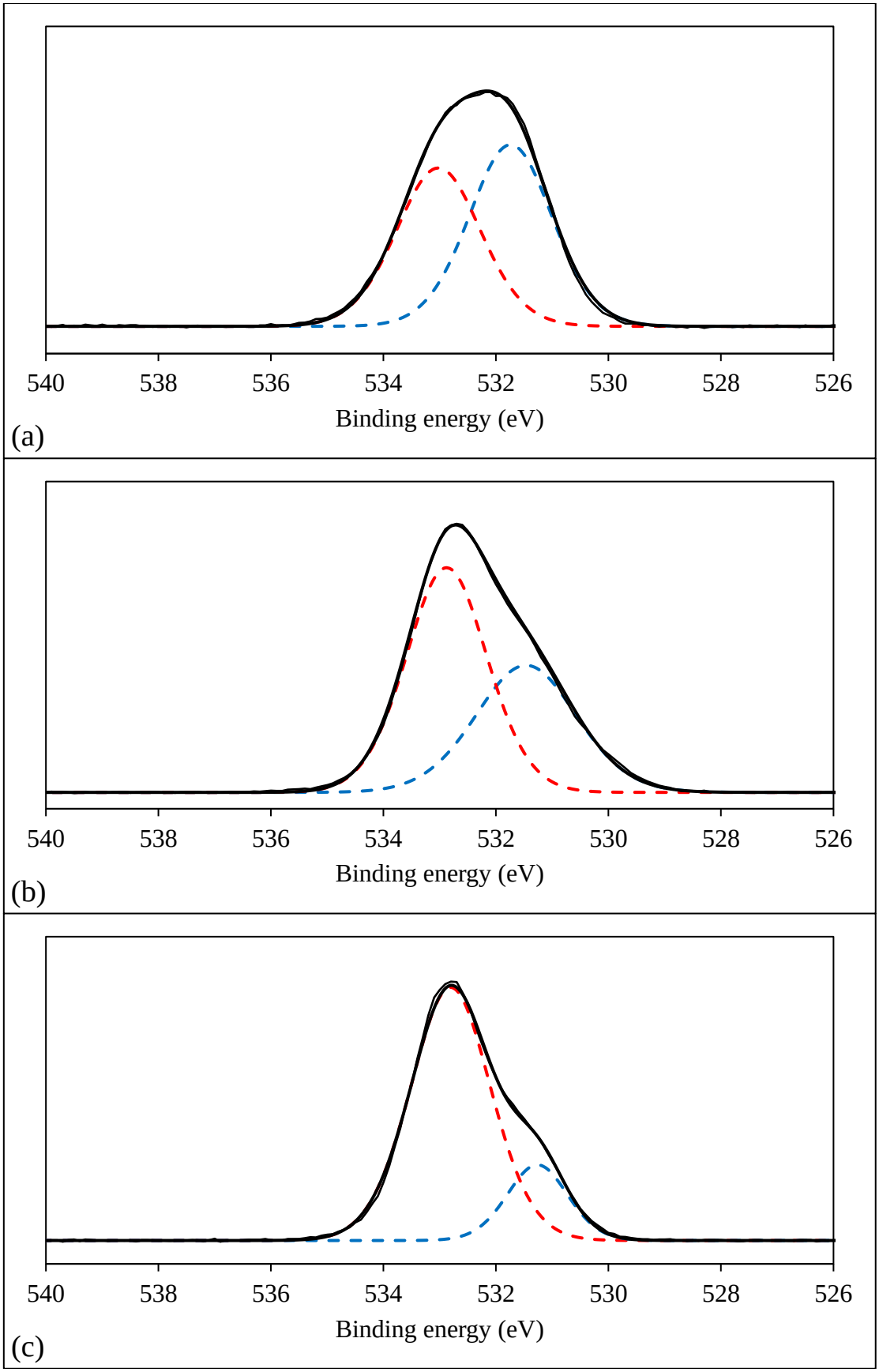


Figure 5-34 O1s spectra of (a) HTC-MR, (b) 0.5DEA-HTC-MR and (c) 0.5PEI-HTC-MR.

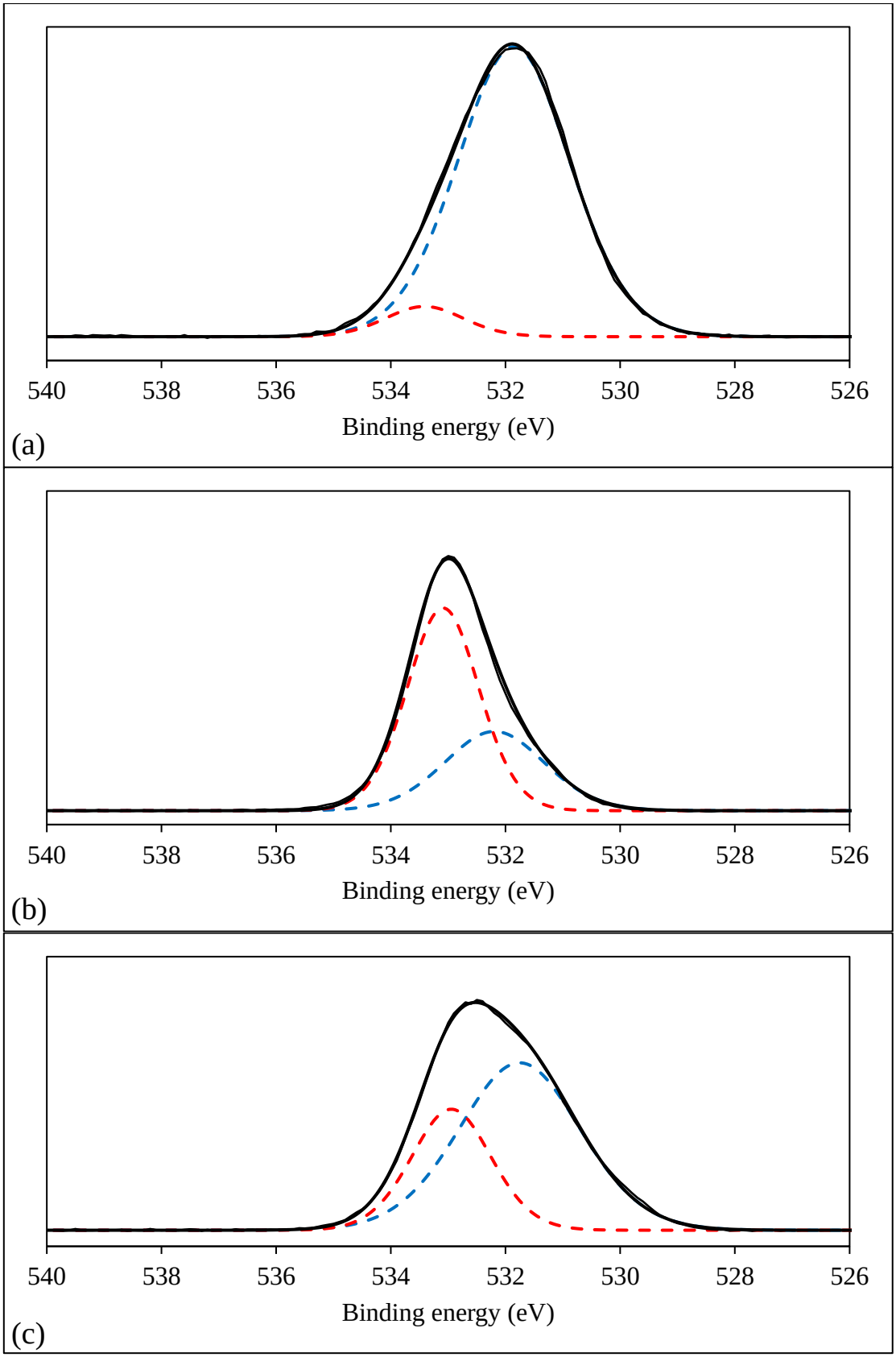


Figure 5-35 O1s spectra of (a) Cr-HTC-MR, (b) Cr-0.5DEA-HTC-MR and (c) Cr-0.5PEI-HTC-MR.

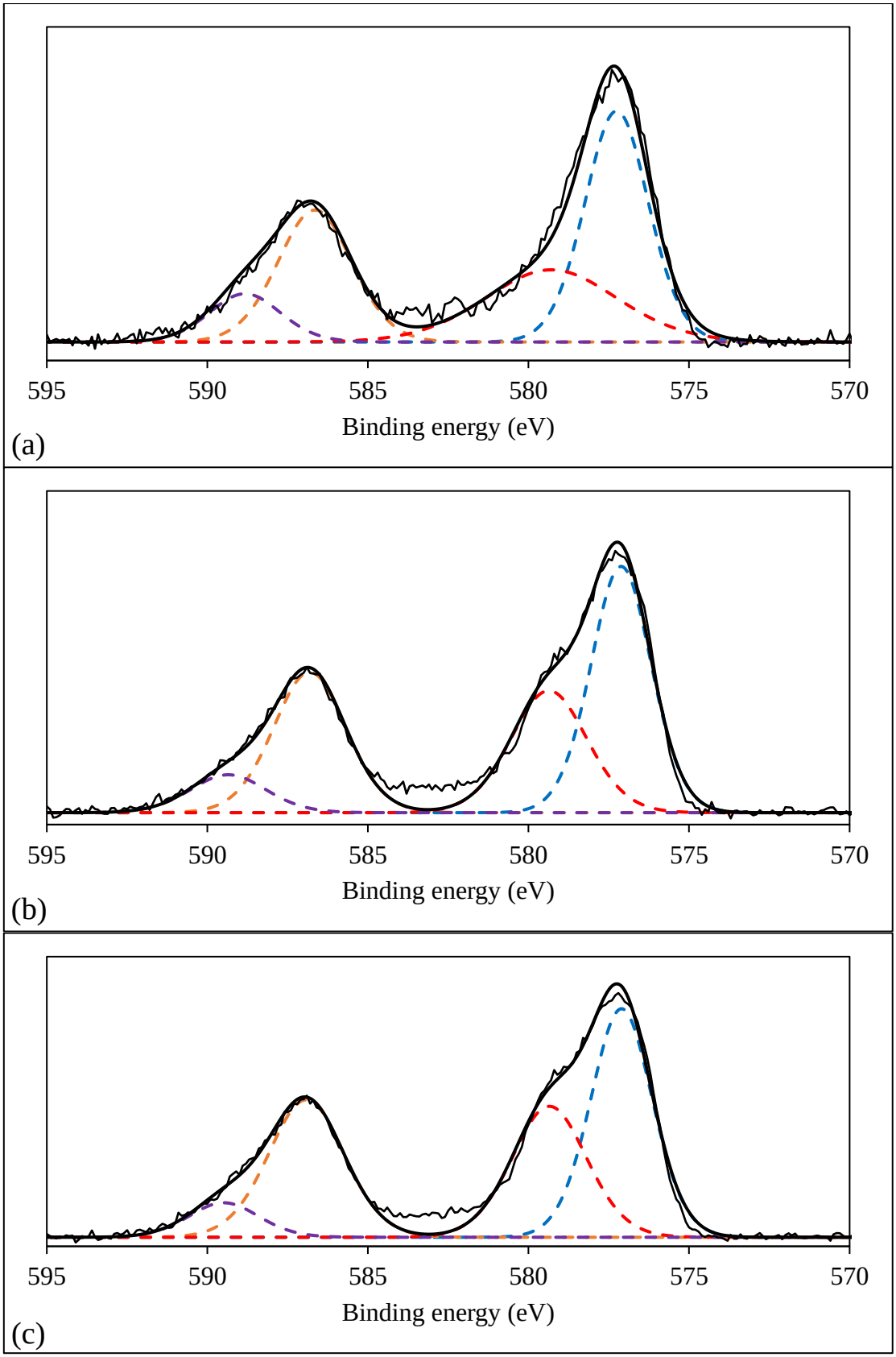


Figure 5-36 Cr2p spectra of (a) Cr-HTC-MR, (b) Cr-0.5DEA-HTC-MR and (c) Cr-0.5PEI-HTC-MR.

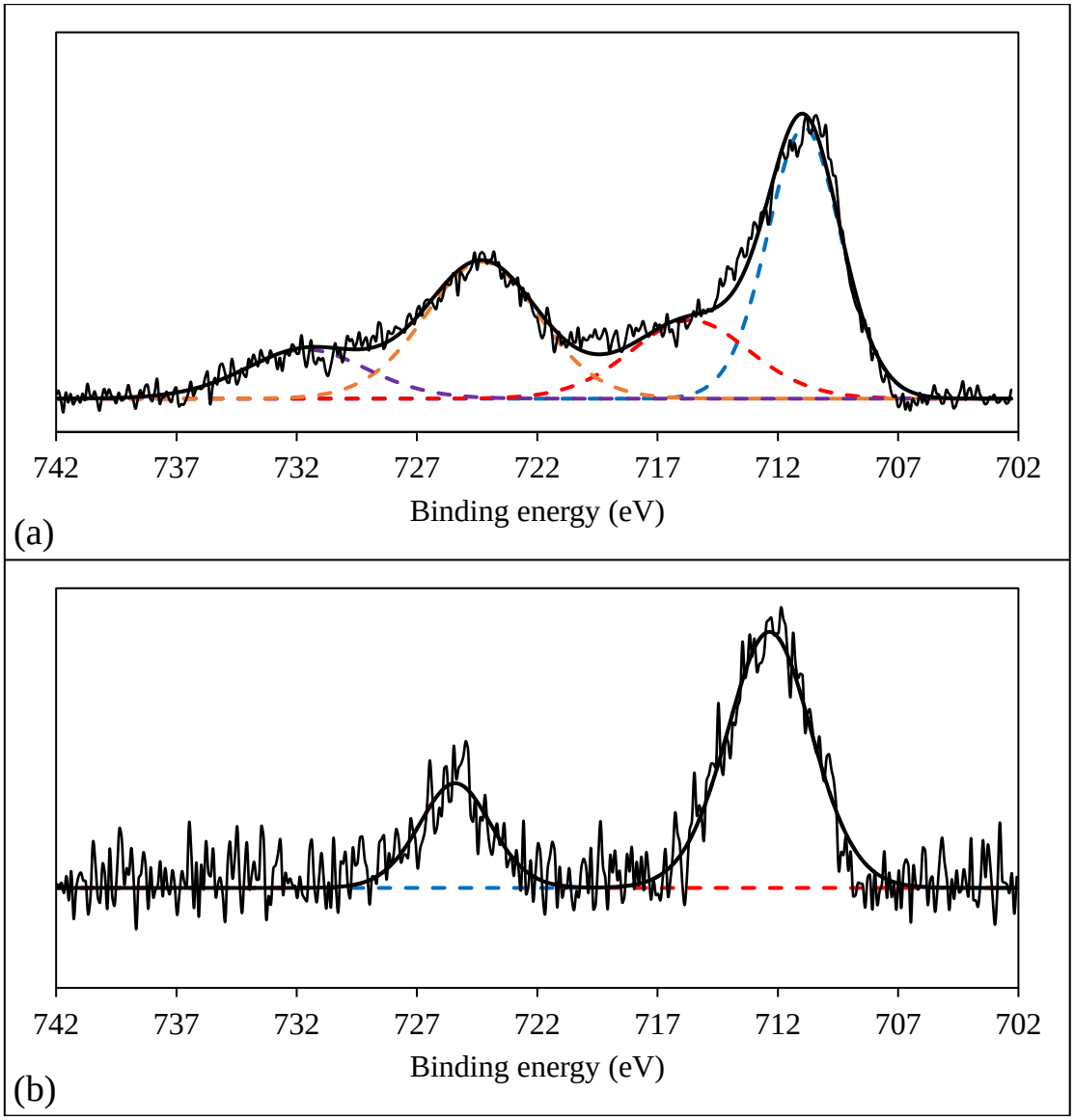


Figure 5-37 Fe2p spectra of (a) pristine and (b) Cr-laden $Fe_3O_4$-0.5PEI-HTC-MR.

Table 5-10 Binding energies, atomic concentration and chemical shift of pristine and Cr-loaded MR, HTC-MR, 0.5DEA-HTC-MR, 0.5PEI-HTC-MR and Fe3O4-0.5PEI-HTC-MR.

| | | MR | | HTC-MR | | 0.5DEA-HTC-MR | | | 0.5PEI-HTC-MR | | | $Fe_3O_4$-0.5PEI-HTC-MR | |
|---|---|---|---|---|---|---|---|---|---|---|---|---|---|
| Assignment | | Pristine | 1 d | Pristine | 1 d | Pristine | 1 min | 1 d | Pristine | 1 min | 1 d | Pristine | 1 d |
| C1s | C-(C, H) | 285.048 | 284.943 | 284.931 | 284.919 | 284.998 | 284.899 | 284.819 | 284.941 | 285.029 | 284.876 | 284.889 | 284.991 |
| | | 59.26% | 50.84% | 58.11% | 60.33% | 40.63% | 17.12% | 30.05% | 55.47% | 61.10% | 48.39% | 40.13% | 27.00% |
| | | / | -0.105 | / | -0.012 | / | -0.099 | -0.179 | / | +0.088 | -0.065 | / | +0.002 |
| | C=C-(O,N) | / | / | 285.943 | 286.312 | 285.879 | 286.641 | 286.339 | 285.599 | 286.283 | 286.259 | 285.675 | 286.280 |
| | | / | / | 14.95% | 20.08% | 5.23% | 52.46% | 50.05% | 11.13% | 19.03% | 30.68% | 15.99% | 35.05% |
| | | / | / | / | +0.369 | / | +0.762 | +0.460 | / | +0.684 | +0.660 | / | +0.605 |
| | C-(O, N) | 286.524 | 286.387 | 286.619 | 287.775 | 286.593 | 288.334 | 287.904 | 286.438 | 287.273 | 287.620 | 286.453 | 287.985 |
| | | 27.82% | 33.92% | 9.29% | 12.36% | 39.71% | 18.71% | 14.52% | 24.51% | 12.52% | 15.48% | 31.76% | 27.46% |
| | | / | -0.137 | / | +1.156 | / | +1.741 | +1.311 | / | +0.835 | +1.182 | / | +1.532 |
| | C=O | 287.924 | 287.997 | 288.085 | 288.685 | 288.158 | 289.77 | 288.811 | 288.024 | 288.386 | 288.567 | 288.046 | 289.676 |
| | | 7.22% | 10.36% | 17.64% | 7.23% | 14.43% | 11.70% | 5.39% | 8.88% | 7.35% | 5.45% | 12.12% | 10.49% |
| | | / | +0.073 | / | +0.600 | / | +1.612 | +0.653 | / | +0.362 | +0.543 | / | +1.630 |
| | O=C-O | 288.861 | 289.076 | / | / | / | / | / | / | / | / | / | / |
| | | 5.70% | 4.88% | / | / | / | / | / | / | / | / | / | / |
| | | / | +0.215 | / | / | / | / | / | / | / | / | / | / |

Table 5-9 (con't) Binding energies, atomic concentration and chemical shift of pristine and Cr-loaded MR, HTC-MR, 0.5DEA-HTC-MR, 0.5PEI-HTC-MR and Fe3O4-0.5PEI-HTC-MR.

| | | MR | | HTC-MR | | 0.5DEA-HTC-MR | | | 0.5PEI-HTC-MR | | | $Fe_3O_4$-0.5PEI-HTC-MR | |
|---|---|---|---|---|---|---|---|---|---|---|---|---|---|
| Assignment | | Pristine | 1 d | Pristine | 1 d | Pristine | 1 min | 1 d | Pristine | 1 min | 1 d | Pristine | 1 d |
| N1s | $NH_2$ | 400.114 | 400.032 | 400.078 | 399.986 | 399.724 | 399.929 | 399.844 | 399.628 | 399.870 | 399.928 | 399.508 | 399.892 |
| | | 73.95% | 83.47% | 84.81% | 93.30% | 89.24% | 50.87% | 95.21% | 84.26% | 84.38% | 95.09% | 88.65% | 70.66% |
| | | / | -0.082 | / | -0.092 | / | +0.205 | +0.120 | / | +0.242 | +0.300 | / | +0.384 |
| | Graphite-N | / | / | 401.166 | 401.478 | 401.083 | 401.765 | 402.049 | 401.08 | 401.237 | 402.191 | 400.917 | 402.143 |
| | | / | / | 15.19% | 6.70% | 10.76% | 49.13% | 4.79% | 15.74% | 15.62% | 4.91% | 11.35% | 29.34% |
| | | / | / | / | +0.312 | / | +0.682 | +0.966 | / | +0.157 | +1.111 | / | +1.326 |
| | $NH_3^+$ | 401.92 | 401.845 | / | / | / | / | / | / | / | / | / | / |
| | | 26.05% | 16.53% | / | / | / | / | / | / | / | / | / | / |
| | | / | +-0.075 | / | / | / | / | / | / | / | / | / | / |
| Cr2p | Cr2p 3/2 of Cr(III) | / | 578.100 | / | 577.257 | / | 577.610 | 577.109 | / | 576.986 | 577.109 | / | 577.466 |
| | | / | 100% | / | 60.56% | / | 56.35% | 61.41% | / | 52.47% | 58.94% | / | 55.73% |
| | Cr2p 3/2 of Cr(VI) | / | / | / | 579.301 | / | 580.248 | 579.357 | / | 579.013 | 579.344 | / | 579.576 |
| | | / | / | / | 39.44% | / | 43.65% | 38.59% | / | 47.53% | 41.06% | / | 44.27% |
| Fe2p | Fe2p 3/2 of Fe(II) | / | / | / | / | / | / | / | / | / | / | 710.925 | 710.292 |
| | | / | / | / | / | / | / | / | / | / | / | 68.00% | 100% |
| | Fe2p 3/2 of Fe(III) | / | / | / | / | / | / | / | / | / | / | 715.631 | / |
| | | / | / | / | / | / | / | / | / | / | / | 32.00% | / |

Table 5-9 (con't) Binding energies, atomic concentration and chemical shift of pristine and Cr-loaded MR, HTC-MR, 0.5DEA-HTC-MR, 0.5PEI-HTC-MR and Fe3O4-0.5PEI-HTC-MR.

| | | MR | | HTC-MR | | 0.5DEA-HTC-MR | | | 0.5PEI-HTC-MR | | | $Fe_3O_4$-0.5PEI-HTC-MR | |
|---|---|---|---|---|---|---|---|---|---|---|---|---|---|
| Assignment | | Pristine | 1 d | Pristine | 1 d | Pristine | 1 min | 1 d | Pristine | 1 min | 1 d | Pristine | 1 d |
| O1s | O-Fe | / | / | / | / | / | / | / | / | / | / | 529.893 | 530.260 |
| | | / | / | / | / | / | / | / | / | / | / | 8.56% | 7.50% |
| | | / | / | / | / | / | / | / | / | / | / | / | +0.367 |
| | O=C | 531.138 | 531.278 | 531.718 | 531.878 | 531.452 | 532.512 | 532.211 | 531.256 | 531.554 | 531.741 | 531.296 | 531.456 |
| | | 8.64% | 11.60% | 53.10% | 93.22% | 41.33% | 63.48% | 35.29% | 18.41% | 49.10% | 67.81% | 22.18% | 14.17% |
| | | / | -0.140 | / | +0.160 | / | +1.060 | +0.759 | / | +0.298 | +0.485 | / | +0.160 |
| | O-C | 532.802 | 532.654 | 533.029 | 533.415 | 532.871 | 534.695 | 533.086 | 532.814 | 532.799 | 532.943 | 532.837 | 532.787 |
| | | 91.36% | 88.40% | 46.90% | 6.78% | 58.67% | 36.52% | 64.71% | 82.59% | 50.90% | 32.19% | 69.26% | 59.69% |
| | | / | -0.148 | / | +0.386 | / | +1.824 | +0.215 | / | -0.015 | +0.129 | / | -0.050 |
| | O-H of $Fe_3O_4$ | / | / | / | / | / | / | / | / | / | / | / | 535.302 |
| | | / | / | / | / | / | / | / | / | / | / | / | 18.64% |
| P2p | P-O | 133.968 | / | 133.636 | / | 134.164 | / | / | 133.813 | / | / | 133.231 | / |

### 5.5.4 Isothermal titration calorimetry (ITC)

The thermodynamic characteristics of the Cr(VI) adsorption on the MR, HTC-MR, 0.5DEA-HTC-MR and 0.5PEI-HTC-MR were investigated by isothermal titration calorimetry (ITC). The ITC experiments were conducted using Malvern MicroCal PEAQ-ITC automated ultrasensitive isothermal titration calorimeter by titration of the 500 ppm Cr(VI) solution with the 0.1 g/L adsorbent suspension. Figure 5-38 to Figure 5-41 show the titration thermograms and the plots of heat release versus molar ratio for the Cr(VI) adsorption on different adsorbents. After each injection, a strong thermopositive peak was observed, indicating there was a strong interaction between the Cr(VI) ions and the adsorbent surface. The heat release resulted from two thermoprocesses: (1) the binding of Cr(VI) on the adsorbent surface; and (2) the dilution of Cr(VI) and adsorbent. The calorific effect of the dilution of Cr(VI) and adsorbent was corrected by a control experiment with the 500 ppm Cr(VI) solution and DDI water.

Table 5-11 summarizes the thermodynamic parameters of Cr(VI) adsorption on different adsorbents. The enthalpy changes (ΔH) of Cr(VI) adsorption on MR, HTC-MR, 0.5DEA-HTC-MR and 0.5PEI-HTC-MR were estimated at -8.415 ± 0.247, -1.575 ± 0.163, -3.210 ± 2.659 and -25.05 ± 6.01 kJ/mol, respectively. The negative values of ΔH indicated the exothermic nature of the Cr(VI) adsorption process. The ΔH values of the Cr(VI) adsorption on 0.5DEA-HTC-MR and 0.5PEI-HTC-MR were more negative than that of HTC-MR, indicating the stronger affinity of Cr(VI) to the amino-functionalized HTC-MR. Moreover, Gibb's free energy

changes (ΔG) of the Cr(VI) binding on MR, HTC-MR, 0.5DEA-HTC-MR and 0.5PEI-HTC-MR were -14.55 ± 0.21, -17.65 ± 5.16, -34.45 ± 10.54 and -16.75 ± 1.63 kJ/mol, respectively. The negative ΔG values revealed that Cr(VI) adsorption was a thermodynamically favorable reaction. The ΔS values of Cr(VI) binding process on MR, HTC-MR, 0.5DEA-HTC-MR and 0.5PEI-HTC-MR were calculated as +20.45 ± 1.54, +53.86 ± 16.85, +104.9 ± 44.4 and +27.85 ± 25.63 J/mol, respectively. The positive values of ΔS implied that the Cr(VI) adsorption increased the degree of disorder of the system. Anionic Cr(VI) ions would be adsorbed on the adsorbent surface through electrostatic interaction. Binding of Cr(VI) on the adsorbent surface would result in the unfolding of the polymeric structure of *M. rouxii* and HTC materials.

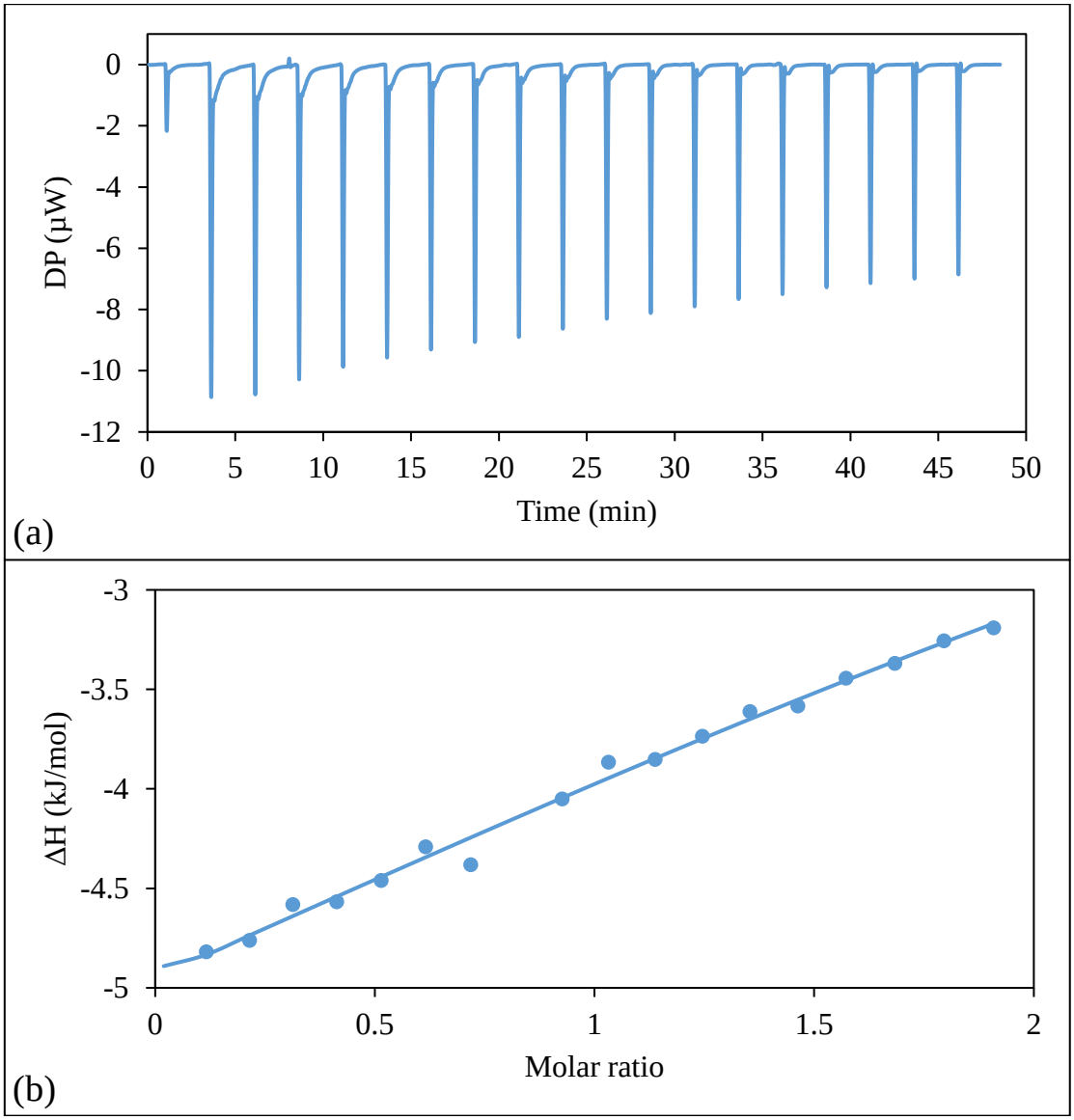


Figure 5-38 (a) Titration thermogram and (b) plot of heat released versus molar ratio for Cr(VI) adsorption on MR.

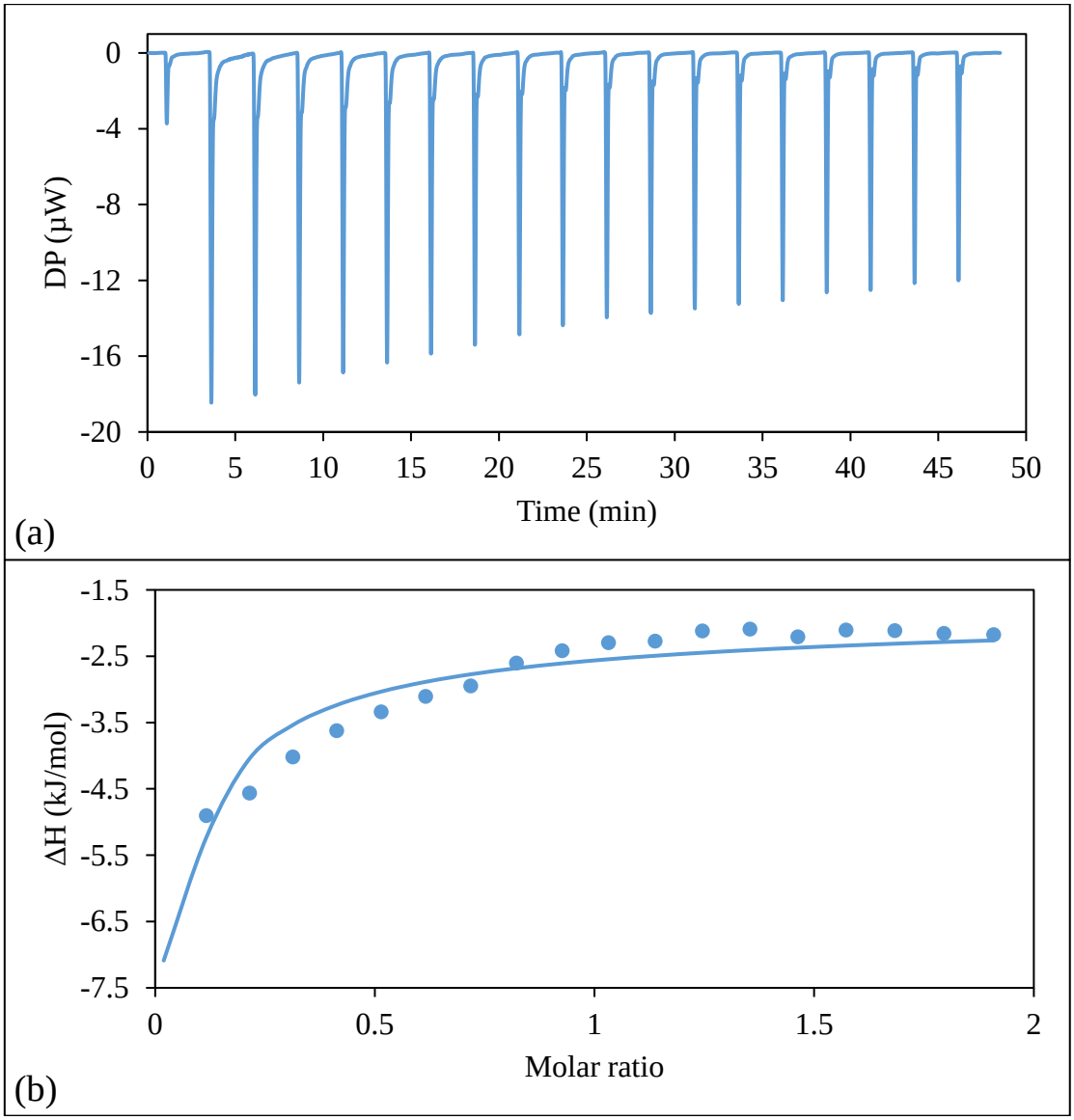


Figure 5-39 (a) Titration thermogram and (b) plot of heat released versus molar ratio for Cr(VI) adsorption on HTC-MR.

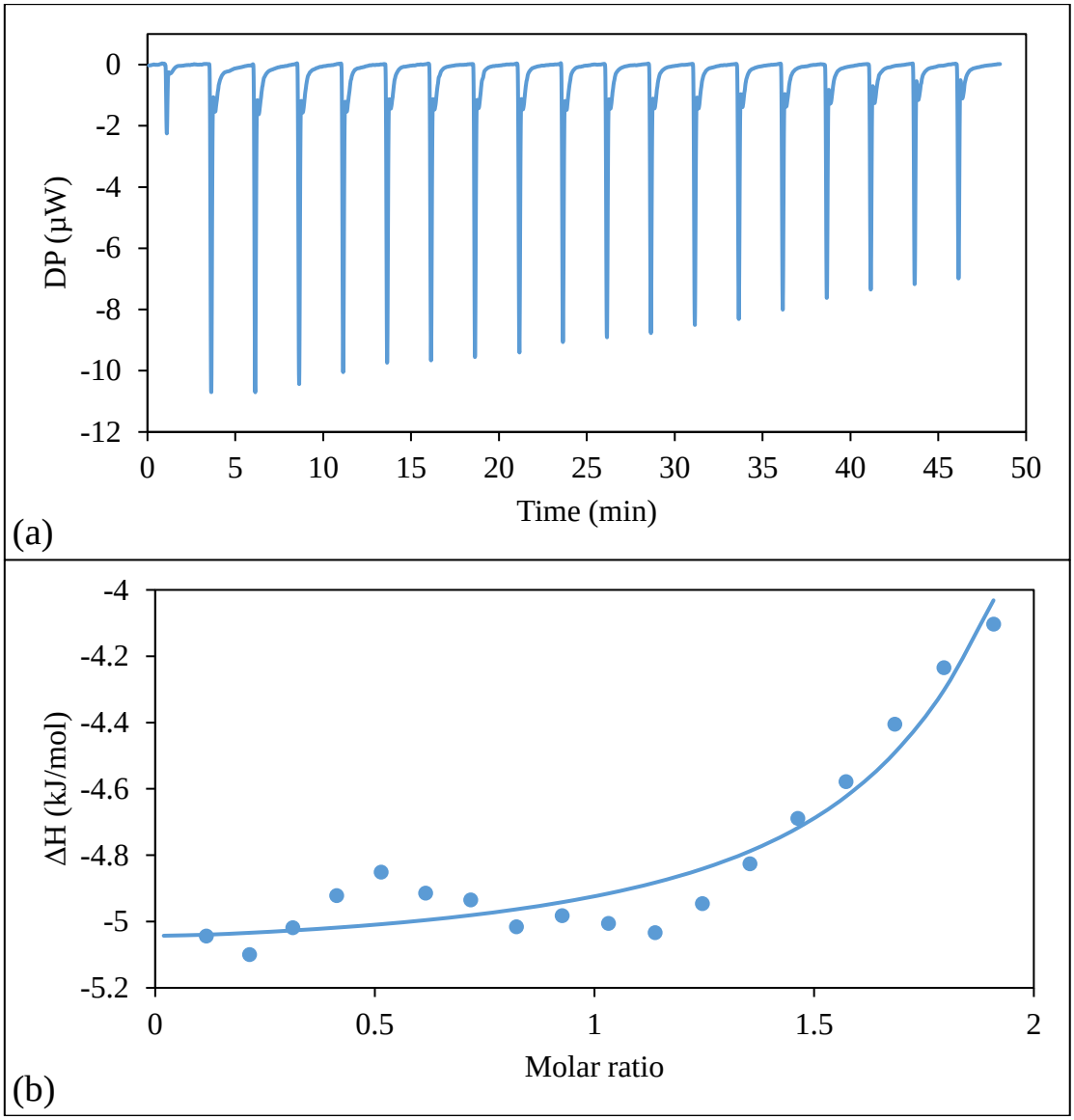


Figure 5-40 (a) Titration thermogram and (b) plot of heat released versus molar ratio for Cr(VI) adsorption on 0.5DEA-HTC-MR.

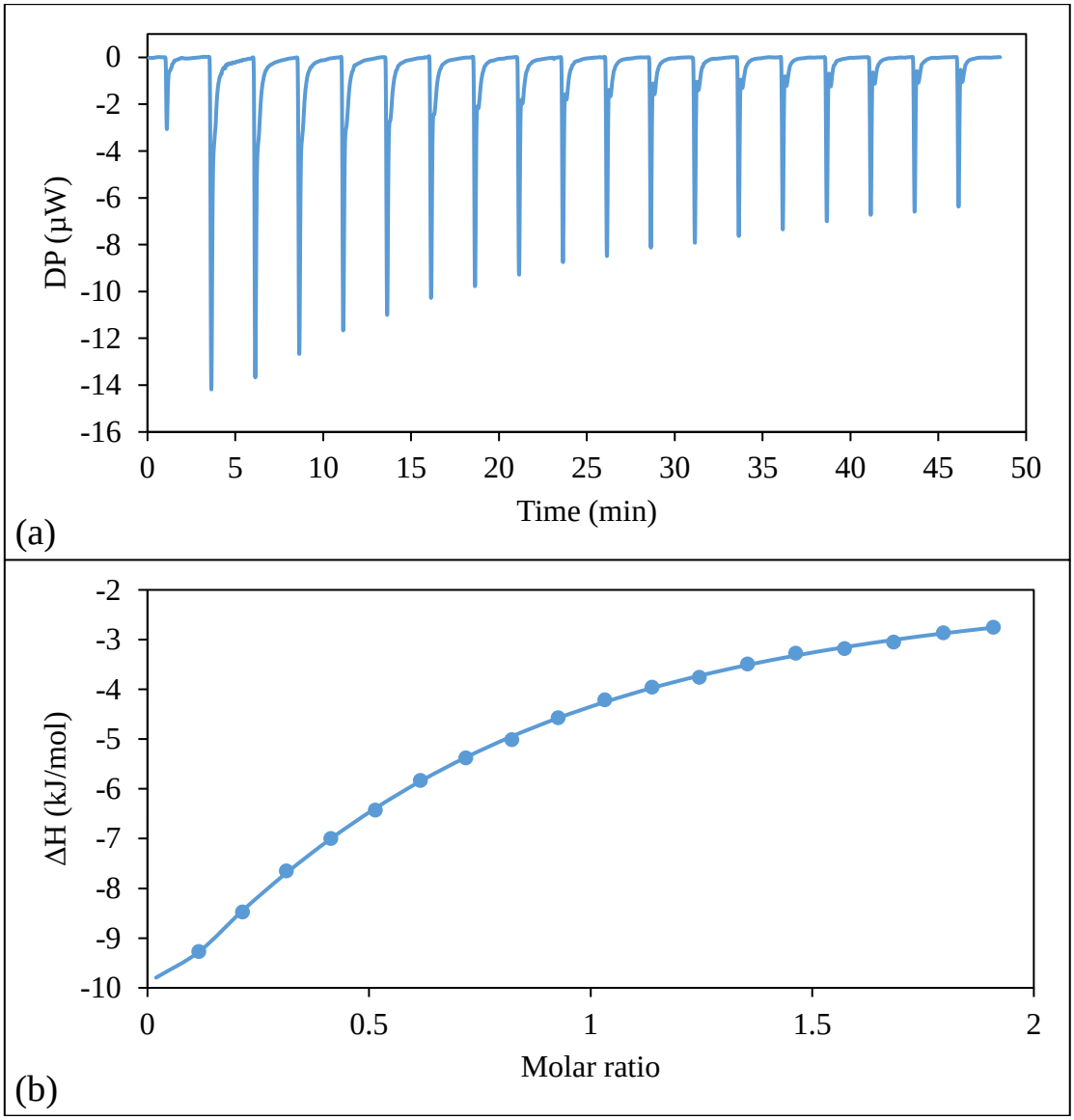


Figure 5-41 (a) Titration thermogram and (b) plot of heat released versus molar ratio for Cr(VI) adsorption on 0.5PEI-HTC-MR.

Table 5-11 Thermodynamic parameters of Cr(VI) adsorption on MR, HTC-MR, 0.5DEA-HTC-MR and 0.5PEI-HTC-MR.

| Adsorbents | ΔH (kJ/mol) | ΔG (kJ/mol) | ΔS (J/mol) |
|---|---|---|---|
| MR | -8.415 ± 0.247 | -14.55 ± 0.21 | +20.45 ± 1.54 |
| HTC-MR | -1.575 ± 0.163 | -17.65 ± 5.16 | +53.86 ± 16.85 |
| 0.5DEA-HTC-MR | -3.210 ± 2.659 | -34.45 ± 10.54 | +104.9 ± 44.4 |
| 0.5PEI-HTC-MR | -25.05 ± 6.01 | -16.75 ± 1.63 | +27.85 ± 25.63 |

## 5.6 Cr(VI) removal mechanisms

Based on the results of Cr(VI) removal studies, the obtained HTC materials (e.g., HTC-MR, 0.5DEA-HTC-MR and 0.5PEI-HTC-MR) exhibited selective removal capacities toward Cr(VI) at pH 2.0. The Cr(VI) removal kinetics revealed that the Cr(VI) was rapidly removed by the HTC materials in the first 1 h at pH 2.0. The results of FTIR, $^{13}C$ NMR and XPS analysis confirmed that the surface of HTC materials contained a large number of nitrogen functional groups (e.g., aliphatic and aromatic amine groups) and oxygen functional groups (e.g., hydroxyl and carbonyl groups). These surface groups would be protonated under the acidic environment. Besides, the results of the zeta-potential analysis demonstrated that the surface charges of the HTC materials were positive at pH 2.0. As we know, Cr(VI) exists as $HCrO_4^-$ and $Cr_2O_7^{2-}$ anions in the 500 ppm Cr(VI) solution at pH 2.0. Thus, the rapid Cr(VI) removal on the HTC materials was contributed by the strong electrostatic interaction between the anionic Cr(VI) ions and the positively-charged adsorbent surface. In addition, the amine-containing modifying agents, such as DEA and PEI, could further functionalize the HTC-MR with the amine groups, so the 0.5DEA-HTC-MR and 0.5PEI-HTC-MR exhibited higher Cr(VI) removal capacity than the HTC-MR.

The Cr2p XPS spectrum of the Cr-laden HTC materials identified the electronic state of the adsorbed Cr. It was found that both the Cr(VI) and Cr(III) were present on the HTC materials surface after the 1-day Cr(VI) adsorption. It was surprising that only one-third of the

adsorbed Cr(VI) was reduced to Cr(III), rather than the complete reduction in the case of raw MR and SCAIM beads. The N1s XPS spectra of the Cr-laden HTC materials indicated that the anionic Cr(VI) ions were adsorbed by the protonated aliphatic and aromatic amine groups on the HTC materials due to the electrostatic interaction. The O1s spectra of the Cr-laden HTC materials suggested that the Cr(III) ions were bound onto the hydroxyl and carbonyl groups in the HTC materials through coordination. Furthermore, a significant amount of Cr(III) was detected in the solution phase after 1-minute contact with the HTC materials. It was deduced that a portion of the adsorbed Cr(VI) was reduced by the electron-donor groups located on the surface of HTC materials. A portion of the reduced Cr(III) was repelled from the positively-charged adsorbent surface due to the electrostatic repulsion.

In the case of $Fe_3O_4$-0.5PEI-HTC-MR, the interaction between the Fe-O groups and Cr(VI) was demonstrated by the O1s XPS spectrum. The hydroxide functional groups on the $Fe_3O_4$ nanoparticles were protonated in the acidic adsorption environment to form the $-OH_2^+$ groups. The Cr(VI) anions were also adsorbed onto the positively-charged of $Fe_3O_4$ nanoparticles due to the electrostatic attraction.

In conclusion, these results proposed that the Cr(VI) ions were removed by the HTC materials through two mechanisms: (1) direct adsorption and (2) adsorption-coupled reduction mechanisms. The first Cr(VI) removal mechanism was the direct adsorption which the anionic Cr(VI) ions bound to the positively-charged functional groups on the HTC material surface by

electrostatic interaction. Therefore, the Cr(VI) was present on the surface of Cr-laden HTC materials. The second Cr(VI) removal mechanism was the adsorption-coupled reduction mechanism which consisted of four steps (Figure 5-42). First, the Cr(VI) ions were adsorbed onto the adsorption surface groups through the electrostatic attraction. Second, the adsorbed Cr(VI) ions were reduced to Cr(III) ions by reductive groups (e.g. hydroxyl and amine groups) on the adsorbent surface. The hydroxyl and amine groups were oxidized to carbonyl and imine groups, respectively. Third, a portion of the reduced Cr(III) ions were adsorbed by the hydroxyl and carbonyl groups through coordination. Forth, the remaining portion of the reduced Cr(III) ions were released back to the solution phase due to the electrostatic repulsion between the positively-charged Cr(III) and the protonated adsorbent's surface. By this mechanism, the Cr(III) could be found on the surface of Cr-laden HTC materials and the solution phase. The co-existence of the direct Cr(VI) adsorption and the Cr(VI) adsorption-coupled reduction mechanisms gave an explanation to the presence of Cr(VI) and Cr(III) ions on the surface of HTC materials and the existence of Cr(III) ions in the solution phase.

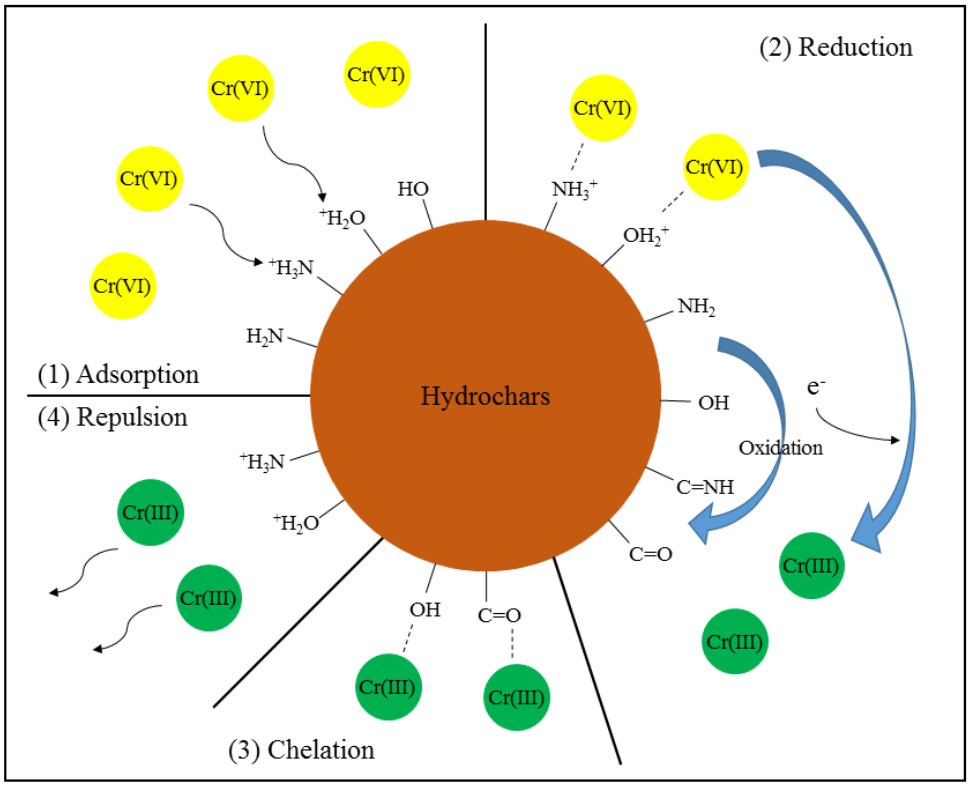


Figure 5-42 The Cr(VI) removal mechanism by the HTC materials.

# 6. Conclusions

In the first part of this study, *Mucor rouxii* was successfully immobilized by the silica-doped calcium alginate and the immobilized *M. rouxii* was applied as an adsorbent for Cr(VI) removal. Silica-doped calcium-alginate-immobilized *M. rouxii* (SCAIM) was demonstrated to be an excellent adsorbent for removal of Cr(VI) in aqueous solutions. Not only the immobilized *M. rouxii* but also the ethylenediamine groups on the silica participated in the Cr(VI) removal and Cr adsorption. Batch Cr(VI) removal study indicated that the optimal pH for Cr adsorption was pH 2.0. The maximum experimental Cr(VI) removal capacity of the SCAIM was 131.8 ±1.4 mg/g. Immobilization of biomass provided a possibility in continuous Cr(VI) removal in a fixed-bed column. Continuous Cr(VI) removal studies showed that the performance of SCAIM column was better at a lower flow rate and a lower influent Cr(VI) concentration. Efficient recovery of Cr(III) was achieved using 2.0 M $HNO_3$. In addition, the adsorbents were characterized using FTIR, SEM, and XPS in order to determine the Cr(VI) removal mechanism. The adsorption-coupled reduction mechanism was confirmed to have occurred in MR and SCAIM. Hence, the SCAIM would be promising adsorbents for detoxifying simulated effluents containing hexavalent chromium in batch and continuous modes.

Moreover, novel silica-doped zirconium alginate immobilized *M. rouxii* (SZAIM) was successfully fabricated from the SCAIM by ion-exchange method. Results of the batch Cr(VI) adsorption study demonstrated that the experimental maximum Cr(VI) removal capacity of SZAIM at pH 2.0 was 169.6 ± 2.6 mg/g, which was much higher than that of SCAIM. The

Langmuir isotherm and the pseudo-second-order kinetic models were the best-fit models to simulate the Cr(VI) removal kinetics and total Cr adsorption isotherm of SZAIM, respectively. XPS analysis revealed that both the electrostatic adsorption and adsorption-coupled reduction were the major Cr(VI) removal mechanisms of SZAIM. Therefore, the novel SZAIM would be a potential adsorbent for the removal of Cr(VI) from contaminated water.

In the second part of this study, the hydrothermal carbonized *M. rouxii* (HTC-MR) was prepared by a simple one-pot hydrothermal treatment of biomass suspension at 200°C for 12 hours. Amine functionalization of HTC-MR was carried out by co-carbonization of *M. rouxii* with the amine-containing modifying agent in the hydrothermal condition. The DEA- and PEI-co-carbonized HTC-MR showed improving Cr(VI) removal capacity and removal rate, implying the successful surface functionalization of HTC-MR. The optimal pH for Cr(VI) removal was pH 2.0 and the Cr(VI) removal kinetics of HTC materials could attain an equilibrium within 1 day. Based on the Langmuir isotherm, the maximum total Cr adsorption capacities of HTC-MR, 0.5DEA-HTC-MR and 0.5PEI-HTC-MR was 115.7 ± 10.8, 269.8 ± 5.9 and 414.6 ± 11.5 mg/g, respectively. Cr-laden HTC materials could be regenerated by the treatment of either acid ($HNO_3$) or alkaline (NaOH) solution. The desorption results showed that the Cr(VI) reduction was catalyzed in acidic desorption agent (2.0 M $HNO_3$) since 100% of the desorbed Cr was Cr(III). Meanwhile, the adsorbed Cr(VI) ions on Cr-laden HTC-MR could be directly desorbed by 2.0 M NaOH. Characterization results from FTIR, XPS and NMR

indicated that the HTC materials contained large amounts of oxygen-containing groups (e.g., hydroxyl, aldehyde and ketone) and nitrogen-containing groups (e.g., aliphatic amine, aromatic amine, amide, pyrrole and furan), which participated in the Cr(VI) adsorption. Low degree of carbonization and aromatization of the HTC materials was further confirmed by the absence of graphitized carbon in the Raman spectrum of HTC materials. The ITC results revealed that the Cr(VI) adsorption process on HTC materials was an exothermic and thermodynamic favorable reaction. Adsorption of Cr(VI) led to an increase in the degree of disorder of the system due to the unfolding of the polymeric structure in the HTC materials. Both Cr(VI) and Cr(III) were found on the surface of Cr-laden HTC materials, suggesting the adsorbed Cr(VI) ions were partially reduced to Cr(III) by reductive groups. In addition, the incorporation of $Fe_3O_4$ nanoparticles in the 0.5-PEI-HTC-MR provided a magnetic characteristic to HTC material without a considerable reduction in Cr(VI) removal capacity. The $Fe_3O_4$-0.5-PEI-HTC-MR would solve the problem in adsorbent recovery after Cr(VI) adsorption.

# 7. Further Studies

In this study, the hydrothermal carbonized *M. rouxii* was demonstrated as an effective Cr(VI) adsorbent, while the silica-doped zirconium alginate method was an excellent immobilizing material that improved the Cr(VI) adsorption capacity. For the further investigations, it would be a great potential to immobilize the polyethyleneimine-modified hydrothermal carbonized *M. rouxii* (0.5PEI-HTC-MR) using the silica-doped calcium-alginate method. The Cr(VI) adsorption performance of the silica-doped calcium-alginate-immobilized hydrothermal carbonized *M. rouxii* bead.(SZA-0.5PEI-HTC-MR) could be then optimized in batch and continuous adsorption modes. The regeneration of Cr-laden SZA-0.5PEI-HTC-MR would be tested using various desorption agents.

Moreover, the removal of anionic pollutants (e.g., As(V), As(III) phosphate and fluoride) by the zirconium-alginate-immobilized *M. rouxii* beads cooud also be analyzed, since the tetravalent Zr(IV) would have a strong interaction to anions.

Lastly, the HTC-MR could be doped with other functional groups, such as carboxylic acid, and thiol groups, and its adsorption capacity to various cationic and anionic pollutants could be examined.

# References

ABBAS, S. H., ISMAIL, I. M., MOSTAFA, T. M. and SULAYMON, A. H. (2014). "Biosorption of heavy metals: a review." Journal of Chemical Science and Technology **3**(4): 74-102.

ABD HAMID, S. B., TEH, S. J. and LIM, Y. S. (2015). "Catalytic hydrothermal upgrading of α-cellulose using iron salts as a lewis acid." BioResources **10**(3): 5974-5986.

AFOLABI, O. O. D., SOHAIL, M. and THOMAS, C. P. L. (2015). "Microwave hydrothermal carbonization of human biowastes." Waste and Biomass Valorization **6**(2): 147-157.

ALATALO, S. M., MAKILA, E., REPO, E., HEINONEN, M., SALONEN, J., KUKK, E., SILLANPAA, M. and TITIRICI, M. M. (2016). "Meso- and microporous soft templated hydrothermal carbons for dye removal from water." Green Chemistry **18**(4): 1137-1146.

AN, Q., LI, X. Q., NAN, H. Y., YU, Y. and JIANG, J. N. (2018). "The potential adsorption mechanism of the biochars with different modification processes to Cr(VI)." Environmental Science and Pollution Research **25**(31): 31346-31357.

ANJANA, K., KAUSHIK, A., KIRAN, B. and NISHA, R. (2007). "Biosorption of Cr(VI) by immobilized biomass of two indigenous strains of cyanobacteria isolated from metal contaminated soil." Journal of Hazardous Materials **148**(1–2): 383-386.

ARICA, M. Y. and BAYRAMOĞLU, G. (2005). "Cr(VI) biosorption from aqueous solutions using free and immobilized biomass of Lentinus sajor-caju: preparation and kinetic characterization." Colloids and Surfaces A: Physicochemical and Engineering Aspects **253**(1–3): 203-211.

BACCILE, N., LAURENT, G., COELHO, C., BABONNEAU, F., ZHAO, L. and TITIRICI, M. M. (2011). "Structural insights on nitrogen-containing hydrothermal carbon using solid-state magic angle spinning 13C and 15N nuclear magnetic resonance." The Journal of Physical Chemistry C **115**(18): 8976-8982.

BAE, S., SIHN, Y., KYUNG, D., YOON, S., EOM, T., KAPLAN, U., KIM, H., SCH FER, T., HAN, S. and LEE, W. (2018). "Molecular identification of Cr(VI) removal mechanism on vivianite surface." Environmental Science & Technology **52**(18): 10647-10656.

BANERJEE, A., NAYAK, D. and LAHIRI, S. (2007). "Speciation-dependent studies on removal of arsenic by iron-doped calcium alginate beads." Applied Radiation and Isotopes **65**(7): 769-775.

BARRERA DIAZ, C. E., LUGO LUGO, V. and BILYEU, B. (2012). "A review of chemical, electrochemical and biological methods for aqueous Cr(VI) reduction." Journal of Hazardous Materials **223-224**: 1-12.

BARRETT, E. P., JOYNER, L. G. and HALENDA, P. P. (1951). "The determination of pore

volume and area distributions in porous substances. I. Computations from nitrogen isotherms." Journal of the American Chemical Society **73**(1): 373-380.

BILGILI, M. S. (2006). "Adsorption of 4-chlorophenol from aqueous solutions by xad-4 resin: Isotherm, kinetic, and thermodynamic analysis." Journal of Hazardous Materials **137**(1): 157-164.

BISHNOI, N. R., KUMAR, R. and BISHNOI, K. (2007). "Biosorption of Cr (VI) with Trichoderma viride immobilized fungal biomass and cell free Ca-alginate beads." Indian Journal of Experimental Biology **45**(7): 657-664.

BOUABIDI, Z. B., EL-NAAS, M. H. and ZHANG, Z. (2018). "Immobilization of microbial cells for the biotreatment of wastewater: A review." Environmental Chemistry Letters **16**(1): 1-17.

BRAGHIROLI, F. L., FIERRO, V., IZQUIERDO, M. T., PARMENTIER, J., PIZZI, A. and CELZARD, A. (2012). "Nitrogen-doped carbon materials produced from hydrothermally treated tannin." Carbon **50**(15): 5411-5420.

BRUN, N., WOHLGEMUTH, S. A., OSICEANU, P. and TITIRICI, M. M. (2013). "Original design of nitrogen-doped carbon aerogels from sustainable precursors: application as metal-free oxygen reduction catalysts." Green Chemistry **15**(9): 2514-2524.

BRUNAUER, S., EMMETT, P. H. and TELLER, E. (1938). "Adsorption of gases in multimolecular layers." Journal of the American Chemical Society **60**(2): 309-319.

CHEN, L. F., LIANG, H. W., LU, Y., CUI, C. H. and YU, S. H. (2011). "Synthesis of an attapulgite clay@carbon nanocomposite adsorbent by a hydrothermal carbonization process and their application in the removal of toxic metal ions from water." Langmuir **27**(14): 8998-9004.

CHEN, M., SHAO, L. L., LI, J. J., PEI, W. J., CHEN, M. K. and XIE, X. H. (2016). "One-step hydrothermal synthesis of hydrophilic Fe3O4/carbon composites and their application in removing toxic chemicals." RSC Advances **6**(42): 35228-35238.

CHEN, T., ZHANG, X. Q., QIAN, J., LI, S. J., JIA, X. H. and SONG, H. J. (2014). "One-step hydrothermal synthesis of carbon@Fe3O4 nanoparticles with high adsorption capacity." Journal of Materials Science: Materials in Electronics **25**(3): 1381-1387.

CHENG, W., DING, C., SUN, Y. and WANG, X. (2015). "Fabrication of fungus/ attapulgite composites and their removal of U(VI) from aqueous solution." Chemical Engineering Journal **269**: 1-8.

CHOY, K. K. H., PORTER, J. F. and MCKAY, G. (2004). "Intraparticle diffusion in single and multicomponent acid dye adsorption from wastewater onto carbon." Chemical Engineering Journal **103**(1): 133-145.

COSTA, C. S. D., QUEIROZ, B. G. M., LANDERS, R., DA SILVA, M. G. C. and VIEIRA, M. G. A. (2018). "Equilibrium study of binary mixture biosorption of Cr(III) and Zn(II) by dealginated seaweed waste: investigation of adsorption mechanisms using X-ray photoelectron

spectroscopy analysis." Environmental Science and Pollution Research.
CRCT. (2015). "FTsalt - FACT Salt Phase Diagrams (284)." Retrieved 25 Jan, 2019, from http://www.crct.polymtl.ca/fact/documentation/FTsalt/FTsalt_Figs.htm.
CUI, X., DAI, X., KHAN, K. Y., LI, T., YANG, X. and HE, Z. (2016). "Removal of phosphate from aqueous solution using magnesium-alginate/chitosan modified biochar microspheres derived from Thalia dealbata." Bioresource Technology **218**: 1123-1132.
DAEMI, H. and BARIKANI, M. (2012). "Synthesis and characterization of calcium alginate nanoparticles, sodium homopolymannuronate salt and its calcium nanoparticles." Scientia Iranica **19**(6): 2023-2028.
DALAL, R. C. (1974). "Desorption of soil phosphate by anion - exchange resin." Communications in Soil Science and Plant Analysis **5**(6): 531-538.
DANESHVAR, N., SALARI, D. and ABER, S. (2002). "Chromium adsorption and Cr(VI) reduction to trivalent chromium in aqueous solutions by soya cake." Journal of Hazardous Materials **94**(1): 49-61.
DE-BASHAN, L. E. and BASHAN, Y. (2010). "Immobilized microalgae for removing pollutants: Review of practical aspects." Bioresource Technology **101**(6): 1611-1627.
DEMIR-CAKAN, R., BACCILE, N., ANTONIETTI, M. and TITIRICI, M.-M. (2009). "Carboxylate-rich carbonaceous materials via one-step hydrothermal carbonization of glucose in the presence of acrylic acid." Chemistry of Materials **21**(3): 484-490.
DEMIRBAŞ, A. (2005). "Adsorption of Cr(III) and Cr(VI) ions from aqueous solutions on to modified lignin." Energy Sources **27**(15): 1449-1455.
DENG, S. and TING, Y. P. (2005). "Fungal biomass with grafted poly(acrylic acid) for enhancement of Cu(II) and Cd(II) biosorption." Langmuir **21**(13): 5940-5948.
DING, D., MA, X., SHI, W., LEI, Z. and ZHANG, Z. (2016). "Insights into mechanisms of hexavalent chromium removal from aqueous solution by using rice husk pretreated using hydrothermal carbonization technology." RSC Advances **6**(78): 74675-74682.
DJAFER, A., KOUADRI MOUSTEFAI, S., IDOU, A. and DOUANI, M. (2013). "Batch and continuous packed column studies biosorption by yeast supported onto granular pozzolana " World Academy of Science, Engineering and Technology **82**: 357-362.
DUBININ, M. M. and RADUSHKEVICH, L. V. (1947). "The equation of the characteristic curve of the activated charcoal." Proceedings of the Academy of Sciences of the USSR: Physical Chemistry Section **55**: 331–337.
ELANGOVAN, R., PHILIP, L. and CHANDRARAJ, K. (2008). "Biosorption of chromium species by aquatic weeds: Kinetics and mechanism studies." Journal of Hazardous Materials **152**(1): 100-112.
ESCUDERO, C., FIOL, N., POCH, J. and VILLAESCUSA, I. (2009). "Modeling of kinetics of Cr(VI) sorption onto grape stalk waste in a stirred batch reactor." Journal of Hazardous Materials **170**(1): 286-291.

FALCO, C., BACCILE, N. and TITIRICI, M.-M. (2011). "Morphological and structural differences between glucose, cellulose and lignocellulosic biomass derived hydrothermal carbons." Green Chemistry **13**(11): 3273-3281.

FALCO, C., MARCO-LOZAR, J. P., SALINAS-TORRES, D., MORALLON, E., CAZORLA-AMOROS, D., TITIRICI, M. M. and LOZANO-CASTELLO, D. (2013). "Tailoring the porosity of chemically activated hydrothermal carbons: Influence of the precursor and hydrothermal carbonization temperature." Carbon **62**(Supplement C): 346-355.

FALCO, C., SEVILLA, M., WHITE, R. J., ROTHE, R. and TITIRICI, M. M. (2012). "Renewable nitrogen-doped hydrothermal carbons derived from microalgae." ChemSusChem **5**(9): 1834-1840.

FECHLER, N., WOHLGEMUTH, S. A., J KER, P. and ANTONIETTI, M. (2013). "Salt and sugar: direct synthesis of high surface area carbon materials at low temperatures via hydrothermal carbonization of glucose under hypersaline conditions." Journal of Materials Chemistry A **1**(33): 9418-9421.

FELLENZ, N., PEREZ-ALONSO, F. J., MARTIN, P. P., GARC A-FIERRO, J. L., BENGOA, J. F., MARCHETTI, S. G. and ROJAS, S. (2017). "Chromium (VI) removal from water by means of adsorption-reduction at the surface of amino-functionalized MCM-41 sorbents." Microporous and Mesoporous Materials **239**: 138-146.

FRESE, N., TAYLOR MITCHELL, S., BOWERS, A., G LZH USER, A. and SATTLER, K. (2017). "Diamond-like carbon nanofoam from low-temperature hydrothermal carbonization of a sucrose/naphthalene precursor solution." Journal of Carbon Research **3**(3): 23.

FREUNDLICH, H. M. F. (1906). "Over the adsorption in solution." The Journal of Physical Chemistry **57**: 385-471.

FU, F. and WANG, Q. (2011). "Removal of heavy metal ions from wastewaters: A review." Journal of Environmental Management **92**(3): 407-418.

FUKAMIZO, T., SONODA, K., TOYODA, H., OUCHI, S. and GOTO, S. (1990). "Solid state 13C-NMR analysis of cell wall components of Fusarium oxysporum." Agricultural and Biological Chemistry **54**(10): 2761-2762.

GAO, S., FAN, H. and ZHANG, S. (2014). "Nitrogen-enriched carbon from bamboo fungus with superior oxygen reduction reaction activity." Journal of Materials Chemistry A **2**(43): 18263-18270.

GARLASCHELLI, F., ALBERTI, G., FIOL, N. and VILLAESCUSA, I. (2017). "Application of Anodic Stripping Voltammetry to assess sorption performance of an industrial waste entrapped in alginate beads to remove As(V)." Arabian Journal of Chemistry **10**: S1014-S1021.

GARZA-GONZ LEZ, M. T., RAM REZ-V ZQUEZ, J. E., GARC A-HERN NDEZ, M. D. L. Á., CANT -C RDENAS, M. E., LI AN-MONTES, A. and VILLARREAL-CHIU, J. F. (2017). "Reduction of chromium (VI) from aqueous solution by biomass of Cladosporium cladosporioides." Water Science and Technology **76**(9): 2494-2502.

GOKHALE, S. V., JYOTI, K. K. and LELE, S. S. (2009). "Modeling of chromium (VI) biosorption by immobilized Spirulina platensis in packed column." Journal of Hazardous Materials **170**(2–3): 735-743.

GONG, X., LI, W., WANG, K. and HU, J. (2013). "Study of the adsorption of Cr(VI) by tannic acid immobilised powdered activated carbon from micro-polluted water in the presence of dissolved humic acid." Bioresource Technology **141**: 145-151.

GOPALAKANNAN, V. and VISWANATHAN, N. (2016). "One pot synthesis of metal ion anchored alginate–gelatin binary biocomposite for efficient Cr(VI) removal." International Journal of Biological Macromolecules **83**: 450-459.

GU, D., MA, R., ZHOU, Y., WANG, F., YAN, K., LIU, Q. and WANG, J. (2017). "Synthesis of nitrogen-doped porous carbon spheres with improved porosity toward the electrocatalytic oxygen reduction." ACS Sustainable Chemistry & Engineering **5**(11): 11105-11116.

GU, J., WANG, W., ZHANG, Q., MENG, Z., JIA, X. and XI, K. (2013). "Synthesis of fluorescent carbon nanoparticles from polyacrylamide for fast cellular endocytosis." RSC Advances **3**(36): 15589-15591.

HAN, X., WONG, Y. S., WONG, M. H. and TAM, N. F. Y. (2007). "Biosorption and bioreduction of Cr(VI) by a microalgal isolate, Chlorella miniata." Journal of Hazardous Materials **146**(1): 65-72.

HARMAS, M., THOMBERG, T., KURIG, H., ROMANN, T., JANES, A. and LUST, E. (2016). "Microporous–mesoporous carbons for energy storage synthesized by activation of carbonaceous material by zinc chloride, potassium hydroxide or mixture of them." Journal of Power Sources **326**: 624-634.

HASSAN, A. F., ABDEL-MOHSEN, A. M. and FOUDA, M. M. G. (2014). "Comparative study of calcium alginate, activated carbon, and their composite beads on methylene blue adsorption." Carbohydrate Polymers **102**: 192-198.

HE, C., GIANNIS, A. and WANG, J. Y. (2013). "Conversion of sewage sludge to clean solid fuel using hydrothermal carbonization: Hydrochar fuel characteristics and combustion behavior." Applied Energy **111**: 257-266.

HE, J. and CHEN, J. P. (2014). "A comprehensive review on biosorption of heavy metals by algal biomass: Materials, performances, chemistry, and modeling simulation tools." Bioresource Technology **160**: 67-78.

HKSAR (1997). Technical memorandum - Standards for effluents discharged into drainage and sewerage systems, inland and coastal waters. CAP358AK. HKSAR.

HUA, X.-W., BAO, Y.-W., WANG, H.-Y., CHEN, Z. and WU, F.-G. (2017). "Bacteria-derived fluorescent carbon dots for microbial live/dead differentiation." Nanoscale **9**(6): 2150-2161.

HUANG, L., HE, M., CHEN, B.-B., CHENG, Q. and HU, B. (2017a). "Highly efficient magnetic nitrogen-doped porous carbon prepared by one-Step carbonization Strategy for Hg2+ removal from water." ACS Applied Materials & Interfaces **9**(3): 2550-2559.

HUANG, M., MISHRA, S. B. and LIU, S. (2017b). "Ethylenediamine and glucose based-assisted coating of activated carbon on silica sand prepared via hydrothermal technique for entrapping Cr(VI) as a glass colorant." Journal of Alloys and Compounds **718**: 270-278.

HUANG, S. H. and CHEN, D. H. (2009). "Rapid removal of heavy metal cations and anions from aqueous solutions by an amino-functionalized magnetic nano-adsorbent." Journal of Hazardous Materials **163**(1): 174-179.

IARC (2012). IARC monographs - Chromium (VI) compounds. **100C:** 147 - 167.

IBRAHIM, B., SCHLEGEL, M. and KANSWOHL, N. (2018). "Effectiveness of biochar from hydrothermal carbonization of wetland biomass for sorption of ammonia." Chemie Ingenieur Technik **90**(3): 340-347.

JAYARAMAN, S., JAIN, A., ULAGANATHAN, M., EDISON, E., SRINIVASAN, M. P., BALASUBRAMANIAN, R., ARAVINDAN, V. and MADHAVI, S. (2017). "Li-ion vs. Na-ion capacitors: A performance evaluation with coconut shell derived mesoporous carbon and natural plant based hard carbon." Chemical Engineering Journal **316**(Supplement C): 506-513.

JIAN, X., ZHUANG, X., LI, B., XU, X., WEI, Z., SONG, Y. and JIANG, E. (2018). "Comparison of characterization and adsorption of biochars produced from hydrothermal carbonization and pyrolysis." Environmental Technology & Innovation **10**: 27-35.

JIANG, W., CAI, Q., XU, W., YANG, M., CAI, Y., DIONYSIOU, D. D. and O'SHEA, K. E. (2014). "Cr(VI) adsorption and reduction by humic acid coated on magnetite." Environmental Science & Technology **48**(14): 8078-8085.

JOO-HEE, H., MYUNG-CHUL, P., SUNG-KYU, H. and BYOUNG-SIK, K. (2009). "Preparation of an anion-exchange membrane by the amination of chlorinated polypropylene and polyethyleneimine at a low temperature and its ion-exchange property." Journal of Applied Polymer Science **112**(2): 830-835.

JUNG, K.-W., JEONG, T.-U., KANG, H.-J. and AHN, K.-H. (2016). "Characteristics of biochar derived from marine macroalgae and fabrication of granular biochar by entrapment in calcium-alginate beads for phosphate removal from aqueous solution." Bioresource Technology **211**: 108-116.

KANG, S., LI, X., FAN, J. and CHANG, J. (2012). "Characterization of hydrochars produced by hydrothermal carbonization of lignin, cellulose, d-xylose, and wood meal." Industrial & Engineering Chemistry Research **51**(26): 9023-9031.

KIRAN, B. and KAUSHIK, A. (2008). "Cyanobacterial biosorption of Cr(VI): Application of two parameter and Bohart Adams models for batch and column studies." Chemical Engineering Journal **144**(3): 391-399.

KUMAR, I. A. and VISWANATHAN, N. (2017). "Fabrication of metal ions cross-linked alginate assisted biocomposite beads for selective phosphate removal." Journal of Environmental Chemical Engineering **5**(2): 1438-1446.

KUMAR, J., MALLAMPATI, R., ADIN, A. and VALIYAVEETTIL, S. (2014). "Functionalized

carbon spheres for extraction of nanoparticles and catalyst support in water." ACS Sustainable Chemistry & Engineering **2**(12): 2675-2682.

KUMAR, S., LOGANATHAN, V. A., GUPTA, R. B. and BARNETT, M. O. (2011). "An assessment of U(VI) removal from groundwater using biochar produced from hydrothermal carbonization." Journal of Environmental Management **92**(10): 2504-2512.

KWAK, H. W., KIM, M. K., LEE, J. Y., YUN, H., KIM, M. H., PARK, Y. H. and LEE, K. H. (2015). "Preparation of bead-type biosorbent from water-soluble Spirulina platensis extracts for chromium (VI) removal." Algal Research **7**: 92-99.

LAGINHAS, C., NABAIS, J. M. V. and TITIRICI, M. M. (2016). "Activated carbons with high nitrogen content by a combination of hydrothermal carbonization with activation." Microporous and Mesoporous Materials **226**(Supplement C): 125-132.

LANGMUIR, I. (1916). "The constitution and fundamental properties of solids and liquids. Part I. Solids " Journal of the American Chemical Society **38**(11): 2221-2295.

LEE, J. H., KIM, J. H., CHOI, K., KIM, H. G., PARK, J. A., CHO, S. H., HONG, S. W., LEE, J. H., LEE, J. H., LEE, S., LEE, S. Y. and CHOI, J. W. (2018). "Investigation of the mechanism of chromium removal in (3-aminopropyl)trimethoxysilane functionalized mesoporous silica." Scientific Reports **8**(1): 12078.

LEI, Y., SU, H. and TIAN, R. (2016). "Morphology evolution, formation mechanism and adsorption properties of hydrochars prepared by hydrothermal carbonization of corn stalk." RSC Advances **6**(109): 107829-107835.

LESMANA, S. O., FEBRIANA, N., SOETAREDJO, F. E., SUNARSO, J. and ISMADJI, S. (2009). "Studies on potential applications of biomass for the separation of heavy metals from water and wastewater." Biochemical Engineering Journal **44**(1): 19-41.

LI, C. L., OU, C. M., HUANG, C. C., WU, W. C., CHEN, Y. P., LIN, T. E., HO, L. C., WANG, C. W., SHIH, C. C., ZHOU, H. C., LEE, Y. C., TZENG, W. F., CHIOU, T. J., CHU, S. T., CANG, J. and CHANG, H. T. (2014a). "Carbon dots prepared from ginger exhibiting efficient inhibition of human hepatocellular carcinoma cells." Journal of Materials Chemistry B **2**(28): 4564-4571.

LI, T., SHEN, J., HUANG, S., LI, N. and YE, M. (2014b). "Hydrothermal carbonization synthesis of a novel montmorillonite supported carbon nanosphere adsorbent for removal of Cr (VI) from waste water." Applied Clay Science **93-94**(Supplement C): 48-55.

LIM, S. Y., KIM, K.-O., KIM, D.-M. and PARK, C. B. (2009). "Silica-coated alginate beads for in vitro protein synthesis via transcription/translation machinery encapsulation." Journal of Biotechnology **143**(3): 183-189.

LIN, F., WANG, Y. and LIN, Z. (2016). "One-pot synthesis of nitrogen-enriched carbon spheres for hexavalent chromium removal from aqueous solution." RSC Advances **6**(39): 33055-33062.

LIU, R., GAO, M., ZHANG, J., LI, Z., CHEN, J., LIU, P. and WU, D. (2015). "An ionic liquid promoted microwave-hydrothermal route towards highly photoluminescent carbon dots for

sensitive and selective detection of iron(iii)." RSC Advances **5**(31): 24205-24209.
LIU, Z. and BALASUBRAMANIAN, R. (2012). "Hydrothermal carbonization of waste biomass for energy generation." Procedia Environmental Sciences **16**(Supplement C): 159-166.
LO, L. S. (2013). The performances and mechanisms of Cd(II) and Cr(VI) removal by a low-cost filamentous fungal biomass. Doctor of philosophy, The Hong Kong Polytechnic University.
LOPEZ-GARCIA, M., LODEIRO, P., BARRIADA, J. L., HERRERO, R. and SASTRE DE VICENTE, M. E. (2010). "Reduction of Cr (VI) levels in solution using bracken fern biomass: Batch and column studies." Chemical Engineering Journal **165**(2): 517-523.
LUO, T., TIAN, X., YANG, C., LUO, W., NIE, Y. and WANG, Y. (2017). "Polyethylenimine-functionalized corn bract, an agricultural waste material, for efficient removal and recovery of Cr(VI) from aqueous solution." Journal of Agricultural and Food Chemistry **65**(33): 7153-7158.
LV, G., LI, Z., JIANG, W.-T., ACKLEY, C., FENSKE, N. and DEMARCO, N. (2014). "Removal of Cr(VI) from water using Fe(II)-modified natural zeolite." Chemical Engineering Research and Design **92**(2): 384-390.
MAKELA, M., BENAVENTE, V. and FULLANA, A. (2015). "Hydrothermal carbonization of lignocellulosic biomass: Effect of process conditions on hydrochar properties." Applied Energy **155**(Supplement C): 576-584.
MEHTA, V. N., JHA, S., BASU, H., SINGHAL, R. K. and KAILASA, S. K. (2015). "One-step hydrothermal approach to fabricate carbon dots from apple juice for imaging of mycobacterium and fungal cells." Sensors and Actuators B: Chemical **213**(Supplement C): 434-443.
MEHTA, V. N., JHA, S. and KAILASA, S. K. (2014). "One-pot green synthesis of carbon dots by using Saccharum officinarum juice for fluorescent imaging of bacteria (Escherichia coli) and yeast (Saccharomyces cerevisiae) cells." Materials Science and Engineering: C **38**(Supplement C): 20-27.
MENAKBI, C., QUIGNARD, F. and MINEVA, T. (2016). "Complexation of Trivalent Metal Cations to Mannuronate Type Alginate Models from a Density Functional Study." The Journal of Physical Chemistry B **120**(15): 3615-3623.
MIN, J. H. and HERING, J. G. (1998). "Arsenate sorption by Fe(III)-doped alginate gels." Water Research **32**(5): 1544-1552.
MTHOMBENI, N. H., MBAKOP, S., RAY, S. C., LESWIFI, T., OCHIENG, A. and ONYANGO, M. S. (2018). "Highly efficient removal of chromium (VI) through adsorption and reduction: A column dynamic study using magnetized natural zeolite-polypyrrole composite." Journal of Environmental Chemical Engineering **6**(4): 4008-4017.
NAKAMOTO, K. (2009). Infrared and Raman spectra of inorganic and coordination compounds. Hoboken, N.J., John Wiley & Sons, Inc.
NATA, I. F., WANG, S. S. S., WU, T. M. and LEE, C. K. (2012). "Carbonaceous hydrogels based on hydrothermal carbonization of glucose with chitin nanofibers." Soft Matter **8**(13): 3522-3525.

OWLAD, M., AROUA, M. K., DAUD, W. A. W. and BAROUTIAN, S. (2009). "Removal of hexavalent chromium-contaminated water and wastewater: A review." Water, Air, and Soil Pollution **200**(1): 59-77.

OZER, T. B., ERKAYA, I. A., UDOH, A. U., DUYGU, D. Y., AKBULUT, A., BAYRAMOGLU, G. and ARICA, M. Y. (2012). "Biosorption of Cr(VI) by free and immobilized Pediastrum boryanum biomass: equilibrium, kinetic, and thermodynamic studies." Environmental Science and Pollution Research **19**(7): 2983-2993.

PAPAGEORGIOU, S. K., KOUVELOS, E. P., FAVVAS, E. P., SAPALIDIS, A. A., ROMANOS, G. E. and KATSAROS, F. K. (2010). "Metal–carboxylate interactions in metal–alginate complexes studied with FTIR spectroscopy." Carbohydrate Research **345**(4): 469-473.

PARAKNOWITSCH, J. P., THOMAS, A. and ANTONIETTI, M. (2009). "Carbon colloids prepared by hydrothermal carbonization as efficient fuel for indirect carbon fuel cells." Chemistry of Materials **21**(7): 1170-1172.

PARK, D., YUN, Y.-S., AHN, C. K. and PARK, J. M. (2007). "Kinetics of the reduction of hexavalent chromium with the brown seaweed Ecklonia biomass." Chemosphere **66**(5): 939-946.

PARK, D., YUN, Y.-S. and PARK, J. M. (2005). "Studies on hexavalent chromium biosorption by chemically-treated biomass of Ecklonia sp." Chemosphere **60**(10): 1356-1364.

PARSHETTI, G. K., CHOWDHURY, S. and BALASUBRAMANIAN, R. (2014). "Hydrothermal conversion of urban food waste to chars for removal of textile dyes from contaminated waters." Bioresource Technology **161**: 310-319.

PAUDYAL, H., PANGENI, B., INOUE, K., KAWAKITA, H., OHTO, K., GHIMIRE, K. N. and ALAM, S. (2013). "Preparation of novel alginate based anion exchanger from Ulva japonica and its application for the removal of trace concentrations of fluoride from water." Bioresource Technology **148**: 221-227.

PILEIDIS, F. D. and TITIRICI, M.-M. (2016). "Levulinic Acid Biorefineries: New Challenges for Efficient Utilization of Biomass." ChemSusChem **9**(6): 562-582.

POERSCHMANN, J., WEINER, B., KOEHLER, R. and KOPINKE, F.-D. (2017). "Hydrothermal carbonization of glucose, fructose, and xylose—identification of organic products with medium molecular masses." ACS Sustainable Chemistry & Engineering **5**(8): 6420-6428.

PRABHAKARAN, S. K., VIJAYARAGHAVAN, K. and BALASUBRAMANIAN, R. (2009). "Removal of Cr(VI) ions by spent tea and coffee dusts: reduction to Cr(III) and biosorption." Industrial & Engineering Chemistry Research **48**(4): 2113-2117.

QIU, B., WANG, Y., SUN, D., WANG, Q., ZHANG, X., WEEKS, B. L., O'CONNOR, R., HUANG, X., WEI, S. and GUO, Z. (2015). "Cr(VI) removal by magnetic carbon nanocomposites derived from cellulose at different carbonization temperatures." Journal of Materials Chemistry A **3**(18): 9817-9825.

RAMRAKHIANI, L., MAJUMDER, R. and KHOWALA, S. (2011). "Removal of hexavalent chromium by heat inactivated fungal biomass of Termitomyces clypeatus: Surface characterization and mechanism of biosorption." Chemical Engineering Journal **171**(3): 1060-1068.

RAMTEKE, L. P. and GOGATE, P. R. (2016). "Treatment of water containing heavy metals using a novel approach of immobilized modified sludge biomass based adsorbents." Separation and Purification Technology **163**: 215-227.

RAWAT, M., RAWAT, A. P., GIRI, K. and RAI, J. P. N. (2013). "Cr(VI) sorption by free and immobilised chromate-reducing bacterial cells in PVA–alginate matrix: equilibrium isotherms and kinetic studies." Environmental Science and Pollution Research **20**(8): 5198-5211.

REN, X., LIU, J., REN, J., TANG, F. and MENG, X. (2015). "One-pot synthesis of active copper-containing carbon dots with laccase-like activities." Nanoscale **7**(46): 19641-19646.

REZA, M. T., ANDERT, J., WIRTH, B., BUSCH, D., PIELERT, J., LYNAM, J. G. and MUMME, J. (2014). "Hydrothermal carbonization of biomass for energy and crop production." Applied Bioenergy **1**: 11-29.

RILLIG, M. C., WAGNER, M., SALEM, M., ANTUNES, P. M., GEORGE, C., RAMKE, H.-G., TITIRICI, M.-M. and ANTONIETTI, M. (2010). "Material derived from hydrothermal carbonization: Effects on plant growth and arbuscular mycorrhiza." Applied Soil Ecology **45**(3): 238-242.

ROHRDANZ, M., REBLING, T., OHLERT, J., JASPER, J., GREVE, T., BUCHWALD, R., VON FRIELING, P. and WARK, M. (2016). "Hydrothermal carbonization of biomass from landscape management – Influence of process parameters on soil properties of hydrochars." Journal of Environmental Management **173**(Supplement C): 72-78.

RONIX, A., PEZOTI, O., SOUZA, L. S., SOUZA, I. P. A. F., BEDIN, K. C., SOUZA, P. S. C., SILVA, T. L., MELO, S. A. R., CAZETTA, A. L. and ALMEIDA, V. C. (2017). "Hydrothermal carbonization of coffee husk: Optimization of experimental parameters and adsorption of methylene blue dye." Journal of Environmental Chemical Engineering **5**(5): 4841-4849.

SAG, Y. (2001). "Biosorption of heavy metals by fungal biomass and modeling of fungal biosorption: A review." Separation and Purification Methods **30**(1): 1-48.

SAKAI, S., ONO, T., IJIMA, H. and KAWAKAMI, K. (2002a). "Aminopropyl-silicate membrane for microcapsule-shaped bioartificial organs: control of molecular permeability." Journal of Membrane Science **202**(1–2): 73-80.

SAKAI, S., ONO, T., IJIMA, H. and KAWAKAMI, K. (2002b). "In vitro and in vivo evaluation of alginate/sol–gel synthesized aminopropyl-silicate/alginate membrane for bioartificial pancreas." Biomaterials **23**(21): 4177-4183.

SAKAI, S., ONO, T., IJIMA, H. and KAWAKAMI, K. (2002c). "Permeability of alginate/sol–gel synthesized aminopropyl-silicate/alginate membrane templated by calcium-alginate gel." Journal of Membrane Science **205**(1): 183-189.

SARANYA, N., AJMANI, A., SIVASUBRAMANIAN, V. and SELVARAJU, N. (2018). "Hexavalent chromium removal from simulated and real effluents using Artocarpus heterophyllus peel biosorbent - Batch and continuous studies." Journal of Molecular Liquids **265**: 779-790.

SAYYADI, S., AHMADY-ASBCHIN, S. and KAMALI, K. (2018). "Biosorption of Cd(II) and Cs(I) from aqueous solution by live and dead cells of Saccharomyces carlsbergensis PTCC 5051." Environmental Technology **39**(4): 450-456.

SELVI, K., PATTABHI, S. and KADIRVELU, K. (2001). "Removal of Cr(VI) from aqueous solution by adsorption onto activated carbon." Bioresource Technology **80**(1): 87-89.

SETSHEDI, K. Z., BHAUMIK, M., SONGWANE, S., ONYANGO, M. S. and MAITY, A. (2013). "Exfoliated polypyrrole-organically modified montmorillonite clay nanocomposite as a potential adsorbent for Cr(VI) removal." Chemical Engineering Journal **222**: 186-197.

SEVILLA, M. and FUERTES, A. B. (2009). "Chemical and structural properties of carbonaceous products obtained by hydrothermal carbonization of saccharides." Chemistry – A European Journal **15**(16): 4195-4203.

SHEN, F., SU, J., ZHANG, X., ZHANG, K. and QI, X. (2016). "Chitosan-derived carbonaceous material for highly efficient adsorption of chromium (VI) from aqueous solution." International Journal of Biological Macromolecules **91**: 443-449.

SHEN, H., CHEN, J., DAI, H., WANG, L., HU, M. and XIA, Q. (2013). "New insights into the sorption and detoxification of chromium(VI) by tetraethylenepentamine functionalized nanosized magnetic polymer adsorbents: Mechanism and pH effect." Industrial & Engineering Chemistry Research **52**(36): 12723-12732.

SHU, C. K. (1998). "Degradation Products Formed from Glucosamine in Water." Journal of Agricultural and Food Chemistry **46**(3): 1129-1131.

SIPS, R. (1948). "Combined form of Langmuir and Freundlich equations." J. Chem. Phys. **16** 490–495.

SIWEK, H., BARTKOWIAK, A., WŁODARCZYK, M. and SOBECKA, K. (2016). "Removal of phosphate from aqueous solution using alginate/iron (III) chloride capsules: a laboratory study." Water, Air, & Soil Pollution **227**(11): 427.

SMITH, B. C. (1999). Infrared spectral interpretation : a systematic approach. Boca Raton, Fla., CRC Press.

SUDARSHAN, N. R., HOOVER, D. G. and KNORR, D. (1992). "Antibacterial action of chitosan." Food Biotechnology **6**(3): 257-272.

SUN, X., CHEN, F., WEI, J., ZHANG, F. and PANG, S. (2016). "Preparation of magnetic triethylene tetramine-graphene oxide ternary nanocomposite and application for Cr (VI) removal." Journal of the Taiwan Institute of Chemical Engineers **66**: 328-335.

SUN, X., YANG, L., LI, Q., ZHAO, J., LI, X., WANG, X. and LIU, H. (2014). "Amino-functionalized magnetic cellulose nanocomposite as adsorbent for removal of Cr(VI):

Synthesis and adsorption studies." Chemical Engineering Journal **241**: 175-183.
SURENDRAN, G. and BARAL, S. S. (2018). "Biosorption of Cr(VI) from wastewater using Sorghastrum Nutans L. Nash." Chemistry and Ecology **34**(8): 762-785.
TAN, J., CHEN, H., GAO, Y. and LI, H. (2015). "Nitrogen-doped porous carbon derived from citric acid and urea with outstanding supercapacitance performance." Electrochimica Acta **178**: 144-152.
TEKIN, K., KARAG Z, S. and BEKTAŞ, S. (2014). "A review of hydrothermal biomass processing." Renewable and Sustainable Energy Reviews **40**: 673-687.
TEMPKIN, M. I. and PYZHEV, V. (1940). "Kinetics of ammonia synthesis on promoted iron catalyst." Acta Phys. Chim. USSR **12**: 327–356.
TIAN, X., WANG, W., TIAN, N., ZHOU, C., YANG, C. and KOMARNENI, S. (2016). "Cr(VI) reduction and immobilization by novel carbonaceous modified magnetic Fe3O4/halloysite nanohybrid." Journal of Hazardous Materials **309**: 151-156.
TITIRICI, M. M., ANTONIETTI, M. and BACCILE, N. (2008). "Hydrothermal carbon from biomass: a comparison of the local structure from poly- to monosaccharides and pentoses/hexoses." Green Chemistry **10**(11): 1204-1212.
TITIRICI, M. M., THOMAS, A., YU, S.-H., M LLER, J.-O. and ANTONIETTI, M. (2007). "A Direct Synthesis of Mesoporous Carbons with Bicontinuous Pore Morphology from Crude Plant Material by Hydrothermal Carbonization." Chemistry of Materials **19**(17): 4205-4212.
TITIRICI, M. M., WHITE, R. J., BRUN, N., BUDARIN, V. L., SU, D. S., DEL MONTE, F., CLARK, J. H. and MACLACHLAN, M. J. (2015). "Sustainable carbon materials." Chemical Society Reviews **44**(1): 250-290.
UZAŞ ı, S., TEZCAN, F. and ERIM, F. B. (2014). "Removal of hexavalent chromium from aqueous solution by barium ion cross-linked alginate beads." International Journal of Environmental Science and Technology **11**(7): 1861-1868.
VELKOVA, Z., KIROVA, G., STOYTCHEVA, M., KOSTADINOVA, S., TODOROVA, K. and GOCHEV, V. (2018). "Immobilized microbial biosorbents for heavy metals removal." Engineering in Life Sciences **18**(12): 871-881.
VIEGAS, R. M. C., CAMPINAS, M., COSTA, H. and ROSA, M. J. (2014). "How do the HSDM and Boyd's model compare for estimating intraparticle diffusion coefficients in adsorption processes." Adsorption **20**(5): 737-746.
VOLPE, M., GOLDFARB, J. L. and FIORI, L. (2018). "Hydrothermal carbonization of Opuntia ficus-indica cladodes: Role of process parameters on hydrochar properties." Bioresource Technology **247**(Supplement C): 310-318.
WAN, J., TAO, T., ZHANG, Y., LIANG, X., ZHOU, A. and ZHU, C. (2016). "Phosphate adsorption on novel hydrogel beads with interpenetrating network (IPN) structure in aqueous solutions: kinetics, isotherms and regeneration." RSC Advances **6**(28): 23233-23241.
WAN, Z., LI, M., ZHANG, Q., FAN, Z. and VERPOORT, F. (2018). "Concurrent reduction-

adsorption of chromium using m-phenylenediamine-modified magnetic chitosan: kinetics, isotherm, and mechanism." Environmental Science and Pollution Research **25**(18): 17830-17841.

WANG, C., XU, Z. and ZHANG, C. (2015a). "Polyethyleneimine-functionalized fluorescent carbon dots: water stability, pH sensing, and cellular imaging." ChemNanoMat **1**(2): 122-127.

WANG, Q., LIU, X., ZHANG, L. and LV, Y. (2012a). "Microwave-assisted synthesis of carbon nanodots through an eggshell membrane and their fluorescent application." Analyst **137**(22): 5392-5397.

WANG, X., LIU, J. and XU, W. (2012b). "One-step hydrothermal preparation of amino-functionalized carbon spheres at low temperature and their enhanced adsorption performance towards Cr(VI) for water purification." Colloids and Surfaces A: Physicochemical and Engineering Aspects **415**: 288-294.

WANG, X., ZHAN, C., DING, Y., DING, B., XU, Y., LIU, S. and DONG, H. (2017). "Dual-core Fe2O3@carbon structure derived from hydrothermal carbonization of chitosan as a highly efficient material for selective adsorption." ACS Sustainable Chemistry & Engineering **5**(2): 1457-1467.

WANG, X. S., CHEN, L. F., LI, F. Y., CHEN, K. L., WAN, W. Y. and TANG, Y. J. (2010). "Removal of Cr (VI) with wheat-residue derived black carbon: Reaction mechanism and adsorption performance." Journal of Hazardous Materials **175**(1): 816-822.

WANG, Y., ZOU, H., ZENG, S., PAN, Y., WANG, R., WANG, X., SUN, Q., ZHANG, Z. and QIU, S. (2015b). "A one-step carbonization route towards nitrogen-doped porous carbon hollow spheres with ultrahigh nitrogen content for CO2 adsorption." Chemical Communications **51**(62): 12423-12426.

WEI, L., KARAHAN, H. E., ZHAI, S., YUAN, Y., QIAN, Q., GOH, K., NG, A. K. and CHEN, Y. (2016). "Microbe-derived carbon materials for electrical energy storage and conversion." Journal of Energy Chemistry **25**(2): 191-198.

WEI, W., LI, A., MA, F., PI, S., YANG, J., WANG, Q. and NI, B.-J. (2018). "Simultaneous sorption and reduction of Cr(VI) in aquatic system by microbial extracellular polymeric substances from Klebsiella sp. J1." Journal of Chemical Technology & Biotechnology **93**(11): 3152-3159.

WEINGARTEN, R., CONNER, W. C. and HUBER, G. W. (2012). "Production of levulinic acid from cellulose by hydrothermal decomposition combined with aqueous phase dehydration with a solid acid catalyst." Energy & Environmental Science **5**(6): 7559-7574.

WEN, G., WANG, B., WANG, C., WANG, J., TIAN, Z., SCHL GL, R. and SU, D. S. (2017). "Hydrothermal carbon enriched with oxygenated groups from biomass glucose as an efficient carbocatalyst." Angewandte Chemie **129**(2): 615-619.

WHO (2011). Guidelines for drinking-water quality. WHO.

WOHLGEMUTH, S. A., WHITE, R. J., WILLINGER, M. G., TITIRICI, M. M. and

ANTONIETTI, M. (2012). "A one-pot hydrothermal synthesis of sulfur and nitrogen doped carbon aerogels with enhanced electrocatalytic activity in the oxygen reduction reaction." Green Chemistry **14**(5): 1515-1523.

WU, B., PENG, D., HOU, S., TANG, B., WANG, C. and XU, H. (2018). "Dynamic study of Cr(VI) removal performance and mechanism from water using multilayer material coated nanoscale zerovalent iron." Environmental Pollution **240**: 717-724.

WU, F. C., TSENG, R. L. and JUANG, R. S. (2009). "Characteristics of Elovich equation used for the analysis of adsorption kinetics in dye-chitosan systems." Chemical Engineering Journal **150**(2): 366-373.

WU, Q., LI, W., TAN, J., WU, Y. and LIU, S. (2015). "Hydrothermal carbonization of carboxymethylcellulose: One-pot preparation of conductive carbon microspheres and water-soluble fluorescent carbon nanodots." Chemical Engineering Journal **266**: 112-120.

WU, R., LIU, J.-H., ZHAO, L., ZHANG, X., XIE, J., YU, B., MA, X., YANG, S.-T., WANG, H. and LIU, Y. (2014). "Hydrothermal preparation of magnetic Fe3O4@C nanoparticles for dye adsorption." Journal of Environmental Chemical Engineering **2**(2): 907-913.

XIAO, D., YUAN, D., HE, H. and LU, J. (2013). "Microwave-assisted one-step green synthesis of amino-functionalized fluorescent carbon nitride dots from chitosan." Luminescence **28**(4): 612-615.

XIAO, L. P., SHI, Z. J., XU, F. and SUN, R. C. (2012). "Hydrothermal carbonization of lignocellulosic biomass." Bioresource Technology **118**(Supplement C): 619-623.

XU, Y., LEI, W., ZHANG, Y., FAN, H., HAO, Q. and GAO, S. (2017). "Bamboo fungus-derived porous nitrogen-doped carbon for the fast, sensitive determination of Bisphenol A." Journal of The Electrochemical Society **164**(5): B3043-B3048.

YANG, Y., CHEN, N., FENG, C., LI, M. and GAO, Y. (2018). "Chromium removal using a magnetic corncob biochar/polypyrrole composite by adsorption combined with reduction: Reaction pathway and contribution degree." Colloids and Surfaces A: Physicochemical and Engineering Aspects **556**: 201-209.

YANG, Y., CUI, J., ZHENG, M., HU, C., TAN, S., XIAO, Y., YANG, Q. and LIU, Y. (2012). "One-step synthesis of amino-functionalized fluorescent carbon nanoparticles by hydrothermal carbonization of chitosan." Chemical Communications **48**(3): 380-382.

YOUNES, I., GHORBEL-BELLAAJ, O., NASRI, R., CHAABOUNI, M., RINAUDO, M. and NASRI, M. (2012). "Chitin and chitosan preparation from shrimp shells using optimized enzymatic deproteinization." Process Biochemistry **47**(12): 2032-2039.

ZANG, T., CHENG, Z., LU, L., JIN, Y., XU, X., DING, W. and QU, J. (2017). "Removal of Cr(VI) by modified and immobilized Auricularia auricula spent substrate in a fixed-bed column." Ecological Engineering **99**: 358-365.

ZHANG, C., SU, J., ZHU, H., XIONG, J., LIU, X., LI, D., CHEN, Y. and LI, Y. (2017). "The removal of heavy metal ions from aqueous solutions by amine functionalized cellulose

pretreated with microwave-H2O2." RSC Advances **7**(54): 34182-34191.
ZHANG, F., ZHU, Z., DONG, Z., CUI, Z., WANG, H., HU, W., ZHAO, P., WANG, P., WEI, S., LI, R. and MA, J. (2011). "Magnetically recoverable facile nanomaterials: Synthesis, characterization and application in remediation of heavy metals." Microchemical Journal **98**(2): 328-333.
ZHANG, X., FU, W., YIN, Y., CHEN, Z., QIU, R., SIMONNOT, M. O. and WANG, X. (2018). "Adsorption-reduction removal of Cr(VI) by tobacco petiole pyrolytic biochar: Batch experiment, kinetic and mechanism studies." Bioresource Technology **268**: 149-157.
ZHAO, H. Y., LU, X. A., WANG, Y., SUN, B., WU, X. H. and LU, H. F. (2017a). "Effects of additives on sucrose-derived activated carbon microspheres synthesized by hydrothermal carbonization." Journal of Materials Science **52**(18): 10787-10799.
ZHAO, L., BACCILE, N., GROSS, S., ZHANG, Y., WEI, W., SUN, Y., ANTONIETTI, M. and TITIRICI, M. M. (2010). "Sustainable nitrogen-doped carbonaceous materials from biomass derivatives." Carbon **48**(13): 3778-3787.
ZHAO, R., LI, X., SUN, B., JI, H. and WANG, C. (2017b). "Diethylenetriamine-assisted synthesis of amino-rich hydrothermal carbon-coated electrospun polyacrylonitrile fiber adsorbents for the removal of Cr(VI) and 2,4-dichlorophenoxyacetic acid." Journal of Colloid and Interface Science **487**: 297-309.
ZHAO, R., WANG, Y., LI, X., SUN, B., LI, Y., JI, H., QIU, J. and WANG, C. (2016). "Surface activated hydrothermal carbon-coated electrospun PAN fiber membrane with enhanced adsorption properties for herbicide." ACS Sustainable Chemistry & Engineering **4**(5): 2584-2592.
ZHOU, L., LIU, Y., LIU, S., YIN, Y., ZENG, G., TAN, X., HU, X., HU, X., JIANG, L., DING, Y., LIU, S. and HUANG, X. (2016). "Investigation of the adsorption-reduction mechanisms of hexavalent chromium by ramie biochars of different pyrolytic temperatures." Bioresource Technology **218**: 351-359.
ZHOU, Q., LIN, X., LI, B. and LUO, X. (2014). "Fluoride adsorption from aqueous solution by aluminum alginate particles prepared via electrostatic spinning device." Chemical Engineering Journal **256**: 306-315.
ZHOU, Q., LIN, X., QIAN, J., WANG, J. and LUO, X. (2015). "Porous zirconium alginate beads adsorbent for fluoride adsorption from aqueous solutions." RSC Advances **5**(3): 2100-2112.
ZHU, H., WANG, X., YANG, F. and YANG, X. (2011). "Promising carbons for supercapacitors derived from fungi." Advanced Materials **23**(24): 2745-2748.